AN ABSTRACT OF THE DISSERTATION OF

R. Brian Jackson for the degree of Doctor of Philosophy in Nuclear Engineering presented on June 15, 2012.

Title: An Experimental Study of Laminarization Induced by Acceleration and Curvature

Abstract Approved:_____

Brian G. Woods

The Generation IV Very High Temperature Reactor (VHTR) design is being actively studied in various countries for application due to its inherent passive safe design, higher thermal efficiencies, and proposed capability of providing high temperature process heat. The pebble bed core is one of two core designs used in gas reactors. In the pebble bed core there are mechanisms present which can cause the flow to laminarize, thus reducing its heat transfer effectiveness. Wind tunnel experiments were conducted using Particle Image Velocimetry (PIV) to investigate boundary layer laminarization due to flow acceleration and convex curvature effects. The flow was subject to acceleration and curvature both separately and together and the flow behavior characterized with velocity flow profiles, mean boundary layer parameters, and turbulence quantities. Laminarization was identified and the influence of acceleration and curvature was characterized.

An Experimental Study of Laminarization Induced by Acceleration and Curvature

by
R. Brian Jackson

A Dissertation
submitted to
Oregon State University

in partial fulfillment of
the requirements for the
degree of

Doctor of Philosophy

Presented June 15, 2012
Commencement June 2013

Doctor of Philosophy dissertation of R. Brian Jackson presented on June 15, 2012.

APPROVED:

Major Professor, representing Nuclear Engineering

Head of Department of Nuclear Engineering and Radiation Health Physics

---

Dean of the Graduate School

I understand that my dissertation will become part of the permanent collection of Oregon State University libraries. My signature below authorizes release of my dissertation to any reader upon request.

R. Brian Jackson, Author

ACKNOWLEDGEMENTS

The completion of this research project and degree would not have been possible without the support and guidance of many faculty, staff, fellow students and friends. I would first like to thank Dr. Brian Woods for being a great advisor to me during my PhD studies. I appreciate the independence he allowed and required for me to discover and define this research project, while providing guidance, encouragement, and the occasional push throughout the research process. I would also like to thank the other members of my committee, Dr. Qiao Wu, Dr. Jose Reyes, Dr. James Liburdy, and Dr. Jack Istok, for their guidance, input, and helpful suggestions on my research objectives and methods.

I would also like to thank Dr. Wade Marcum for allowing me to use his lab space and Particle Image Velocimetry System. In addition to sharing his resources, the many discussions and suggestions were instrumental in this research project.

I would also like to thank the many staff and students who provided instruction and assistance in the different areas of this project. Seth Cadell for his general assistance throughout from test section construction to uncertainty analysis, Aaron Weiss for his Matlab and Labview assistance, Jeff Luitjens for his help with instrumentation, Steve Smith for help in the wiring and manufacturer of various experimental apparatus components, Chris Thompson for the quick assistance with computer support, my brothers Nathan and Aaron for advice with test section construction and electronic components respectively, and Brian Hallee, Phil Jensen, and JJ Utberg for always being willing to help me move things in the lab.

TABLE OF CONTENTS

TABLE OF CONTENTS (Continued)

Section Page

TABLE OF CONTENTS (Continued)

LIST OF FIGURES

Figure Page

LIST OF FIGURES (Continued)

Figure Page

LIST OF FIGURES (Continued)

Figure Page

LIST OF TABLES

Table Page

LIST OF APPENDICES

LIST OF APPENDIX FIGURES

Figure Page

LIST OF APPENDIX FIGURES (Continued)

Figure Page

LIST OF APPENDIX TABLES

Table Page

Nomenclature

A		Cross section flow area
C		Form coefficient
C_f	$c_f = 2\tau_w / \rho U^2$	Skin friction coefficient
c_f		Forchheimer coefficient
C_p		Heat capacity
D		diameter
dS		Integration interfacial surface area
g		gravity
G		Mass flux
h		Convection coefficient
h		Metric used in boundary layer equations in curvilinear coordinates
H	$H = \delta^* / \theta$	Shape factor
k		Turbulent kinetic energy
K		Permeability
K	$K = \frac{\nu}{U_\infty^2}\frac{dU_\infty}{dx}$	Acceleration Parameter
l_m	$l_m = \left(\tau/\rho\right)^{0.5} \Big/ \left(dU/dy\right)$	Mixing length parameter
l_{mf}		Mixing length parameter for flat plate
$\dot{m}$		Mass flow
n		Normal vector
P		Pressure
q^+	$q^+ = q_w'' A / \dot{m} T_i$	Non-dimensional heating parameter
Pr		Prandtl number

$\bar{R}$		Drag in REV due to solid matrix
Re_θ	$u\theta/\nu$	Momentum Reynolds number
Ri	$Ri = Gr/\mathrm{Re}^2$	Richardson number
St	$h/U_\infty \rho C_p$	Stanton number
t		Time
T		Temperature
U_∞		Free stream velocity
u_τ	$u_\tau = \sqrt{\tau_w/\rho}$	Friction velocity
V		Volume
V_f		Fluid volume in REV
V_{tot}		Total volume in REV
x		Streamwise direction
x_i^+	$x_i^+ = \dfrac{\left(5\cdot 10^{-4} n \,\mathrm{Re}_i + 1\right)^{1/n} - 1}{2 q_i^+ \,\mathrm{Re}_i \,\mathrm{Pr}_i}$	Length for laminarization to complete by heating
y		Cross-stream direction
β		Thermal expansion coefficient
β		Constant in mixing length parameter
γ		Intermittency function
δ_{ij}		Kronecker delta operator
δ		Boundary layer thickness
δ^*	$\delta^* = \int_0^\infty \left(1 - u/U\right) dy$	Displacement thickness
Δ	$\Delta = \dfrac{4\mu_w}{D_h \sqrt{\rho_w g_c \tau_w}} > 0.02$	Onset of laminarization parameter by heating
Δp	$\Delta p = \dfrac{\nu}{u_\tau^3} \dfrac{dp}{dx}$	Pressure gradient laminarization parameter

$\Delta\tau$	$\Delta\tau = \frac{\nu}{\rho u_\tau^3}\frac{d\tau}{dx}$	Shear stress laminarization parameter
κ		Inverse radius of curvature
Λ	$\Lambda = -\frac{\delta}{\tau_w}\frac{dp}{dx}$	Pressure gradient parameter
μ		Viscosity
μ_{eff}		Effective viscosity
ν		Kinematic viscosity
ρ		Density
τ_w		Wall shear stress
ϕ	$\phi = V_f / V_{tot}$	Porosity
θ	$\theta = \int_0^\infty u/U\left(1 - u/U\right)dy$	Momentum thickness

Acronyms

AVR	Arbeitsgemeinshaft Versuchs Reaktor
BWR	Boiling Water Reactor
CFD	Computational Fluid Dynamics
DNS	Direct Numerical Simulation
DOE	Department of Energy
DTHT	Deteriorated Turbulent Heat Transfer
GFR	Gas Cooled Fast Reactor
GIF	Generation IV International Forum
HTGR	High Temperature Gas Reactor
HTR-M	High Temperature Reactor-Module
IHF	Iso-Heat Wall Flux
INL	Idaho National Laboratory
LES	Large Eddy Simulation
LFR	Lead Cooled Fast Reactor
MSR	Molten Salt Reactor
NGNP	Next Generation Nuclear Plant
NRC	Nuclear Regulatory Commission
PBMR	Pebble Bed Modular Reactor
PWR	Pressurized Water Reactor
RCCS	Reactor Cavity Cooling System
REV	Representative Elementary Volume
SCWR	Supercritical Water Cooled Reactor
SFR	Sodium Cooled Fast Reactor
THTR	Thorium High Temperature Reactor
TRISO	Tristructural –Isotropic Fuel
VHF	Variable Wall Heat Flux
VHTR	Very High Temperature Reactor

1 INTRODUCTION

1.1 Background

Nuclear power has been a significant source of the world's electricity production since its beginnings in the 1950s. Today, 17% of the world's electricity is generated by nuclear power. The 104 nuclear reactors in operation in the United States provide 20% of the country's electricity, and this number looks to increase in the future. The U.S. Department of Energy (DOE), in its energy outlook for 2010, predicts electricity demand will increase by 1.0% per year from 2008 to 2035 [1]. Meeting this demand will require a 30% increase in electricity production, the equivalent of over 100 new 1000-MW power plants. In this day of environmental concern associated with global warming, pollution, and land preservation, nuclear power is an attractive electricity source given its reliability, concentrated energy, cost stability and minimal environmental impact.

There are 58 nuclear power reactors under construction throughout the world, with many more in preliminary stages of planning and licensing [2]. Since 2007, the U.S. Nuclear Regulatory Commission (NRC) has received combined license applications for 26 new power reactors [3]. The technology of nuclear reactors has advanced greatly from the present fleet of reactors in operation in the U.S. today. The PWRs and BWRs in operation today in the U.S. are generation II reactors. Currently, reactors in construction around the world and in the licensing stages in the U.S. are generation III, and generation III+ reactors. Both generation II and III designs provide a reliable, affordable and safe energy source. Generation III reactors add on the performance of Generation II reactor designs by using advanced concepts of safety by implementing passive safety systems.

Looking towards more advanced nuclear power reactors, in 2002 the Generation IV International Forum (GIF) [4] was established to look at new reactor designs that would meet demands for the future. The primary objectives of Generation IV reactors are to:

- Advance Nuclear Safety
- Address Nuclear Nonproliferation and Physical Protection Issues
- Be Competitively Priced
- Minimize Waste and Optimize Natural Resource Utilization

From the many reactor designs that were looked at, six were chosen to be developed as Generation IV reactors. These are:

- Very High Temperature Reactor (VHTR)
- Supercritical Water Cooled Reactor (SCWR)
- Gas Cooled Fast Reactor (GFR)
- Lead Cooled Fast Reactor (LFR)
- Sodium Cooled Fast Reactor (SFR)
- Molten Salt Reactor (MSR)

These reactors were chosen for their ability to meet the primary objectives of Generation IV reactor designs.

Of the reactors being researched in the U.S., priority has been given to the Very High Temperature Reactor. The VHTR design is a part of the High Temperature Gas Reactor (HTGR) class of reactor designs. Most of these are helium cooled, graphite moderated reactors with a design outlet temperature of 750–900 ^{o}C. This general technology that the VHTR will employ has been demonstrated in gas reactors that have operated in the past, both in this country and abroad. The VHTR has inherent passive safety features in its design. This includes a low power density, large amount of graphite in the core, and use of TRISO fuel particles that provide multiple barriers [5]. These safety features provide that in an accident scenario, the thermal response of the reactor is slow, thus limiting the peak fuel temperatures below those associated with TRISO fuel failure and the associated risk of a radioactive release. In 2003 the U.S. Department of Energy (DOE) established the Next Generation Nuclear Plant (NGNP) project that employs the VHTR concept [6]. This project has long term goals of an

outlet temperature of 1000 ^{o}C, with current outlet temperature targets of 750-850 ^{o}C. In addition to the inherent safety features of this type of gas reactor design, the high operating temperatures increase the efficiency limits and could also provide process heat. One of these processes is the use of the high outlet temperatures for hydrogen production.

Initially two core designs were investigated for the VHTR as part of the NGNP project. The prismatic block and pebble bed design. In the prismatic block design, the core consists of stacked graphite blocks, which contain many cylindrical rod shaped fuel elements, and well defined coolant channels through which the helium coolant flows downward as it is heated. In the pebble bed design, the core barrel acts like a large hopper which contains many thousands of fuel pebbles randomly distributed. The helium is heated as it flows between and around these pebbles downward through the core. There are many complexities associated with this type of flow that inhibit a thorough understanding and modeling of the core flow, which in turn affects the operation and safety of the reactor. These include the random packing of the pebbles, wall effects, the unsteady nature of flow past pebbles, and turbulence characteristics of the flow. One specific phenomena of concern in gas reactors is that of laminarization. Laminarization occurs when turbulence in a turbulent flow is reduced such that the flow characteristics such as flow profile, heat transfer and bulk boundary layer parameters are more characteristic of a laminar flow regime. In the literature there are many examples of laminarization. This is of concern in gas reactors because laminarization decreases the local heat transfer which can affect the efficiency and safety of the reactor. There are mechanisms that are known to cause laminarization that are present in both types of gas reactors, and specifically pebble bed gas reactors. This research work is focused on acquiring experimental data to better characterize these laminarization causing mechanisms in geometries characteristic of pebble bed reactors.

1.2 Laminarization

If turbulent flow can be described as flow that is characterized by irregularity, diffusivity, energy dissipation, and local velocity and pressure fluctuations, then

laminarized flow can be described as flow that once had these turbulent characteristics, but has lost them and now acts like streamline laminar flow. For flow over surfaces, previous researchers have identified the flow as laminarized if the initial turbulent boundary layer develops characteristics more in line with laminar boundary layers. These include changes to the shape of the boundary layer, frequency of bursts of turbulence from the wall, thickness of the boundary layer, thickness of the viscous sublayer, wall shear stress values, and levels of turbulent intensities in different layers of the boundary layer and outside the boundary layer in the bulk flow. While there is not a consensus in criteria of laminarization, Narasimha [7] proposed that laminarized flow is flow that can be understood and its flow development predicted without any turbulence shear models. From this definition, and as shown in experiments, flow can be considered laminarized even if there are residual velocity fluctuations as long as they are not sufficient to affect the mean flow. From a practical standpoint, given that laminarization in pebble bed reactors is a boundary layer phenomenon, in this dissertation laminarization is defined as a boundary layer flow that has transitioned from turbulent to laminar as evidenced by a laminar shaped velocity flow profile, a thinning of the boundary layer, a thickening of the viscous sublayer, and a reduction in the skin friction coefficient.

Laminarization has been known to occur due to many mechanisms. Three conditions in particular that are present in the pebble bed core that can cause flow to laminarize are flow acceleration due to geometry convergence, convex boundary layer geometries, and high local heating. The first two mechanisms are geometry dependent. These are present in the pebble bed core due to the flow paths created between the randomly packed pebbles. Heating of gases also can cause laminarization due to the change in temperature dependent gas properties. The heating decreases the gas density, thus increasing the flow acceleration due to conservation of mass. In addition, heating causes an increase in gas viscosity. This increase in viscosity has the effect of increasing the viscous dissipation in the flow, thus reducing the levels of turbulence.

There is not a conclusive quantitative criterion that is used to identify a flow as having transitioned from turbulent to laminar, though many criteria have been proposed.

These include a disappearance of the large eddy structure near the wall, a departure from the law of the wall, and decay of turbulent intensities. Quantitative criteria that have been proposed have been focused on the beginning of the process of laminarization, not when it completes. While some previous studies have focused on establishing criteria for this phenomenon, the focus of most laminarization studies is on the flow response as it becomes more laminar-like when it is subject to laminarization causing mechanisms.

1.3 Motivation

In the prismatic core design, the helium flows through well defined coolant channels. Because of this the heat transfer can be well characterized and predicted using established correlations for the applicable flow regime. On the other hand, the flow paths in a pebble bed reactor are created by the random packing of the pebbles in the core. Therefore the exact local characteristics of the flow are unknown. While there are various pebble bed reactor designs that differ slightly from one another, during normal operations they are all designed to operate in the turbulent flow regime given bulk flow packed bed parameters. Established heat transfer correlations for turbulent flow in packed beds can be used for the overall bed heat transfer behavior. However, in the pebble bed core geometries the local mechanisms that are present can reduce the levels of turbulence, thus causing the flow to laminarize on a local scale. The Next Generation Nuclear Plant Research and Development Program Plan [7] states:

> While criteria for this occurrence [laminarization] have been hypothesized for turbulent boundary layer flows, none is known for converging flows in porous media. Appropriate measurements are needed to quantify this phenomenon and, hence, to determine its importance in pebble bed reactor technology.

While studies have been performed in the past to look at laminarization due to different mechanisms, these experimental studies have been performed for simplified

geometries such as channels, flat plates, or simple bends. The most common methodology for these experimental studies is to perform many runs varying the laminarization mechanism of interest (acceleration, curvature, heating) while studying the flow response. Additionally some researchers have correlated the level of the laminarization causing mechanisms with the occurrence of laminarization. Usually the method of identification of laminarization is directly related to the measurement method in the experiment, i.e. flow profile, turbulent intensity, etc. The occurrence or absence of laminarization for different amounts of acceleration, curvature, or heating is then used in the development of a non-dimensional parameter to be used to predict when laminarization will occur. The non-dimensional parameter, or laminarization parameter, is often a pressure- or acceleration-gradient parameter using initial flow or boundary conditions. Characterizing laminarizing flows in this manner with these types of parameters has some shortcomings. The first is that some of these laminarization parameters are given in terms of bulk flow characteristics. While this is convenient to use, and good agreement has been shown between predictions using these bulk flow laminarization parameters and the laminarization phenomenon, these parameters do not directly contain any boundary layer information where the laminarization phenomenon occurs. Other studies have presented the laminarization parameter using boundary layer variables which may be more descriptive of the flow phenomenon and better identify what is occurring, but is of little use to the engineer as usually the boundary layer information that makes up the parameter is unknown unless measured directly.

Due to the complexity of the laminarization phenomenon, very little analytical work has been accomplished. This is due to the fact that an analytical model needs to be capable of turning off turbulent energy production for conditions that cause laminarization. Even for the simple case of laminarization due to acceleration over a flat plate, the proposed analytic treatment of the turbulent boundary layer equations is very incomplete. If a complete predictive model is beyond current capabilities, at least an accurate understanding of these laminarization causing mechanisms and the resulting turbulence characteristics are desired for pebble bed reactor flows [8]. In the literature, various turbulence modeling techniques have been proposed for packed beds. These

include Reynolds Averaged Navier Stokes turbulence models averaged over volumes containing both fluid and pebble components. These models calculate general turbulence production and dissipation rates for the flow, though due to the volume averaging applied, local effects, such as boundary layer laminarization is lost. Other methods include large scale three dimensional computational fluid dynamics (CFD) modeling where the computational grid is applied to all fluid paths. This has the limiting constraint of requiring very large computing resources due to the fine grid required to mesh the complex and large geometries of pebble bed cores. In addition, Reynolds Averaged Navier Stokes (RANS) turbulence models have difficulty properly suppressing turbulence production when subject to the mechanisms that can cause laminarization. The final wrinkle in CFD modeling is that without information of the specific packing in the pebble bed, it can only be applied to regular packed bed geometries.

Experimental work has provided much understanding for the mechanisms that can cause laminarization, but absent in the experimental work is how the specific conditions can cause the flow to laminarize on a local scale between fuel pebbles. This is primarily due to the difficulty associated with obtaining local measurements between the pebbles. Added to this difficulty is the challenge of properly characterizing the boundary conditions upstream of the area where laminarization is expected to occur. While these challenges present obstacles in quantifying the laminarization phenomenon in pebble beds, there are still areas of experimental research that would provide new information necessary in the advancement to quantify pebble bed laminarization. One specific area is further study on the tendency for a flow to laminarize when subject to both acceleration and flow over convex surfaces. Considering this, this dissertation focuses on laminarization flows subject to levels of acceleration and curvature to be expected in pebble beds. The cumulative effect of both these mechanisms together is investigated by performing experimental runs for the mechanisms alone and together. In addition to providing necessary data to advance the research of laminarization in pebble beds, this data provides additional general laminarization experimental data for conditions new to the open literature.

There have only been a few previous studies that have studied the combined effects of flow acceleration and convex surface curvature on the turbulent characteristics of the flow. Of these only one study successfully investigated the laminarization phenomenon in the boundary layer [106]. This study was performed for flow characteristics expected over swept wing leading edges, and only qualitatively focused on the effect of the combined laminarization causing mechanisms. The current work is focused on conditions expected in pebble bed reactors. In addition to being unique from the previous study in the value of acceleration and radius of curvature, another major difference is the amount of length that the acceleration is applied. The length that the acceleration is applied is usually given in terms of a length normalized by the initial boundary layer thickness. In the random packing of the pebble bed, the convergence causing the acceleration occurs due to the packing of the pebbles next to each other. While the acceleration of the flow between the pebbles can be very large, the length that the acceleration is applied is relatively short.

The general motivation for the study of laminarization is reflected in its practical definition. Its definition does not preclude velocity fluctuations, or that the turbulent history of the flow is completely lost. Instead, the laminarization definition assists the engineer in determining applicable flow regimes and models to use to predict the flow and its accompanying effects on the system, such as heat transfer, skin friction, and pressure drop. Understanding the accurate flow regime in a pebble bed reactor is important because laminarization can affect the operational and safety aspects of the reactor. Safety concerns dealing with laminarization are related to accurate predictions of the local heat transfer. The presence of turbulence aids in heat transfer as evidenced by a larger heat transfer coefficient due to the turbulent eddies, when compared to laminar flow. Reduced local heat transfer can expose the pebbles and reactor internal components to hotspots. Hotspots are detrimental to the fuel because this can damage both the fuel pebble matrix, and most importantly can damage the TRISO fuel particles in the pebble. TRISO fuel particles are designed such that the outer layers act to contain the fission gases. Prolonged exposure to hotspots can damage these layers thus reducing the particle efficiency in containing the fission gases. Hotspots can also cause

damage to internal core components both from local thermal damage and fatigue of where the laminarization is occurring, and also if laminarization causes less uniform coolant gas temperatures which exit from the core, thus increasing the likelihood that hot streaking will occur in lower plenum and downstream regions subjecting components to elevated temperatures.

Laminarization would also affect the operational aspects of the system. Reduced core heat transfer can result in lower outlet gas temperatures, reducing the efficiency of the system. From a pressure drop standpoint, laminarization may not necessarily be a negative result due to the reduction in wall skin friction coefficients that can result, however accurate knowledge of the flow and corresponding pressure drop requirements are needed for operation of the system.

In addition to providing a description of the flow response when subject to these conditions, the results are compared to the predicted occurrence of laminarization using previous researchers' prediction methods of laminarization for flat plate and curvature geometries to determine the applicability of these parameters to cases with both curvature and acceleration.

1.4 Objectives

The objective of this research is to study the flow response behavior for flows subject to conditions present in pebble bed reactors that are known to suppress turbulence and promote laminarization. This data is used to characterize the laminarization phenomenon for these specific conditions. This includes the following objectives:

1. Collect laminarization criteria parameters that are applicable to the physical phenomena expected in pebble bed reactors. Use these parameters to predict operational conditions for which these parameters predict that laminarization may occur.
2. Conduct experiments to investigate the impact laminarization mechanisms of acceleration and curvature as expected in the pebble bed reactors, both

separately and together, have on the flow response to laminarize. In addition investigate the effect of applied length of the mechanisms on the flow.

3. Determine the applicability of current acceleration driven laminarization parameters to experimental results in predicting flow response when subject to both acceleration and curvature.

1.5 Outline of Dissertation

This chapter describes the background for this study, the motivation, and the objectives.

Chapter 2 provides descriptions of various pebble bed reactor designs. While this will not be a complete description of all pebble bed reactor designs and accompanying systems, sufficient description will be presented as it applies to the laminarization phenomenon for flow in the pebble bed core designs.

Chapter 3 presents and summarizes previous studies performed focused on laminarization caused by mechanisms present in pebble bed reactors. This includes laminarization due to acceleration, flow over convex surfaces, and local heating.

Chapter 4 describes the experimental program of this dissertation research. This includes a description of the test apparatus, instrumentation, test matrix and procedure, and data analysis.

Chapter 5 presents the results for what was the bulk of this research, specifically the PIV laminarization experiments.

Chapter 6 contains the discussion of results and interpretation of the physical phenomena that occurred. Included in this chapter's discussion is the methodology for laminarization identification, and the relative impact of the different geometric mechanisms on the flow response.

Chapter 7 contains conclusions, new and significant findings, and recommended future work.

2 PEBBLE BED CORE GAS REACTOR DESIGNS

2.1 General Design and Safety Considerations

The first concept of a pebble bed reactor was proposed by Dr. Daniels at Oak Ridge National Lab [9]. His concept included using helium as a coolant to remove heat from uranium oxide pebbles. Implementation of his concept consists of containing a large number of fuel pebbles in the core barrel of a reactor vessel. These fuel pebbles contain many small nuclear fuel particles held together in a pebble shape of ceramic composition usually made of graphite. The ceramic composition of the particle is made of different layers which act as moderator and fission product barrier. Most designs contain pebbles that are 6 cm in diameter. Criticality occurs by bringing the pebbles together.

The pebbles are contained within a core barrel, through which the helium coolant is circulated. The coolant carries away the fission heat and can then go directly to the turbine, or operate through a steam generator loop. Some of the benefits of pebble bed designs are related to the use of helium coolant. Helium has a very low neutron cross section and as such does not become very radioactive during operation in the reactor. This provides minimal risk when using this design with a direct power cycle. Helium also has a very high heat capacity and as such the reactor can operate at higher temperatures with respect to light water reactors. This increases the thermodynamic efficiency of the system to 41-45% and allows for production of higher temperature process heat. As mentioned previously, one of the uses of this process heat is for hydrogen production. The sulfur-iodine cycle produces hydrogen and its efficiency is highly temperature dependent (Figure 2-1 [6]).

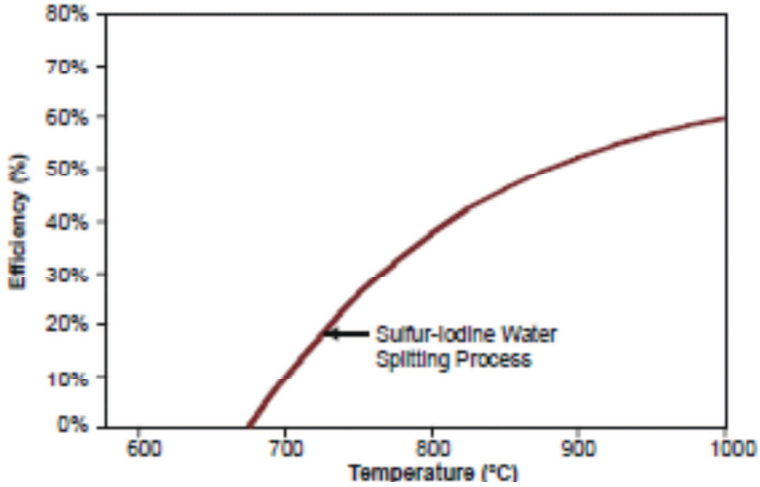

Figure 2-1: Temperature Dependence of Sulfur-Iodine Water Splitting

Another benefit of pebble bed reactor designs is their online refueling. During the lifetime of the reactor, the fuel pebbles slowly move down the core. Fuel pebbles are removed from the bottom of the core and are inspected for burnup. If the pebbles still have utility they are dropped into the top of the core and start the slow process of moving down the core again. Most pebble bed designs specify five to ten fuel pebble cycles. The benefit of online refueling is reducing the amount of time the reactor is offline.

Safety features of the pebble bed gas reactor are related to accident scenarios. Much of the complexity of light water reactor designs is related to the different safety systems to ensure that the core remains below temperature limits. Gas reactors in general are designed such that in loss of cooling situations the high thermal inertia of the graphite in the core allows slow thermal response times. This coupled with negative temperature reactivity of the core allows the core to shut itself down when high temperatures are reached, while the thermal characteristics of the fuel and graphite provide structural integrity even while being subject to high temperatures. This results in passive heat removal by conduction, convection and radiation from the reactor during accident scenarios.

2.2 History

One of the first pebble bed reactor demonstration plants was built in 1967 in Germany [10]. The Arbeitsgemeinshaft Versuchs Reaktor (AVR) was a 46 MWt graphite moderated, helium cooled reactor that operated until 1988 with outlet temperatures up to 990 ^{o}C. Different to later designs, the helium flowed upward in the AVR. The primary purpose of the AVR was to show the viability of a pebble bed design and to test different fuels. During its 21 year operation, 18 different pebble fuel types were tested. The fuel pebble to be used in the NGNP design is based on the most successful AVR fuel pebble which uses TRISO fuel particles. The AVR operated at a pressure of 1.1 MPa and had a core power density of 2.5 MW/m^3. As can be surmised from the operation lifetime of this reactor, results were positive as they showed the feasibility of a pebble bed reactor design.

Germany continued with pebble bed research bringing the 750 MWt Thorium High Temperature Reactor (THTR) to criticality in 1983. This reactor used thorium and uranium fuel and had approximately 670,000 6 cm diameter fuel pebbles. It operated with outlet temperatures of 750 ^{o}C at a pressure of 3.9 MPa. With its higher core power density of 6.0 MW/m^3, it did not have passive safety systems. It produced power to the grid for two years, but during maintenance in 1988 upper head bolts were found in the hot gas duct. In the post Chernobyl nuclear political environment, and due to rising operational costs, the THTR was decommissioned in 1989 [11]. Following in the THTR design was the HTR-500 design. It had a design power of 1390 MWt and was designed specifically for electricity production. It was designed with a power density of 6.6 MW/m^3, an outlet temperature of 700 ^{o}C and system pressure of 5.5 MPa. While there were plans to build this reactor, it never happened due to the factors affecting the THTR shutdown [12].

Another pebble bed reactor design from Germany in the 1980s was the HTR-M, sometimes referred to as the HTR-Modul-200 from Kraftwerk Union AG [13]. Its design and power specifications came from the assumption that heat transfer during accident scenarios should only occur by passive means and that the fuel element temperature should not exceed 1600 ^{o}C. The value of 1600 ^{o}C comes from limits of the

fuel particles in the fuel pebbles. This reactor design also used TRISO fuel particles, a photograph of which is shown in Figure 2-2 [6].

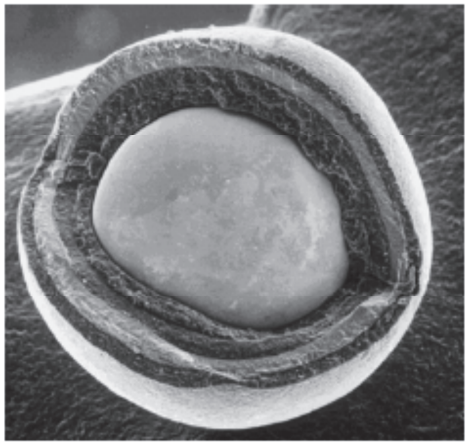

Figure 2-2: TRISO Fuel Particle

This type of fuel particle has multiple layers where the innermost is the fuel particle kernel made of uranium oxide, with layers of carbon complexes outside of this. One layer is that of silicon carbide which serves to contain the fission products. At temperatures greater than 1600 ^{o}C, the fission product cesium gas is found to diffuse through this layer. Approximately 15,000 of these particles are contained in each graphite fuel pebble.

The passive heat removal from this reactor design is conduction and radiation. Due to these safety requirements, the HTR-M core design is a tall skinny core with a height of 9.4 m and diameter of 3.0 m. The core contains approximately 360,000 pebbles and has a core power of 200 MWt (Figure 2-3) [13]. This results in a lower core power density of 3.0 MW/m^3.

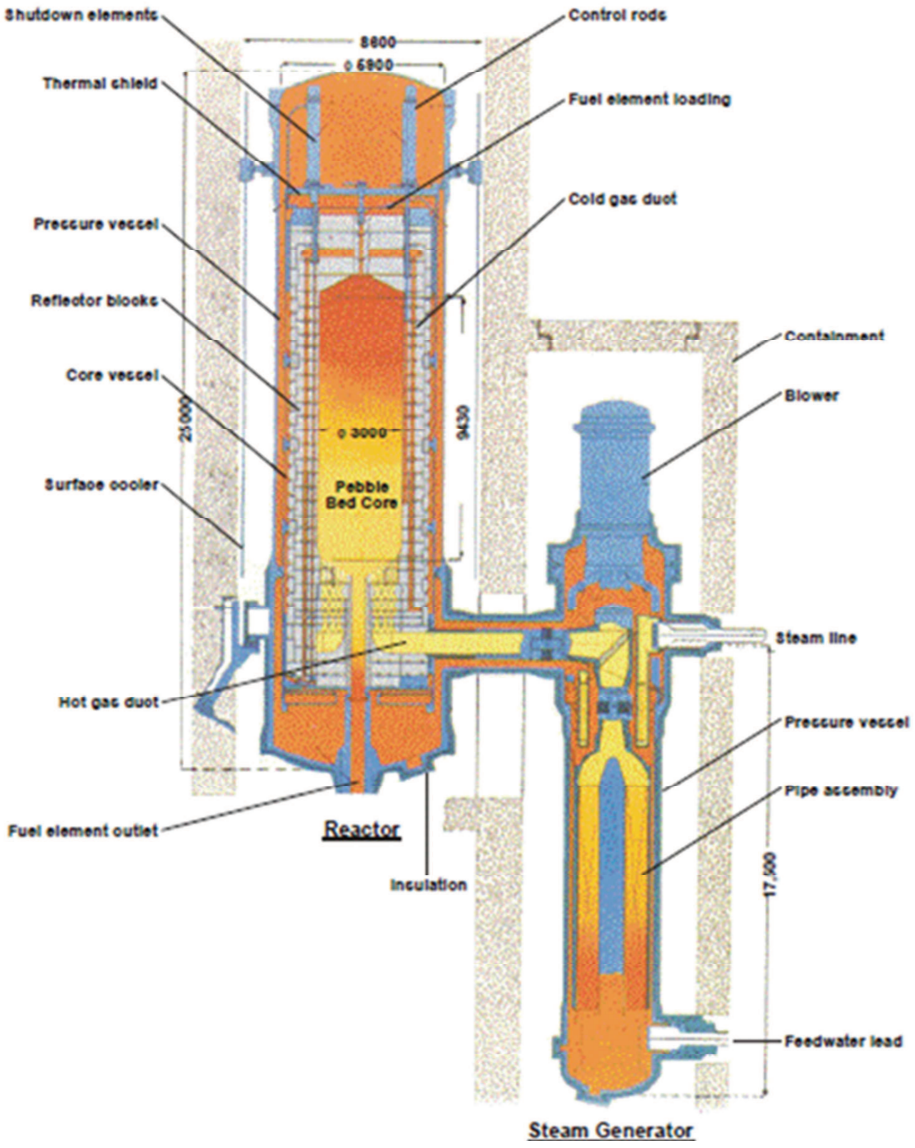

Figure 2-3: HTR-Modul-200

Helium is circulated down through the core with an inlet temperature of 250 ^{o}C and outlet temperature of 700 ^{o}C operating at a system pressure of 6.0 MPa. While both the AVR and THTR used higher enriched uranium fuel, the HTR-M was designed for low enriched uranium, with an average of 15 cycle passes through the core for each pebble.

For safety the core has a negative reactivity temperature coefficient. Shutdown occurs by gravity driven control rods that move in channels in the side reflector. A

secondary shutdown system employs borated pebbles that can be inserted to holding areas in the inner area of the side reflector. The final heat removal from the reactor vessel is by radiation that occurs to a surface cooler system that is placed on the inner wall of the concrete cavity which contains the reactor vessel. This surface cooler system has three independent trains that are each capable of removing 100% of the accident scenario heat. This reactor design has been the basis for later pebble bed reactor designs.

In the 1980s Russia advanced two pebble bed reactor designs. The first was the VTR-M with a thermal rating of 200 MWt, which was very similar to the HTR-Modul-200. It had a design outlet temperature of 740 ^{o}C with the possibility of adjusting the bypass flow to increase this to 950 ^{o}C. The other was a large design, the VG-400, which was rated 1060 MWt [12].

Currently in China the HTR-10 pebble bed reactor is in operation. First criticality occurred in 2000. This is a demonstration modular design that employs many of the same design features as the HTR-Modul-200. This includes a core geometric layout that prevents fuel temperatures from reaching 1600 ^{o}C during accident scenarios, use of TRISO fuel with its negative temperature reactivity coefficient to cause self shutdown in addition to control rods and borated pebbles that go into the side reflector. The reactor also uses helium coolant with a flowrate of 4.3 kg/sec and graphite reflectors with a core diameter of 1.8 m and 1.97 m in height. Core coolant temperatures are 250-700 ^{o}C at an operating pressure of 3.0 MPa. Approximately 27,000 pebbles are contained in the core for a power density of 2 MW/m^3. The pebbles pass through the core five times during their lifetime. Two independent, 100% water cooled cavity cooler systems are used on the inner side of the confinement concrete connected to air coolers on the top of the reactor building [14]. A schematic of the plant is shown in Figure 2-4 [15].

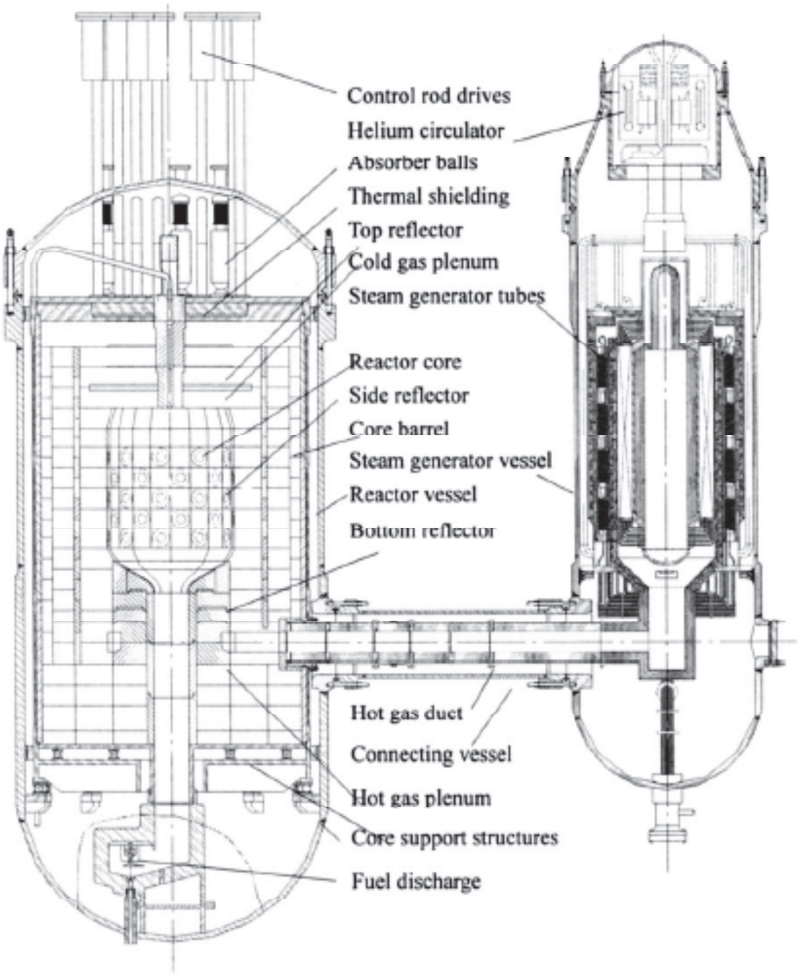

Figure 2-4: HTR-10 Reactor

Following on the successful operation of HTR-10, China began a project in 2001 to design a large HTR demonstration plant [16], the HTR-PM. This is a two reactor plant with each reactor operating at 250 MWt, and attached to a steam generator. The steam from both these generators is fed to one turbine. It has a core temperature rise of 250 – 750 ^{o}C and a system pressure of 7.0 MPa. The active core diameter is 3 m and core height of 11 m with 420,000 fuel pebbles for a power density of 3.22 MW/m^3. This plant is designed to finish construction in 2013.

As a result of analyses of the expected growth in demand of electricity in South Africa, the pebble bed concept was chosen to meet these needs. The South African utility company ESKOM began designing this reactor in the early 1990s. The small Pebble Bed Modular Reactor (PBMR) design was chosen as this could be used in parts of the country where a small power plant was more applicable, and with the goal that the modular units could be clustered together to form larger power plants as needed. A decision was made early on to use a direct cycle where the helium coolant would flow directly to the turbine. This configuration as opposed to using an intermediate steam generator has been made possible due to the advances in gas turbine technology that had taken place in the 1980s. The use of direct cycle also has the added safety feature of reducing the risk of a water ingress accident.

The first design was for a 3.5 m diameter, 8.5 m high 268 MWt core. Previous to this design, all cores for pebble bed reactors consisted of the randomly stacked fuel pebbles in a cylindrical core barrel. This was the first design to employ a center reflector. 330,000 fuel pebbles were stacked in an annulus arrangement in the core barrel, with 110,000 graphite pebbles of the same size stacked in the center part creating the center reflector [17]. Therefore coolant was allowed to flow through the pebbles making the center reflector column. Upon analysis, it was calculated that the center reflector pebbles would need to be replaced mid-life of the reactor. Due to this, and the reduced efficiencies from coolant flowing through the unheated center reflector pebbles led to an update of the design to use a solid center graphite reflector. This current design is rated to 400 MWt, with a core diameter of 3.7 m, a center reflector diameter of 2.0 m, and a core height of 11 m. The design pressure is 9.0 MPa with a core temperature rise of 500 to 900 ^{o}C for an efficiency of 41.2%. This design uses 452,000 fuel pebbles circulated through the core 6 times during their lifetime resulting in a higher power density of 4.8 MW/m^3. The control rods insert into the outer reflector, while the reserve shutdown system that uses the borated graphite spheres is located in the center reflector [18].

The PBMR is designed with many of the same passive safety features of earlier pebble bed reactors including passive heat removal from the core to the pressure vessel

walls during accident scenarios, use of TRISO fuel with its negative temperature reactivity coefficient, and passive radiative heat transfer from the vessel wall to the Reactor Cavity Cooling System (RCCS). In the PBMR, the RCCS consists of many vertical standpipes around the vessel containing water which can operate by natural circulation to remove heat.

As stated in the Background section, the Department of Energy has chosen the Very High Temperature Reactor to be used in the Next Generation Nuclear Plant. One of these concepts is the pebble bed version of the VHTR. The NGNP is similar in design to that of the PBMR. One of the design requirements of the NGNP is having an output of 600 MWt in addition to having passive safety. Early designs of the PBMR core were cylindrical. At a power output greater than 300 MWt it was impossible to insert enough negative reactivity during cold shutdown with the control rods for a cylindrically shaped core. Therefore for the NGNP 600 MWt design, an annular core design was used that provided control rods in the center reflector to provide the necessary negative reactivity. Larger designs were also analyzed in the design process of the NGNP [6].

Initial requirements in addition to the 600 MWt power was that of an inlet temperature of 600 ^{o}C and outlet temperature of 1000 ^{o}C. The inlet value of 600 ^{o}C was chosen to be consistent with initial prismatic core designs so the designs could be more easily compared to one another. Later Idaho National Laboratory (INL) documents also contain specifications for a design with an inlet temperature of 490 ^{o}C [8, 19]. The dimensions of the core geometry design was chosen as a result of a manual search, and then later an advanced optimization algorithm to provide enough excess reactivity to allow for power control, and that would restrict fuel pebble temperatures below 1600 ^{o}C during accident scenarios. This core geometry analysis was performed for 300, 450, 600 and 700 MWt designs. Average core power density for these designs vary from 3.5 MW/m^3 for the 300 MWt design to 5.7 MW/m^3 for the 600 MWt design. The 700 MWt design actually has a lower power density due to its much larger volume. Its geometry was determined by optimizing the core eigenvalue, accident fuel temperatures, the outer reflector size and necessary pumping power.

Passive safety features of the NGNP designs mostly follow those of the PBMR design. The primary difference is the allowance of control rod insertion into the center reflector. Two additional safety features allow for passive insertion of the control rods into the core. In the first design a flow path in the upper head is designed such that if the normal coolant flow ceases, the pressure holding the control rods out of the core is eliminated, and the control rods are inserted. The other design utilizes magnets that keep the control rods out. If the core temperature rises, the electrical resistance associated with the magnets increases, therefore the magnetic field strength needed to suspend the rods is not met, and the rods drop into the reflectors [6].

2.3 Pebble Bed Reactor Design Parameters

In pebble bed reactors designs, the laminarization causing mechanisms that are present are acceleration of flow, flow over convex surfaces, and local heating. The full bed parameters considered here that affect these mechanisms are core geometry, power, power density, mass flowrate, number of fuel pebbles, system pressure, and temperatures. Pebble size was not considered because all these reactors use the same fuel pebble design. Values for the different current reactor designs are listed below. In addition to the reactor core parameters, calculated superficial velocities, Pore Reynolds numbers, and fuel pebble heating rates are listed. Superficial velocity is the gas velocity that would exist through the core if it were empty. Pore Reynolds numbers use the pebble diameter as the characteristic length and the superficial velocity. For ease of reading, the tables have been divided into two, one for early designs, and the other for versions of the NGNP. Values listed in black are design parameters as found in the literature, while those in blue are estimated calculations from other literature parameters assuming simple cylindrical or annular core geometry, the helium absorbs the full thermal reactor power, and fuel pebbles fill up the active core.

Table 2-1: Small PBR Reactor Parameters

	HTR-10	HTR-Modul-200	PBMR 268	PBMR 400[+]
Center reflector radius (m)	None	None	0.87	1.0 (0.875)
Core Radius (m)	0.9	1.5	1.75	1.85 (1.85)
Core Height (m)	1.97	9.4	8.4	11.0 (9.0)
Active core volume (m^3)	5.01	66.4	81.8	83.7
Power (MWt)	10	200	268	400
Power Density (MW/m^3)	2	3.0	3.3	4.8 (3.25)
Number of fuel pebbles	27,000	360,000	330,000	452,000 (330,000)
Mass flow rate (kg/s)	4.3	85.6	126	185
System Pressure (MPa)	3.0	6.0	7.0	9.0 (7.0)
Inlet Temperature (^oC)	250	250	503	500
Outlet Temperature (^oC)	700	700	908	900
Superficial Velocity (m/s)	0.62	2.23	4.05	4.40
Pore Reynolds Number	3460	24,800	27,000	37,850
Heating Rate (W/m^2)	32,750	49,120	71,810	78,250

[+] Primary values are those published by PBMR company related articles [18, 20, 21]. Numbers in parentheses are those contained in an INL report [6].

Blue values are calculated estimations.

Table 2-2: NGNP PBR Reactor Parameters

	NGNP 300	NGNP 600 (optimized)	NGNP 600 (Later Reports)	NGNP 700
Center reflector radius (m)	0.40	0.90		0.96
Core Radius (m)	1.75	2.23		2.30
Core Height (m)	9.4	8.05	9.5	10.74
Active core volume (m^3)	85.7	105.5	92.3	146.6
Power (MWt)	300	600	600	700
Power Density (MW/m^3)	3.5	5.7	6.5	4.8
Number of fuel pebbles	462,230	569,023	497,828	790,700
Mass flow rate (kg/s)	144	288	288	336
System Pressure (MPa)	7.1	7.1	7.1	7.1
Inlet Temperature (^oC)	600	600	490	600
Outlet Temperature (^oC)	1000	1000	1000	1001
Superficial Velocity (m/s)	4.07	5.68		6.32
Pore Reynolds Number	22,575	31,480		35,000
Heating Rate (W/m^2)	57,390	93,230		78,275

3 LITERATURE REVIEW

The literature surveyed includes laminarization due to dissipation, acceleration, convex curvature effects, and local heating. Related, but not included in this review is porous media flow research. While the core of a pebble bed reactor can be considered as a type of porous media flow, the laminarization phenomenon is a localized effect. A review of turbulence in porous media and the treatment of it on the macro- and microscale is contained in a previous review document [22].

3.1 Laminarization Studies

In the literature, transition from turbulent to laminar flow is known as reversion, retransition, laminarization, and relaminarization. In this dissertation, these terms are used interchangeably, though preference has been given to laminarization, for its prevalent use in the recent literature, and for its descriptive nature of the phenomenon.

While the transition from laminar flow to turbulent flow has been studied for some time, transition from turbulent to laminar flow has only recently garnered interest in the past 50 years. While its existence had been known for some time earlier, even if it was not characterized as a reversion from turbulent to laminar flow, most efforts in the field of turbulence were first interested in the transition from laminar to turbulent. One of the first experiments describing flow laminarization was observed by Taylor in 1929 [23]. His experimental setup consisted of a horizontal glass tube with an initial straight section. Following the straight section, the tube was configured into an angled helical geometry, and finishing with another straight section. He observed with the use of injected dye, that contingent on the imposed flowrate, the flow could be turbulent in both the initial and final straight sections, but that laminar streamlines existed through the helical section. His findings were later reproduced and visualized by Viswanath et al. in 1978 [24].

Another early example was that of turbulent jets being suppressed by stably stratified fluids. Richardson [25] reported this for atmospheric flows in 1920 and then in 1934 Prandtl reported similar phenomena of suppression of turbulent jets due to

stably stratified fluids in turbulent shear flows [26]. Viswanath et al. [24] also visually reproduced this phenomenon.

The majority of studies into laminarization have been experimental in nature. Initially the primary objective of these studies was to verify the phenomenon. This proved to be formidable because of the difficulty in accurate experimental measurements that could be used to identify whether the laminarization occurred. Often, a deviation from the logarithmic law of the wall was used as identification of laminarization, though it some complex flows, this deviation can occur without laminarization. From the experimental data it was difficult to differentiate deviations from expected turbulent flow behavior as laminarization, or simply a lack of understanding of turbulent flows. As researchers became better able to identify laminarization from experimental data, studies focused on the characteristics that caused this phenomenon and provided descriptions of the flow process. Many of these studies presented criteria predicting when laminarization would occur using empirical parameters of the flow.

While there are many mechanisms that can cause laminarization, four specific ones that are applicable to the pebble bed geometry will be reviewed here. Laminarization due to a reduction in the bulk turbulence levels, due to highly accelerated flow, due to flow over curved boundaries, and due to local heating.

3.1.1 Laminarization Due to Dissipation

The Reynolds number is often used to characterize flow regimes with respect to turbulence. A decrease in the bulk Reynolds number indicates an increase in the ratio of viscous forces to inertial forces, and thus a decrease in the bulk turbulence of the flow. For directional flow, if the downstream Reynolds number decreases sufficiently, it can be expected that a turbulent flow will approach a laminar profile. This is perhaps the simplest mechanism to understand how laminarization can occur. One way in which this can occur for pipe flow is from an expansion of the pipe diameter or channel at an angle to ensure that flow separation does not occur. With respect to the Reynolds

number, with an expansion of this type, the velocity decreases quicker than the diameter increases. With this decrease in velocity, the inertial forces are less with the relative viscous forces being larger, thus the viscous forces have a larger impact on turbulence decay. Therefore laminarization in pipe flows is mainly due to viscous effects causing the turbulent dissipation. Laufer [27], Sibulkin [28] and Badri Narayanan [29] performed experiments investigating this type of laminarization.

Laufer [27] and Sibulkin [28] independently looked at this case for air flows through pipes. Laufer used an initial pipe inner diameter (ID) of 0.8 cm, and a final diameter of 2.0 cm with a 1^o diffuser section. This resulted in an initial Reynolds number of 3500 going to a final of 1380, which is below the critical value to sustain turbulence. Sibulkin used an initial pipe ID of 0.49 cm and final of 2.2 cm with a 3^o diffuser angle. Sibulkin reported four cases where the final Reynolds numbers are 600, 1200, 1800, and 2400. The corresponding initial Reynolds numbers were different for each case given mass continuity in the flow, yet all were initially in the turbulent regime. Both investigators measured mean and fluctuating velocities.

Badri Narayanan [29] conducted channel experiments using air at Reynolds numbers of 625, 865, 980, and 1250 corresponding to the conditions after the expansion with the characteristic length being the channel half width in search of a critical Reynolds number corresponding to laminarization. Mean velocity profiles and decay rates of the fluctuating velocity components as a function of axial distance were measured using a hot-wire.

For the cases of Laufer and those of Sibulkin with Re =600, 1200, the mean velocity profile reverted to a laminar regime. For the Reynolds number of 1800 investigated by Sibulkin, the flow profile never reaches a laminar state, though this is expected to be due to the experimental pipe section length not being sufficiently long enough because from fluctuating velocity measurements, the turbulence was decreasing. All studies found that the centerline turbulence energy spectrum shows similarity along the direction of flow. Measurements of Laufer show $\overline{u'^2}$ decays exponentially with the direction of flow for regions near the centerline and the wall. Sibulkin found the related

result that the decay of $\overline{u'^2}$ occurs more slowly in the middle region (0.4 < r/R < 0.6) between centerline and wall region.

Badri Narayanan reported that mean velocity profiles and skin friction coefficients (c_f) become more laminar like after the channel expansion. He also reported that $\overline{u'^2}$ and $\overline{v'^2}$ decrease exponentially and that $\overline{u'v'}$ decreases linearly and becomes zero at a specific Reynolds number. By plotting the turbulent quantities decay rates versus Reynolds number, it was predicted that the critical Reynolds number below which laminarization will occur is 1400 ± 50.

3.1.2 Laminarization Due to Acceleration

Initially, laminarization due to acceleration seems counterintuitive. Typically when thinking of pipe flow or flat plate flow, a larger velocity is associated with higher levels of turbulence. All other things held constant, a larger velocity results in a higher Reynolds number, which is characteristic of identifying the turbulent regime. Therefore the questions must arise, what causes and to what extent does laminarization occur when a flow is subject to acceleration? And what specifically happens to the flow that it is more characteristic of laminar flow as opposed to turbulent flow?

Laminarization due to acceleration was first reported in 1954 by Sternberg. This reversion in turbulent boundary layers was discovered accidently while studying high speed flow being subject to high acceleration [30]. His experiment was designed to look at the equilibrium surface temperatures of high speed compressible flow for well defined laminar and turbulent boundary layers that was subject to a large pressure gradient. The geometry employed was angled flow over a cone with the cone base connected to the top of a cylinder and the flow direction beginning with the apex, flowing over the angled surface, and then on the outside along the axial length of the cone, across the shoulder with the cylinder, and along the length of the outside of the cylinder. It was found when turbulence was induced by surface roughness on the cone, surface temperatures at the beginning of the cylinder corresponded to laminar flow

profiles, thus indicating a reversion from turbulent to laminar flow. Shadowgraphs were taken which corroborated the surface temperatures indicating this reversion.

Most early works were focused on identifying the existence of the laminarization phenomenon and when it would occur. Some early studies that confirmed this phenomenon of laminarization when the flow was subject to an acceleration were done by Holder in 1956 [31], Senoo in 1957 [32], and Sergienko in 1959 [33]. Senoo experimentally studied boundary layer flow through turbine nozzles. He found that the boundary layer became laminar at the nozzle throat due to the steep pressure gradient even though it was turbulent upstream from this point. He deduced when laminarization occurred from looking at the measured flow profiles.

Sergienko and Holder both looked at laminarization of high speed flows. Sergienko performed experiments confirming the reversion from turbulent to laminar boundary layers for supersonic air flows through a tube of 76.0 mm ID with a supersonic nozzle attached at the end. At the critical diameter of the nozzle, the flow had a Mach number of 2.6. In the initial section of the tube, the boundary layer transitioned from laminar to turbulent as expected. Then as the acceleration increased through the nozzle the boundary layer experienced reversion to laminar shown from an investigation of the shape profile as measured by Sergienko at the outlet of the nozzle. Holder predicted that the wake of high speed flows past a body caused decay in turbulence.

Following these initial studies that verified the occurrence of laminarization when the flow was subject to large acceleration, studies began focusing on answering the questions of what happens when the flow laminarizes, what causes this, and can it be predicted. One of the first experimenters to provide a numerical criterion for when this occurs was Launder [34] in 1964. He experimentally studied laminarization of the boundary layer using air flow over a flat plate subject to a large acceleration caused from a contraction in the flow geometry. He investigated turbulent boundary layers with momentum thickness Reynolds (Re_θ) numbers ranging from 300 to 1650. As a result of his experimental findings, he proposed the following acceleration parameter to predict laminarization using bulk flow parameters.

$$K = \frac{\nu}{U_\infty^2}\frac{dU_\infty}{dx} \geq 2 \cdot 10^{-6} \quad (1)$$

While many later researchers have criticized the use of this parameter because it is based on bulk flow parameters while the laminarization phenomenon is a boundary layer event, it does have its basis in boundary layer considerations. One characteristic of the flow that many researchers use to identify the occurrence of laminarization is a departure from the law of the wall. Launder developed his acceleration parameter assuming that departure from the law of the wall, as exhibited in his experiments, occurs when the pressure gradient term is of the same order as the wall shear stress. This is described mathematically as: $-dp/dx \cdot y \sim \tau_w$, where τ_w is the wall shear stress. Substituting the free stream velocity convection term for the pressure gradient, and applying the following equality as the boundary of when the logarithmic profile is applicable, $yu_\tau/\nu = 30$, where u_τ is the friction velocity, results in the following:

$$\frac{\nu}{U_\infty^2}\frac{dU_\infty}{dx}\left(\frac{c_f}{2}\right)^{-3/2} \sim 10^{-2} \quad (2)$$

This uses the definition of friction velocity and skin friction coefficient. Choosing a value of 0.006 for the skin friction coefficient results in the approximate value of the acceleration parameter as given above in Eqn. (1). In a later study, Launder presents the criterion parameter in its more general form of $Kc_f^{-3/2}$ [35]. Despite the criticism of the use of this acceleration parameter to predict when laminarization will occur, it is the parameter most widely used in the literature for predicting laminarization. This is due to both its success in predicting the laminarization phenomenon, and because of its ease of use because it is based on bulk flow parameters.

In addition to providing a parameter whose value predicts if laminarization will occur, Launder helped answer the question of what causes laminarization. He described the laminarization as occurring in two phases. In the first phase the turbulence structure in the inner region of the boundary layer was not able to adjust to the changing environment due to the sudden change in streamwise pressure gradient. This exhibited itself by a departure from the law of the wall for the flow profile. In the second phase the dissipation exceeds turbulence production resulting in the boundary layer becoming laminar. Even though this laminarized boundary layer was found to still contain a high residual turbulence signal, the overall behavior was laminar. Residual turbulent fluctuations in the outer layer of the boundary layer and bulk flow essentially remains frozen, but there influence decreases due to the higher streamwise velocities imposed over them. It was found that the mean velocity profile was consistent with the Blasius solution for a laminar boundary layer, the turbulent shear stress had become negligible in comparison to viscous forces, and the separation tendencies of the boundary layer were consistent with laminar boundary layer behavior.

Moretti and Kays [36] performed experiments to investigate the effect that large acceleration on low velocity air flows has on heat transfer characteristics and to provide data for theoreticians to establish a useful engineering correlation for these flows. Air was flowed through a duct where the bottom wall was configured as a heat flux source and surface temperatures were measured. The opposite wall was a flexible wall to create a converging flow to provide the specific acceleration desired. Experimental Stanton number ($h/U_\infty \rho C_p$) results were compared to analytical solutions that employed solving an energy integral equation assuming a relationship between surface heat flux and the energy thickness of the boundary layer. Given that the laminarization phenomenon is a boundary layer event, Moretti proposed that the boundary layer thickness should be used in some way as part of the correlation with reversion to laminar flow, but ultimately he also used the acceleration parameter (K) for ease of use. It was found that there was a sharp decrease in Stanton number for $K > 3.3 \times 10^{-6}$. After this decrease the Stanton numbers approximate those of purely laminar flow. For K greater than this, no greater depression in Stanton number was found, indicating that for

K greater than this value the flow had reversed to laminar. Full reversion was seen in runs with K as low as 2.52 x 10^{-6}, indicated from the measured Stanton numbers corresponding to laminar values. For moderate values of K, a depression when compared to the analytical solution of Stanton number was found, suggesting that while the flow still was turbulent, the amount of turbulent intensity had decreased.

Schraub and Kline et al. [37, 38] performed low speed accelerating water tests in a channel using hot wire anemometry and a hydrogen bubble dye-tracing technique to extend the physical description of the boundary layer behavior when subject to this large acceleration. Dye was injected from the surface to witness turbulent ejections from the surface. By using this dye-tracing technique, they were able to witness the interactions between the wall, buffer layer, and the outer layer of the turbulent boundary layer taking place as bursts of ejected fluid from the wall. Laminarization was identified by a decrease in bursts coming from the wall. A correlation between bursts of turbulence from the wall and the acceleration parameter was found. It was found that bursts completely died out for K=3.5 x 10^{-6} [38]. In addition to the acceleration term, the use of a modified acceleration parameter was proposed that comes from a non-rigorous analysis of the turbulent kinetic energy equation assuming zero turbulence production. This parameter is $K/c_f^{0.5}$. Ultimately results were presented in terms of K for easy comparison with other studies, and the successful correlation that occurs using K. It is postulated that the bursting phenomenon plays a vital role in turbulence production and transfer of energy between the inner and outer layers of the boundary layer [38].

From these early studies there was success in predicting laminarization using the acceleration parameter (K), even though this parameter carries no information about the boundary layer behavior, and specifically in the viscous sublayer, where the laminarization phenomenon originates. When looking for a prediction parameter, Launder initially wanted to use the momentum thickness Reynolds number but comments that this parameter still does not capture what is happening near the wall since the associated length scale of the momentum thickness is primarily a function of the outer 4/5 of the boundary layer [34, 35]. When selecting a critical parameter to

predict the laminarization, researchers have attempted to balance a parameter that is capturing the most important behavior, but is also convenient to use or measure. Therefore later researchers proposed the use of other parameters to predict the laminarization phenomenon.

In 1965 Patel [39] and then later in 1968 Patel and Head [40] argued against using a boundary layer Reynolds number in defining a criterion for the onset of laminarization because from earlier data from wind tunnel measurements [39] the reversion to laminar was found to be independent of this. In the earlier study Patel recommended the use of a pressure gradient parameter:

$$\Delta p = \frac{\nu}{u_\tau^3}\frac{dp}{dx} \tag{3}$$

This is formed from the length and velocity scales near the wall. This parameter was recommended because it was suggested that even though a Reynolds number represents the laminarization phenomenon, the pressure gradient causes it. Patel later withdrew this parameter recommendation because of results in his later experiment [40]. These experiments employed a round cylinder with a domed top and streamlined back that was placed in a pipe flow with the axial length of the cylinder parallel to the pipe thus creating an annulus flow path. The flow entered the annular section passing over the domed top first. The streamlines in the back of the cylinder creating the annulus produced favorable pressure gradients in front of, and around the cylinder. For a turbulent boundary layer that is in equilibrium, the production and dissipation of turbulence is in balance in the wall region. In providing input to the question of what causes laminarization, they proposed that the onset occurs due to a departure from this equilibrium which is caused by large shear stress gradients that accompany large favorable pressure gradients. Given that K is not capable of describing the flow profile in the wall region, they proposed the use of a shear stress parameter in the reversion to laminar criterion:

$$\Delta\tau = \frac{\nu}{\rho u_\tau^3}\frac{d\tau}{dx} \tag{4}$$

In the search for a velocity profile distribution that could provide a smooth transition from the fully turbulent regime to the sublayer, a modified mixing-length relation was employed with a continuous eddy viscosity model assuming linear shear stress distribution. This velocity distribution is a function of this parameter ($\Delta\tau$). Using this derivation, they show that mathematically, an imposed pressure gradient causes a change in the boundary layer velocity distribution, which result was found in their experiments. It was found when $\Delta\tau < -0.009$, turbulence cannot be maintained in the wall region and the flow is in the process of reversion to laminar. This criterion should be used with caution because in their experiments, the wall shear stress was not measured directly. Instead it was inferred from the flow profile deviation from the expected flow profile in the wall region based on a mixing length model proposed by Townsend [39, 41-43]. Of note, Patel and Head found that the onset of laminarization closely coincided with a minimum in the shape factor (H), which was also observed by Launder [34] though the absolute value of the shape factor for laminarization from case to case did not reveal a pattern. Even though Patel and Head proposed the use of a different parameter which they believe better captures the important physics, when the acceleration parameter (K) was calculated for their experiments, it was found that the critical value corresponding to reversion was 3.7×10^{-6}, very similar to 3.5×10^{-6} which was suggested by Schraub [37] and Moretti [36].

In 1966 Fiedler and Head [44] studied laminarizing flow subject to an acceleration using an intermittency function (γ), which is the ratio of time at a specific point that the flow is turbulent with respect to total time. Experiments were performed in a blower tunnel with a flexible wall to create flow acceleration. Hot wire measuring the intermittency in the boundary layer and the use of smoke introduced into the boundary layer for picture taking were used for measurements. Two primary contributions to the

knowledge of what occurs when a flow laminarizes were provided from these measurements. The first is that when subject to a large acceleration, the shape factor (H) drops to a minimum then rises as laminarization occurs. This minimum in H agrees with findings of Launder [34] and Patel [39]. The other finding is that as the shape factor decreases, the intermittency expands over the entire thickness of the boundary layer, indicating that the flow is reverting to laminar conditions.

Occurring concurrently during the previous experiments in the mid 1960s were experiments performed by Back and Seban [45, 46]. These were heat transfer experiments for boundary layers on a flat surface with an acceleration parameter (K) greater than 2×10^{-6}. Laminarization was identified to have occurred due to heat transfer and skin friction data that was much less than predicted for turbulent boundary layers. The heat transfer coefficients were found to be up to 40% less than expected values. They attribute this to a reduction in the turbulent transport caused by the acceleration.

As an extension to experiments done in 1968 for channel flow, Badri Narayanan with Ramjee [47] performed low speed wind tunnel experiments for boundary layers subject to various levels of acceleration measuring mean velocity profiles, longitudinal velocity fluctuations, and wall shear stresses. Given that previous work defined laminarization in terms of free stream variables in the use of K, or local variables affecting the wall region in the use of Δp, the present authors work aimed to describe laminarization in terms of a decrease in turbulent fluctuations and that from this a greater understanding of the underlying physics may result. Results found were in agreement with other studies with a decrease in wall skin friction coefficient values, a decrease, then minimum and increase in shape factor (H), and a tendency to revert to a more laminar-like mean velocity profile with a thickening of the viscous sublayer. It was found that the wall region adjusts itself to laminar conditions sooner than the outer region of the boundary layer. Correlating their work with previous, the laminarization process is presented as occurring in three stages, the first where large eddies disappear, described by the acceleration parameter (K) or bursting frequency given by Schraub [37]. In the second stage a breakdown of the law of the wall occurs due to a thickening

of the viscous sublayer. This is described by the pressure driven parameter (Δp) or shear stress parameter (Δτ). In the last stage turbulent fluctuations decrease. This decrease in $\left(\tilde{u}/U\right)$ begins when the $Re_\theta \leq 300 \pm 100$.

In 1969 Bradshaw [48] tied together conclusions from different authors suggesting that previously presented criteria for laminarization were specific cases of a general Reynolds number criterion. In a study to determine the minimum Reynolds number necessary to have turbulent boundary layers, Preston [49] suggested that a logarithmic region must exist between the viscous sublayer and the beginning of the outer layer. As summarized above, Patel and Head [40] give a deviation from the law of the wall as a criterion for laminarization. Looking at the overlap of the energy containing and dissipating eddy sizes at the outer edge of the viscous sublayer, Bradshaw suggests that the start of reversion occurs when the boundary layer region usually associated with a logarithmic velocity profile has shrunk to zero. This physically-based criterion, in terms of an eddy Reynolds number is:

$$\left\{\left(\tau/\rho\right)^{1/2} y/\nu\right\}_{\max} = 30 \tag{5}$$

The value of 30 comes from Preston from his definition of viscous effects being described by $u_\tau y/\nu = 30$ for this region [50]. In practice it appears that the maximum eddy Reynolds number occurs at the outer layer of the sublayer. Both criteria presented by Preston and Patel are in agreement with this criterion. Bradshaw suggested the use of this criterion for the onset of reversion as a criterion that can be applicable to more general flow cases.

With the progress of computational capabilities, Jones and Launder [51, 52] presented a new two-equation turbulence model specifically suitable for low Reynolds numbers flows in an attempt to capture the flow behavior associated with accelerating flows exhibited in experiments. They equated the Reynolds shear stress terms to the

product of velocity gradient and turbulent viscosity, where this viscosity is a function of experimental constant, density, turbulent kinetic energy (tke) and dissipation. Unique differential equations for turbulent kinetic energy and dissipation are used for high and low Reynolds numbers flows, where the low Reynolds number flows include viscous dissipation of turbulent kinetic energy and dissipation. Some terms in these equations have physical reasoning, while others were simply needed to match experimental data. Given that the driving force behind their work was for the laminarization that occurs for accelerating flows, and specifically in the near wall region, good agreement is found for these types of flows with respect to the hydrodynamic and thermal results of the thickening of the viscous sublayer that accompanies laminarization. Alternatively, their results for zero pressure gradient flows were not as successful, especially for low Reynolds numbers.

In an attempt to better describe the cause of the laminarization process, experiments to look at the role large eddy structures have in accelerating flows for this phenomenon were performed by Blackwelder, Kovasznay, and Kibens [53, 54]. Air in a wind tunnel where a contraction was used to get the proper acceleration was used. To ensure that laminarization occurred, a flow corresponding to an acceleration parameter greater than the critical value presented in other studies was used. Results characteristic of laminarizing flows was found including that the intermittency factor decreased consistent with the findings of Kline [38] showing that turbulence only occurred intermittently between pockets of non-turbulent flow. They found that as the flow accelerated, the turbulent intensities decreased, but that this was primarily a function of the increasing free stream velocity used in their normalization. The absolute values of the fluctuating velocities remained relatively constant. Piecing together their experimental findings with that of others they propose that after the flow enters the high acceleration region, bursting from the surface ceases. This results in a change in the shear stress gradient which results in a loss of the logarithmic law of the wall profile. Without the bursting from the wall, momentum exchange occurs more slowly which causes the thickening of the sublayer.

In 1973 [55] Narasimha and Sreenivasan presented analytical work on the laminarization phenomenon and then later in 1979 and 1982 presented comprehensive overviews of the laminarization process and a review of work of others [7, 56]. They divided the laminarization phenomenon into four stages. The first stage was an initial fully turbulent boundary layer stage, followed by a transition stage. The third stage is termed a quasi-laminar stage where the boundary layer acts laminar, though turbulence does remain in the flow. The final stage is a retransitional phase where the flow returns to turbulent characteristics. For the quasi-laminar stage they presented analytical work where the Reynolds averaged equations were used and the boundary layer was divided into an inner and outer layer. The outer layer they treated with an integral method and the inner using a similarity function. In solving their model for the quasi-laminar stage, a limiting case where the pressure gradient is much larger than the Reynolds stresses was employed. They then compared their results with experimental data where they met relative success. With their theory they were able to match Re_θ, and skin friction coefficients relatively well, but velocity profiles did not match up very well, especially near the transition point. Absent from their analytical model was explicit accounting of the Reynolds stresses. Instead use of their calculated velocity profiles for the inner and outer layers were used with other theories to describe flow oscillations and decay. They describe the laminarization not as occurring because of an increase in the ratio between dissipation and turbulent production, but instead because pressure forces dominate over shear stresses, which remain relatively constant.

Most of the work presented up to this time was flat plate geometry flows. In 1983 Murphy, Chambers and McEligot published extensive experimental work for a different type of converging geometry flow [57, 58]. In their experimental apparatus flow began in a slot geometry with a large aspect ratio. The long lengthwise sides stayed parallel for the entire flow, while the short sides of the slot were both angled towards each other creating a convergence in the flow geometry, thus reducing the slot aspect ratio along the flow direction. The exit from the geometry was an exit hole from one of the long lengthwise parallel plates, thus creating an exit at a right angle from the flow direction. It was desired to see if this type of accelerating flow exhibited the same behavior as

other laminarizing flows due to acceleration, and if the same acceleration parameter (K) could be used to predict laminarization. Experimental measurements consisted pressure distributions and local shear stresses along the length of the converging channel. It was found that when the acceleration parameters of K, and $\Delta\tau$ were of values characteristic of laminarizing flows in flat plate geometry, the measurements corresponded to laminar predictions. However, for this geometry, values of Δp corresponding to laminarized flow did not agree with previously published values very well.

Up to the 1980s, most work studying the laminarization phenomenon was experimental in nature. The experimental results had provided good agreement for the critical values of laminarization parameters and also had provided a good description of what occurs in the flow during and because of the laminarization. In the 1980s, some researchers began focusing more effort on predictive and computational models, both with the goal to predict the flow, but also to provide further insight into the underlying physics of the behavior. In 1988 Finnicum [59] presented a conceptual and computational model of turbulence close to the wall to gain a better understanding of how flow in favorable pressure gradients affects the drag. Scaling relations were presented to predict the location of the outer edge of the viscous wall layer and how this boundary changes for zero pressure gradient and favorable pressure gradient flows. These values for the viscous sublayer boundary were then used in a numerical model to predict the boundary layer flow profile, and turbulent quantities. It was found that using the scaling relations with the numerical model gave good agreement with previous experimental work. Occurring concurrently to this work was a direct numerical simulation study by Spalart [60]. Similar values for Reynolds stress terms were found between these two studies that were consistent with experimental results of Narasimha [7].

In Sreenvasan's comprehensive review [56] noted above, a number of needs for the future was identified. Among these was shear stress measurements. Much of the previous work had induced or calculated the shear stress values for the accelerating flows. With technological advances, more accurate measurements of the shear stress was possible. In 1998 Escudier [61] performed laminarization experiments very similar

to previous work in a low speed wind tunnel. The objective of the study was to provide more detail in wall shear stress and intermittency measurements. Results were consistent with previous results. It was found that the ($\overline{u'v'}$) Reynolds stress decreases in the boundary layer but that the streamwise fluctuating velocity does not show significant decrease. Despite this lack of decrease in the value of the streamwise fluctuating velocity, its effect on the flow does decrease, because the relative intensity, with the higher bulk velocities decreases. Another significant finding of this work was that the intermittency stays at appreciable levels. This is a result of residual fluctuations remaining from before the acceleration, while very little high frequency turbulence is produced during the acceleration.

Occurring at the same time as the work of Escudier, Fernholz [62] and Warnack [63] released two papers describing their experimental work also focused on obtaining better data in near wall regions and measuring the wall shear stress, and turbulent fluctuations. They performed experiments in a low-turbulence wind tunnel that used displacement bodies placed at the tunnel centerline around which the flow was directed to created acceleration. Their contribution to the knowledge base primarily dealt with their recommendation that no single criterion could be used to predict the beginning or end of the breakdown of the law of the wall. They found that for flow with low acceleration where laminarization did not occur, there still was a breakdown of the law of the wall and a slight reduction in turbulent intensities. This lends itself to describing laminarization not as a threshold phenomenon, but instead as a gradual change.

Almost all the laminarization studies performed previously were that of steady flow. In 1999 Greenblatt and Moss [64] performed experimental and numerical work to see if flow response for acceleration due to temporally applied pressure gradients was similar to that of steady flow responding to spatially applied acceleration. They performed their experiments with water in a tube using a downstream valve to temporally apply acceleration. Similarities between time applied pressure gradients and spatially applied pressure gradients were found. When the pressure gradient term (Δp) was of the value corresponding to laminarization in steady flows, the resulting velocity profiles adjusted to the laminar solution.

Higher order characteristics of the turbulence were studied by Ichimaya experimentally [65] in a wind tunnel to obtain measurements of statistical properties such as the probability density function, power spectrum, and scales of small eddies during acceleration driven laminarization. Results of mean flow profiles and a minimum in the shape factor (H) suggest laminarization took place, though intermittency measurements suggest that the flow is not intermittent in the boundary layer, counter to what was found by Fiedler [44] and Blackwelder [54] for laminarized flows. From these results, a more focused description of the process was found from statistical measurements. It was found that vorticity in large eddies increases and vorticity in small eddies decreases during the laminarization process, while bursting decreases with respect to a non-dimensional convection time.

Despite the many experiments that had looked at acceleration driven laminarization to this point, a thorough understanding of how the large pressure gradient causes the laminarization was incomplete. In 2008 Cal [66] applied similarity analysis to the equations of flow for flows subject to a favorable pressure gradient with the objective to gain a better understanding of the scales and similarity constraints in laminarizing flows. By assuming that the velocity components can be written as a function of two variables, the streamwise momentum equation is converted into a second order differential equation. Using an order of magnitude analysis, the scales of and relationships between different terms in the equation were deduced. Their scaling constraints were then compared to experimental data. Similar to what had been seen in experiments, it was found that there is a correlation between the pressure gradient term (Λ) and a reduction in skin friction, where the pressure gradient term is defined as:

$$\Lambda = -\frac{\delta}{\tau_w}\frac{dp}{dx} \tag{6}$$

with δ being the boundary layer thickness. A maximum value of $\Lambda \cong 0.47$ was found for laminarizing flows. In a follow up to this study [67], experimental measurements by

use of Laser Doppler anemometry of mean velocity profiles and Reynolds stresses near the wall subject to surface roughness and favorable pressure gradients were performed. It was found that an increase in surface roughness increases turbulence production, while an increase in pressure gradient decreases it. When both surface roughness effects and a favorable pressure gradient are applied, the effect of the roughness is not felt in the outer regions of the boundary layer.

As laminarization research continues in the future, numerical modeling will play a larger role. Specifically with the advances of computational resources, Large Eddy Simulations (LES), and direct numerical simulations (DNS) will become more prevalent. It is hopeful that these modeling techniques will give larger insight into the laminarization process. Due to their large computational requirements, two-equation turbulence models will still be needed, but perhaps the results from LES and DNS experiments will provide assistance in determining which two-equation models work best for flows with laminarization. Two current researchers employing LES to investigate accelerating flows are Piomelli and Radhakrishnan. Piomelli [68] performed Large Eddy Simulations (LES) for accelerating flows with an acceleration coefficient (K) sufficient for laminarization. While the imposed acceleration was not imposed long enough for reversion to occur, there is a breakdown of the law of the wall and thickening of the sublayer occurs. It was found that there was a decrease in the intensity and number of vortices in the accelerating region. Radhakrishnan [69] has been performed various LES studies for accelerating flows using different numerical methods for the near wall, outer layer of the boundary and outer flow.

3.1.3 Laminarization Due to Convex Curvature

Considerably less research has been performed looking into the stabilizing effects that curvature can have on turbulence in a flow. A few early experimental studies in the 1930s by Wattendorf, Wilcken and Schmidbauer [70-72] looked at flow bounded by a convex surface and the resulting mean velocity profiles for turbulent and laminar flows. Later, around the same time that interest was being focused on acceleration driven

laminarization, a renewed interest began in the effects of curvature on flow, and specifically the turbulent quantities. While experimentally studying convective heat transfer for flow over gas turbine blades in 1954, Wilson and Pope [73] noticed that the heat transfer coefficient for flow over the convex side was lower than predicted from theoretical models. In 1957, Wilson [74] suggested that the flow acceleration caused by the flow over the convex surface may have caused the boundary layer to revert from turbulent to laminar. Following Wilson's initial findings in 1954, Eskinazi and Yeh [75] reviewed the results from the early studies [70-72] and found that flow through curved channels exhibited a stabilizing effect on the convex side and a destabilizing effect on the concave surface.

In 1967 Rotta [76] presented theoretical analyses compared to experimental findings for the curvature effect on the flow profiles and turbulent kinetic energy budget. In his analysis, pressure and therefore density and viscosity were treated as varying through the boundary layer, due to the curvature. For flow over convex surfaces this varying density causes a decreasing effect on the turbulent intensity in the boundary layer. While his analysis predicted this characteristic trend of curved flows, it actually under predicted the full extent of the stabilizing and destabilizing effect on the flow when compared with the experimental findings of Wattendorf [70] and Eskinazi [75]. This conclusion is repeatedly found for curved geometries; that theoretical considerations for curved flows underestimate the curvature effect on the flow.

In 1969 Bradshaw [77] presented an algebraic analogy to look at the similarities of turbulence suppression in buoyancy driven and curved flows. He applied an analysis usually used to derive the Richardson numbers from the governing equations for buoyant flows to the equations of motion for curved flow to derive a similar non-dimensional parameter. He applied the analysis to buoyant flows for the gradient Richardson number (ratio of buoyancy to inertial forces), flux Richardson number (ratio of turbulent energy production from buoyancy to production from shear stresses), and gave a corresponding non-dimensional parameter for curved flows. In curved flows the flux Richardson number is the ratio of the absorption term to the production term and the gradient Richardson number is the ratio of inertia to curved effects. From a

comparison to experimental data and theoretical analysis to the equations of motion, it was found that when the shear layer is larger than 1/300 of the radius of curvature, it can affect the length scale distribution by 10%. Bradshaw presented a relation for the ratio of the mixing length for a flat plate (l_{mf}) to that for a convex plate (l_m) as:

$$l_{mf} / l_m = 1 + \beta Ri \tag{7}$$

where β is between 7 and 10 for convex flows. The mixing length parameter is defined as:

$$l_m = \left(\tau / \rho\right)^{0.5} \Big/ \left(dU / dy\right) \tag{8}$$

The Richardson number here is the curvature Richardson number, correlating to the gradient Richardson number for buoyant flows. This is defined as:

$$Ri = \frac{2\left(U / R\right)^2 \frac{\partial}{\partial y}(UR)}{\left(\frac{\partial U}{\partial y}\right)^2} \tag{9}$$

When this correlation, which is derived from the buoyancy effects analysis, is applied to experimental data, agreement is good.

In analysis of curvature effects often it is difficult to separate the effects of the curvature from other effects, such as a favorable pressure gradient. Typical geometry

used for curvature effects experiments have been in channel flows that initially have a straight section, following which they are subjected to a bend. The change in geometry from straight to curved flow affects the flow, as does the length of the curved part. Despite these difficulties that are introduced for curved flow, valuable experimental data has been obtained. In 1972 So and Mellor [78] provided the first experimental turbulence measurement data isolating the curved channel effect. In their geometry channel, the flow was initially flat plate flow, and then as it flowed through the curved section, the radius of curvature was increased. By taking measurements at various points along the flow, they obtained data for varying values of $\kappa\delta$ ranging from 0.074 to 0.0897, where κ is the inverse radius of curvature. Some form of $\kappa\delta$ is often used to characterize curved flows. They found that the Reynolds stress decreases near the wall and disappears at the midpoint of the boundary layer, though they did find that very near the wall turbulent production was very similar to that of a flat plate, regardless of curvature. Following the suggestion of Bradshaw they observed a critical Curvature Richardson number of ~ 0.30. This is similar to the value of 0.20 found by researchers [77, 79] for the gradient Richardson number suggested by Bradshaw for buoyancy flows.

In 1978 Ramaprian and Shrivaprasad [80] conducted experiments to look at the effect of curvature on boundary layers for a mild curvature. They looked at a curvature corresponding to a value of $\delta\kappa = 0.013$. They found that the turbulent production occurred very close to the surface in a thin region when compared to flat plate flows. While the curvature did not seem to affect the magnitude of turbulent production very much, it did inhibit the diffusion and transport of turbulence from this inner region to outer regions of the boundary layer, similar to the findings of So [78].

As part of his literature review paper [7], Narasimha presented theoretical considerations for the stabilizing effect of curvature on turbulence in boundary layers. Due to the centrifugal force of curved flow, for a given streamline, it is assumed the centrifugal force and normal pressure are in balance. If a particle travels outward from the surface due to the centrifugal force it will be exposed to a larger normal pressure, which inhibits its outward travel having a stabilizing effect on the flow and decreasing

turbulent exchange. There is also a large difference in the large scale motion when compared to flat plates. Due to the curvature the large scale structures are destroyed in the boundary layer and this affects the smaller frequency fluctuations [81-83].

Two important experimental studies performed in the 1980s were done by Gillis and Johnston [84] and Muck et al.[85], both of which were similar to that of So [78]. The work by Gillis and Johnston was focused on the flow response near the onset of the curvature and the flow recovery once the flow was allowed to return to flat plate geometry, and that of Muck focused on a better understanding of the process for both convex and concave curvatures. Gillis and Johnston took turbulence measurements and found results similar to previous works. Two important advances were that due to the suppression of turbulence in the boundary layer, the large scale eddies which carry upstream information are destroyed and the initial conditions are lost, and that this length scale reestablishes very slowly. Muck concluded that the behavior of flow over convex when compared to flow over concave surfaces is a separate phenomenon and should be treated as such. This conclusion is opposite to findings from the direct numerical simulation study by Moser and Moin in 1987 [86] designed to look at the comparison between convex and concave flows. They found that turbulent statistics were similar for the two walls when scaled with local wall variables. Other turbulent quantities obtained from Moser and Moin compared favorably with experimental findings.

Gibson [87] provided valuable theoretical insight as a result of his experiments. The motive of his work was an attempt to predict turbulent and heat transfer using a second moment closure model. While that model development was unsuccessful, it was proposed that the change to the law of the wall that results in convex flows could be accounted for by an additive constant in the law of the wall equation for the non-dimensional streamwise mean velocity.

In 1997 Patel [88] provided a robust review and description of the phenomena associated with curved flow. From looking at others' data, it is assumed in curved flows the boundary layer flow profile also has a logarithmic region, though this region is closer to the wall in comparison to flat plate flows. Experimental data has shown that

deviation from the logarithmic law of the wall occurs at lower values of y+ for larger curvatures [88]. It has also been found that the effects of curvature are nonlinear, being proportionately larger for smaller curvatures. Using scaling considerations, the discrepancy about the differences between curved effects predicted from theory and seen in experiment was highlighted. The second order momentum equations derived from the instantaneous boundary layer equations in curvilinear orthogonal coordinates is given as:

$$\frac{\overline{u}}{h}\frac{\partial \overline{u}}{\partial x}+\overline{v}\frac{\partial \overline{u}}{\partial y}+\kappa\overline{u}\overline{v}+\frac{1}{h}\frac{\partial}{\partial x}\left(\frac{P}{\rho}+\overline{u'^2}\right)+\frac{\partial}{\partial y}\left(\overline{u'v'}\right)+2\kappa\overline{u'v'}-\nu\frac{\partial}{\partial y}\left(\frac{\partial \overline{u}}{\partial y}-\kappa\overline{u}\right)=0$$

$$-\kappa\overline{u}^2+\frac{\partial}{\partial y}\left(\frac{P}{\rho}+\overline{v'^2}\right)=0$$

$$\frac{1}{h}\frac{\partial \overline{u}}{\partial x}+\frac{\partial \overline{v}}{\partial x}+\kappa\overline{v}=0 \qquad (10)$$

where h is a parameter that accounts for different curvatures at different points in the coordinate system, and κ is the inverse radius of curvature for that specific (h). From scaling considerations, curvature effects on the boundary layer parameters can be expected to be of the order of (κδ), but in experiments it has been shown that the effect on the properties is an order of magnitude greater than this.

Mokhtarzadeh-Dehghan and Yuan in 2002 [89] performed experiments looking at both convex and concave curvature effects and specifically the bursting behavior associated with the flow. They find that for $y/\delta \geq 0.4$, turbulent shear stresses are suppressed to negligible levels. It was found that bursting from the wall only decreased slightly due to the curvature. So while turbulence is emitted from the wall, its transport to outer layers is inhibited.

Gretler [90] and Munch [91] both looked at the behavior of curvature effects numerically. Munch used Large Eddy Simulations to look at the effect the radius of curvature has on the flow. Mean velocity profiles differed from the logarithmic law of

the wall, and this deviation increased for increasing curvature. Gretler applied a Reynolds stress model to solve for the turbulent flow characteristics. In comparison to the turbulent intensities measured by Eskinazi [75], fair agreement with his model was found.

Mukund et al. in 2006 [92] performed experiments where flow was subject to both curvature and favorable pressure gradients to see the effect of curvature on these types of flows. They performed experiments in a low speed wind tunnel for both flat plate and convex surface flows. Mean velocity profiles and parameters, and turbulence quantities were measured. Looking at the behavior of parameters affected by laminarization, they found that due to the acceleration laminarization occurred in both the flat plate and convex surface geometries, but that it occurred more quickly and completely in the curved flow. Holloway [93] also looked at flow subject to acceleration and curvature, but alternatively applied or removed the acceleration. Measurements of the response of turbulent quantities were consistent with other curvature studies. Upon application of the acceleration, caused with the use of a convergence, it was found that turbulent quantities were suppressed.

3.1.4 Laminarization Due to Heating

It has long been known that an increase in temperature results in an increase in viscosity for gases. In a turbulent gas flow, this increase in viscosity subjects the local eddies to an increase in viscous dampening and therefore can reduce the local turbulence. If local heating is sufficient, viscous effects can be sufficient to cause the flow to revert from turbulent to laminar. Early studies that identified this reversion from turbulent to laminar due to heating were done by Bankston et al. [94] while studying flow distributions for heated flow in parallel systems, and by Perkins and Worsoe-Schmidt [95] while studying varying gas properties in flows.

In 1970 Bankston [96] investigated laminarization in circular tubes due to heating for hydrogen and helium flows with bulk pipe Reynolds numbers of 2350 to 12,500. As a result of these experiments it was found there were many similarities between

laminarization due to heating with acceleration driven laminarization. In both, acceleration of the fluid occurs as does a thickening of the viscous sublayer. Heat transfer coefficients and wall shear stresses were obtained from measured wall temperatures and compared to what was expected for strictly turbulent or laminar flow. Turbulent intensities were measured as a function of axial position at the pipe centerline of the flows using a hot wire anemometer to verify laminarization. Similar to the acceleration parameter used for external boundary layer flows (K), a corresponding acceleration parameter using the average bulk velocity can be written in terms of the bulk temperature assuming small changes in pressure and a constant flow area. This allows the laminarization criterion to be written in terms of bulk temperature values, without affecting the critical values proposed for acceleration driven laminarization associated with this transition to laminar.

$$K'_{Bank} = \frac{\nu_b}{U_b^2}\frac{dU_b}{dx} \cong \frac{1}{\mathrm{Re}}\left(\frac{1}{T_b}\frac{dT_b}{d\left(x/D\right)}\right) \tag{11}$$

where subscript b refers to bulk values.

It was found that the flow was not considered fully turbulent when this critical value varied from 8.0 x 10^{-7} to 1.14 x 10^{-6}, similar to values found for acceleration studies. By comparing Nusselt numbers for the experiments to those expected for fully turbulent, or laminar flows, Bankston was able to predict the heated length required for laminarization to complete assuming that the modified acceleration parameter $\left(K'_{Bank}\right)$ is in the range needed to cause laminarization. This length parameter is given as:

$$x_i^+ = \frac{2x/D}{\mathrm{Re}\,\mathrm{Pr}} = \frac{\left(5\cdot 10^{-4} n\,\mathrm{Re}_i + 1\right)^{1/n} - 1}{2q_i^+\,\mathrm{Re}_i\,\mathrm{Pr}_i} \tag{12}$$

where q^+ is a non-dimensional heating parameter defined with initial fluid properties:

$$q^+ = \frac{q''_w A_{cs}}{\dot{m} C_{p,i} T_i} \tag{13}$$

and n is the exponent dependency of temperature on viscosity for gases.

McEligot et al. [97, 98] looked at heating caused laminarization in tubes in the 1960s. At the entrance to the test section, the flow was turbulent, but downstream of the heated section, flow characteristics diverged from turbulent flow correlations. Upon plotting a non-dimensional heat flux parameter against the Reynolds number, the trend of this highly heated flow was seen to differ from that of laminar or turbulent. For flow where the Mach number is low, and changes in pressure are small compared to changes in pressure, the following formulas for the acceleration parameter were developed. For iso-heat flux (IHF) conditions, a modified acceleration parameter was developed:

$$K'_{IHF} \cong \frac{4q^+}{\mathrm{Re}_i}\left[1 + 4q^+ \frac{x}{D}\right]^{a-d-1} \tag{14}$$

where a and d represent power law variations of the viscosity and heat capacity of the fluid. For conditions with variable wall heat flux (VHF), the following parameter was proposed where k is the fluid thermal conductivity:

$$K'_{VHF} \approx \frac{8q''_w D_h}{\mathrm{Re}_b^2 \,\mathrm{Pr}\, k_i T_i} \tag{15}$$

These parameters were also derived employing an energy balance, therefore the critical reversion values are the same as those used for acceleration driven laminarization.

Coon [99] obtained data for internal flows subject to local heating and the resulting behavior towards laminarization. Similar to Bankston, a modified acceleration parameter was derived. By assuming that changes in pressure are small compared to changes in temperature, and assuming perfect gas behavior, the acceleration parameter can be written in terms of the wall heat flux and bulk temperature. This reduces to the parameter proposed by Bankston (Eqn. (11)) assuming the kinetic energy terms are negligible.

$$K'_{Coon} = \frac{4}{G^2 D}\frac{\mu}{T_b}\frac{q''_w}{C_p} \tag{16}$$

For Reynolds number = 7,000, the following value of the criterion was presented for this modified acceleration parameter: K'_{Coon} = 1.5 x 10^{-6}, which is very close to that used in highly accelerated flows. Flow response to the heating was similar to the flow response to an acceleration.

Perkins in 1975 [100, 101] performed experiments with the objective of providing data and theoretical considerations for heated gas flows with low Reynolds numbers (Re< 10,000). He compared his experimental results for the wall heat transfer and temperature profiles to that predicted using various turbulence models. From an investigation of different integral parameters of the flow, it was found that the following parameter was a good predictor of the onset of laminarization from local quantities.

$$\Delta = \frac{4\mu_w}{D_h\sqrt{\rho_w g_c \tau_w}} > 0.02 \tag{17}$$

Perkins performed many runs with different heating rates and initial Reynolds numbers. It was found that the flow heat transfer characteristics could not be predicted by turbulent or laminar correlations for the following regime:

$$6.5\text{x}10^{-14} < q^{+}\,\text{Re}^{-2.78} < 4.0\text{x}10^{-13} \tag{18}$$

For Reynolds=7000, this corresponds to a critical value of the Coon modified acceleration parameter $\left(K'_{Coon}\right)$ of 1.8 x 10^{-6}, similar to the value suggested by Coon of 1.5 x 10^{-6}.

In 1979 Kawamura [102] analyzed the application of two-equation turbulence models to heated pipe gas flows by comparison to experimental data. Due to a lack of satisfactory agreement with experimental data using a k-ε and k-ω models, Kawamura proposed a new turbulence model based on a k-kL model of Rotta [103] with a modification to account for molecular viscosity and property variation due to heating. During gas flow laminarization the model constants were revisited by comparison to experimental data for strong heating. Comparisons were made to experimental data of Bankston [96] and Coon [99] for different heating rates. Agreement was favorable for runs with small heat transfer, though were less successful when strong heating occurred as the model under predicted the heat transfer coefficient, though it was better than that predicted with the k-ε and k-ω models.

Most of the studies to this point attributed the laminarization to be primarily caused from gas viscosity effects caused by the heating. In 1997, Torii [104] proposed that the primary mechanism causing laminarization to be the acceleration that accompanies the change in density due to the heating. Therefore he proposed that heated caused laminarization is actually just acceleration driven laminarization. Previous to this time most experiments had just measured flow profiles, so Torii performed numerical simulations using a k-ε turbulence model. Modifications to turbulent constants were employed to account for transition between turbulent and laminar flow regimes. It was

found that turbulent kinetic energy was reduced near the wall and that this decreases the heat transfer. From Stanton number comparisons with those of the experiments of Bankston [96], the general trends were replicated, though the specific values differed. It was also found that temperature variation in the tube decreased as a result of laminarization and as a result the temperature gradients near the wall were decreased.

In 1998 Shehata [105] performed experiments for strongly heated vertical air tube flows where the mean structures in the viscous layer were measured. Even though the flow is vertical where buoyancy contributes to the mean flow, forced convection dominated for the flow ranges studied. The experimental results were later used in two numerical studies for comparison, direct numerical simulations (DNS) by Satake et al. [106] and Large Eddy Simulations (LES) by Xu [107]. Turbulent quantities decreased along the flow length until they are small in comparison to molecular effects due to the local heating. Both numerical studies showed good agreement with the experiments for mean velocity and temperature characteristics. The DNS study showed that vortices are repressed upon being subjected to the strong heating, and remain so during heating. The LES study showed a thickening of the viscous sublayer and that this caused a suppression of turbulence in the near wall region. No visible eddies were evident near the wall for the laminarized cases.

Due to the concern of laminarization, this can cause a deteriorated turbulent heat transfer (DTHT) regime in gas reactors. Lee in 2008 [108, 109] performed experimental studies looking at strong heating in a vertical tube considering both buoyancy and heating effects. A heat transfer regime map was proposed for heated upflow. While the reduction in heat transfer ability is differentiated due to being caused by buoyancy or acceleration effects due to the heating, it is only mildly useful to the present study because it still has the limitation of only being relevant for upflow conditions. It was found that heating caused acceleration effects resulted in heat transfer reductions up to 70% of turbulent flow. The threshold for when the flow laminarizes in terms of the modified acceleration parameter was given as $K'_{Coon} = 2.5\text{x}10^{-6}$. For the range of flow subject to DTHT, a Nusselt number correlation

was developed modified from the Gnielinski correlation [110] for turbulent flows with the additional variable of non-dimensional wall heat flux.

Following the investigation into the DTHT regime in gas reactors due to the buoyancy and acceleration causing laminarizing effect, Kim [111] performed CFD turbulence modeling to look at this effect and how correlations could be used in a one-dimensional analysis code to predict this phenomenon. While the CFD analysis was able to capture the flow behavior for buoyancy caused laminarization, less success was found for acceleration driven laminarization, and therefore correlations proposed by Lee [109] from his experimental results better capture the behavior than the CFD analysis.

3.2 Laminarization Prediction in Pebble Bed Reactors

As presented in the literature review above, there have been a number of different parameters that have been proposed associated with laminarization. In a pebble bed geometry, three laminarization causing mechanisms are being considered as part of this dissertation; acceleration, flow over convex geometry, and local heating, and two of them will be investigated experimentally. In the tables below, parameters presented for laminarization due to acceleration and local heating are presented [7]:

Table 3-1. Acceleration Driven Laminarization Parameters

Reference	Parameter	Criterion for laminarization
Launder	$K = \frac{\nu}{U_\infty^2}\frac{dU_\infty}{dx}$	$K \geq 2 \cdot 10^{-6}$
Launder (later study)	$Kc_f^{-3/2}$	
Moretti and Kays	K	$K \geq 3.5 \times 10^{-6}$
Schraub and Kline	K	$K \geq 3.5 \times 10^{-6}$; $K/c_f^{0.5}$
Patel and Head	$\Delta p = \frac{\nu}{U_*^3}\frac{dp}{dx}$	$\Delta p < -0.025$
Patel and Head	$\Delta \tau = \frac{\nu\alpha}{\rho U_\tau^3}$	$\Delta \tau < -0.009$
Fiedler and Head	Spreading of intermittency function across boundary layer	
Back and Seban	K	$K > 3 \times 10^{-6}$
Escudier	Decrease in $\overline{u'v'}$	
Fernholz and Warnack	No single criterion can be used	
Cal	Λ	Correlation with reduction in skin friction

Table 3-2: Heating Driven Laminarization Parameters

Reference	Parameter	Criterion for laminarization
Bankston	$K'_{Bank} = \frac{\nu_b}{U_b^2}\frac{dU_b}{dx} \cong \frac{1}{\mathrm{Re}}\left(\frac{1}{T_b}\frac{dT_b}{d\left(x/D\right)}\right)$	$K \geq 1.14\cdot 10^{-6}$
McEligot	$K'_{IHF} \cong \frac{4q^+}{\mathrm{Re}_i}\left[1+4q^+\frac{x}{D}\right]^{a-d-1}$	$K \geq 2.0\cdot 10^{-6}$
McEligot	$K'_{VHF} \approx \frac{8q''_w D_h}{\mathrm{Re}_b^2 \,\mathrm{Pr}\, k_i T_i}$	$K \geq 2.0\cdot 10^{-6}$
Coon	$K'_{Coon} = \frac{4}{G^2 D}\frac{\mu}{T_b}\frac{q''_w}{C_p}$	$K \geq 1.5\cdot 10^{-6}$
Perkins	$\Delta = \frac{4\mu_w}{D_h\sqrt{\rho_w g_c \tau_w}} > 0.02$	$\Delta > 0.02$
Perkins	$q^+\,\mathrm{Re}^{-2.78} = \frac{q''_w A_{cs}}{\dot{m} C_{p,i} T_i}\mathrm{Re}^{-2.78}$	$6.5\mathrm{x}10^{-14} < q^+\,\mathrm{Re}^{-2.78} < 4.0\mathrm{x}10^{-13}$
Lee	$K'_{Coon} = \frac{4}{G^2 D}\frac{\mu}{T_b}\frac{q''_w}{C_p}$	$K \geq 2.5\cdot 10^{-6}$

The reasoning behind the use of these parameters is varied. While most employ some theoretical reasoning in relation to the behavior of the boundary layer, others attempt to capture this behavior more explicitly by the use of boundary layer parameters. This results in some of these criteria being less predictive in nature, and more a description of the response in the boundary layer. Specific laminarization criteria presented in the literature are less abundant for flow over convex surfaces. This is perhaps because laminarization caused by curvature effects seems to be more of a gradual change when compared to other forms of laminarization. The literature has suggested that turbulence quantities are affected when $\delta/R > 1/300$ or when the Curvature Richardson number is greater than 0.30. Though in contrast to acceleration based parameters, for which there is one value at each axial location, the Curvature Richardson number is calculated across the boundary layer, and then at locations where it is greater than 0.30, this is where turbulence is cannot exist.

Given the random packing nature of the pebble bed, all possible conditions cannot be investigated. Instead using the laminarization parameters as a guide, the conditions where these parameters predict laminarization can be identified in the pebble bed reactor and related to the expected conditions. This identification can consider the laminarization causing mechanisms individually. Due to the random packing in the pebble bed reactors, convergence flow paths between pebbles are extremely varied. While it is impossible to identify all such geometry configurations that may be present that cause the sufficient acceleration for laminarization to occur, the necessary flow area convergence necessary for sufficient acceleration can be calculated.

4 EXPERIMENTAL PROGRAM

4.1 Research Focus Area

As stated in the literature review section, acceleration driven laminarization is usually described with use of the non-dimensional acceleration parameter (K). This parameter is a property of the free stream acceleration of the flow and gas properties. Most proposed critical values of this laminarization parameter vary from 2.5×10^{-6} to 3.0×10^{-6}. Assuming mass continuity, when considering the flow paths that are created from randomly packed pebbles, it is quite easy for flows to be established where the expected acceleration is greater than the threshold value. In fact, given the random packing, many different values of the acceleration parameter will exist, both those below the laminarization threshold and those above.

While there are no established threshold criteria for when laminarization will occur due to convex curvatures, it has been shown experimentally that values of the non-dimensional curvature (δ/R) as low as 0.003 can have an appreciable effect on repressing turbulence in the flow. From the equations of motion, this is surprising. The boundary layer equations of motion for flow over convex surfaces come from an order of magnitude analysis applied to the Reynolds Averaged Navier Stokes equations written in curvilinear coordinates where terms that are on the order of (1.0) are kept. From this analysis, curvature effects in the streamwise direction should only be of sufficient magnitude to affect the boundary layer equations if (δ/R) is on the order of (1.0). But this has been shown to not be true. It has been generally accepted that curvature effects are an order of magnitude greater than would be predicted from the equations of motion. Because of this, the second order boundary layer equations are often employed which contain terms of order (δ/R) in addition to terms of the order of (1.0).

While (δ/R) is not the only parameter used to describe curvature effects experimentally, it is the most widely used. Relating this term to flow through packed beds is problematic given the unknown nature of the boundary layer thickness going over the pebbles. Two cases that can be considered are the boundary layer thickness for

flow over a single sphere, or for flat plate flow with an arbitrary leading length. Given that the actual value is unknown, a range of curvatures will be tested in the test apparatus that correspond to conditions that may exist and can be classified as mild, moderate and strong curvature. This will assist in determining impact of curvature when combined with acceleration.

4.2 Description of Test Apparatus

4.2.1 Description of Test Section

A benchtop wind tunnel was constructed for the study of laminarization. The experiment apparatus was designed and constructed by the author with the assistance of Oregon State University Radiation Center employees. A number of factors and limitations were considered in the design. These included physical lab space, velocity limits of the PIV system, entrance section length, camera focal length, and wind tunnel wall material capable of producing curvature effects. The final constructed wind tunnel apparatus is shown below. It consists of an axial blower, flow conditioning section, and test section. The axial blower, flow conditioning frames, and test section supports were constructed of plywood, while the test section was made of acrylic. The bulk of the wind tunnel was supported on an optical breadboard tabletop. The breadboard enabled accurate positioning of the wind tunnel and PIV components.

The blower section made up the entrance to the wind tunnel and used a public wind tunnel design as its template [112]. Many wind tunnels position the blower at the exit of the test section, but due to the test section modularity needed to test the geometric laminarization causing mechanisms, this was not possible. While some researchers have recommended that the blower be positioned at the exit of the wind tunnel to aid in minimizing flow disturbances, this benefit is debatable for once through wind tunnels [113]. The blower is shown below in Figure 4-1.

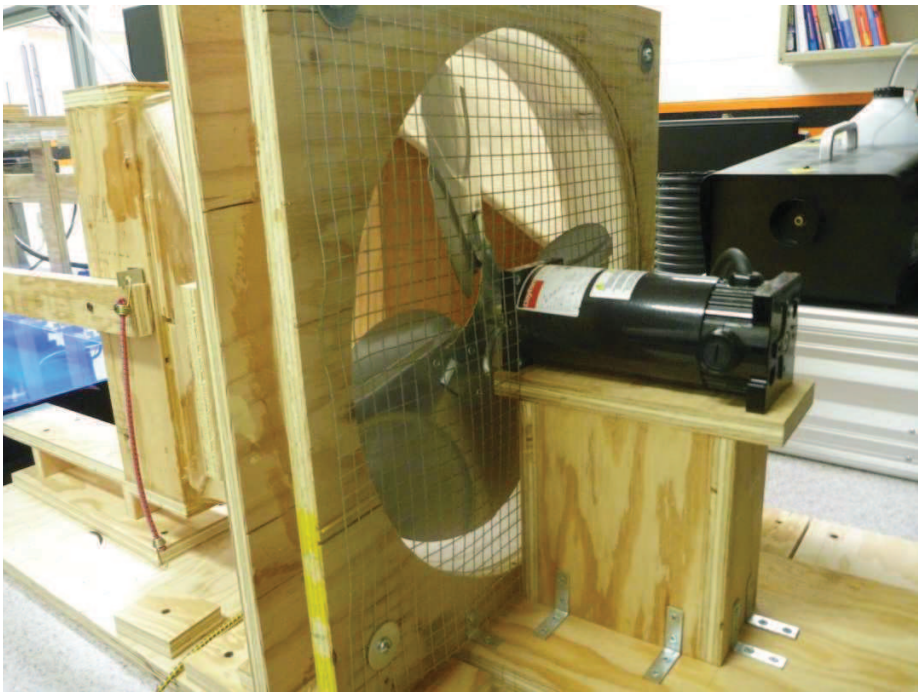

Figure 4-1: Entrance View of Blower Section

Grainger parts of a 16" aluminum fan blade (part 2C359), 1/6th hp 180 VDC motor (part 1Z851) and DC speed controller (part 5JJ56) were used. The blade and motor were chosen for their flowrate capacity for the expected pressure drops for the experiments. The DC motor was chosen as opposed to an AC motor because of the wider range of flowrate operability with applicable controllers. The motor was attached to a plywood base and the fan blade was contained in a plywood frame. This frame transitions from the circular flow area of the axial fan blade to the rectangular flow area of the flow conditioning and test sections. Two plywood arms protrude along the direction of flow which are used for aligning the flow straightening section. The circular flow area and the curved surfaces of the transitioning section were made from poster board covered in fiberglass cloth which was hardened using polyester resin. This created a smooth surface on the interior of the blower section, while providing structure for the curved walls. A metal screen was attached at the blower entrance for safety.

Figure 4-2: Downstream View of Blower Section

The flow straightening section immediately follows the blower section. This section is made of a number of rectangular plywood frames containing screens and honeycombs whose window area corresponds to the test section flow area. Using separate frames allows for removal for cleaning as needed due to dirt and dust collection and also flexibility in screen arrangement to maximize their efficacy in straightening the flow. The purpose of the straightening section is to reduce the mean velocity variation and reduce both lateral and longitudinal components of turbulence. The aluminum honeycomb frame was used first as recommended in the literature [114]. This is used to reduce both the large lateral components of turbulence and swirl introduced from the upstream axial fan. The cell size is 1/4" and has a cell length to cell diameter of 7.24, which follows recommendations for a ratio six to eight for maximum effectiveness in reducing lateral components of turbulence [113]. Following the honeycomb frame, four mesh screens are used; three in frames and one that is cinched between the flow straightening section and the test section. The screens are attached by wood staples to

one side of the frame. Weather stripping is used to line the opposite side of the frame to create a tight seal between frames. The frames are aligned between the two plywood arms from the blower section and bungee cords are used to compress the frames together. Figure 4-3 and Figure 4-4 show the honeycomb frame, a single screen frame, and the frames together with the blower section. Screen selection is described in further detail below.

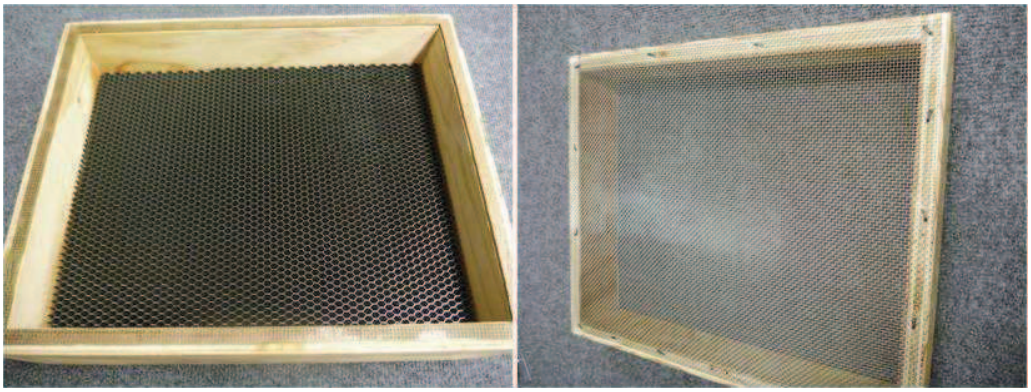

Figure 4-3: Honeycomb and Wire Screen Frames

Figure 4-4: Blower with Flow Straightening Section

The test section has a flow area of 11” in width by 14” in height, and 56” in length. In design of the test section, the following three features were required: visual clarity through the walls for PIV, curved walls, and modularity for the distinct geometries of the test cases. Acrylic met these three requirements and was used for the four test section walls. Plywood was used for the supporting structure. The top and bottom walls were constructed of $1/8^{th}$ in. thick clear acrylic and were cut in an approximate L-shape to be used for both the straight test cases and for the curved cases. Figure 4-5 shows their dimensions and footprint.

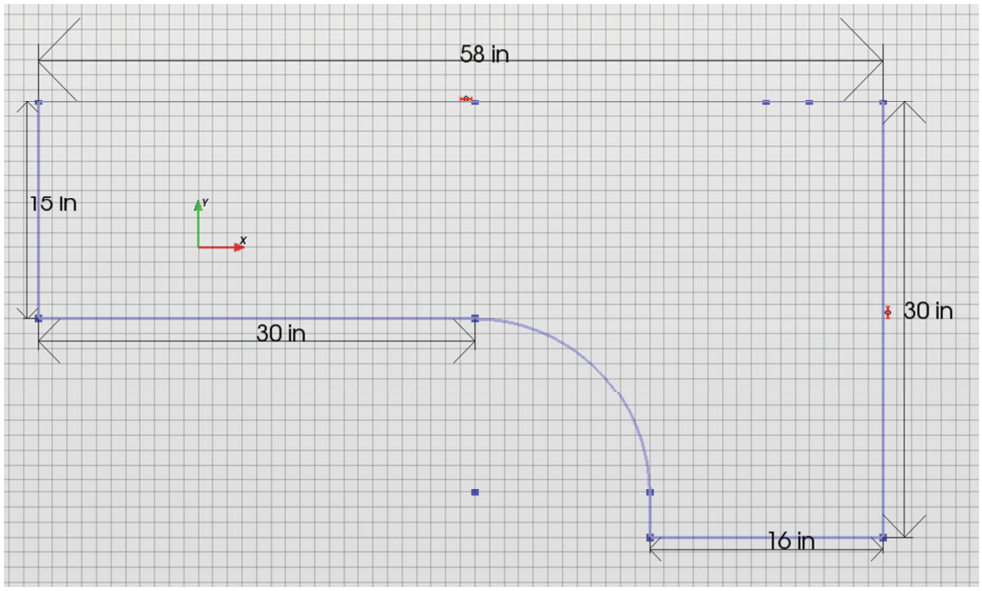

Figure 4-5. Dimensions of Top and Bottom Acrylic Walls

The side walls were constructed of thin, 1/16 in. thick acrylic which provided adequate flexibility to create the curved conditions for the different test cases. Dimensions are shown in the figure below.

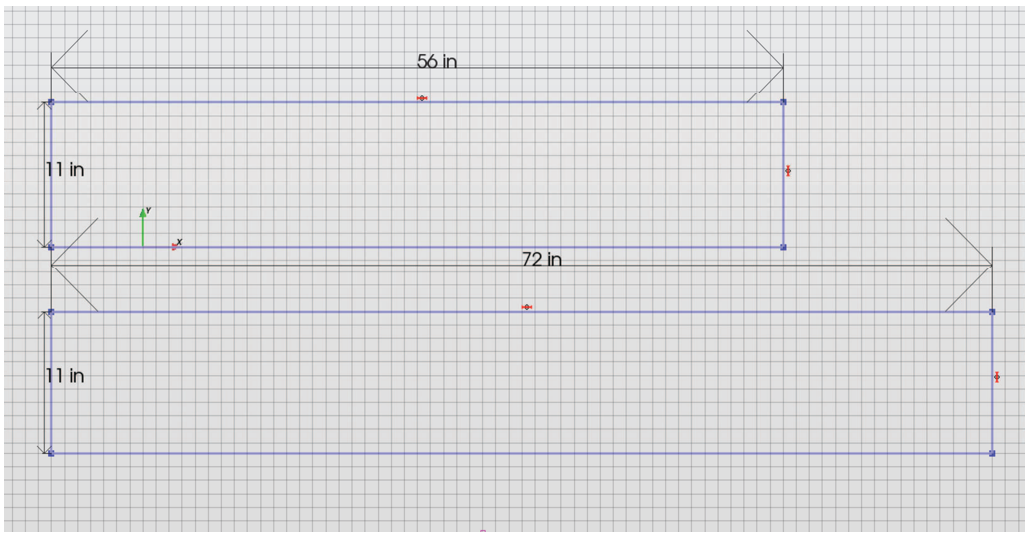

Figure 4-6. Dimensions of Side Acrylic Walls

The longer of the two walls was longer than the 56 in. test section length because this wall was used as the converging wall for the converged cases and the outer curved surface for the curvature cases. The 11”x 14” flow area was preserved for the first 30 inches of the test section. This first 30 inches of the test section is defined as the entrance length. Curvature and/or convergence was applied following this entrance region by bending the acrylic walls, either just the outer side wall for the straight convergence cases, or both walls for the curvature cases. Measurements were taken for the 20 inches following the entrance region along the shorter of the two of the side walls and is defined as the measurement region. By using one piece of acrylic for each wall, it created a smooth transition from the straight entrance region to the curved sections.

Due to the modularity needed for the different test cases, the four walls could not be permanently attached to one another. Instead acrylic tabs attached to the side walls were used to bolt the side walls to the top and bottom acrylic sheets as shown in Figure 4-7. These tabs were attached to the acrylic side walls with a solvent-type bonding agent. Often in wind tunnel construction, bolts which protrude into the wind tunnel are used to attach the walls together. The use of tabs avoided this situation to preserve the smooth internal surfaces, though due to this method of attachment, through-holes in the top and bottom sheets were necessary for the bolt attachment. For the higher converged cases the holes necessary for tab attachment were located in the footprint of the non-converged cases. To minimize the effect any holes may have, the holes were only drilled immediately before the specific test case, and the order of the test matrix progressed from non-converged to higher converged cases, moving the longer vertical side wall inward for the test matrix progression. When holes were present in the top and bottom walls of the specific case, rubber plugs were used in the holes and positioned at the same height as the internal surface of the top or bottom wall.

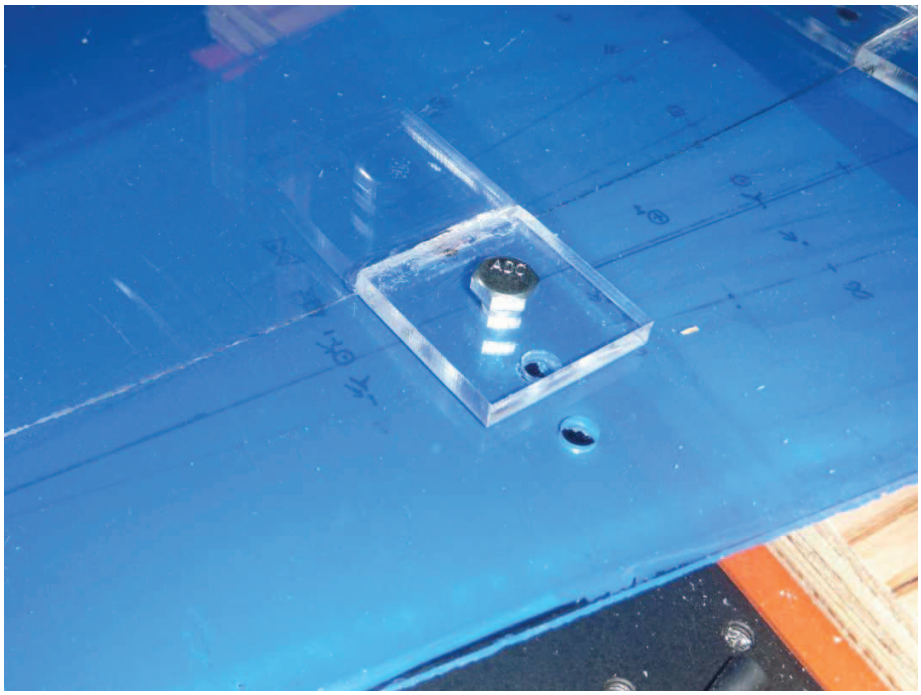

Figure 4-7. Acrylic Tabs Used for Modularity in Attaching Side Wall to Bottom Acrylic Sheet.

Images of the test section are shown below for two configurations; a straight converged case, and a converged curvature case.

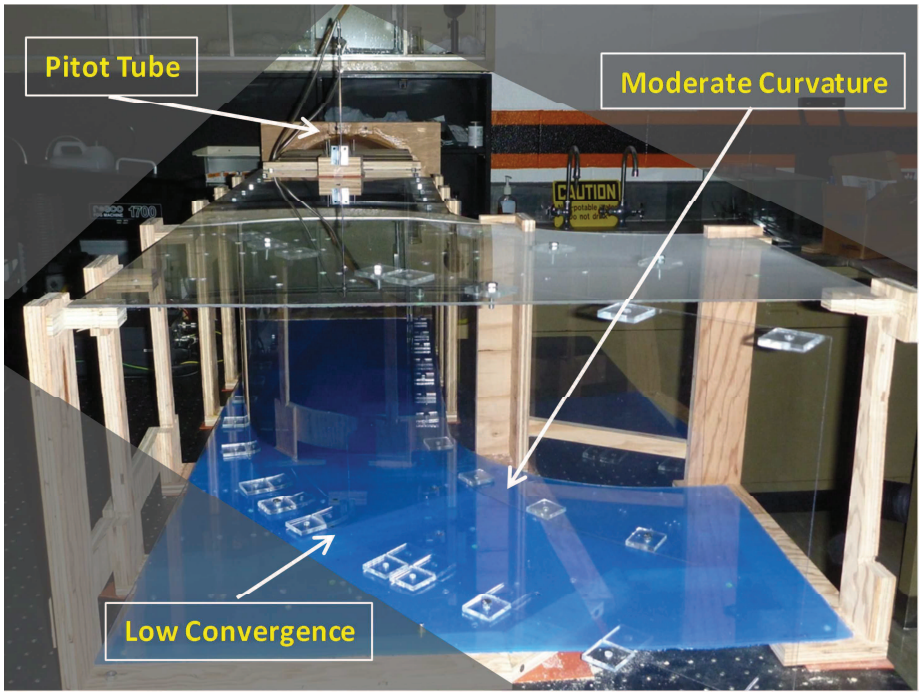

Figure 4-8. Curved Wall Test Section Configuration Example

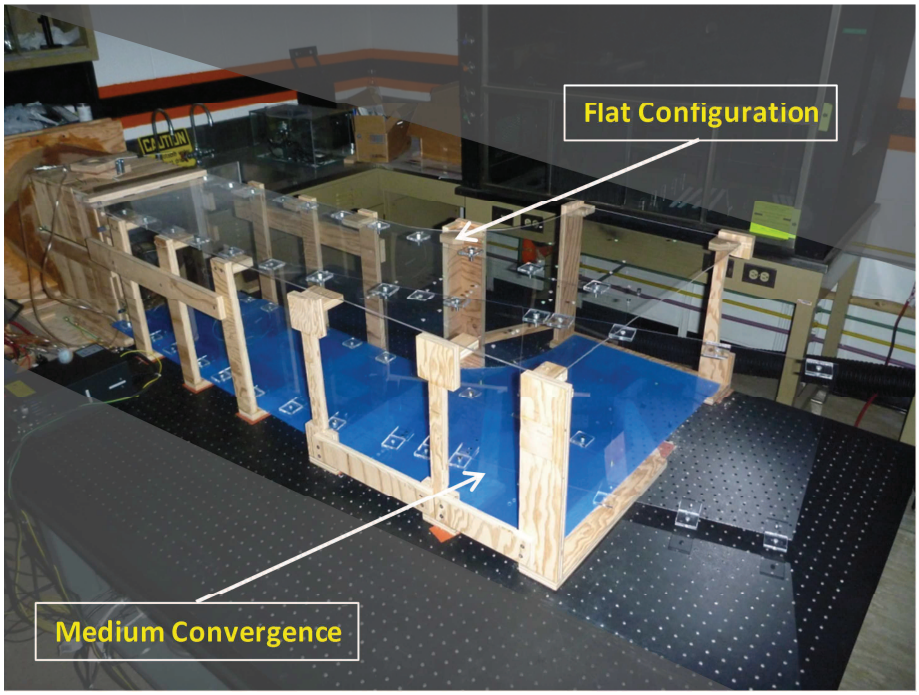

Figure 4-9. Flat Wall Test Section Configuration Example

4.2.2 Screen Characterization

The purpose of screens in the flow straightening section is twofold: to reduce the streamwise velocity variation, and to reduce the levels of turbulence. A screen provides a drag force that is proportional to the flow velocity going through it, and therefore has the effect of flattening out the velocity profile. In the apparatus used in the current study this is very important because the use of the axial fan upstream from the flow introduces large velocity variation. As the axial fan circulates the air, it has the effect of throwing the air to the outside walls of the test section. When velocity measurements were taken at the beginning of the entrance region without the use of any honeycombs or screens, the velocity ratio between the outer 25% of the test section and the center was 7:1. This was due to the dead spot created from the axial fan blade support. With adequate use of screens, this difference in flow velocity was eliminated.

The second purpose of the screens is to reduce the levels of turbulent fluctuations. Screens primarily reduce the level of axial turbulence more than lateral turbulence. The long honeycomb cell length in comparison to the cell diameter assists in reducing lateral turbulence. When the Reynolds number based on screen wire diameter is about 80, the screen produces small scale turbulence wakes from the wires that quickly dampen out [115]. Three parameters used to characterize screens, which are dependent on each other are β, K, and f. β is the open-area ratio, K is the pressure drop coefficient, and f is the turbulence reduction factor:

$$\beta = \left(1 - \frac{d}{M}\right)^2 \tag{19}$$

$$K = \Delta P \Big/ 0.5\rho U^2 \tag{20}$$

$$f_{axial} = \frac{1}{1+K}, \qquad f_{lateral} = \frac{1}{\sqrt{1+K}} \tag{21}$$

where d is the mesh wire diameter and M is the mesh length. Various correlations for the value of K have been presented that have the form K = f(β,Re) [115-119]. Different studies have shown variations up to 50% from the predicted value for K and those measured experimentally. Similar variability is encountered in the quantification of f as well. It has been shown that a screen with a pressure drop coefficient equal to 1.5 reduces yaw and swirl angles by 70% [113], with a pressure drop coefficient equal to 2.0 reduces non-uniformities in total pressure [117] and with a value of 2.8 reduces small longitudinal variations in the flow [120]. While it has been shown that a pressure drop coefficient of 2.8 essentially completely reduces the small longitudinal variations

of the flow, in practice it is not possible to use a single screen with this value of pressured drop without introducing other complications. Specifically, screens with values of $\beta < 0.57$, and therefore a higher pressure drop, have been shown to produce flow instabilities from coalescing neighboring jets. This results in trailing vortices of various sizes which can negatively affect the development of a two dimensional boundary layer. In addition, screens with values of β above 0.63 have been shown to not affect the flow substantially in reducing flow variations due to the large open area ratio [115]. Therefore it is recommended to use a number of screens in series with open area ratios between 0.57 and 0.63. The following table presents the characteristics of the screens tested.

Table 4-1. Screen Characteristics

Identifier	Material	Mesh Size	Open Width	Open Ratio	Wire diameter	30x open width
A	Uncoated plain steel	8 x 8	0.097”	60.2	0.028”	2.91”
B	304 SS	10 x 10	0.077”	59.3%	0.023”	2.31”
C	Polyester	10.9 x 10.9	0.0709”	61%	0.0197”	2.13”
D	Epoxy coated steel	24 x 24	0.0327”	61.6%	0.009”	0.981”
E	Brass	30 x 28	0.0253” x 0.0277”	59%	0.008”	0.831”

Another consideration in screen placement in the flow straightening section is spacing. The minimum spacing should be no less than the large energy containing eddy size so that turbulence caused from the first screen can dampen out before the next. Two recommendations suggested for screen spacing include greater than 30x the open

width, and spacing greater than 500x the wire diameter [115]. The open width is the actual open space between parallel wires. Screen spacing between screens used in the current wind tunnel was 2 inches.

A number of screen combinations were tested to obtain a screen configuration that provided the flattest velocity profile, while considering the effect on overall wind tunnel pressure resistance and its effect on maximum flowrate. In order to have the capability for the highest velocities in the wind tunnel, initial tests were performed with as few as two screens in series, and then later tests increased the number to five. The order of screens progressed from larger to smaller screen open widths, which also corresponded to decreasing Reynolds numbers based on screen wire diameter. These screen combinations were tested at different percentages of the axial fan motor's capacity. Due to the different pressure resistance introduced by the different screen combinations, these motor settings did not correspond to the same velocity values for the different cases, though ultimately the objective was to identify a screen series configuration that minimized velocity variation as a function of spanwise direction to ensure a two-dimensional boundary layer. The following configurations were tested. The mesh combination gives the screens used and their order. As stated in the Test Section Description section, one screen was not attached to a wooden frame, but instead was a free standing mesh screen that was cinched between the flow straightening section and the acrylic sheets of the test section. It served as an additional screen in the configuration series, as well as reducing the effect any lip that may exist between the last frame of the flow straightening section and the acrylic sheets may have. This was an additional (D) identifier screen and is the reason in the configurations presented below, the final screen is often (D).

Table 4-2. Screen Combination Test Cases

Configuration	Mesh Combination	Percentage Motor Setting of Max
1	A, D	50%
2	B, D	50, 100%
3	A, E	50%
4	A, D, D	50%
5	A, E, D	50%
6	B, C, D	25, 50, 75, 100%
7	D, E, D	25, 50, 75, 100%
8	B, C, D, D	25, 50, 75, 100%
9	B, C, D, E, D	25, 50, 75, 100%

Table 4-3 presents results for screen configurations (6)-(9). For these characterization runs, a pitot tube was used to measure velocity as a function of vertical height at 7 heights. The velocities were taken at 10 hz for 60 seconds for each vertical location. Presented is the velocity percentage difference between the highest and lowest value of the vertical direction for a given configuration and the average velocity for the 100% motor setting. The velocity difference value is averaged for the three motor settings of 50%, 75%, and 100%.

Table 4-3. Flow Variability for Screen Combinations

Configuration	Average Maximum Velocity Difference	Average 100% Setting Velocity (m/s)
6	21.5%	3.67
7	11.7%	3.58
8	4.8%	3.59
9	8.2%	3.32

Configurations (8) and (9) were identified as providing a sufficiently flat velocity profile where the streamwise velocity differed by less than 10%. Due to the added screen used in configuration (9), the maximum average velocity was reduced by 8% between configurations (8) and (9). This velocity for configuration (9) corresponded to the highest velocity case in the test matrix, though this velocity occurred when the test section was in its non-converged straight configuration, so a higher pressure drop and corresponding lower maximum velocity would be expected for the curved or converged test section configurations. From these results, screen configuration (8) was identified to be used for the test matrix cases. A more complete set of this data is presented in Appendix B.

4.2.3 Boundary Layer Trip

A boundary layer trip was used to develop a thick turbulent boundary layer before the flow was subjected to the laminarizing geometric mechanisms. Due to the spatial resolution limits of the measurement system, a thick boundary layer was desired. The trip was also needed due to the short entrance length of the test section. The flat plate Reynolds numbers for the test cases investigated using the entrance region as the characteristic length varied from 62,000 to 170,000, well below the transition value. Despite these low Reynolds numbers, previous studies have shown that a well developed turbulent boundary layer can be achieved with the proper tripping device [121, 122].

Three boundary layer trips were investigated: fish tank silica sand attached to two sided Scotch tape, a trip wire, and fish tank silica sand glued to a trip wire. Following the recommendation of Rona [121], initially the fish tank silica sand attached to two sided scotch tape was used. The rational was that while a trip wire produces streamwise turbulence, a layer of thin sand, or sandpaper would produce vorticity in the other directions as well. Two sizes of silica sand particles were tested; approximately 1.3 mm and 2.0mm. The pieces of Scotch tape that the sand particles were attached to were

3/4” wide strips in the streamwise direction and tests were performed for the two sizes of particles with one to four pieces of scotch tape. The trip wire used was a welding rod of 1/8” diameter. The final tripping method was by gluing 1.3 mm sand particles to a welding rod. This resulted in a boundary layer trip of 3/16” height. This was to introduce both the spanwise vorticity as well as streamwise and flow-normal vorticity to assist in the development of a turbulent boundary layer. The distance from the boundary layer trip to the start of the measurement region was approximately 300 boundary layer trip height lengths. Figure 4-10 shows the different boundary layer trips tested.

Figure 4-10. Boundary Layer Trips Investigated.

The flow profile plotted with both inner and outer variables, boundary layer thickness, and shape factor were used in determination of the effectiveness of the boundary layer trips. In addition to tripped flow, a non-tripped flow was investigated.

Velocities for the different cases varied to correspond to those of the test matrix. The measurements used for this analysis were time averaged velocity profiles taken with the PIV system, which is described in detail in a later section. Table 4-4 gives the test cases investigated. The purpose of these cases was to determine which boundary layer trip to use. Therefore not all combinations of velocity and boundary layer trip were investigated. For example, if a high velocity case with a specific boundary layer trip did not result in a well developed turbulent boundary layer, the lower velocity cases were not tested. For all these cases in this section, the measured data corresponds to the location at the end of the entrance region, and therefore beginning of the test section.

Table 4-4. Boundary Layer Trip Devices

Configuration	Tripping Device	Tripping Height (mm)	Streamwise Extent (mm)	Velocity (m/s)
A	None			
B	Silica Sand	1.3	19	2.5
C	Silica Sand	1.3	38	2.5
D	Silica Sand	2.0	19	2.5
E	Silica Sand	2.0	38	2.5
F	Silica Sand	2.0	57	2.5
G	Silica Sand	2.0	57	1.3
H	Silica Sand	2.0	76	2.5
I	Silica Sand	2.0	76	1.3
J	Welding Rod	3.18	3.18	2.5
K	Welding Rod	3.18	3.18	1.3
L	Sand and Rod	4.76	4.76	2.5
M	Sand and Rod	4.76	4.76	1.3

Figure 4-11 shows the boundary layer profiles normalized by outer variables for a case with the large diameter sand particles, the welding rod for both a higher and lower velocity, and also the sand covered welding rod for the low velocity case. (a) and (c) of Figure 4-11 show a profile that follows the shape of the Blasius laminar curve indicating that development of a thick turbulent boundary layer has not occurred. On the other hand, Figure 4-11 (b) and (d) show a profile that follows the $1/7^{th}$ power law profile for turbulent boundary layers. From outer variables it appears that the welding rod, while sufficient for tripping the boundary layer at higher velocities, is not sufficient for the low velocity case.

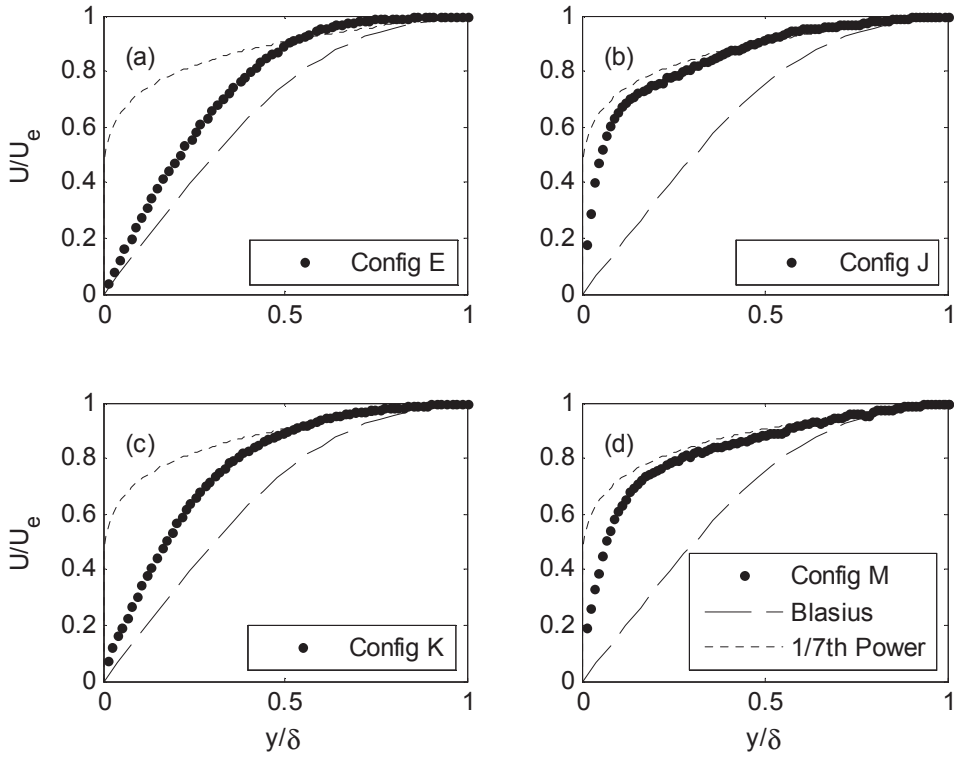

Figure 4-11. Boundary Layer Trip Profiles Plotted by Outer Variables

Figure 4-12 shows the profiles plotted in inner variables. Plotted as reference is the linear profile for the viscous sublayer and the characteristic logarithmic profile where von Kármán constant (κ) equals 0.41 and the 5.1 is used for the additive constant (B) [123, 124]:

$$u^+ = \frac{1}{\kappa}\ln y^+ + B \tag{22}$$

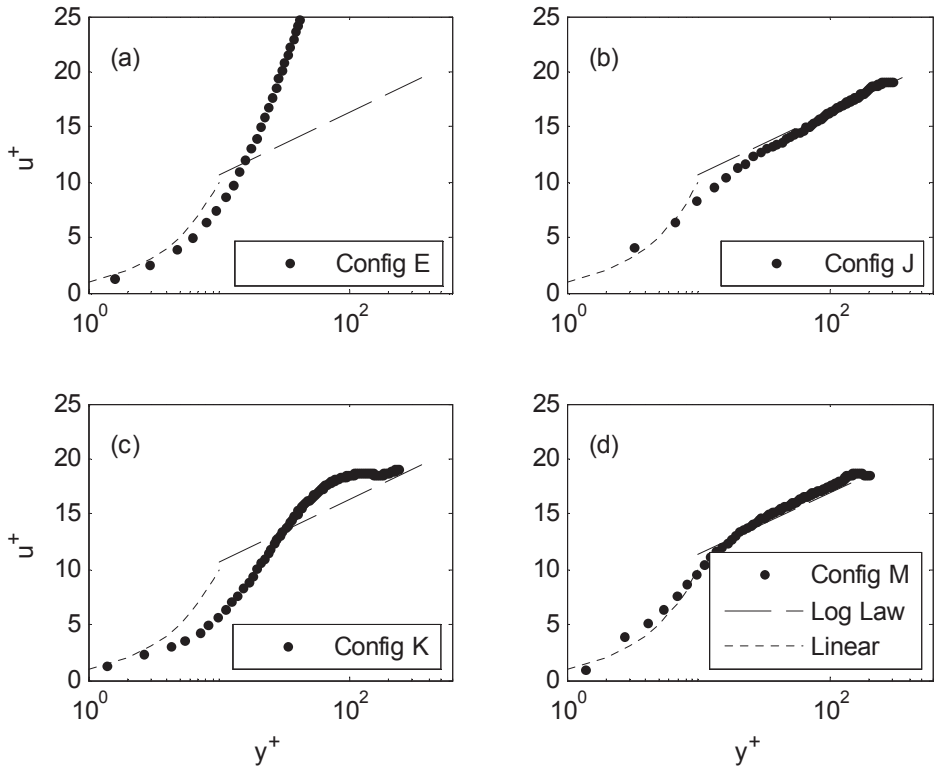

Figure 4-12. Boundary Layer Trip Profiles Plotted by Inner Variables

Confirming the outer variable normalized plots are these inner variable normalized plots. The sand particles used in Configuration E does not affect the inner profile at all, while Figure 4-12 (c), the linear region advances too far out into the flow to suggest

fully developed turbulent flow. Both Figure 4-12 (b) and (d) follow the logarithmic curve very well indicating a well established turbulent boundary layer.

As a result of this, the welding rod was used as the boundary layer trip for the cases of flow velocity equal and above 2.5 m/s, while the sand covered rod was used for the slow velocity cases of 1.3 m/s.

4.3 Instrumentation

4.3.1 Pitot Tube Velocity Measurement System

A pitot tube with pressure transducers and thermocouple was used to measure inlet point velocity. This system was used for two purposes. The first was to characterize the wind tunnel including tests for screen characterization and motor setting repeatability. The second purpose was to verify that bulk inlet velocity remained constant during PIV tests. This section describes this velocity measurement system.

A Dwyer pocket size 12” insertion length, 1/8” diameter pitot tube was used. This pitot tube has a 3/64” hole for the total pressure and 8 equally spaced 0.020” diameter holes for static pressure 1/2" from the leading point. Tygon tubing was used to connect the pitot tube ports to the pressure transducers. A 0-30 PSIA pressure transducer (Omega PX139-030A4V) with 0.5% full scale (FS) accuracy was used for static pressure and high accuracy, low pressure (0”-0.1”) differential pressure transducer (Omega PX655-0.1DI) with 0.5% FS accuracy was used for differential pressure. A K-type exposed tip, 304 stainless steel 1/16” thick sheath thermocouple was used (Omega KTSS-116E-12) with an accuracy of 1.1 C. The pitot tube was inserted into the test section through holes drilled in the acrylic sheets and held in place at the desired depth by use of through hole plug and positioning device constructed by the author. When the pitot tube hole was not used, a non-holed plug was used.

The pressure transducer output signals were a calibrated 4 volt and 4-20 mA current for the static and differential pressure transducers respectively. The differential pressure transducer output signal was run through a 0.1% accurate resistor and the

voltage drop was measured as the output signal to relate to pressure. An NI CompactRIO system with applicable modules was used for collection of thermocouple and pressure transducer output signals as well as transducer excitation requirements. A LabVIEW Virtual Instrument (VI) was written by the author for signal collection, averaging, uncertainty analysis, and output writing to EXCEL. Appendix A describes the uncertainty analysis method.

4.3.2 Particle Image Velocimetry

4.3.2.1 PIV Description

Particle image velocimetry (PIV) is a non-intrusive, velocity field measurement technique. All PIV systems contain three fundamental components: tracer particles in the flow, an illumination source, and an imaging system [125]. For the measurement region of interest, the tracer particles pass through a light sheet and are illuminated. For the current system used, the imaging system records the illuminated particles in image pairs within short time intervals. The particles in the two images of the pair are then statistically analyzed to obtain the velocity field from their displacement, as captured by the image pairs, and the time between the images [126].

$$V(x,t) = \frac{\Delta x(x,t)}{\Delta t} \tag{23}$$

Because the particles are used to obtain the velocity it is important that the particles are small enough and have similar buoyancy to the medium fluid so that they follow the flow. But at the same time they must be large enough, and have the necessary properties to scatter sufficient light so they can be imaged. Depending on the fluid medium under study, different particles can be used. In gas flows olive oil, fog, and metal oxides are often used. In liquid studies polystyrene, hollow glass spheres, and

different types of granules can be used [127]. Figure 4-13 shows a schematic of a general 2-D PIV setup.

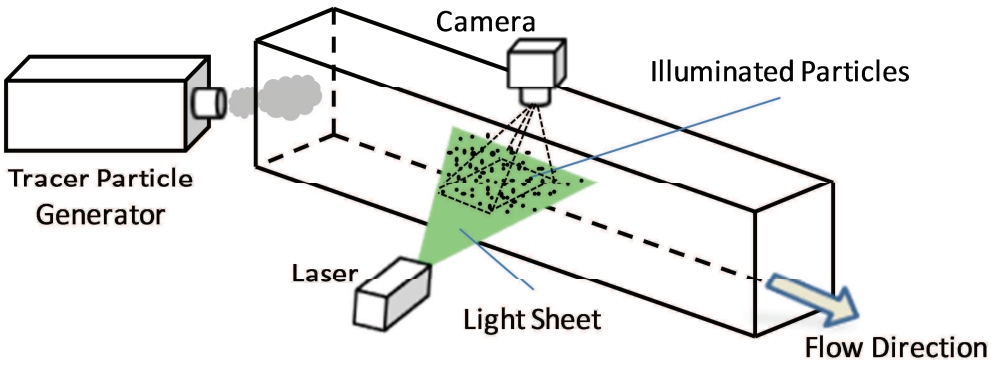

Figure 4-13. Setup for PIV System

The light sheet is formed from optics placed in front of a laser, which is typically pulsed twice corresponding to the image pair timing. While a steady light sheet can be used, this often results in streaking particles in the image due to the particles moving during the exposure time. The pulse can come from a dual cavity laser system, or from an electronic signal for a continuous wave laser. The energy per pulse that is required depends on the flow medium, flow velocity, and particles. Typical PIV lasers provide 1 to 200 mJ/pulse [128], though some current systems have lasers that can go much higher. The timing of the pulse, and other parameters is controlled by a timing box. In addition to controlling the timing, it accurately measures and records the timing as this is needed for the velocity calculations. There are three primary timing parameters: the pulse width, the time between pulses, and the trigger rate which is the frequency at which image pairs are recorded. The pulse width is the amount of time the laser light sheet is illuminated. The faster the flow, the shorter the laser pulse width must be to avoid particle streaking, though it must be long enough so that the particles reflect enough light so their image is captured by the imaging system. For high speed flows, this balancing act can be a challenge. The second timing parameter is the time between pulses. This represents the Δt in Equation (23) that is used for the velocity calculation.

The Δt needed in Equation (23) is usually much faster than the frame rate of even high speed cameras. If the Δt between laser pulses is too great, the particles will have moved too far between images and establishing the spatial correlation between the images needed for the velocity calculation will not be possible. Therefore, typically the two laser pulses for an image pair straddle the end and beginning of progressive camera exposures, as shown in Figure 4-14. For the bulk of the camera exposure, particles are not being imaged, but only during the pulse width. This illustrates the need to limit ambient light. As shown in Figure 4-13, for 2-D PIV the camera lens is positioned 90^{o} from the laser light sheet.

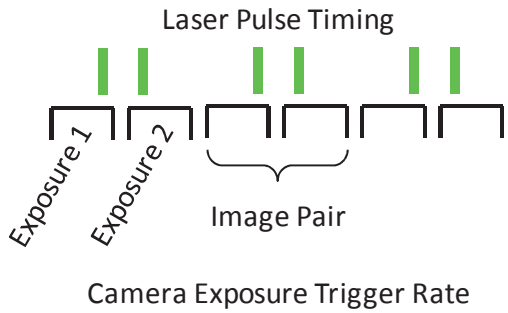

Figure 4-14. PIV Synchronization

The last timing parameter is the trigger rate at which image pairs are taken. This is a function of the physics that are being studied, and often limited by the camera frequency.

Once image pairs are taken, these are statistically analyzed to obtain the velocity field. Each image pair results in one vector field plot. The individual vectors are calculated by dividing the image into a grid pattern of smaller sections, typically squares, called interrogation areas. Figure 4-15 shows a hypothetical image pair with interrogation areas. As can be seen, there is only small displacement during the Δt between pulses. One independent velocity vector is given for each interrogation area for the image pair, though the interrogation windows can be overlapped to increase

vectors, but then neighboring vectors are dependent. A typical interrogation area size is 32 x 32 or 64 x 64 pixels [128].

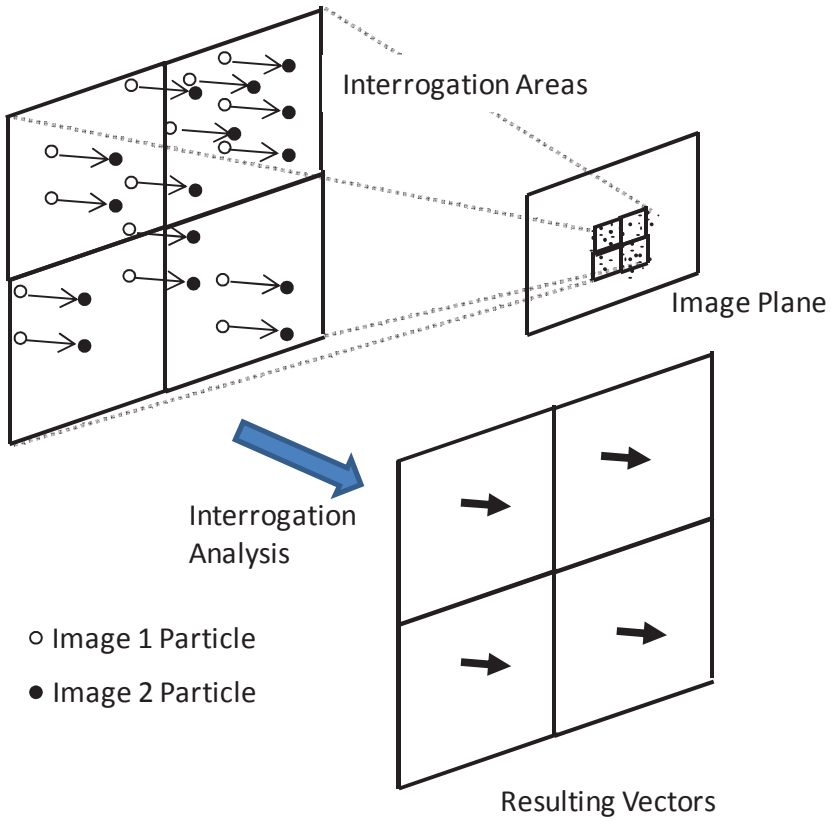

Figure 4-15. Interrogation Area Analysis Method. Patterned after Adrian [128]

Cross correlation is performed for each interrogation area pair to obtain velocity. An interrogation area pair refers to one interrogation area location in space in the image plane and the two images in time corresponding to the camera exposures of the light pulse pair. The actual correlation is performed in Fourier space because it requires less computational operations, but has the effect of shifting one of the image pair interrogation windows in space in the image plane with respect to the other interrogation window. A cross correlation estimator is calculated for each of the respective shifts. This is given as:

$$R(s) = \int_{W_1} I_1(X) I_2(X+s)\, dX \tag{24}$$

where R is the cross correlation estimator, I(X) is the intensity distribution of that interrogation area, and s is the shift. It has the effect of determining the shift in space where the intensity distributions of the interrogation area pair line up. This occurs at the maximum of R(s). For sufficient particles in the interrogation areas, the largest correlation coefficient corresponds to the true displacement of the particles. This displacement is used to calculate the velocity of that corresponding interrogation area. An example cross correlation peak map is shown in Figure 4-16.

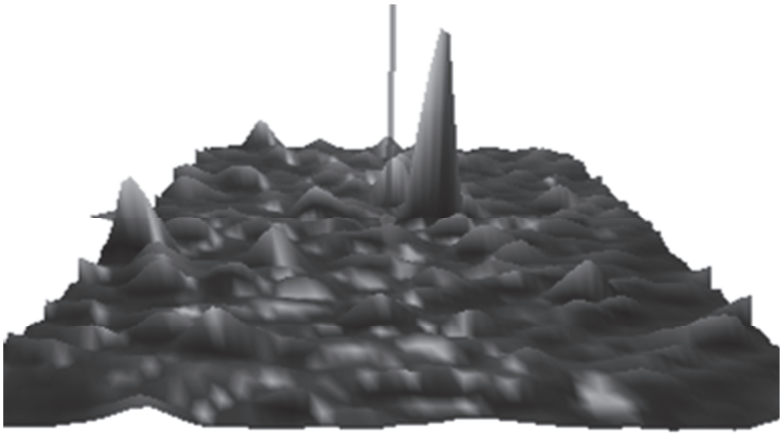

Figure 4-16. Example Cross Correlation Map Acquired from Test Data

Since interrogation pairs in space in the image plane are correlated with themselves, and not with their neighbors in space, it is important that most of the particles in the interrogation window remain in that window between the image pairs in time and that there are sufficient particles in each area. It is recommended that there are 5-10 particles in each area, and that the particles travel less than $1/4^{th}$ the interrogation window side length between pulses [128]. The software used for this study recommends that travel be less than 1/2 the side length [129].

In calculation of velocity vectors, there are many options that can be used to refine the method. Three specific options that are used in this study are adaptive interrogation size stepping, windows, and validation. Adaptive correlations use larger initial interrogation areas followed by smaller interrogation areas. By using larger areas, accuracy is increased because there will be more particles in the area, and most of the particles will remain in the same interrogation area pairs between image pairs, therefore the true value of velocity has a higher probability of being captured accurately. But this increase in accuracy substitutes for a decrease in the resolution of the velocity vector field. In the next step when smaller interrogation areas are used, the software uses the previous velocity field information to determine the velocity when analyzing the smaller interrogation area's cross correlation map. This method assists in reducing the number of false spurious vectors. Commercial PIV software provides the user with the ability to set the beginning and ending interrogation area sizes for adaptive correlation processes.

The cross correlation method is implemented by fast Fourier transform, as opposed to direct implementation because it is much faster. This operates under the assumption that the intensity distribution of the interrogation areas is cyclic. For example, particles near the left edge of the interrogation area are also assumed to be present to the right of the right boundary and so for velocity to the right, images to the left of the right boundary would be correlated with these cyclic particles. For a high concentration of uniformly distributed particles that primarily stay in the interrogation area for both images of the pair, the highest cross correlation peak will correspond to the true velocity, but this assumption of cyclic intensity pattern is a source of error. This cyclic noise can be reduced or eliminated by the use of windows. Windowing occurs when the gray scale of the pixels near the outer border of the interrogation area, typically 25% in area, is either masked completely, or in proportion to the distance away from the center of the interrogation area. Setting the gray scale to 0 in this outer border area is called a top hat window, while reducing the gray scale as a function of distance is a Gaussian window.

Validation methods can be used to identify when the vectors provided by the analysis method are not a true representation of the velocity vectors at that location. Peak height validation sets a minimum ratio limit that the highest correlation peak must be with respect to the second highest peak calculated in the cross correlation map. When this limit is not met, it indicates that there may be ambiguity with which cross correlation peak is representative of the true velocity. Another validation method is to look at the velocity vectors of the near neighbors of an interrogation area. An acceptance factor and a definition of near neighbors can be set to identify vectors that differ greatly from their neighbors. When identified, these spurious vectors are replaced by interpolation of the near neighbors.

The instantaneous velocity vector fields can then be used to calculate derived and statistical quantities. Commercial PIV software typically has many options for analyzing the flow for this purpose. This includes vector averaging, subtraction to obtain fluctuating velocity, calculating vorticity, and turbulent statistics.

4.3.2.2 PIV Equipment and Settings of Current Experiment

A Dantec Dynamics PIV system for time resolved flows up to 5 m/s consisting of laser, camera and software was used for this study. The camera used was a VisionResearch 2 MP, complimentary metal-oxide semiconductor (CMOS) sensor, gray-scale camera. The camera has a maximum frequency of 1016 images per second at full resolution, and a maximum frequency of 150,000 at the lowest possible resolution. Pixel size on the sensor is 11.5 μm and an 8, 12, or 14-bit gray scale can be used. Acquired images are first saved in the onboard memory of the camera, and then are transferred to the computer by Ethernet. Some PIV cameras allow continuous transfer of images to the computer, albeit for a slower acquisition rate, but this is not possible for the camera for the current experiment. The onboard memory stores 770 image pairs at full pixel image area. A 60mm Nikon lens was used. The exposure time frames for both image 1 and image 2 of the image pair was 980 μs. This was the maximum for the camera. The 8 bit gray scale was used.

The camera was mounted on an aluminum frame above the wind tunnel test section looking downward on the horizontal laser light sheet. The frame was constructed with linear slides to allow for three dimensions of camera motion. Figure 4-17 shows the aluminum support frame and camera above the test section.

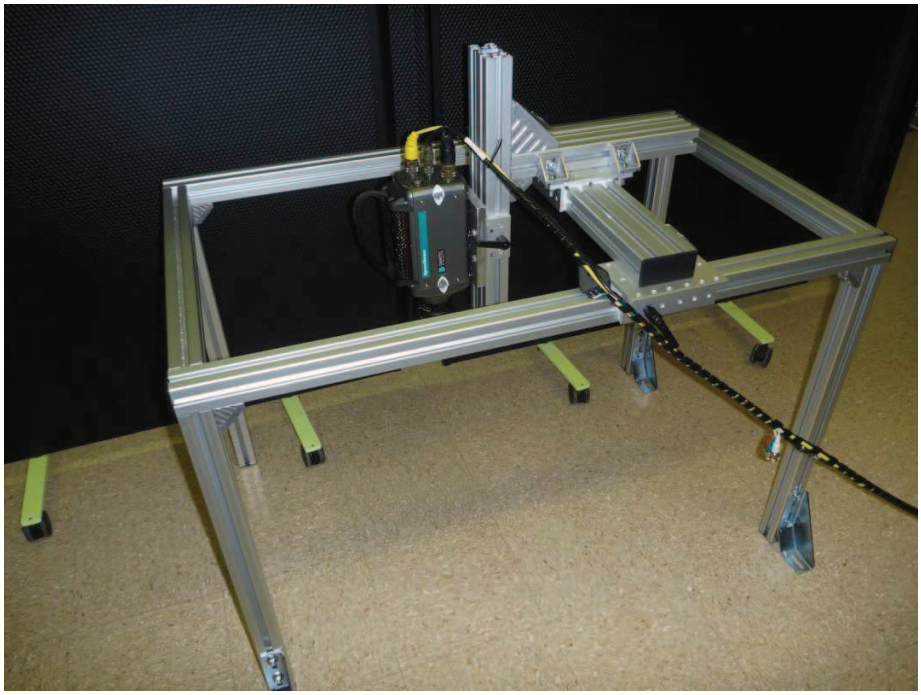

Figure 4-17. Camera Support and Linear Motion Frame

A 5 W, 532 nm wavelength, continuous wave, Nd:YAG diode laser was used. The laser has variable power output and an adjustable focus. Light sheet optics were used that adjusted the laser beam to a light sheet. The optics allowed flexibility in setting the light sheet thickness and divergence angle. The adjustable focal length was adjusted for the specific test case so the light sheet thickness was kept constant for the region of light sheet directly under the camera, and therefore used to illuminate the tracer particles imaged for that run. The laser was mounted on a 2-D linear translational stage attached to a platform that was connected to the lab optical table breadboard. The platform could be moved for the third degree of motion. Figure 4-18 shows this system. The camera

and laser were controlled by a high resolution DantecDynamics timer box. This timer box has eight output channels and provides a true hardware time stamp with a resolution of 12.5 nanoseconds.

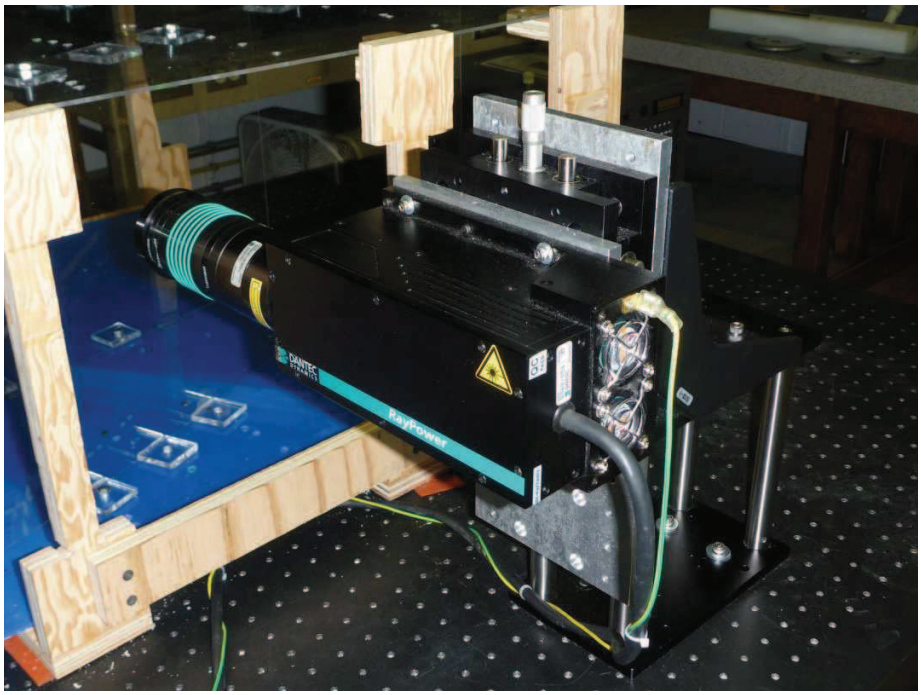

Figure 4-18. Laser and Two-Axis Linear Stage

A Rosco 1700 fog machine with variable fog level control was used to produce the seeding particles from a glycerol-water solution. The fog machine was placed at the entrance to the wind tunnel and produced particles of approximately 5.0 microns in diameter [130, 131].

Laser and fog machine settings for the different test cases of the test matrix were not held constant. For convergence flow geometries, the air accelerates substantially along the length of the test section. In order to acquire images with sufficient particles per interrogation area, while creating a large contrast in gray scale between particles and surroundings, and reducing particle streaking, it was necessary to adjust both laser and

fog machine settings. Typical pulse widths were from 45 to 90 μs and Δt between pulses was 100 μs. The trigger rate ($t_{trigger}$) for all experiments was 100 hz.

The time settings and interrogation area settings are chosen to capture the physics of interest. A theoretical analysis was conducted for flow over a flat plate for bulk velocities to be used in the test matrix to obtain estimates for the spatial and time scales of the flow geometry. The boundary layer thickness was estimated using [132]:

$$\delta = \frac{x \cdot 0.37}{\mathrm{Re}_x^{0.2}} \tag{25}$$

where the bulk velocity and entrance length are used in the calculation of Re_x. For this analysis a boundary layer tripping device was assumed to be not used. The skin friction coefficient is defined as:

$$C_f \equiv \frac{\tau_w}{0.5\rho U_\infty^2} \tag{26}$$

Many correlations for turbulent flat plates have been proposed in the literature. Used here [123]:

$$C_f = 0.0594 \cdot \mathrm{Re}_x^{-1/5} \tag{27}$$

The velocity scale for the turbulence as a whole for a turbulent boundary layer can be estimated as being on the order of the friction velocity [133, 134]. The friction velocity can be obtained using the wall shear stress from the previous two equations:

$$u_* = \sqrt{\frac{\tau_w}{\rho}} \tag{28}$$

The length scale of the largest eddies associated with boundary layers can be approximated as being on the order of the size of the boundary layer thickness [134]. A Reynolds number associated with the turbulence can be calculated using these scales. The Taylor microscale can then be estimated with the relationship of turbulent scales [134, 135]. This length scale is used to assist in selection of interrogation area size.

$$\lambda = \delta\sqrt{10}\,\mathrm{Re}_T^{-1/2} \tag{29}$$

A velocity and time scale characteristic of the Taylor microscale can be estimated from the relationship between the Turbulence Reynolds number and the Taylor microscale Reynolds number. This time scale is used in selection of the trigger rate for recording of image pairs [134].

$$\mathrm{Re}_\lambda = \left(\frac{20}{3}\cdot \mathrm{Re}_T\right)^{0.5} \tag{30}$$

$$\mathrm{Re}_\lambda = \frac{u_\lambda \lambda}{\nu} \tag{31}$$

$$t_\lambda = \frac{\lambda}{u_\lambda} \tag{32}$$

The time between laser pulses comes from the need for particles to remain in the same interrogation area in both image pairs. As stated above, suggested with this requirement is that the Δx for particles between image pairs remain below 1/4 to 1/2 the length of an interrogation area side. For a velocity of 5 m/s, a time associated with particle travel across half the interrogation area was calculated. The maximum pulse rate of the PIV system met this requirement.

Table 4-5. Calculated Scales and Time Settings

U_∞	λ (mm)	u_λ (m/s)	t_λ (sec)	$t_{trigger}$ (sec)	λ/x_{window}	$t_{1/2}$	Δt
3.6	4.6	0.15	0.03	0.01	3.6	1.57×10^{-4}	1.0×10^{-4}
2.5	5.6	0.11	0.05	0.01	4.3	1.57×10^{-4}	1.0×10^{-4}
1.3	8.1	0.06	0.13	0.01	6.2	1.57×10^{-4}	1.0×10^{-4}

The dynamic velocity range (DVR) and dynamic spatial range (DSR) represent the ratio of resolvable scales of the PIV system given by:

$$DVR = \frac{u_{\max}}{\sigma_u} = \frac{M_0 \Delta x_{p,\max}}{c_\tau d_\tau} \tag{33}$$

$$DSR = \frac{l_x}{\Delta x_{p,\max}} \tag{34}$$

where

u_{max} Full scale velocity
σ_u Rms error in the velocity [128]
M_0 Magnification

$\Delta x_{p,max}$	Maximum particle displacement
c_τ	Constant dependent on analysis to determine particle displacement[126]
d_τ	Particle diameter in image
l_x	Field of view in the fluid

Both these values were greater than 200, thus allowing for resolution of large and small scales simultaneously.

4.3.2.3 PIV Sources of Error

The uncertainty of PIV is complex because of the many factors that affect the resulting velocity vector fields. Of these factors, some uncertainties can be calculated with straight forward methods employing such methods as the Kline-McClintock method to account for the base uncertainties associated with primary instruments and equipment. Typically results of PIV are presented after some sort of time averaging, so other factors must be accounted for through statistical means. The final source of uncertainty is due to the algorithms that are used to convert the raw images to vector maps. This is quite complex due to the wide range of processing procedures that have been developed, such as windowing, sub-pixel estimators, interrogation area deformation methods. Then for commercial software, these methods are implemented with proprietary pieces of software. When the effectiveness of the techniques is needed to be tested beyond that done by the developers, typically synthetic PIV is used to create images where particle density, particle translation, particle size, peak intensity and background noise are controlled to test the various processing procedures. These synthetic PIV studies have been used to establish best practices guidelines to follow for PIV.

The most straight forward uncertainty analysis for PIV is to calculate the uncertainty for the velocity of a single particle using the equation for velocity:

$$u = \frac{\Delta x}{\Delta t} \tag{35}$$

In this equation, the uncertainty in velocity comes from the uncertainty in distance traveled and the time between laser pulses. The uncertainty in time is due to the timing equipment. The uncertainty in Δx comes from the uncertainty of the particle location for the two images of the pair. If a part of the particle covers anywhere between ±0.5 of the pixel, then that pixel is identified as corresponding to a particle location. Therefore location uncertainty is 0.5 pixels, while the uncertainty for Δx with a starting and ending point is 1.0 pixel. This is a conservative estimate for this uncertainty because the software employs methods of pixel interpolation that can reduce the uncertainty in location to 0.05 pixels. This uncertainty in pixel location is converted to meters using the magnification factor related to the image and measurements planes. These uncertainties can be combined using the Kline-McClintock method. For the present experiment, the typical number of pixels corresponding to Δx is at most 32. Uncertainty in the timing instruments was 12.5 ns. This results in uncertainties between 4.0 to 12.0% for a single particle movement depending on the velocity. This can be seen as an upper limit for the instantaneous velocity vector because in practice, each interrogation area contains multiple particles. In addition, uncertainties for the mean velocity can be calculated using the Kline-McClintock method considering both the uncertainty in the individual measurements, and the standard deviation across time for the dataset using Eqn. (55). Due to the large dataset, these uncertainties are below 2.5%. This uncertainty primarily comes from the scatter in the velocities for the dataset.

A more robust method of uncertainty analysis considers the four primary sources of uncertainty in PIV experiments which are equipment, particle lag, sampling size, and the processing algorithm [136, 137]. The general methodology of PIV is to determine the displacement and time interval associated with the particles to obtain the velocity. Displacement in the image plane and displacement in the measurement plane is related

through a scaling or magnification factor. The resulting equation for velocity is given by:

$$u = \psi \frac{\Delta x}{\Delta t} \tag{36}$$

where Δx is the pixel displacement in the image plane and Ψ is the scaling factor defined as:

$$\psi = \frac{l}{L} \tag{37}$$

L is the length in the image plane given in pixels for the calibration length, and l is the corresponding length in the measurement plane given in length units (m). The scaling factor can also be related by the distance from the measurement plane to the camera lens and lens focal length.

For calibration for each test run, a calibration target with a printed grid on it was placed level at the laser height and an image was taken. The same calibration target and calibration length on the grid was used for each test run. The heights of the calibration target and laser were kept constant for each test run. The uncertainties associated with the scaling factor are a combination of the uncertainties in the calibration length on the calibration target given in meters, the uncertainty in the calibration length on the image plane in pixels, and the uncertainty in the distance from the calibration target to the camera lens. The uncertainty in calibration length on the calibration target was estimated from measuring errors. The uncertainty in the separation length between target and camera lens was estimated from the visible unevenness of the flatness of the calibration target. Given that the calibration target procedure was the same for each test

run, the calibration length on the image plane in pixels should be constant, but in actuality there was variability. The standard deviation of this variability was used as the uncertainty for the pixel calibration length. Uncertainty in Δt comes from the uncertainty in the timer box used to control the laser. The Kline-McClintock method was used to calculate an uncertainty for velocities. Equipment errors give a velocity uncertainty of less than 2.0%. Appendix D contains these calculations.

The second source of uncertainty is due to particle lag. In PIV the velocity is obtained from tracking the tracer particles, therefore it is necessary that the particles follow the flow. A force balance with respect to the particles includes buoyancy, Stokes drag, history term associated with momentum diffusing from the particle surface, variation in fluid stress around particle, and a lift force associated with particle shear and rotation. Typically, aside from the body force and the Stokes drag force, most of these forces can be neglected for gaseous flows with very small particles [125]. The resulting force balance gives:

$$m_p \frac{dv_p}{dt} = \frac{1}{6}\pi d_p^3 \left(\rho_p - \rho_f\right)\vec{g} + 3\pi\mu_f d_p \phi\left(v_p - u_{\mathrm{f}}\right) \tag{38}$$

where the first term is the acceleration term of the particle, the second is the buoyancy force that results from the difference in density between particle and fluid, and the last is the quasi-steady viscous drag force. Subscripts (p) refer to particle, and (f) to fluid. ϕ is a function that depends on the particle Reynolds number and accounts for the difference in viscous drag dependent on the local flow regime.

Due to the density difference between the fluid and the particle, the gravity body force creates a mean settling velocity relative to the fluid. This buoyancy difference can be quite large in gas flows due to the atomized fluid particles that are used. Though due to the small particle size, the corresponding force that causes the settling velocity typically is not of great concern for once through wind tunnels. Though is can be of

most concern in return-loop wind tunnels. This velocity can be obtained by setting the acceleration term in Equation (38) to zero:

$$v_p - u_f = \frac{\bar{\rho} - 1}{\bar{\rho}} \vec{g} \tau_0 \Big/ \phi \tag{39}$$

where $\bar{\rho}$ is the ratio of particle to fluid density and τ_o is the characteristic time constant. During one pass in the current experiment using particle diameter of 10 μm, and the most conservative estimates free stream velocity (slowest), the particle would drop less than 0.1 cm due to buoyancy. Similar to the buoyancy force, outward radial drift can occur due to the flow around the convex surface. This can be calculated by substituting centrifugal acceleration for the gravity term. For the case with the highest velocity for the entire length of the flow and the highest radius of curvature, the resulting acceleration is approximately twice that of gravity resulting in outward drift of slightly less than 0.2 cm.

The third particle slip velocity is due to the experienced acceleration from the fluid. The particle time constant can be used to determine the effect of this acceleration. This time constant accounts for the effect of density difference on change of acceleration between particle and fluid:

$$\tau_p = \frac{\left(\rho_p - \rho_f\right) d_p^2}{18 \rho_f \nu_f \phi} \tag{40}$$

Calculated for the current experiment, the particle time constant is 102 μs. The local fluid time scale can be estimated from the boundary layer thickness length scale and the local mean velocity. Conservative estimates of high local velocity and small

boundary layer thickness still result in uncertainty in the PIV measurement due to particle lag as less than 2.0%.

Statistical (mean) and turbulent quantities (rms, Reynolds Stresses) were ensemble averaged from instantaneous realizations. It is necessary that enough realizations are used such that the quantities are converged. It was found that statistical quantities converged in approximately 300 realizations, while turbulent quantities converge to within 2.0% in approximately 625. Datasets included a much larger set of realizations where convergence was within 1.0%. Appendix E contains plots of the convergence of these quantities.

In order to minimize uncertainty and error associated with the software algorithms, design rules were followed as recommended from previous Monte Carlo synthetic PIV analysis studies [138-140]. These include having greater than 10 particles in each interrogation area, having particle displacement less than 1/2 the interrogation side length, and having particles diameters in image plane between 2 and 4 pixels. Other PIV studies have shown that the primary source of uncertainty is due to equipment and particle lag uncertainty [136].

During the analysis in the PIV software, sometimes a strong cross correlation peak does not result for an interrogation area, or the highest to lower peak ratios is not strong enough to conclusively give a resulting velocity vector. When this occurs, a substituted velocity vector is output that is interpolated from its near neighbors. In the time averaging analysis used, only non-substituted vectors were used. Therefore for each interrogation area used, the time averaged velocity has an associated non-substituted fraction that is the ratio of vectors used/total vectors of the time sequence. A value of 1.0 corresponds to all the velocity vectors in the time sequence being non-substituted for the time average for a given interrogation area. For the time averaged data used herein, the majority of the interrogation area's non-substituted fractions was greater than 90%. If the average value was less than 80% for a given dataset, the dataset was repeated. Appendix F provides further data on the non-substituted fraction values.

4.4 Experiment Test Matrix and Process

4.4.1 Boundary Conditions of Study

Following the convention as presented in the literature review, acceleration effects will be described using the acceleration constant (K), and curvature effects described using (δ/R). Listed below are the target convergence and curvature effects that were studied for this study. As both the acceleration parameter and non-dimensional curvature parameter are functions of the flow, and not the boundary conditions, the values given here are the targets for these values. Actual values for the test runs varied from these somewhat.

Table 4-6: Target Geometric Flow Characteristics

Acceleration Parameter (K)	Non-dimensional Curvature (δ/R)		
	flat	0.015	0.05
None	X	X	X
1.8×10^{-6}	X	X	X
6.4×10^{-6}	X	X	X
2.0×10^{-5}	X	X	X

The specific values of the acceleration parameter chosen to be studied were selected for conditions that could exist in pebble bed cores. They were calculated assuming incompressibility for flow through a two-dimensional convergence created by two neighboring pebbles at velocities and gas properties typical of pebble bed reactors. The cross sectional area of the convergence was calculated assuming the two two-dimensional pebbles are arranged as part of a body-cubic-centered configuration as shown in Figure 4-19. The body centered packing structure was chosen to evaluate the two-dimensional convergence because its packing fraction is similar to that for a randomly packed bed of spheres. Initial velocities going through this two-dimensional

convergence corresponded to the range of superficial velocities for pebble bed reactor designs presented in Table 2-2.

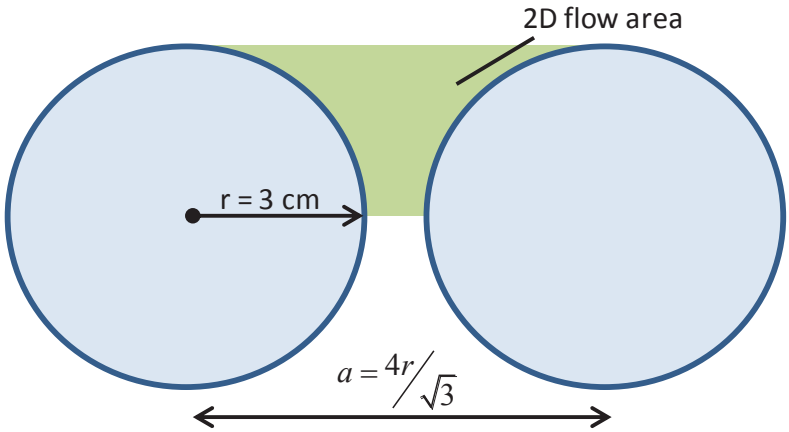

Figure 4-19. Theoretical Pebble Convergence

From this, three acceleration parameters were chosen for the test matrix. The two larger values were chosen as estimates corresponding to normal operation and a low flow situation, such as coastdown or natural circulation through the convergence geometry described above. The third and smallest value (1.8×10^{-6}) was chosen because this is just below what is reported as being necessary to cause laminarization for flat plate geometries. Therefore it was chosen to see its effect when combined with curvature effects.

Two curvature levels were investigated in this study. For both of these δ/R values, the radius of curvature used was 3.0 cm. corresponding to fuel pebbles. The smallest value of the curvature parameter corresponds to the boundary layer thickness using the classical boundary layer thickness [141]:

$$\delta = \frac{D}{2\,\mathrm{Re}_D^{0.5}} \tag{41}$$

The boundary layer thickness for the larger curvature parameter corresponds to a study looking at stagnation point laminar boundary layers for flows in porous media [141]. The envelope of the test matrix was chosen because the values selected will be beneficial to both advance the understanding of laminarization for pebble bed conditions of acceleration and curvature and to general laminarization knowledge for these mechanisms.

The specific settings for the test run included initial velocity, test section geometry configuration and boundary layer trip type and location. The advertised velocity limits of the PIV system is up to 5 m/s. It was desired to have as high an initial velocity as possible to assist in the development of a thick, turbulent boundary layer before application of the laminarizing causing geometric conditions. So the velocity for the different runs was chosen such that the velocity near the outlet was between 4 and 5 m/s. Since the different convergence test runs accelerate the flow at different rates, different initial flowrates were used for the different cases.

The configuration of the test run included both the convergence characteristics, and also the curvature. The required convergence for the different test runs was calculated assuming uniform flow, a linear reduction in the flow area cross section as a function of test section axial length, and considering the velocity limits.

The radius of curvature needed to satisfy the (δ/R) targets for the test runs was calculated following measurements of the initial boundary layer thicknesses for the velocity levels of the specific cases. Initial boundary layer thickness refers to the location at the onset of curvature effects. It was desired that for a specific curvature setting, the four cases of non-converged to highly-converged could be compared. Since the physical configuration of the curvature was kept constant for the curvature setting, it was necessary to ensure that the boundary layer thickness was the same for the four cases. As stated in the Boundary Layer Trip section, the welding rod was used as the boundary layer trip for cases with initial velocity above 2.0 m/s and the sand covered welding rod was used for the lower velocity case. Due to the thickness of the sand covered welding rod, in order to preserve the boundary layer thickness for the different test runs, this boundary layer trip was attached farther downstream closer to the

measurement section. For the higher velocity cases, where the welding rod was used, its location was 28 inches before the measurement section. The sand covered welding rod was located 15 inches before the test section. Table 4-7 lists the specific settings for the different test runs. Measurements were taken and data is presented at 6 axial locations equal spaced every four inches in the measurement section. Results are presented by their tag number (i.e. B2-AP4).

Table 4-7. Test Matrix

Tag # (Case – AP)		Vel (m/s)	Angle of convergence	Radius of Curvature (in)	Qualitative Configuration Description	
Case	Axial Position (AP)				Convergence	Curvature
A1	1 (x = 0 in.)	2.5	None	None	None	Flat
	2 (x = 4 in.)					
	3 (x = 8 in.)					
	4 (x = 12 in.)					
	5 (x = 16 in.)					
	6 (x = 20 in.)					
A2	1	3.3	5.71	None	Low	Flat
	2					
	3					
	4					
	5					
	6					
A3	1	2.5	13	None	Medium	Flat
	2					
	3					
	4					
	5					
	6					
A4	1	1.3	20	None	High	Flat
	2					
	3					
	4					

Tag # (Case – AP)		Vel (m/s)	Angle of convergence	Radius of Curvature (in)	Qualitative Configuration Description	
Case	Axial Position (AP)				Convergence	Curvature
	5					
	6					
B1	1	2.5	None	78.74	None	Low
	2					
	3					
	4					
	5					
	6					
B2	1	3.3	5.71	78.74	Low	Low
	2					
	3					
	4					
	5					
	6					
B3	1	2.5	13	78.74	Medium	Low
	2					
	3					
	4					
	5					
	6					
B4	1	1.3	20	78.74	High	Low
	2					
	3					
	4					
	5					
	6					
C1	1	2.5	None	23.62	None	Moderate
	2					
	3					
	4					
	5					
	6					
C2	1	3.3	5.71	23.62	Low	Moderate
	2					
	3					
	4					
	5					

Tag # (Case – AP)		Vel (m/s)	Angle of convergence	Radius of Curvature (in)	Qualitative Configuration Description	
Case	Axial Position (AP)				Convergence	Curvature
	6					
C3	1	2.5	13	23.62	Medium	Moderate
	2					
	3					
	4					
	5					
	6					
C4	1	1.3	20	23.62	High	Moderate
	2					
	3					
	4					
	5					
	6					

The following figures give the geometric footprint of the test section flow area for the test cases, and the axial measurement positions. The 20 inches corresponding to axial measurement location is measured along the measure wall.

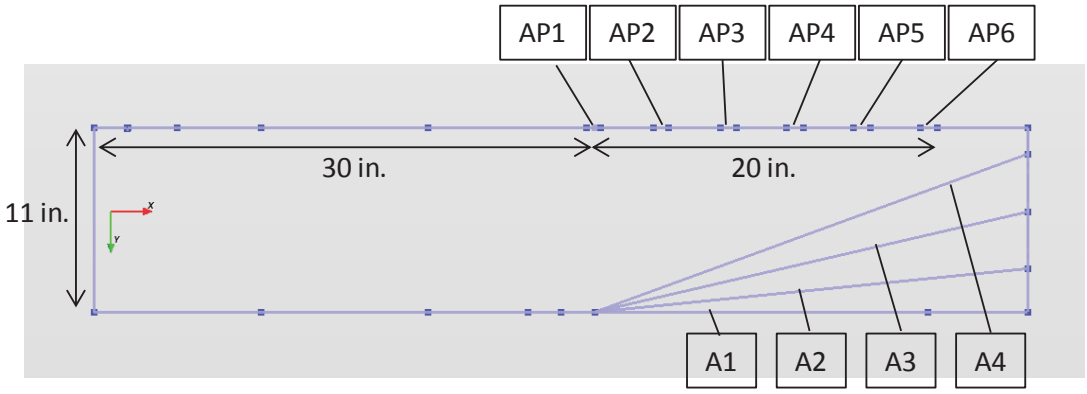

Figure 4-20. Flat Geometry Test Cases

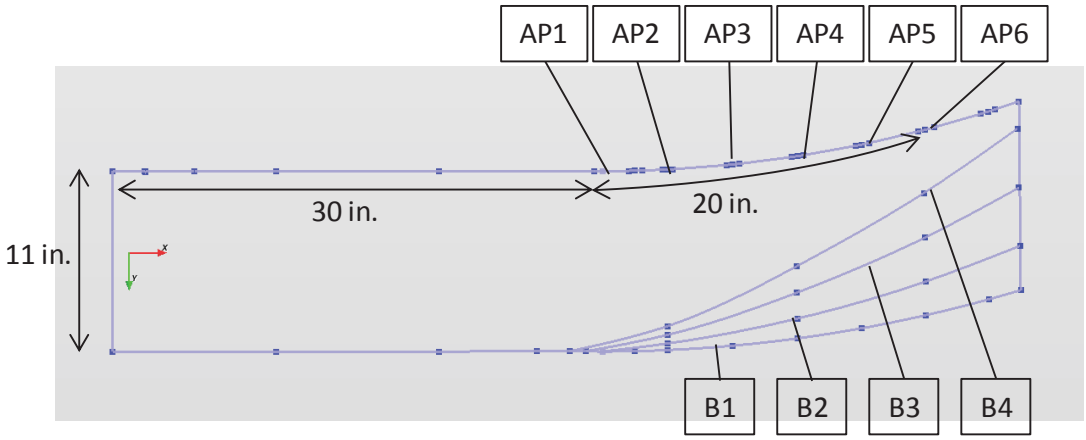

Figure 4-21. Low Curvature Test Cases. 20 inch measurement section corresponds to wall length

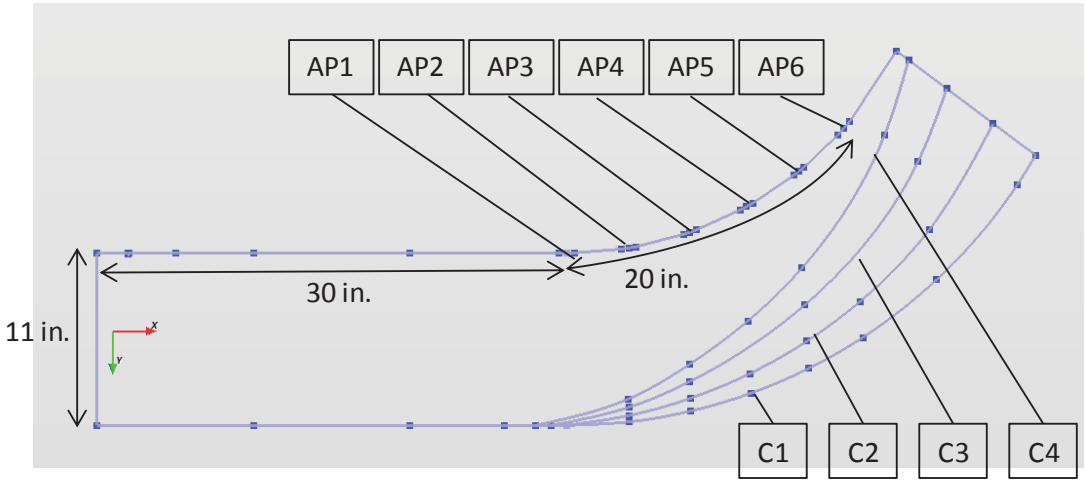

Figure 4-22. Moderate Curvature Test Cases. 20 inch measurement section corresponds to wall length

4.4.2 Test Procedure

For each test case listed in Table 4-7, PIV images were taken next to the measurement wall as identified in the previous images out into the bulk section. This vertical wall was the inner wall for the curved cases, and the wall opposite the convergence. Image datasets were taken at different axial locations along the length of the measurement section, which is immediately after the 30 inches of the entrance section. For integral boundary layer parameters, such as the shape factor, a velocity profile from the wall to the bulk region is required. This distance was larger than the PIV image field of view, so the camera was shifted across the boundary layer in steps, with an image dataset being recorded at each location. In summary, test cases correspond to the geometric conditions of the wind tunnel as a whole, axial position refers to the axial length along the wind tunnel measuring region, and datasets refer to the set of images recorded at one camera location. The camera was stepped across in a direction perpendicular to the wall. This perpendicular direction depended on the curvature configuration of the wind tunnel. While the camera support structure allowed for three dimensions of motion, it did not allow for rotation. So as the camera was stepped across the flow area for the curvature cases, it was shifted both in the X and Y directions of the camera support structure and the resulting boundary layer line in the images cut across the images at an angle. Simple trigonometry was used for accurate position stepping to ensure a boundary layer profile perpendicular to the wall and to identify in the image map the pixels corresponding to this boundary layer line. The lack of rotation of the camera with respect to the normal from the wall also meant that the streamwise velocity component with respect to the wall contained both u and v velocity components in the image coordinate system. Figure 4-23 shows a schematic of measurement datasets for two axial locations of one test run: one for a straight section, and another for a curved section. The number of datasets across the boundary layer is not typical, but is shown to describe the process.

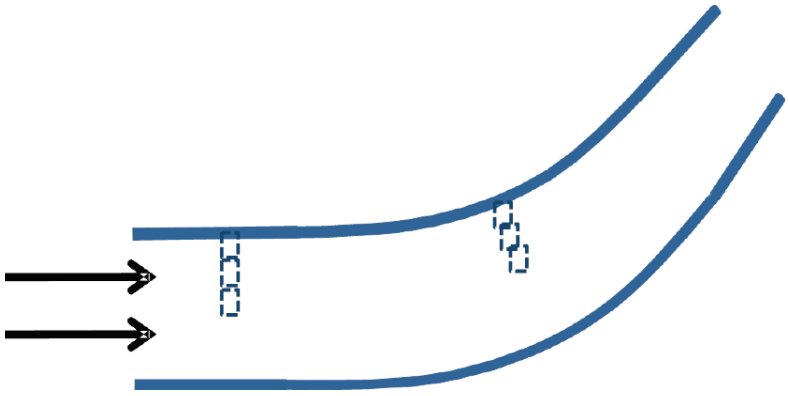

Figure 4-23. Example Image Dataset Position Stepping Across the Flow Area. The number of datasets across the flow is not typical of the test cases.

The vertical height of the test section is 14". Measurements were taken at a horizontal measurement plane 10.5" from the bottom. This height was chosen for two reasons. The first was because of the zoom limitations of the camera. The size of the interrogation areas are representative of the spatial scales that can be captured and analyzed using PIV. Therefore it is necessary to zoom in sufficiently so the interrogation area sizes meet this requirement. Vertically lower measurement planes could not be imaged at this zoom resolution because the top acrylic wall inhibited the camera lens from increasing the zoom. The second reason for the height of the horizontal plane was to reduce the amount of fog between the horizontal light sheet and the camera lens because these ambient, non-illuminated fog particles attenuate the light reflected from the tracer particles.

It is important that the measurements at the horizontal plane of interest represent two-dimensional flow. Both for quantification of the phenomena, and also to avoid out of plane flow from the horizontal light sheet. The height of the test section was designed so that for the entire length of the test section, the maximum spatial contribution of the boundary layers on the upper and lower walls was less than 13% of the test section height. The measurement plane was well inside this region. As described in the screen characterization section, pitot tube measurements were taken

across the height of the test section and the measured time averaged velocity varied by less than 5 %.

As stated above, each test run in Table 4-7 consisted of 6 axial locations. Each axial location consisted of 3-10 datasets taken from the wall to the middle of the flow. This number depended on the amount of convergence of the test run at that specific axial location though for most axial locations, 5 datasets across the boundary layer were taken. Each dataset consists of 2308 image pairs taken at a frequency of 100 hz. This number of images was the maximum available onboard camera memory. Justification for this time scale was presented above in the PIV section.

Before measurements at each axial location wind tunnel flowrate verification and camera positioning was performed. Point velocity measurements were taken with the pitot tube at the beginning of the entrance region and time averaged over 2 minutes. This step was to ensure that the time averaged inlet velocity was constant during the duration of each test run. The largest variation for the time averaged point velocity measurement between the test run average and any given axial location was less than 2%, though most runs had variation less than 0.5%. Occasionally the blower motor setting had to be adjusted to bring it into this range, though most test runs stayed in this steady range without adjustment. Appendix C presents these time averaged velocity measurements for the different test runs. Camera positioning for the dataset next to the wall was performed by taking an image that showed the wall position from illumination. For the matrix testing datasets, the laser pulse width is so short that little reflection occurs from the acrylic side wall. But when the laser is run continuously, reflection from the sidewall occurs. An image of this was recorded for use in analysis of where the acrylic wall is in the PIV images. For each dataset recorded, the lights in the room were turned off to eliminate ambient light that reduces the contrast between illuminated particles and the image background. In addition, before each test case the axial fan motor was run for approximately 10 minutes to ensure steady state.

4.5 Data Analysis Procedure

The data analysis procedure was performed for all matrix testing. Figure 4-24 shows a flowchart of this. Flowchart boxes shaded in blue were performed in the DantecDynamics software, peach colored shaded boxes were performed in MatLab, and green shaded box represents the process being performed in Excel.

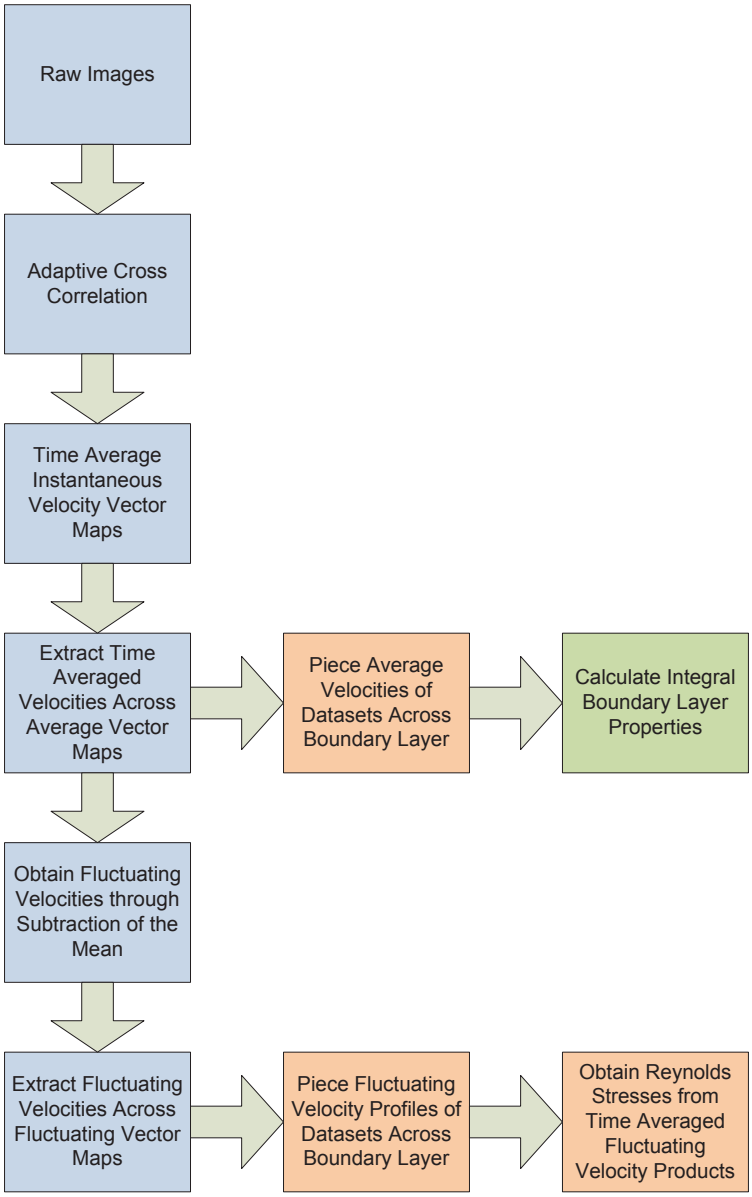

Figure 4-24. Data Analysis Procedure. Color coordinating corresponds to software used for method.

Even though the camera has a full resolution of 1632 x 1200 pixels, for the test matrix datasets, a smaller pixel region was used. There were two reasons for this. The first is because the limit of the camera on board memory. The second is because even though a full image area dataset provides substantial quantitative information of the

flow field, ultimately the quantification of the laminarization phenomenon uses data at specific axial locations. Therefore, by using a smaller pixel area region for image capture, more individual realizations can be acquired in a given dataset as limited by the onboard memory. Three pixel areas were used for the raw images: 1632 x 400, 544 x 1200, and 544 x 600. These pixel areas correspond to the following dimensions in the light sheet plane: 43mm x 10.7mm, 14.3mm x 32mm, and 14.3mm x 16mm respectively. The choice depended on the axial location of the dataset; whether it was along a flat region, or a curved section. As stated above, the linear motion of the camera positioning system did not follow the curve of the test section, so the normal from the acrylic side wall, as seen in the image field cut across the image at an angle. This angle determined the interrogation areas used for the datasets for that specific axial location. 2308 image pairs were taken for each dataset.

The raw images were analyzed with DantecDynamics' adaptive cross correlation method. 64 x 64 pixel interrogation areas were used with 75% overlap, with a starting interrogation area size of 256 x 256 in the initial step of the adaptive process. Initially it was desired to use interrogation areas of 32 x 32, but the capability of time between laser pulses, and corresponding Δx of particles between image frames did not justify this. A Gaussian window was used with a k value of 1.2. This corresponds to a weighting function that reduces the non-weighted window length to 85% of the interrogation area side length. Local validation was used with a 3 x 3 local validation neighborhood where deviations larger than 15% resulted in an interpolated substituted vector being used.

The Dantec software was used to time average the instantaneous vector plot realizations and subtract the mean from the instantaneous plots. For the time averaging steps, only non-substituted vectors were used. The time averaged and fluctuating velocities where exported into Matlab along the boundary layer line perpendicular from the wall out into the bulk. This line was pieced together in Matlab from the different datasets for the specific axial location of the test run. During the acquisition of images, this line in pixel coordinates in the image plane was recorded for each dataset. Rotation of coordinate system for the curved wall cases, and calculation of and time averaging of

the turbulent intensities and Reynolds stresses was also done in Matlab. Final time averaged boundary layer data was then exported into a formatted Excel worksheet where the integral boundary layer parameters were calculated.

Most of the calculations for the boundary layer mean flow parameters are straight forward. These include boundary layer, displacement and momentum thicknesses, shape factor, and R_θ. The final mean-flow parameter is the skin friction coefficient, which necessitates knowing the shear stress at the wall. Many different methods have been used by other researchers studying the flow over a flat plate. These have included methods as distinct as the Clauser plot method to very accurate hot film gauges. The risk of the Clauser plot method when studying laminarization is that a logarithmic profile is assumed, even though this is known to be affected or in transition due to the laminarization effects. Though some researchers have argued that as long as the logarithmic region is present, even if it has diminished in size, this method will work.

In the present study, the mean wall gradient method was used [142]. The resulting output from the PIV system was a well resolved profile near the wall. Typically, the test cases had two dependent data points under y+ = 5.0, and usually another under 7.0. Linear interpolation was used between the first two data points to obtain the velocity gradient. For AP1, where a fully developed turbulent layer is expected, linear interpolation of the first two data points typically resulted in the logarithmic region lying on the expected family of logarithmic curves [124]. Due to the step change in physical space of the PIV interrogation areas coupled with inconsistencies of camera location with respect to the wall, additional interpolation between the first and third, and second and third data points was calculated. If any of these data points was greater than y+ = 7.0, they were not used. The range of the resulting skin friction coefficients calculated from these varied by as much as 30%.

The vector components of the fluctuating velocities were exported to Matlab to be time averaged for calculation of turbulent intensities and Reynolds Stresses. As mentioned above, when calculating time averaged vector plots in the PIV software, the option to only use non-substituted vectors was available. In calculation of fluctuating velocity fields, the software did not provide the option to not use the substituted vectors.

This resulted in some very large spurious vectors. The time series of fluctuating velocities for each location on the boundary layer profile line were run through a filter and the outliers were removed following Chauvenet's [143] criterion for outliers.

5 RESULTS

5.1 Flow Boundary Conditions

The operational envelope presented in the test matrix of Table 4-6 was chosen to study the boundary layer response when subject to different levels of acceleration and convex curvature effects. The values of these non-dimensional parameters that quantify the acceleration and curvature were chosen because previous studies have shown different flow response when subject to different levels of just one of these laminarizing mechanisms. Because these non-dimensional values depend on flow characteristics that are difficult to perfectly meet during the design phase of the experiment, these values are target values. The following table presents the actual experimental values of the acceleration parameter and the curvature parameter for the specific test cases.

Table 5-1. Experiment Boundary Conditions

Test Case	K_{max} x 10^6	δ/R
A1	N/A	N/A
A2	1.85	N/A
A3	6.12	N/A
A4	18.20	N/A
B1	N/A	0.0145
B2	1.77	0.0150
B3	6.92	0.0147
B4	18.40	0.0143
C1	N/A	0.0483
C2	1.93	0.0478
C3	5.58	0.0475
C4	21.30	0.0483

5.2 Full Field Results

Presented below is an example of an image acquired with the PIV system color inverted. As stated in the description of the test procedure analysis, a smaller image area was used for data collection to increase the number of images to be stored in the on

board memory of the camera, while imaging a slice across the boundary layer to minimize datasets required for collection out to the bulk region.

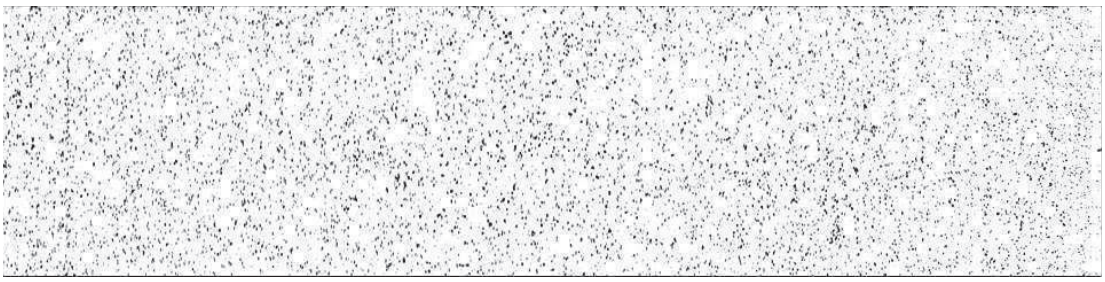

Figure 5-1. Instantaneous PIV Image

The raw images were analyzed to give instantaneous vector maps. An example is shown in Figure 5-2. The flow structure does not show very much uniqueness because the streamwise mean velocity is much greater than local flow detail. The wall is positioned at the right side of the image, and therefore the gradient of vectors moving right to left represents an increase in velocity. The mean was subtracted from the instantaneous vector maps to give fluctuating velocity maps. Figure 5-3 gives an example of this. Panning through the time sequence of fluctuating velocity maps reveals coherent structures throughout time.

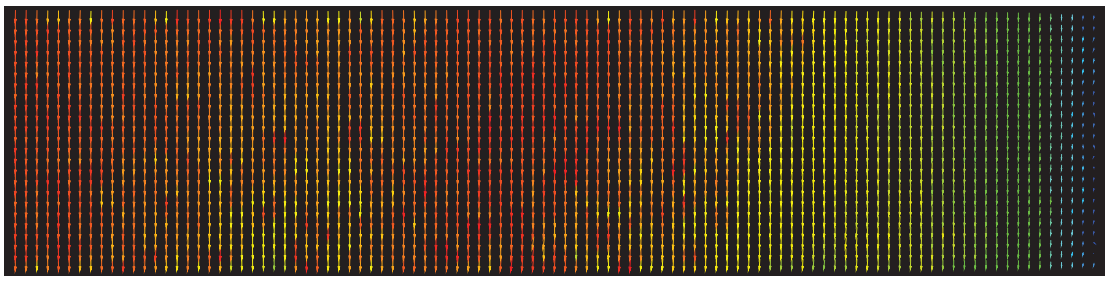

Figure 5-2. Example Instantaneous Vector Map

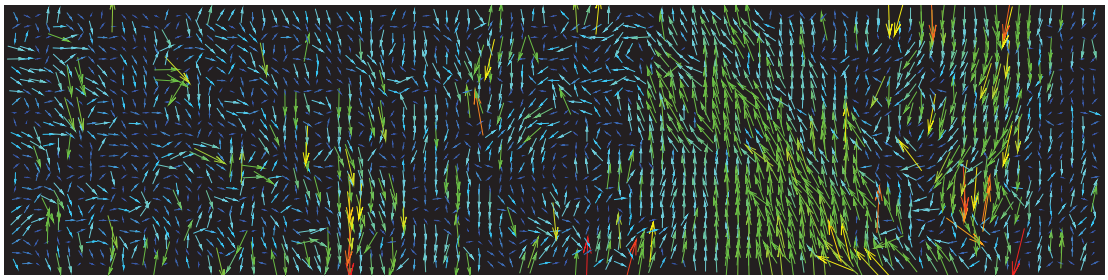

Figure 5-3. Fluctuating Velocity Map

5.3 Mean Velocity Profiles

The mean streamwise boundary layer velocity profiles were normalized by outer and inner variables. As stated in the literature review, flow response to an acceleration typically occurs first at the wall, and then gradually grows outward into the flow. Therefore it is beneficial to examine the flow profiles in both outer and inner variables. Measurements were taken for the twelve test cases at the six axial positions. While some of the flow profiles for the test cases are very similar and therefore could be grouped together, since each test case is subject to a different level of acceleration, curvature, or both, it is beneficial to investigate the change in flow profile for each test case. Profiles at locations AP1, AP3 and AP6 are plotted to show the basic evolution of the flow profile. Half data point sets from the PIV output plot resolution is used to make viewing the trends easier. Comprehensive velocity profiles are contained in Appendix G.

Figure 5-4 shows the boundary layer at AP1 for the reference base configuration of flat wall, non-convergence. The shape is characteristic of a lower Reynolds number turbulent boundary layer flow.

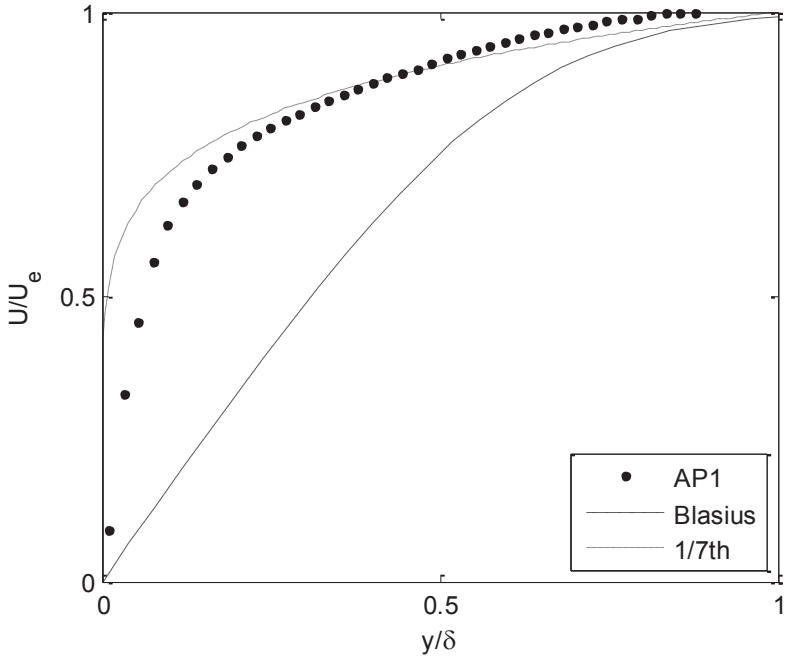

Figure 5-4. A1-AP1 Mean Velocity Profile in Outer Variables

Test case A2, which from recommended laminarization parameter values does not have sufficient acceleration to cause laminarization, is shown in Figure 5-5. The slight change in resulting boundary layer profile is as expected. Due to the imposed pressure gradient, there is a slight decrease in the velocity defect near the shoulder.

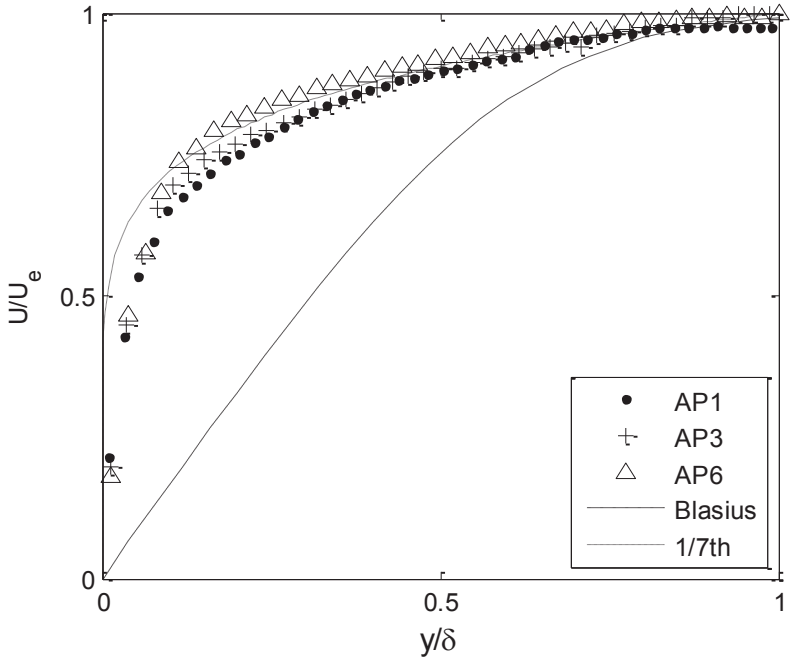

Figure 5-5. Test Case A2 Mean Velocity Profiles in Outer Variables

Laminarization was expected for cases A3 and A4. Similar to A2, a decrease in the velocity defect near the center of the flow is seen at AP3 for both cases (Figure 5-6 and Figure 5-7). In fact, this velocity defect is seen immediately at AP3 for all acceleration test cases. At first glance, this decrease in velocity defect appears as a more full profile, like a higher Reynolds number flow, though it is characteristic of laminarization studies and corresponds well to the results of Launder [34], Narasimha [7], Mukund [92] and other. With sufficient fidelity and resolution of the measurement in the near wall region, it can be seen that this change in profile is not more full like a higher Reynolds number flow, but instead has adjusted to become less steep in velocity gradient near the wall. The inset of Figure 5-6 shows this deviation from the steep velocity gradient at the wall characteristic of turbulent flows. While this phenomenon is difficult to capture because of its proximity to the wall (typically less than 3 PIV data points), most of the results from this study do show this behavior as the flow is transitioning. In agreement with the findings of Badri Narayanan, Patel, and others, the near wall region adjusts

first towards laminar behavior before the rest of the boundary layer does. In the following figures, it is interesting that even for the high acceleration case (A4) the flow profile in outer variables is not represented by the Blasius solution, especially in the outer portions of the boundary layer, partly because before it has adjusted to laminar profile, the decrease in velocity defects takes it away from a Blasius profile. For cases A3 and A4, there is some evidence of transition towards the Blasius profile in the near wall region.

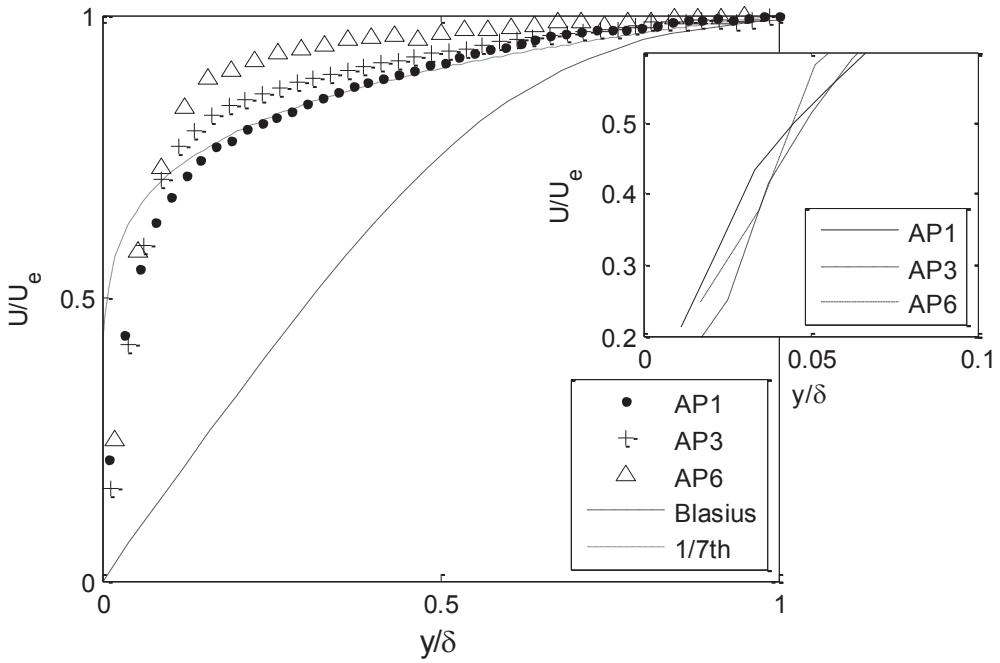

Figure 5-6. Test Case A3 Mean Velocity Profile in Outer Variables

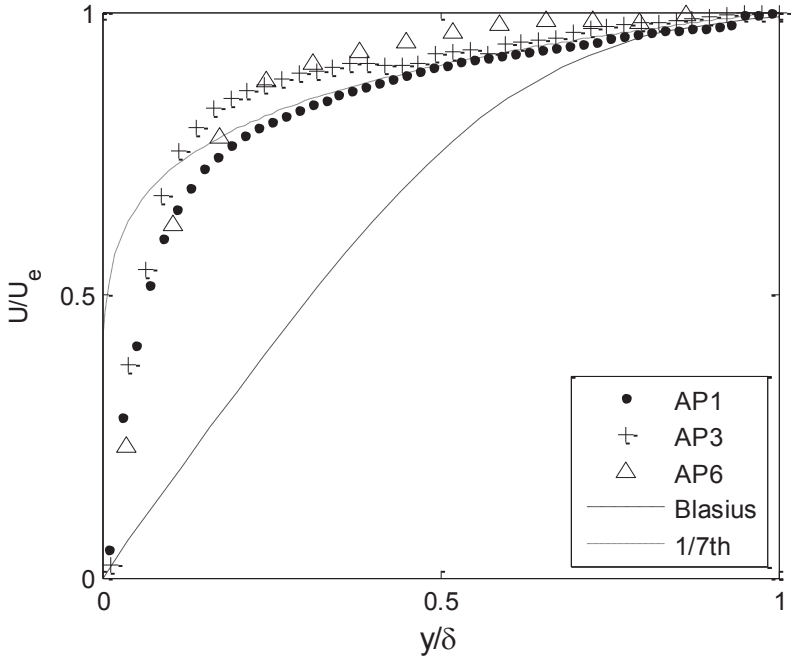

Figure 5-7. Test Case A4 Mean Velocity Profile in Outer Variables

Figure 5-8 shows the first case of low curvature. It shows a gentle lowering of the boundary layer profile for the low curve, non-converged case, similar to that seen by Muck et al [85] and So and Mellor [78]. The inner plots provide more insight.

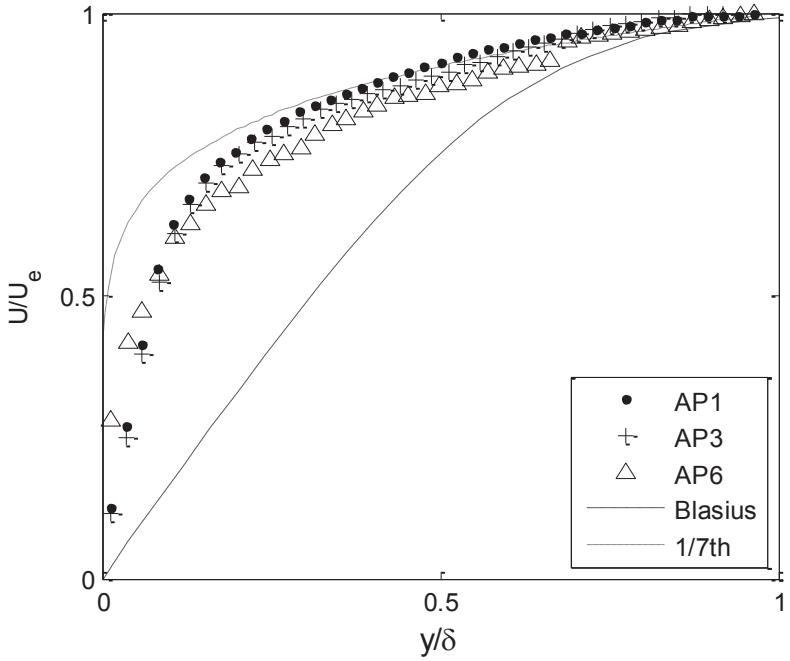

Figure 5-8. Test Case B1 Mean Velocity Profile in Outer Variables

Beginning with test case B2, all other configurations contain both acceleration and curvature effects (except C1). In comparison between the flat walled cases, and B1, both effects can be seen; an initial velocity defect due to the imposed pressure gradient, followed by a transition of the profile towards the laminar solution. Figure 5-9 illustrates this well, with pressure forces visible at AP3, and transition towards the Blasius profile at AP6. It should be noted also, that flow subject to either the low convergence (A2) or low curvature (B1) did not show any visible transitioning towards laminar with respect to the outer wall variable plot, but with both forces acting simultaneously, this transition is visible.

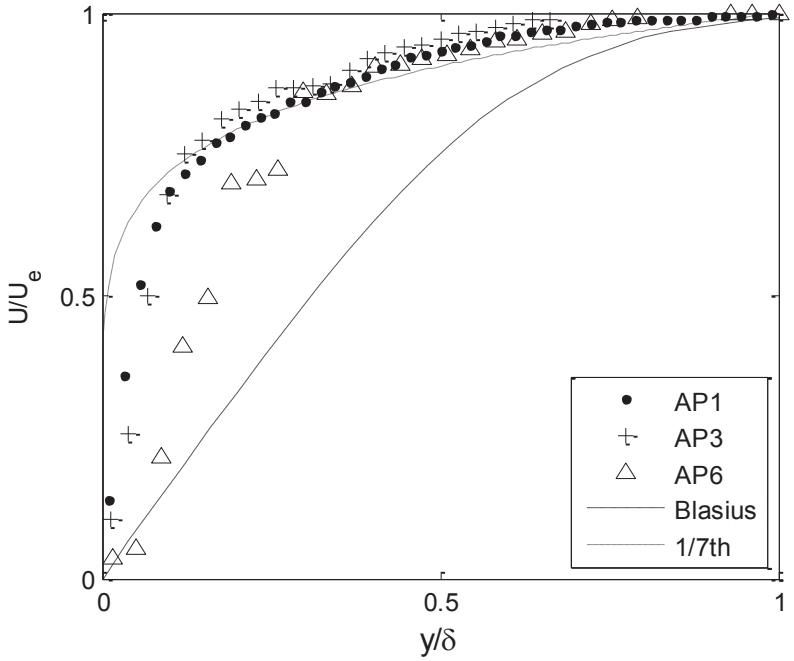

Figure 5-9. Test Case B2 Mean Velocity Profile in Outer Variables

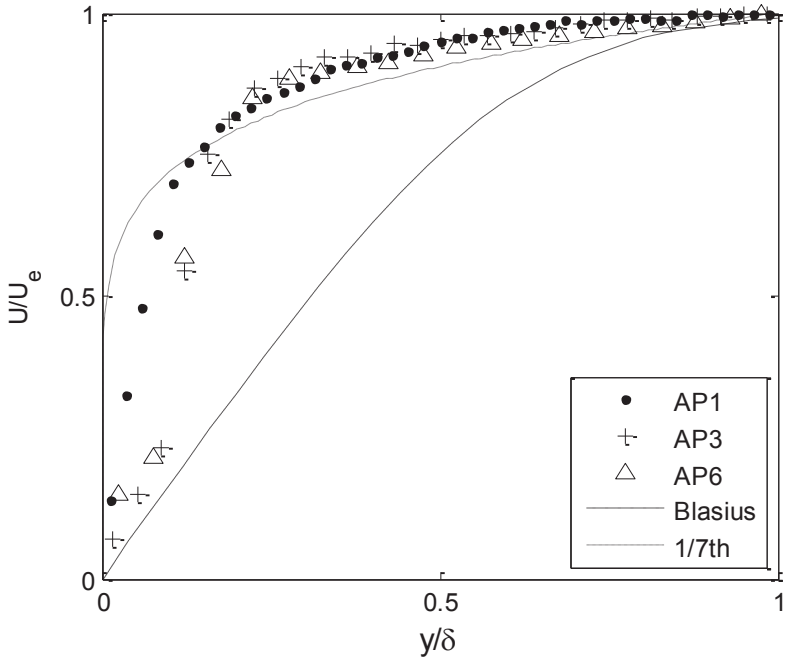

Figure 5-10. Test Case B3 Mean Velocity Profile in Outer Variables

Test cases B4 (Figure 5-11) and C- (Figure 5-12 to Figure 5-15) show significant transition towards the laminar boundary layer profile. This is in agreement with the low Reynolds number acceleration flow of Badri Narayanan [29]. The inset in Figure 5-13 shows the gradual change towards laminar for AP4 - AP6. For ease of visibility, lines are used in this figure.

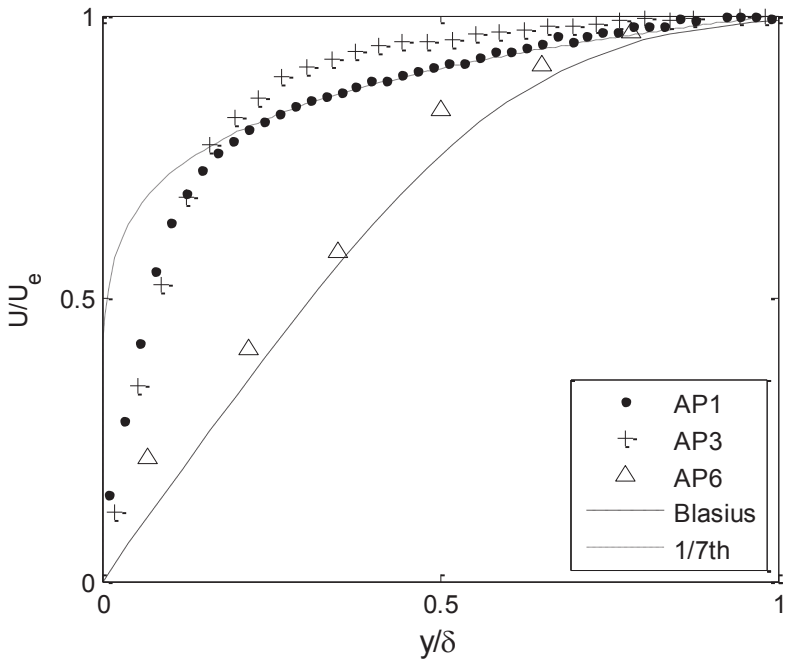

Figure 5-11. Test Case B4 Mean Velocity Profile in Outer Variables

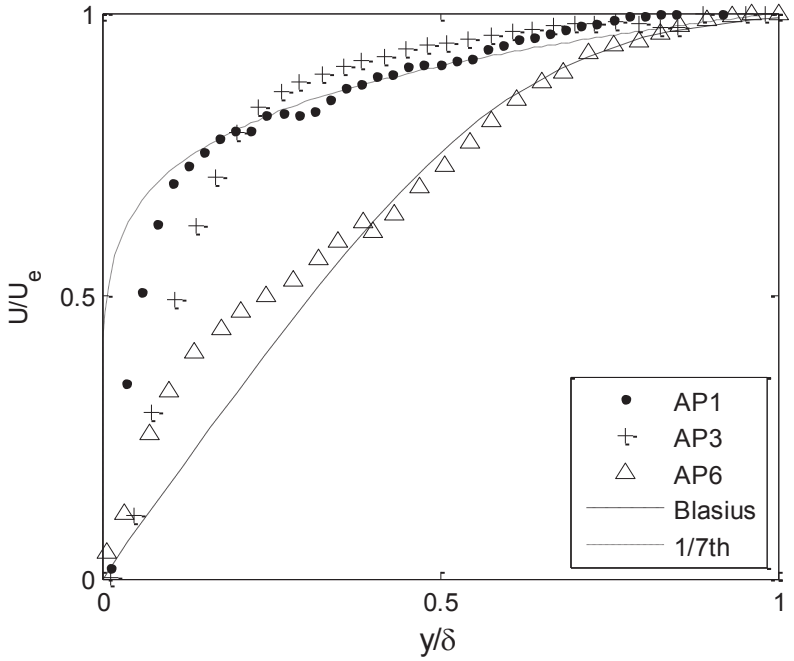

Figure 5-12. Test Case C1 Mean Velocity Profile in Outer Variables

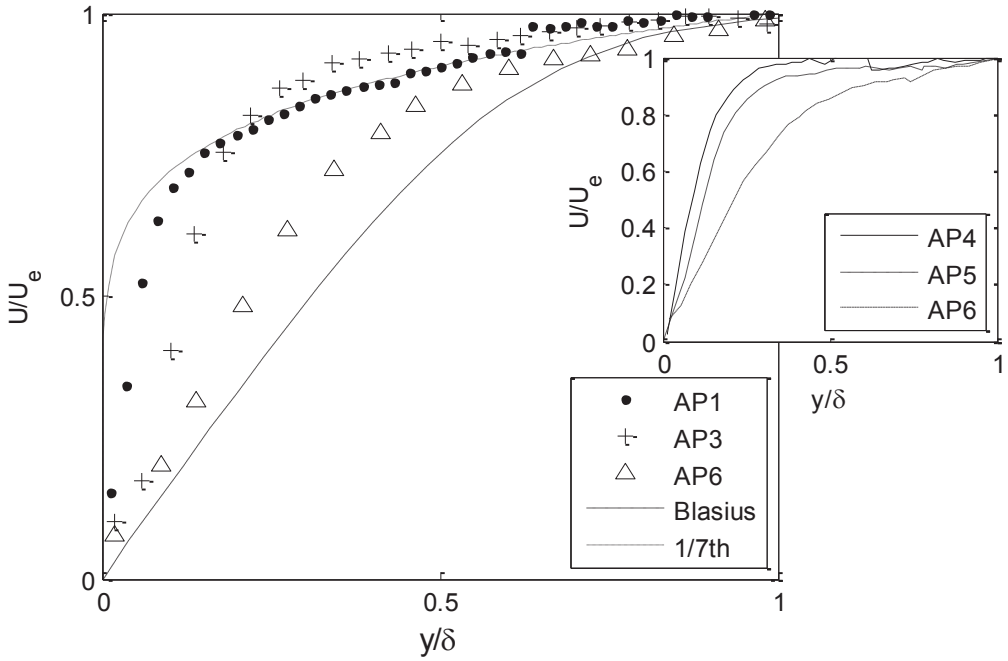

Figure 5-13. Test Case C2 Mean Velocity Profiles in Outer Variables

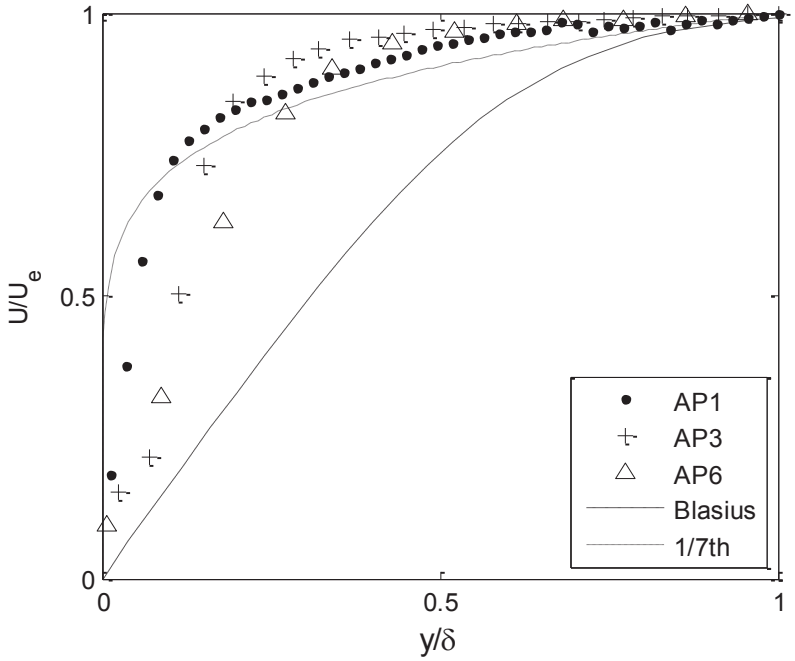

Figure 5-14. Test Case C3 Mean Velocity Profiles in Outer Variables

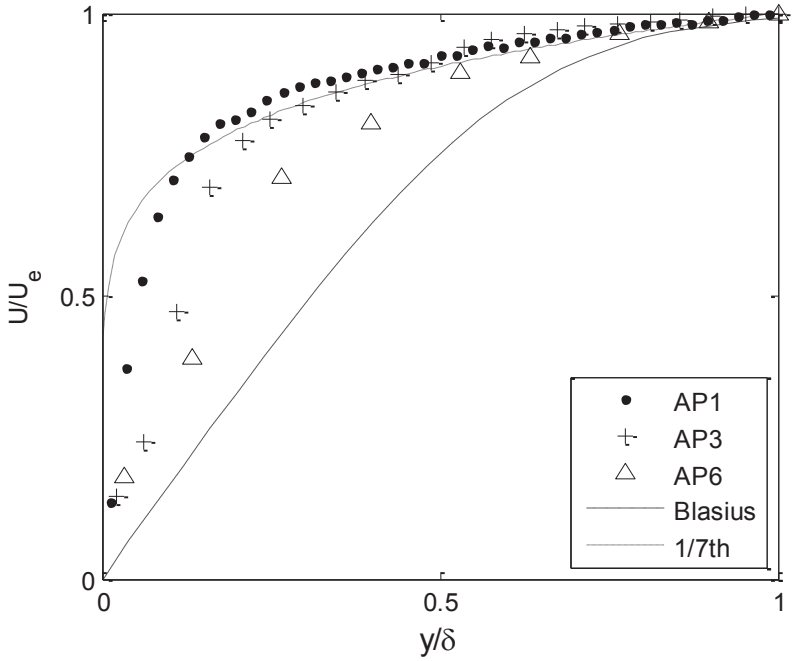

Figure 5-15. Test Case C4 Mean Velocity Profiles in Outer Variables

As described in the literature, the laminarization process affects the near wall region first, and then the outer flow adjusts. Therefore, it can be expected that changes in the flow profile will be apparent in plots normalized by near wall variables even when no gross changes are visible when plotted by outer variables. AP1 measurements for all runs show an extended logarithmic region confirming initial conditions of turbulent flow. Plotted with the experimental data is the linear profile characteristic of the viscous sublayer, and the logarithmic curve ($\kappa = 0.41$; B=5.1) [123].

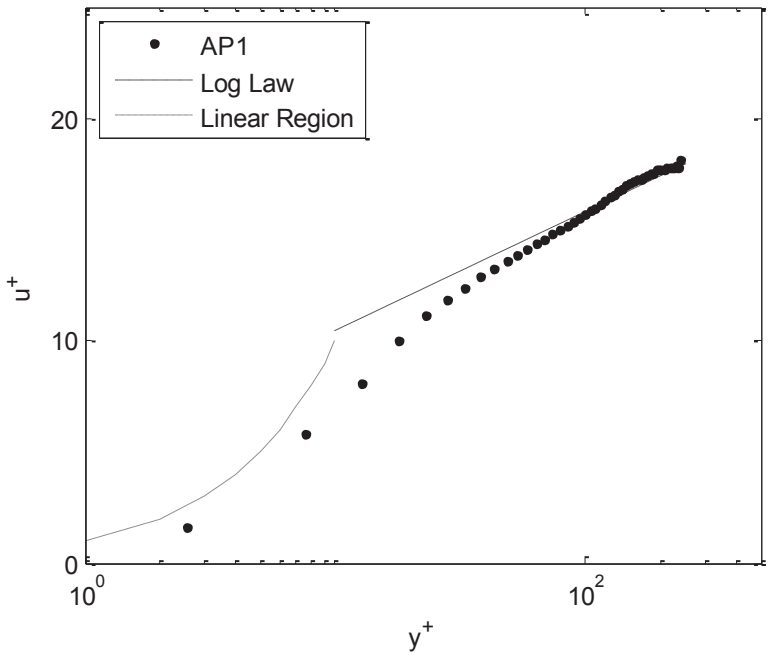

Figure 5-16. A1-AP1 Mean Velocity Profile in Inner Variables.

One characteristic of laminarization is a deviation from the law of the wall profile. In fact, researchers Okomoto [145], Launder [35], and Patel and Head [40] have used a departure from the log law as the criterion for laminarization. All test cases aside from A1 show some flow response to the acceleration or curvature. Figure 5-17 through Figure 5-19 show flow response typical of accelerated boundary layers. For these

flows, the first effect is a thickening of the linear region near the wall. This occurs, even while the logarithmic layer remains relatively unaffected. This is visible even in case A2 when comparing profiles at AP1 and AP6, though the data does still follow the logarithmic profile relatively well. This thickening of the viscous sublayer, and its resulting flow profile in this region varies from a departure of the profile in this region from a logarithmic curve, all the way to following a linear profile as the viscous sublayer gets thicker. One of the reasons that most researchers have focused on identifying the onset of laminarization is because this thickening of the sublayer is one of the first flow responses to an acceleration or curvature. And this thickening of the viscous sublayer has the effect of changing the surface phenomena of the flow, in particular the skin friction and the heat transfer capabilities. So it is of focus, because even though the rest of the boundary layer may not appear to be very laminarized, the near wall behavior precludes the use of turbulent correlations when considering the flow.

In Figure 5-18 it can be seen that the viscous sublayer has increased in thickness and the offset of the velocity curve with the logarithmic curve indicates the onset of laminarization as the skin friction coefficient drops quicker than the velocity profile can adjust to the new conditions. This shift of the profile, even though the profile does follow a generic logarithmic curve outside the linear region, is used to identify the flow as transitional by Patel and Head [40]. In Figure 5-19, the flow essentially only has a linear region out to the bulk flow indicating laminarization. This is to be expected since the imposed acceleration was greater than 1.0×10^5, much greater than that predicted to be needed for laminarization.

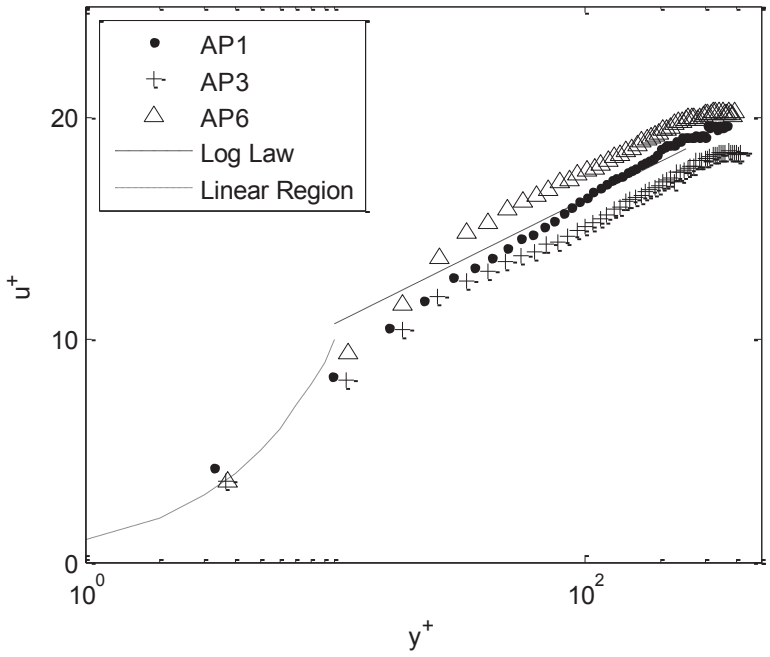

Figure 5-17. Test Case A2 Mean Velocity Profiles in Inner Variables

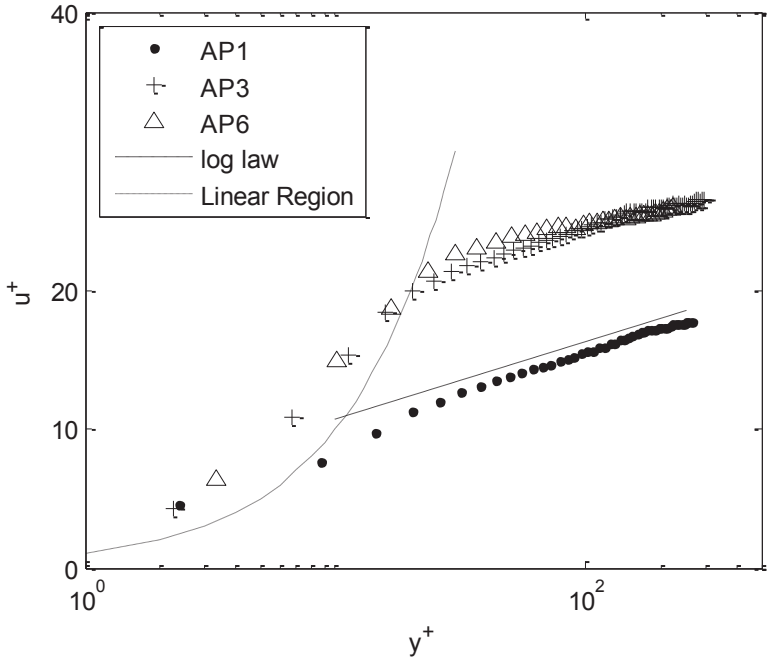

Figure 5-18. Test Case A3 Mean Velocity Profiles in Inner Variables

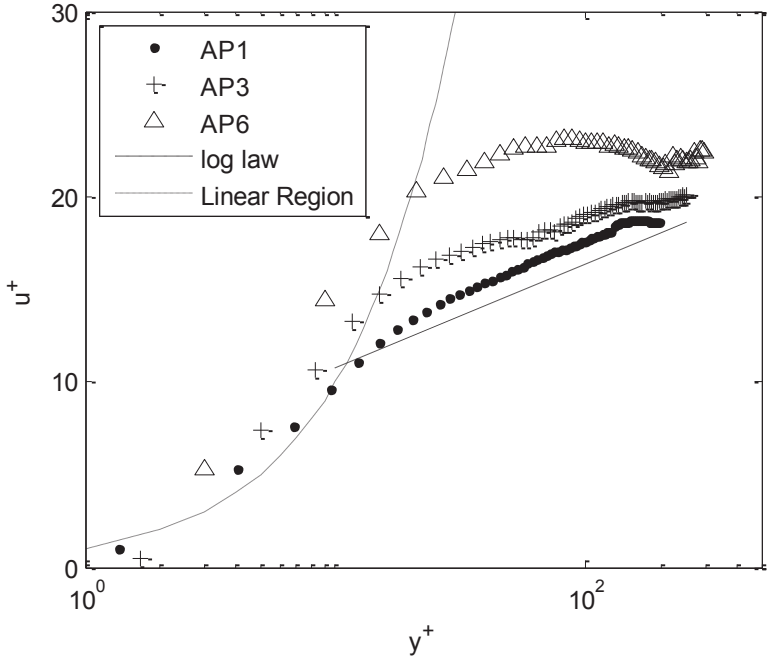

Figure 5-19. Test Case A4 Mean Velocity Profiles in Inner Variables

Test case B1 in Figure 5-20 shows flow response typical of small curvature effects and is similar to that found by Muck [85], Patel [40] and Gillis [84]. Similar to Muck, as the flow continues along the curvature, the deviation from the logarithmic region increases. Jumping ahead to Figure 5-24, the moderate curvature, non-converged case, is beneficial for comparison with the present profile plot. It can be seen that not only does the deviation from law of the wall increase along the axial direction for a specific flow, but it increases when subject to the greater curvature. That trend is in contrast to findings of Gillis, but in agreement with the results of So and Mellor [78]. While the resulting profile at AP6 does not completely follow the 1:1 linear curve, it does have a general linear profile out to y+ ≈ 100, indicating a large deviation from turbulent flow.

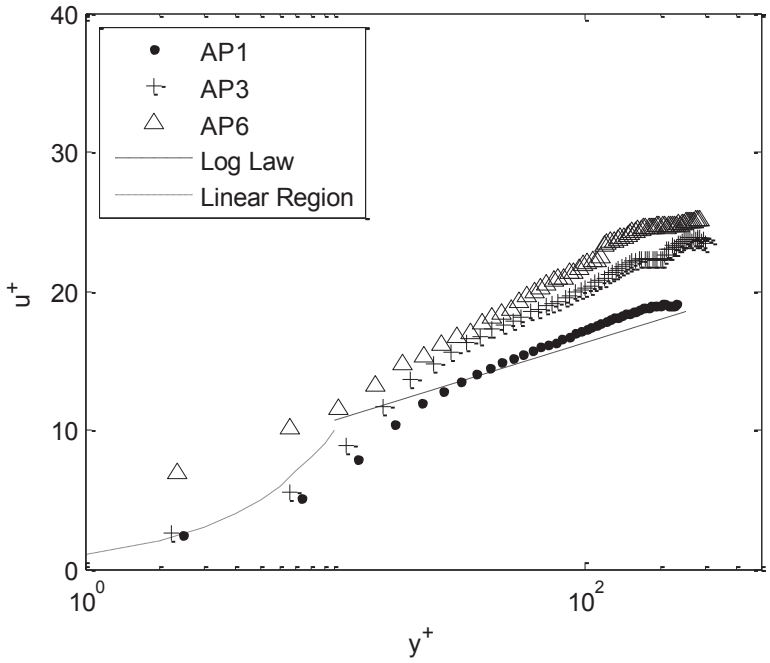

Figure 5-20. Test Case B1 Mean Velocity Profiles in Inner Variables

Corresponding to the observations from the outer profile plots, cases B2-B4 show a thickening of the linear viscous sublayer and a reverting flow. Case B3 shows a very

small logarithmic curve, albeit not characteristic of the typical constant values associated with the law of the wall, and then in B4, the profile is linear in wall variables out to the bulk flow, indicating a full reversion to laminar.

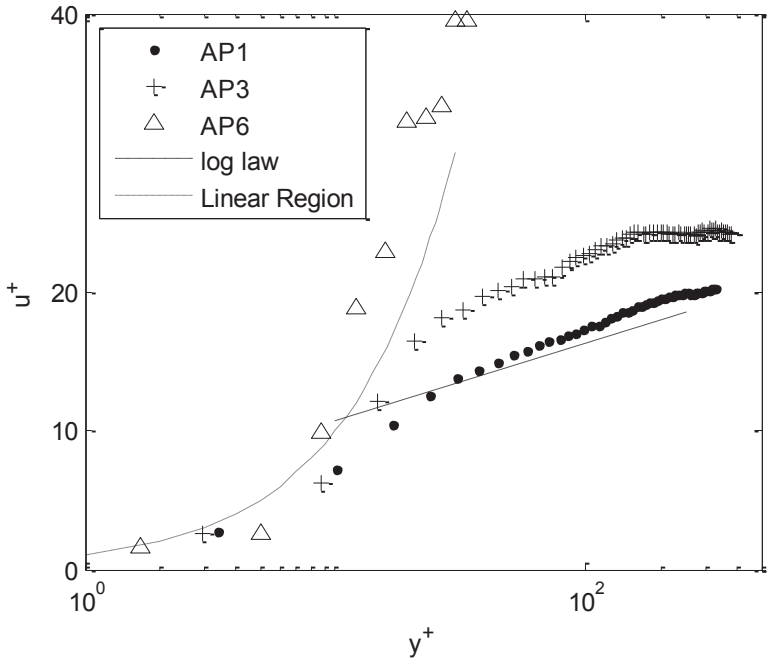

Figure 5-21. Test Case B2 Mean Velocity Profiles in Inner Variables

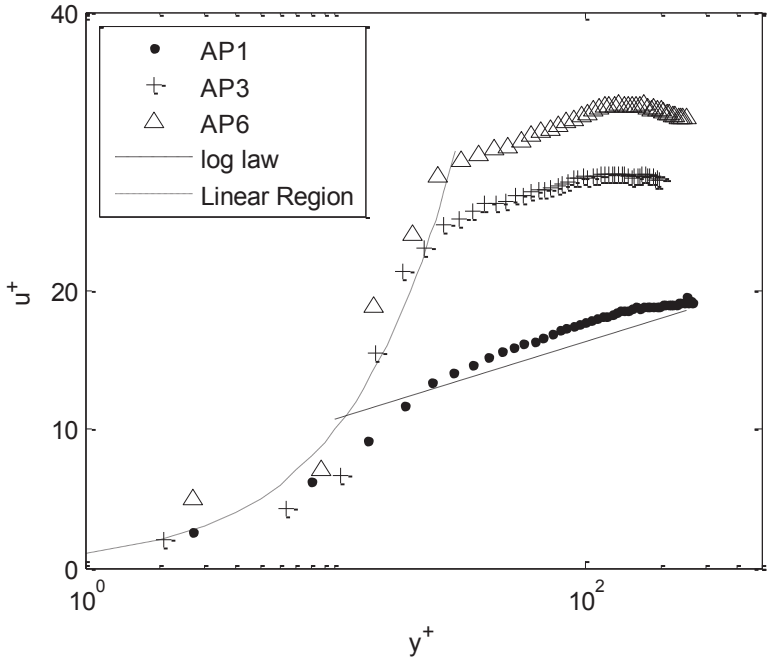

Figure 5-22. Test Case B3 Mean Velocity Profiles in Inner Variables

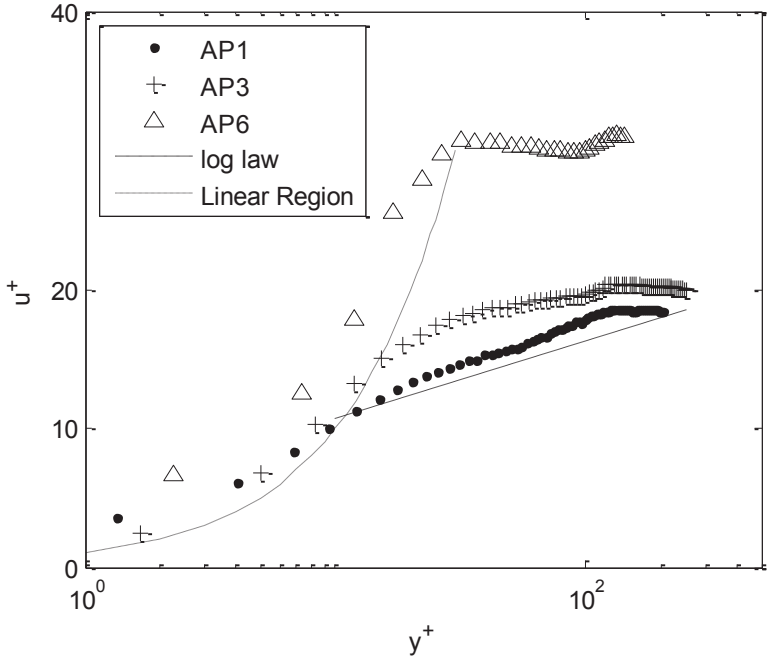

Figure 5-23. Test Case B4 Mean Velocity Profiles in Inner Variables

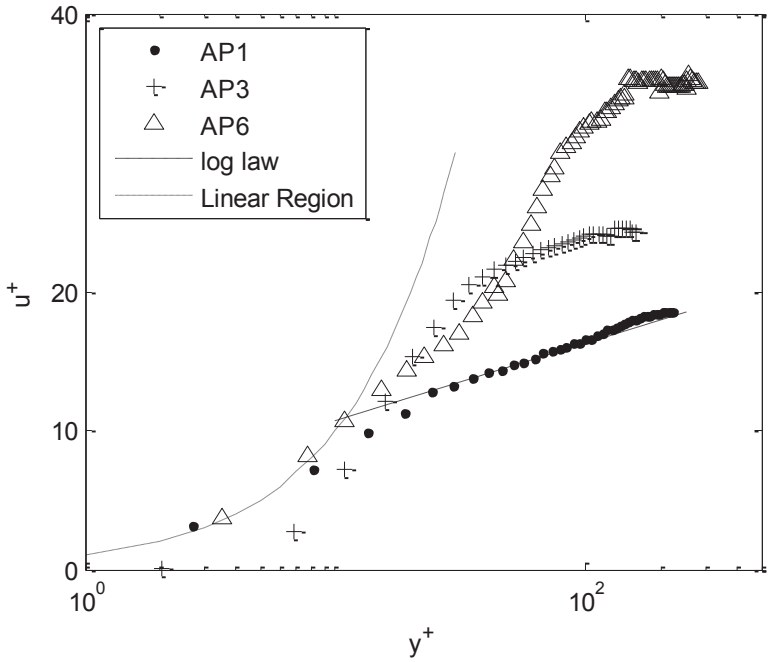

Figure 5-24. Test Case C1 Mean Velocity Profiles in Inner Variables

Given the deviations from the law of the wall for the convergence cases of small curvature, the profiles for the moderate curvature cases are as expected. In Figure 5-27, the profile at AP3 lies with that at AP6, indicating that the changes in flow profile have occurred previous to AP6.

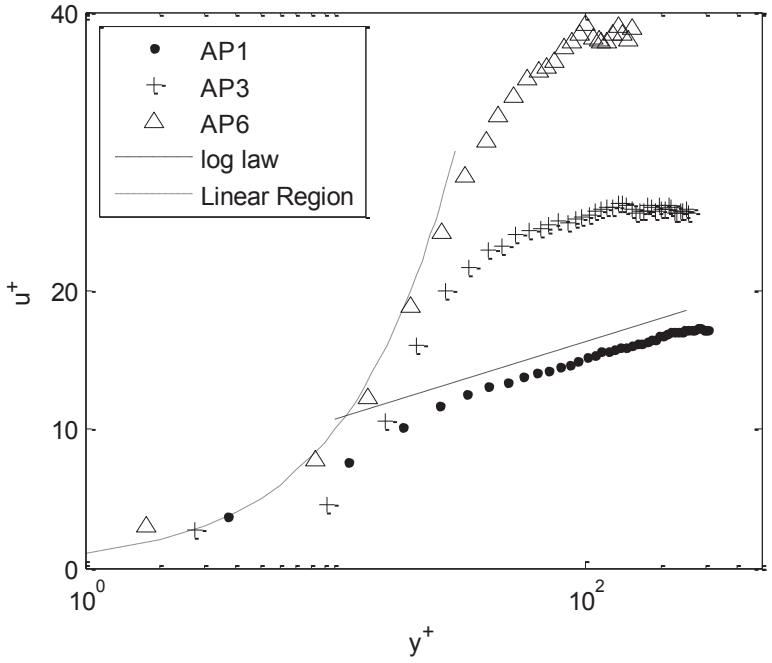

Figure 5-25. Test Case C2 Mean Velocity Profiles in Inner Variables

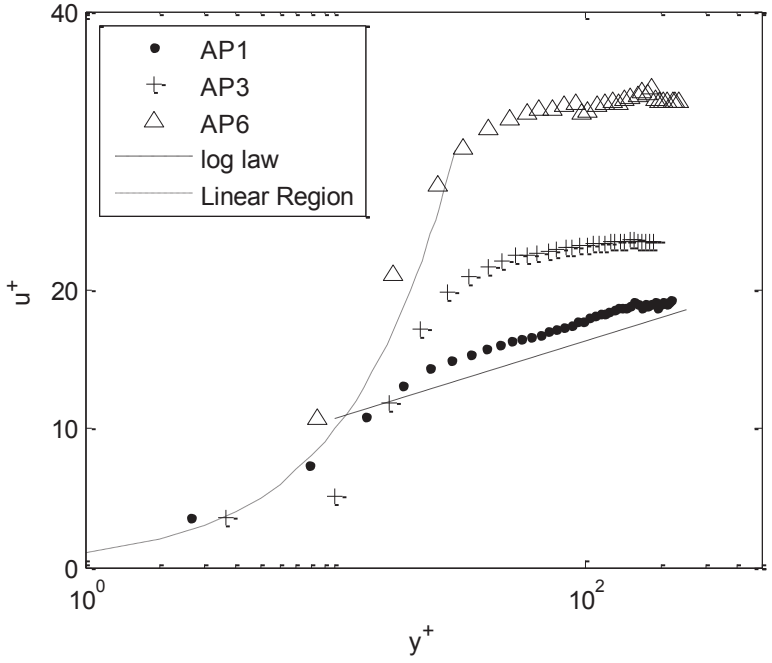

Figure 5-26. Test Case C3 Mean Velocity Profiles in Inner Variables

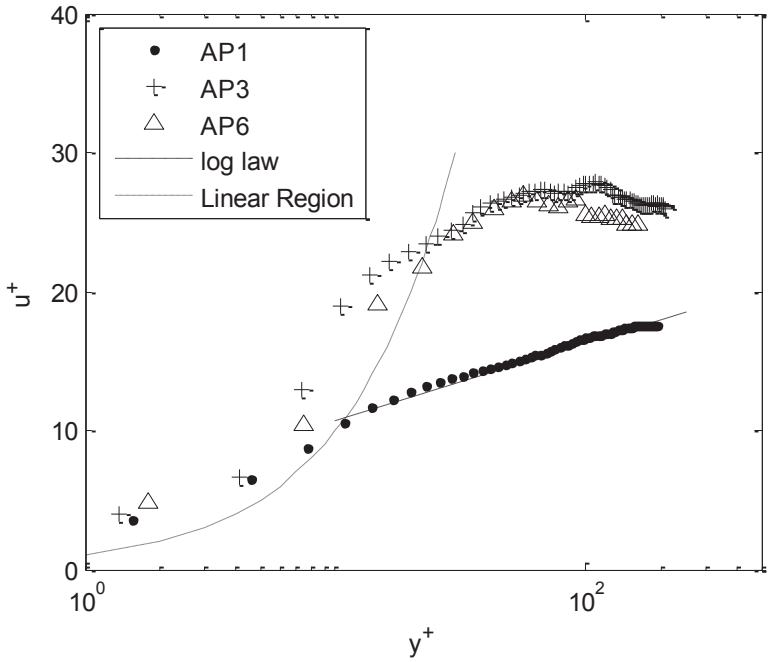

Figure 5-27. Test Case C4 Mean Velocity Profiles in Inner Variables

5.4 Mean Flow parameters

The axial variation of δ, H, c_f, and Re_θ were measured for all test cases and all axial positions. The purpose of this section is to show the influence of the acceleration and curvature on the boundary layer response and how the extent of this response is dictated by the respective levels of acceleration or curvature. Therefore all mean flow parameters are not presented here, but only those that emphasize similarities and differences due to the geometry mechanisms. All raw mean flow parameters and some relative parameter changes for all axial positions and test cases are contained in Appendix H.

Figure 5-28 shows boundary layer thickness change with respect to initial boundary layer thickness for the specific test case as a function of axial position grouped together

by curvature. For all test cases, the initial thickness of the boundary layer at AP1 ranged from 28.5 mm to 32.5 mm.

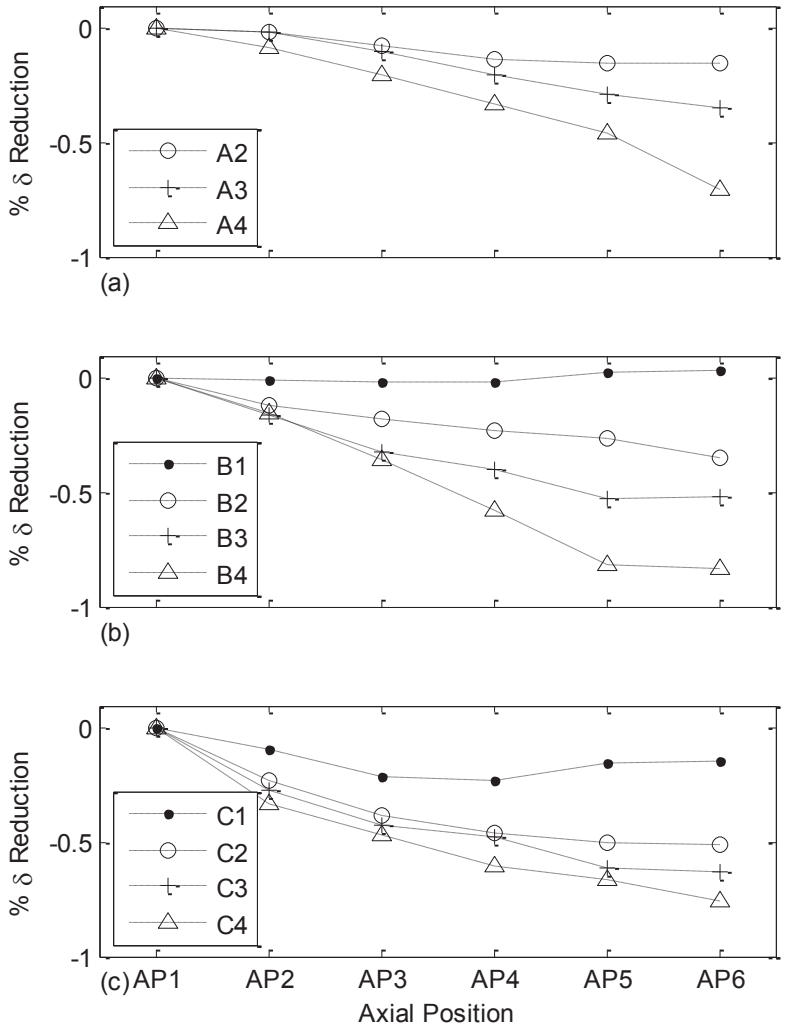

Figure 5-28. Boundary Layer Thickness Reduction

Development of a boundary layer thickness for a typical turbulent boundary layer can be predicted by:

$$\frac{\delta}{x} = \frac{0.37}{\mathrm{Re}_x^{0.2}} \tag{42}$$

For a non-accelerated case, the thickness should increase as a function of $x^{4/5}$. But as can be seen, typical of highly accelerating flows, there is a large reduction in boundary layer thickness. Test cases B1 and C1 show the behavior for the curved, non-converged cases. For the application of low curvature, there is not a corresponding reduction in boundary layer thickness, though the growth of the boundary layer is reduced. This reduction in boundary layer growth is expected and in agreement with Muck [85]. Case C1 actually shows a slight reduction in boundary layer thickness. Other test case behavior is as expected for accelerated boundary layers, and fully laminarized flows. Part of the action of the thinning of the boundary layer is due to the increased applied pressure. As the pressure field increases due to the convergence, it adjusts and pushes outward on the boundary layer.

Shape factors are shown in Figure 5-29 to Figure 5-31. Figure 5-29 compares the shape factor as a function of axial position for the flat walled cases. These results show the typical shape factor response for highly accelerated flows [7, 56] with an initial decrease followed by a rise. This minimum is often reported as an indication of laminarization, and has been proposed as a critical factor for laminarization by Patel but is not seen for all present cases. One of the reasons for this is many of the previous studies that show this minimum include measurements of a region before the convergence. Shape factor for test case A1, without any acceleration, remains relatively constant throughout suggesting no substantial change to boundary layer profile while the other three cases show an increase in shape factor that is loosely related to the level of acceleration applied. Even though the laminar shape factor is on order of 2.3, shape factors usually do not rise to this value in laminarization studies. This is because the laminarization process affects the near wall region first, and later the outer region. Therefore for these types of flows, surface quantities may accurately be described with

laminar values, and the researchers identify the flows as such, even though the outer region shape factor lies between turbulent and laminar values.

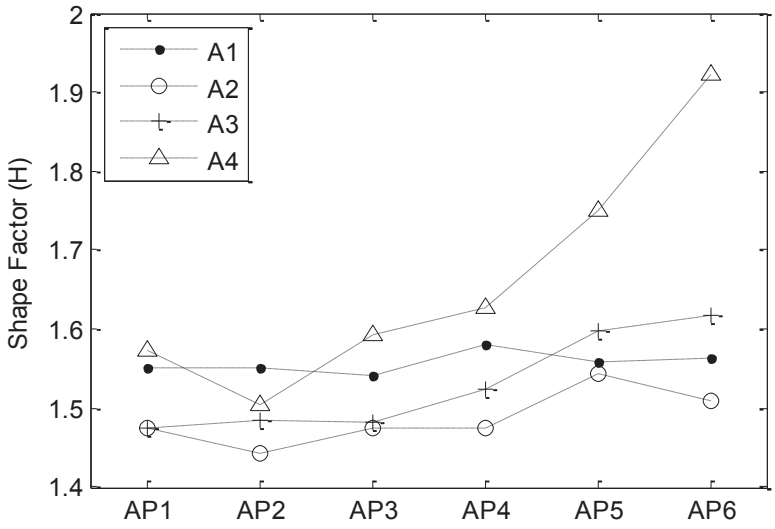

Figure 5-29. Shape Factor for Flat Walled Test Cases

Percent changes in shape factor were plotted in Figure 5-30 and Figure 5-31 to show the effect of curvature and convergence. Test cases in Figure 5-30 are not subject to convergence, but the single effect of moderate curvature has the effect of increasing the shape factor for case C1 as a function of axial distance. This trend is common in boundary layer flows over convex surfaces, though there is not agreement in the slope of this rise of shape factor [88, 146].

For a significant rise of the shape factor to occur for the low curvature cases, flow convergence is necessary. This supports the interesting result that was also seen with respect to the velocity profiles. When only a low curvature or low convergence is applied, no appreciable change in the shape factor is observed, but with both of them together, a large increase is exhibited. The final observation from Figure 5-30 and Figure 5-31 is the difference in axial location at which there is a rise in the shape factor between B and C cases. If a rise in the shape factor can be related to laminarization, not

only is there a threshold acceleration value for which laminarization will occur, but the magnitude of this value is associated with the quickness of this phenomenon.

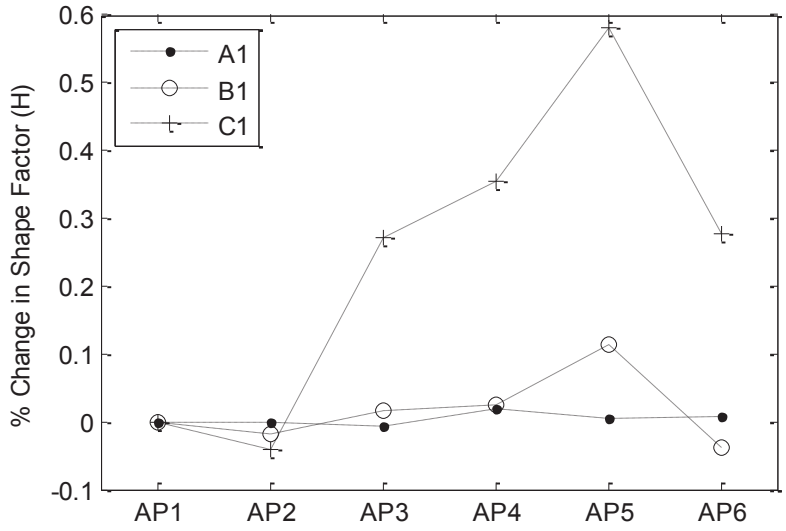

Figure 5-30. Evolution of Shape Factor for Non-Converged Cases

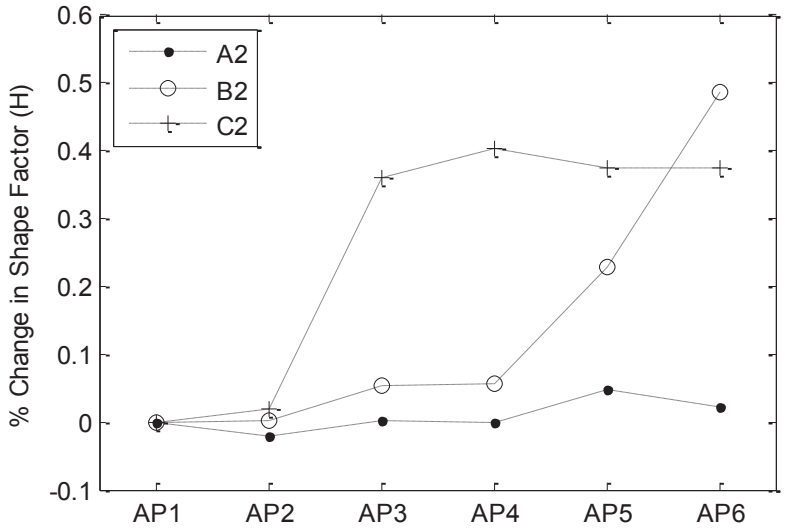

Figure 5-31. Evolution of Shape Factor for Low-Converged Cases

Skin friction values are plotted in Figure 5-32 to Figure 5-34. Due to the differences in velocity used for the different test cases, the corresponding turbulent and laminar values, as predicted from flat plate theory, varied for each case. Therefore to show the change toward laminar values, the skin friction values are normalized between turbulent and laminar prediction values [123, 132]. All initial skin friction values varied from 0.004 to 0.006. Numerical values are presented in Appendix H.

As expected in Figure 5-32, flat walled test cases with acceleration below the predicted threshold value did not show much change from beginning to end, while the higher accelerated cases did exhibit this. The change in skin friction, which suggests behavior towards laminar, is consistent with the shape factor development presented in Figure 5-29.

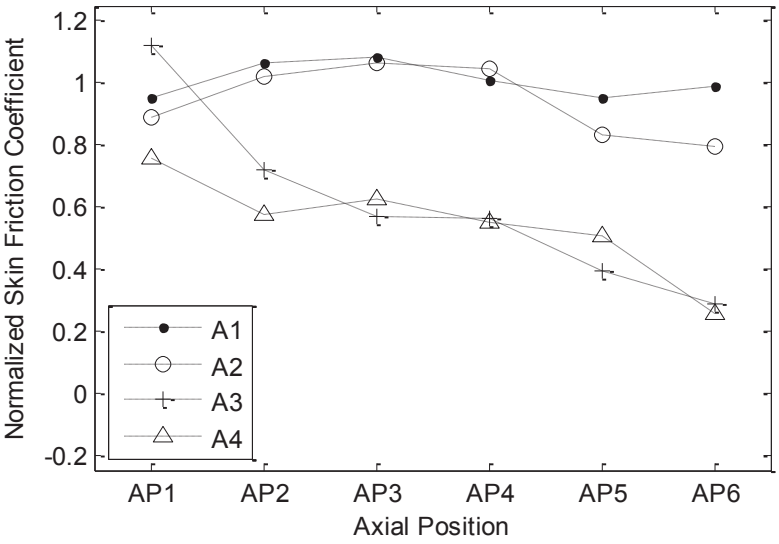

Figure 5-32. Skin Friction: Flat Plate Configuration Test Cases. Normalized with Flat Plate Predictions. Turbulent = 1.0; Laminar = 0.0

Comparison between Figure 5-33 and Figure 5-34 show the effect of curvature. Substantial drops in the skin friction coefficient occur for all curvatures of the middle converged case. Considering the results for the flat walled cases, this is to be expected

and in agreement with result summaries from Patel. Both low and moderate levels of curvature are sufficient for a reduction in the skin friction coefficient.

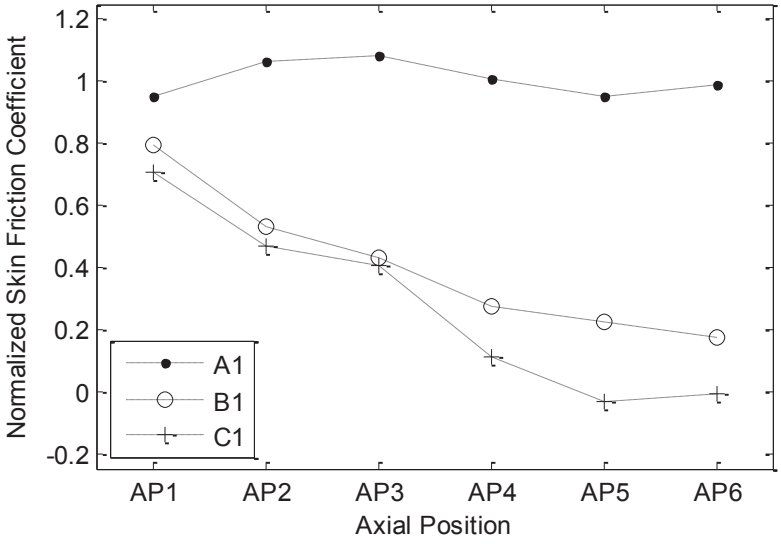

Figure 5-33. Skin Friction: Non-Converged Test Cases. Normalized as above.

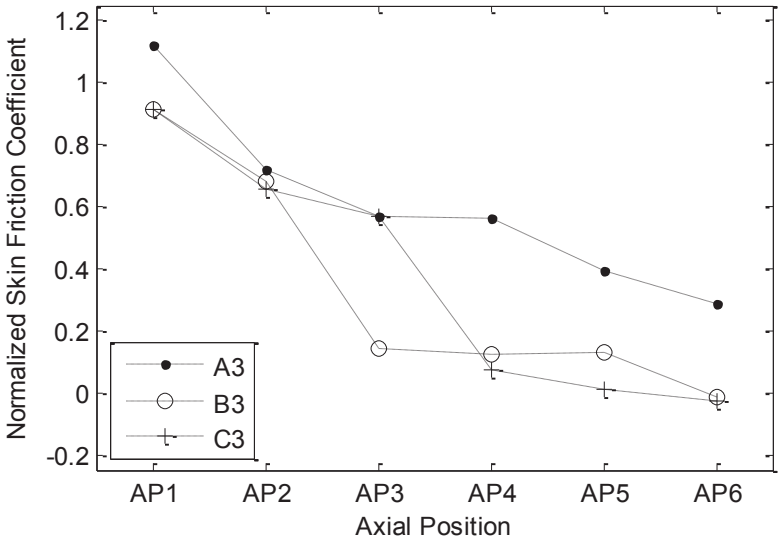

Figure 5-34. Skin Friction: Medium Convergence Test Cases. Normalized as above.

Initial momentum Reynolds numbers ranged from 500 to 700. Plotted here are the changes with respect to axial distance for the low convergence cases. The general trend is as expected for accelerated boundary layers, as the momentum layer thickness thins quicker than the increase in velocity. As expected, there is very little drop for the flat walled case, though the drop in Reynolds number does appear to be dependent on curvature effects. Badri Narayanan [47] proposed that laminarization may be dependent on the momentum thickness Reynolds number, and the effect of the acceleration is to lower this value sufficiently that turbulence cannot be sustained. These experiments are consistent with his findings that once the Re_θ has dropped below 300, the flow transitions to laminar due to the decay of turbulence. Though other researchers have investigated low Reynolds number flows and determined that the laminarization effect is not a Reynolds number effect (Jones and Launder [51, 52], Back and Seban [45, 46], and Okomoto [145]).

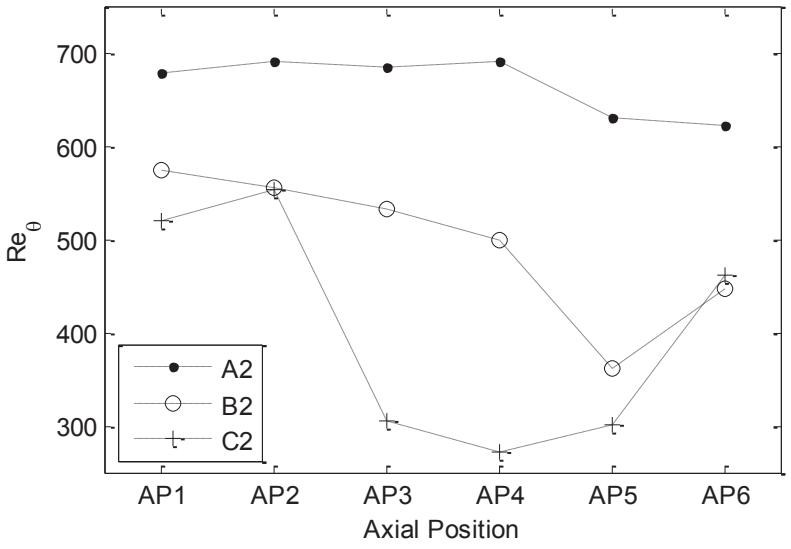

Figure 5-35. Momentum Reynolds Numbers for Medium Converged Cases

5.5 Turbulent Quantities

Streamwise and spanwise turbulent intensities and Reynolds stresses were measured. Figure 5-36 to Figure 5-38 show the turbulent quantities for test case A2. Due to the low level of acceleration, these quantities do not change substantially along the axial length of the flow. Similar results are found for case A1. Figure 5-39 shows the spanwise turbulent intensity for case B2.

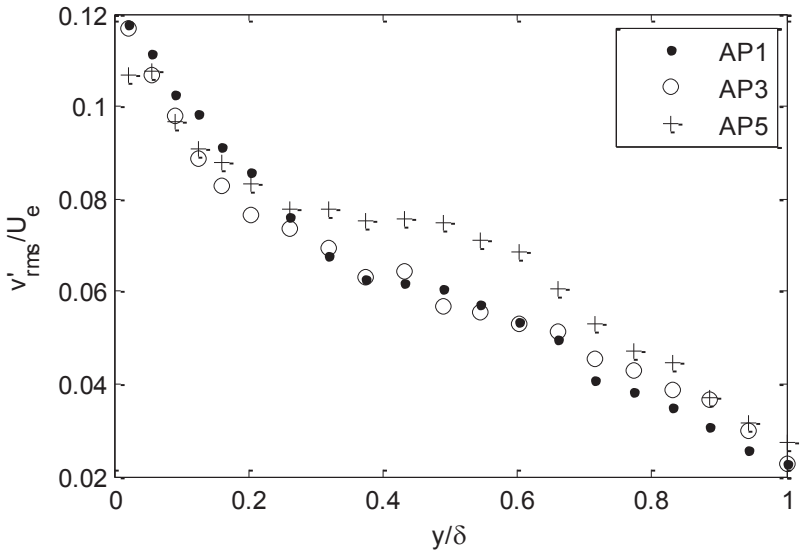

Figure 5-36. Root Mean Square Streamwise Velocity Profiles of Test Case A2

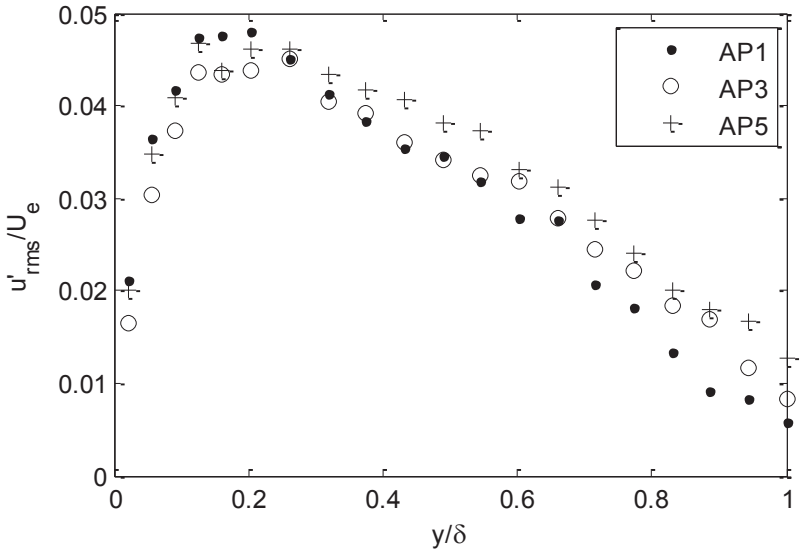

Figure 5-37. Root Mean Square Spanwise Velocity Profiles of A2

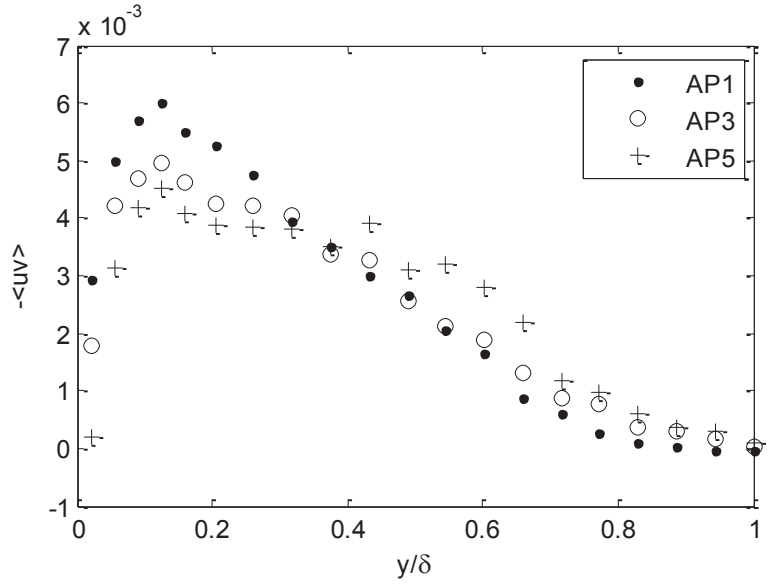

Figure 5-38. Normalize Reynolds Stress Profile for A2

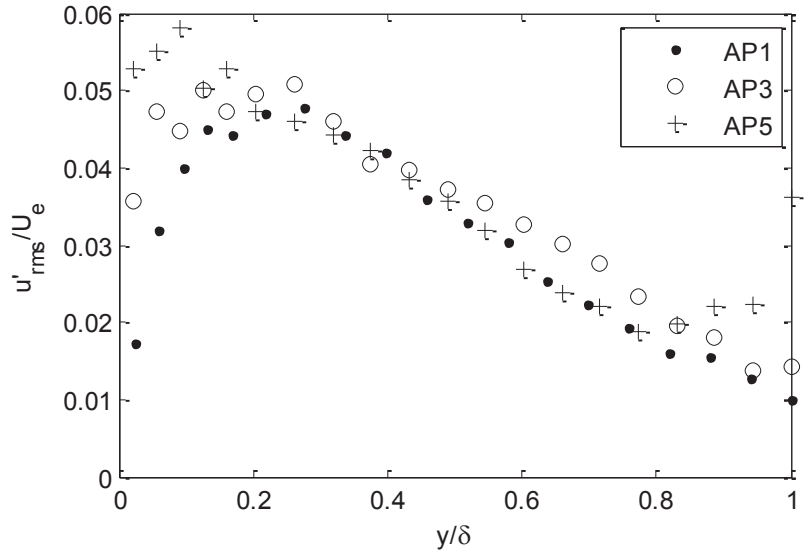

Figure 5-39. Spanwise Turbulent Intensity for Case B2

Results of the turbulent quantity measurements for other cases, specifically for cases with higher acceleration where other characteristics of the flow trend towards laminar were not as expected because there were discrepancies with results of other researchers. In general, there is a consensus that during the laminarization process there is a decay in turbulent intensity. In fact, Badri Narayanan [29, 47, 81], and to a related extent, Fiedler and Head and Schraub and Kline used turbulence decay as an establishing characteristic of laminarization. While all the behavior is not completely consistent for accelerating flows, some flows studied by Badri Narayanan did see an increase in parts of the flow, the general understanding is that the turbulence does not decrease as much as it gets diluted by the increase in bulk flow. Though for curvature cases, researchers have seen a decay in the turbulence at $y/\delta = 0.4$. Even though there is not an increase in intensity above in Figure 5-39, there is not a visible decrease as would be expected. And many of the cases show this.

For some other cases, the turbulent intensities increased with axial position. Below are two characteristic plots for higher convergence and curvature cases. The following figure is of case A4, with high acceleration that shows an increase in Reynolds stress.

Figure 5-41 shows a decrease in the turbulent intensity near the wall, but without a tailing off outward through the boundary layer.

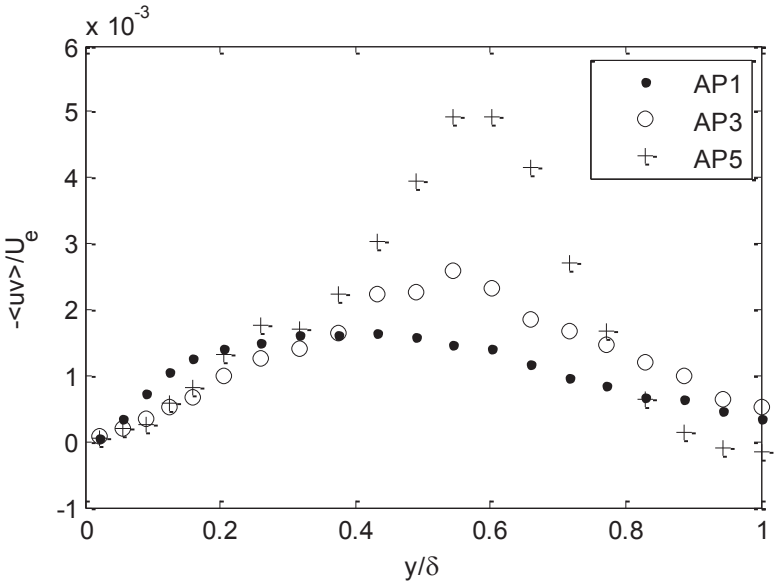

Figure 5-40. Reynolds Stress Profile for A4

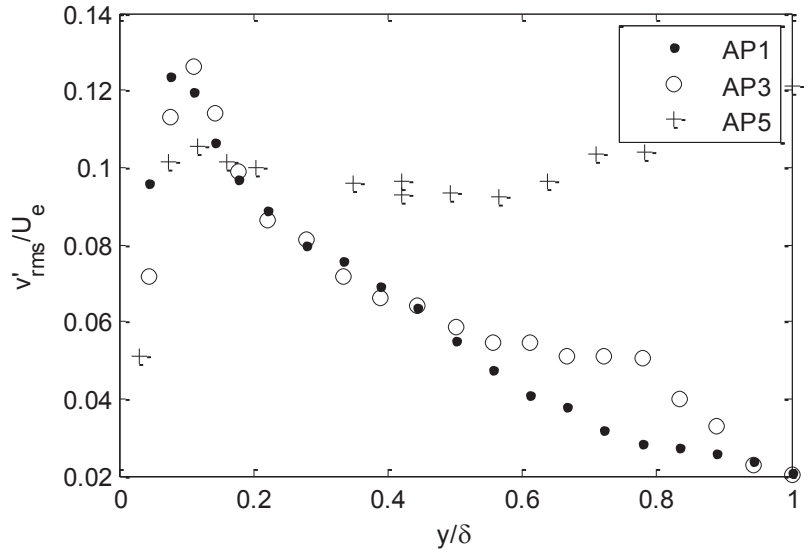

Figure 5-41. Streamwise Turbulent Intensities of B1

It is expected that this is partly due to the spatial averaging that takes place for the PIV measurements. In typical turbulent fluctuation measurements, essentially a point measurement device is used. The current PIV system, with its spatial averaging, acts as a band pass filter for the small scales. In addition, due to the reduction in the Reynolds number during the laminarization process, there is a shift in the energy spectra. With lower Reynolds number the spectra gets shifter to higher wave numbers. This results in an increased overlap between energy and dissipation spectra. This shift in energy range due to a decrease in the Reynolds number is interesting because Bradshaw theorized that the onset of laminarization occurs due to the viscosity independent region shrinking to zero, and the energy producing and dissipating scales overlapping.

6 DISCUSSION

6.1 Identification of Laminarization

To assess the suitability of laminarization parameters to the current data for flows subject to both curvature and acceleration, identification of laminarization with respect to test cases was needed. As can be surmised from a review of the literature, this is no concretely defined task. For laminarizing flow, there is an onset, which many researchers have established methods for identifying, and if the conditions are sufficient, there can be a complete transition to laminarization. In a theoretical view, a fluid has laminarized when its flow can be described without any turbulence closure models. Though in a practical view, specific characteristics of the flow may be better described with laminar correlations, even though at that instance, the flow may still retain its turbulent history and for an accurate description of its further development, turbulent models are needed. Some of the methods used to identify laminarization is a deviation from the law of the wall, cessation of bursting at the wall, a minimum and rise in the shape factor, reduction in skin friction and heat transfer, and a decrease in turbulent intensity.

In the present study, laminarization is identified by a combination of the velocity flow profile, and a substantial drop in the skin friction coefficient. These two are used as metrics both for practicality and theory. From a practical standpoint, in its application to pebble bed reactors, understanding the flow regime is important for heat transfer and friction losses. Even if the flow retains a turbulence signal, if the wall phenomena are governed by laminar characteristics, then this is the limiting factor for these processes. But from a physical behavior standpoint, simply a skin friction coefficient, or Stanton number that is more in-line with laminar values than turbulent values does not necessitate laminar flow. There is variability in turbulent flows. A lack of agreement with equilibrium, high Reynolds number turbulence laws does not imply that the flow is laminar.

In addition to the two flow characteristics on which the metrics will be focused, the other measured parameters will be considered, though as would be expected in a

laminarizing flow, parameters typically transition towards laminar values concurrently. The other thing to remember is that laminarization is not an abrupt event, but instead is gradual. So while some flows may be able to be identified as laminarized, or still others turbulent, others will be in a transitional state. A transitional state which does not guarantee a full laminarization. These flows will be identified as such.

The Blasius boundary layer flow profile, in outer coordinates is first used for laminarization identification. From visual inspection, it is apparent that some of the test case flow profiles at AP6 meet this criterion; specifically test cases B4 (Figure 5-11) and C1 (Figure 5-12). A non-dimensional deviation from the Blasius solution was calculated the flow profile error with respect to the laminar solution.

$$\varepsilon_{blas}^2 = \frac{1}{N}\sum_i \left(\frac{U_{norm,meas}\left(y/\delta\right) - U_{norm,Blas}\left(y/\delta\right)}{U_{norm,Blas}\left(y/\delta = 0.3\right)} \right)^2 \tag{43}$$

U was normalized with the free stream velocity. The normalizing value of U+(0.3) was used to avoid excessive weighting of the error between the two profiles at small values near the wall because later profile comparisons with inner variables focuses on the near wall region. Similar equations were used to calculate the deviation from the log law, and the linear law. The log law was applied for $y^+ > 35$, and the percent error from the linear law was calculated for y^+ to 50 and 100. A large error for the log law represents departure from turbulent behavior, while for all other errors, the error minimized relates to similarity to laminar behavior.

$$\varepsilon_{Ln}^2 = \frac{1}{N}\sum_i \left(\frac{U_{meas}^+\left(y^+\right) - U_{Ln}^+\left(y^+\right)}{U_{Ln}^+\left(y^+\right)} \right)^2_{y^+>35} \tag{44}$$

$$\varepsilon_{Linear}^2 = \frac{1}{N}\sum_i \left(\frac{U_{meas}^+\left(y^+\right) - U_{Linear}^+\left(y^+\right)}{U_{Linear}^+\left(y^+\right)} \right)^2_{y^+<50,100} \tag{45}$$

Two types of error in the skin friction coefficient were calculated. The first was the difference between the measured value at AP6 and that predicted with the flat plate laminar solution. The second percentage error was comparing the difference between the turbulent and laminar value, as predicted by theory, and the difference measured from the beginning of the test section to the end. The following two correlations were used for flat plate geometries [132]:

$$\begin{aligned} c_{f,turb} &= \frac{0.0592}{\mathrm{Re}_x^{0.2}} \\ c_{f,lam} &= \frac{0.664}{\mathrm{Re}_x^{0.5}} \end{aligned} \tag{46}$$

The characteristic length was taken as the entrance length of the test section. Presented in the table below are the resulting errors. The values used for calculation of these errors were the average velocity values, and do not contain the measurement uncertainties as presented in the section on PIV uncertainty.

Table 6-1. Test Case Laminarization Metric Errors

	Blasius	Log Law	Linear(y^+=100)	Linear(y^+=50)	C_f	ΔC_f
A2	54.0%	0.6%	64.4%	46.9%	163.0%	89.7%
A3	64.6%	50.0%	53.7%	30.2%	56.0%	22.8%
A4	52.3%	44.7%	51.5%	33.3%	35.0%	41.1%
B1	41.6%	91.4%	50.6%	33.0%	32.7%	28.2%
B2	35.2%	179.4%	37.5%	34.6%	44.2%	18.6%
B3	45.5%	97.1%	45.1%	23.2%	2.3%	1.8%
B4	10.1%	92.9%	47.0%	23.3%	18.6%	1.2%
C1	11.5%	88.9%	51.6%	39.0%	1.1%	11.7%
C2	16.7%	129.7%	39.3%	19.4%	18.0%	1.7%
C3	40.9%	102.2%	44.5%	20.1%	5.1%	0.4%
C4	26.0%	61.8%	51.0%	28.0%	5.0%	1.1%

Typically the identification of laminarization is principally a practice in engineering experience and judgment, though the presentation of these errors does assist in understanding the changes that the flows experience. Of note is the effect that both curvature and acceleration has on the skin friction coefficient. Test cases B3, B4 and C2-4 all experienced a representative skin friction coefficient drop characteristic with that to be expected for a transition from turbulent to laminar flow. Even while other characteristics of these test cases differed from the Blasius solution, the change of the parameter most critical in engineering applications for these flows to the acceleration and curvature is within a few percent of predicted, albeit it should be noted regarding the uncertainty described earlier due to the wall shear stress calculation methodology.

Another interesting finding that is witnessed in these errors is the lack of a comprehensive transition for cases A3 and A4. The largest acceleration constant proposed in the literature to be needed for laminarization is 3.5×10^{-6}. Both these test cases had larger than this, but the overall change in the boundary layer profile was not very extreme, though this is not surprising. The results are similar to those of others and in the typical study of laminarization, the focus is on the onset of the phenomenon, and therefore the parameter values used to predict laminarization often do not represent a very large extent of it. The departure from the log law, and shrinking of the boundary

layer are similar to the findings of others for flat plate geometries [34, 35, 40] and indicate a transition has begun to occur.

Despite all the normalized errors presented in Table 6-1, it is important not to lose sight of the information that can be gleaned from visual inspection of the flow profiles. Specifically test cases A3 and A4. The inner variable plots (Figure 5-18 and Figure 5-19) show a thickening of the viscous sublayer as the linear portion of the profile expands to greater values of y^+. While test case A3 still shows a logarithmic region, test case A4 hardly has any logarithmic curve left.

With the errors from laminar behavior presented in Table 6-1, their corresponding relative strength of laminarization can be ranked. Any final assignment of numerical values as cutoffs for the errors to determine laminarization will contain judgments and arbitrariness. Instead the following table identifies some test case flows as transitional. These are flows that have departed from typical turbulent flow and therefore it is not justified to use fully turbulent equilibrium models and correlations. While from the flow profile, it appears these flows have not fully laminarized, they are in a transitional state where specifically using turbulent skin friction or heat transfer correlations will result in large errors.

Table 6-2. Ranking of Relative Laminarization

Test Case	Average Relative Error From Laminar Conditions	State
C2	15.9%	Laminarized
B4	21.2%	Laminarized
C3	21.5%	Laminarized
B3	23.5%	Laminarized
C1	24.3%	Laminarized
C4	28.2%	Laminarized
B2	28.4%	Transitional
B1	35.8%	Transitional
A4	48.1%	Transitional
A3	49.6%	Transitional
A2	89.6%	Turbulent

Both the flat walled, and low curvature cases are progressively more laminarized as a function of acceleration. Also, in comparison between these two test case sets, all of the low curvature cases develop more laminar like characteristics than the flat walled cases. The impact of curvature is seen due to the increased laminar like behavior for the low curvature cases. Consider cases A2, B1 and B2. A2 shows very little departure from traditional flat plate turbulent characteristics, and this is to be expected due to the relatively low acceleration it is subject to. Similarly, case B1 has a minor departure from turbulent behavior. In the region of y+=30-40 there is a departure from the log law, but the resulting profile does not follow the laminar trend. But when the two influences of acceleration and curvature are combined, the effect is quite visible. The inner wall plot for case B2 shows an inner profile that follows the linear curve up to approximately y+=50. This impact is quite important. All acceleration driven laminarization parameters exclude the value corresponding to case B2, but with the added effect of curvature, the laminarization effect is increased.

The response of the moderate curvature cases was not as anticipated. While the impact of curvature on laminarization is shown due to all of them laminarizing, the influence of acceleration is not evident. Part of the reason may be due to the ranking system because all moderate curved cases did show laminarization, especially from the inner wall flow profiles.

The case of C1, and to a lesser extent cases B1, B2, and C2 show the impact of acceleration combined with curvature. The extent of the transition to laminar for these cases is larger than has been seen before in other curvature effect experiments. Part of this maybe due to the momentum Reynolds numbers at which these were tested. Badri Narayanan [29] suggested a laminarization criterion of $Re_\theta = 300$, as this is known to be the Reynolds number for flat plate transition and has been seen as a threshold in previous experiments by Sibulkin [28] as well. The acceleration has the effect of lowering the Reynolds number. This correlation between a drop in Reynolds number and laminarization is what led Patel to suggest that the laminarization process is a Reynolds number phenomenon. Though, the present data does not completely support

this because for the curvature cases (B1, C1), there is not any pressure gradient to induce a lowering of the Reynolds number, but still laminar-like flow response is seen.

6.2 Required Length for Laminarization

From a review of the flow profiles and integral parameters, the different test cases resulted in different distances required for the onset of laminarization to occur. When considering the skin friction coefficients and shape factors for test cases that laminarized, it is informative to look if there was a large change in parameter value between specific axial locations, and if so, at which location. The results in Table 6-2 are interesting in that the ranking did not follow explicitly as might be expected considering flows subject to higher curvature, or convergence. But when considering the required length toward a transition, the behavior was more as expected, where moderate curved wall test cases tended to show a profile change earlier than those for low curvature cases. Table 6-3 identifies the location of a minimum in the shape factor, and where the skin friction factor dropped by more than 30%. If no minimum in the shape factor occurred, the location corresponding to the largest increase in shape factor is identified.

6-3. Location of Parameter Characterization Change

Test Case	Minimum in H	Location $\Delta C_f > 30\%$
B3	4	8
B4	12	12
C1	4	12
C2	4	4
C3	0	12
C4	0	8

For most of these test cases the minimum in shape factor precedes the drop in skin friction coefficient. This is not surprising because the minimum in shape factor indicates that the shape of the velocity profile is departing from turbulent flow. As a

result of this occurring and the flow becoming more laminar-like, the skin friction coefficient drops. Closely related to the location of rise in shape factor is the departure from the log law. Test cases B2-C4 show this relationship. This is not surprising because the change in flow profile at the bottom end of the log law region accompanies a shift in the relative contribution of the momentum thickness to the shape factor. This similar trend was seen by Badri Narayanan and Patel.

Considering the minimum in shape factor and the velocity profiles plotted with inner variables, the occurrence of laminarization so early in the axial distance of the flow for test cases C1-C4 has direct impact on pebble bed reactors. The flow over the individual pebbles represents a moderate curve. Combined with the small convergence paths that are created in a packed bed, and the short distance needed, laminarization could occur in the pebble bed. Implicit in the laminarization would be an increase in the viscous sublayer, and a corresponding decrease in surface heat transfer. The acceleration parameter represents a force balance between the surface shear stress and the pressure gradient. It can be explicitly related to a decrease in the momentum Reynolds number through the integral momentum equation. While it is debatable the role of the Reynolds momentum number on laminarization, for sufficiently low Reynolds numbers, turbulence cannot be sustained. For two cases with the same convergence flow area, a higher acceleration parameter results from lower velocity values. During accident scenarios, and especially coastdown, on a localized scale the reactor fuel is in a state of high decay heat and depending on the flow paths, a higher acceleration parameter which corresponds to lower heat transfer.

6.3 Stability Map

With the flow measurements of velocity, skin friction coefficient, and momentum thickness having been taken, the corresponding laminarization parameters from literature can be calculated to compare to the data. Table 6-4 contains these values and the critical values.

Table 6-4. Laminarization Parameter Values for Test Cases

Test Case	$K > 2.0x10^{-6}$	$\Delta_P > 0.025$	$Re_\theta < 300$	$\Lambda > 50$	δ/R
A2	1.85x10-6	0.012	632	19.9	N/A
A3	6.12x10-6	0.094	341	17.8	N/A
A4	1.82x10-5	0.158	150	19.8	N/A
B1	N/A	N/A	492	N/A	0.0145
B2	1.77x10-6	0.044	433	22.4	0.015
B3	6.92x10-6	0.199	219	23.6	0.0147
B4	1.84x10-5	0.221	139	14.3	0.0143
C1	N/A	N/A	261	N/A	0.0483
C2	1.93x10-6	0.033	271	11.2	0.0478
C3	5.58x10-6	0.178	211	19.5	0.0475
C4	2.13x10-5	0.286	95	18.9	0.0483

K, Δ_p, and Λ all represent non dimensional pressure gradients. Λ represents the pressure gradient needed to treat the flow with equations of motion that neglect Reynolds stresses, and reduce to two layered laminar equations. The critical value of 50 represents the asymptote of pressure gradient as the quasi-laminar equations become more applicable, but from the present data, this value seems unjustly high. While it may represent a flow that has essentially completely transitioned to laminar, the necessary pressure gradient needed for this value is already past the point when the flow no longer can be considered turbulent, and laminar mean property values must be used.

The pressure gradient parameter (Δ_p) matched the data, but the data did not correspond near its limit. Therefore it is difficult to quantify the fit of the criterion to laminarization, though the case that did not have any characteristics of laminar flow was below the critical value, and all the rest that were at least transitional had corresponding values. The use of the Reynolds number matches well except for cases A3 and B2. These two cases were transitional, but from the inner wall velocity profile, they did develop a thickened viscous sublayer.

Of all the parameters, only K consists of values known without measuring wall parameters, but this is only because it makes an approximation regarding the skin friction coefficient. But the cost of this approximation is that it does not balance the

forces between the current pressure gradient and shear stress, but instead the expected shear stress for equilibrium conditions. But assuming conditions are typical at the application of the pressure gradient, then if these conditions are met, onset of laminarization can be expected. But because it only considers a force balance due to the pressure gradient, it cannot account for curvature effects.

From the calculated data in Table 6-4, none of the laminarization parameters are able to predict the flow behavior due to the combined effect of acceleration and curvature. It is desired that the levels of acceleration and curvature for the test cases be related to the occurrence of laminarization. In order to account for both curvature and acceleration effects, some sort of radius of curvature parameter is needed. In the curvilinear equation of motion, the equations indicate that the effect of curvature should be felt on the order of δ/R. These two parameters, the acceleration parameter that represents the balance of force between the shear stress and pressure gradient, and the curvature parameter can be used together to create a stability map for laminarization.

It should be cautioned that there may be other physical phenomena in addition to acceleration and curvature that may be present that have an impact on the occurrence of laminarization whose effect was not captured in the present experiments. One specific factor is that of the Reynolds numbers. Due to the relatively narrow band of velocities tested due to the axial fan and PIV limits, the range of the corresponding momentum Reynolds numbers of the various test cases was small, with all initial momentum Reynolds numbers less than 1000. Therefore, the stability map below corresponds to low momentum Reynolds number boundary layer flows.

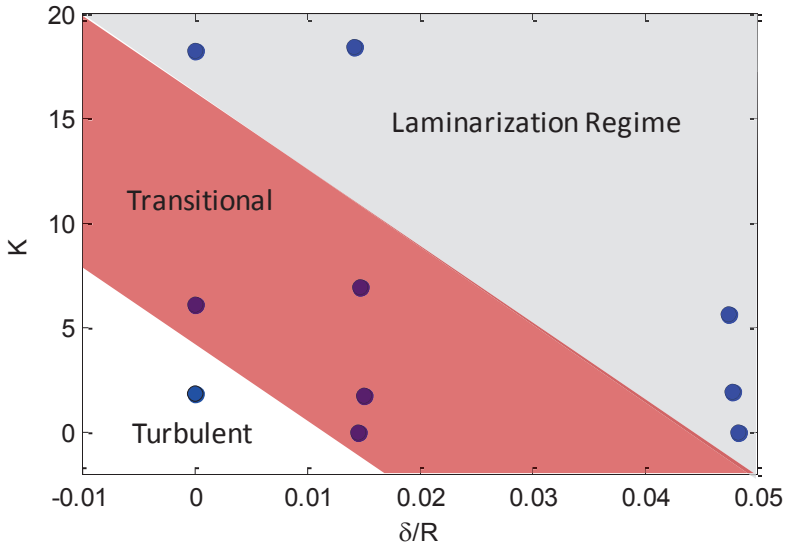

Figure 6-1. Stability Map

The experimental data fits general diagonal bands across the map very well. It illustrates that the influence of acceleration and curvature compound their effects on the flow regime. Of importance is that laminarization can occur for lower levels of acceleration, or curvature if they are both present. This has added importance to pebble bed reactors, because the surfaces creating the physical convergences are also convex in surface curvature. With the current dataset, the area of the transitional region has been estimated.

7 CONCLUSIONS

7.1 Observations

The primary objective of this study was to investigate the role that acceleration and convex curvature have on the laminarization phenomena for boundary layer flows. Experiments were conducted in a wind tunnel made of non-rigid acrylic walls that allowed for variation of the flow area, thus causing an acceleration due to a flow convergence, and variation of the wall curvature. Unique test cases corresponded to combinations of four levels of acceleration and three levels of curvature for a total of twelve test cases. Boundary layer velocity profiles were measured using 2D-PIV. Calculated parameters including displacement thickness, momentum thickness, shape factor, skin friction coefficient and turbulent quantities were used to characterized the boundary layer response to the acceleration and curvature effects. These parameters were used to identify the occurrence of laminarization by comparing these values for the different test cases to those of laminar flow. A stability map of laminarization due to acceleration and curvature was constructed.

For the bulk of the test cases, the experimental data, in the form of velocity flow profiles, mean flow parameters, and turbulent quantities characterized flow transition from turbulent to laminar. It was found that curvature and acceleration have a compounding effect on the flow to cause it to transition towards laminar flow both quicker and to a larger extent. Due to the added effects of curvature, the acceleration, and pressure based parameters used to predict the onset of laminarization do not appear to be sufficient. For this purpose the stability map was constructed to account for both these mechanisms that influence a flow to laminarize considering the range of applicability corresponding to the initial momentum Reynolds number.

7.2 Significant Findings

Three significant findings can be taken from this work with regards to laminarization. While they aren't all entirely unique, the extent to which they occurred

is significant. The first is the influence of the curvature. Many previous studies have shown that convex curvature has the effect of repressing and stabilizing turbulence, and that the effect is greater than what would be predicted from the governing equations. Typically for most studies this is evidenced by a slight departure from the logarithmic law. The current experimental findings show not just a departure from turbulent flow, but a transition to laminar. Case C1, with an absence of acceleration, but moderate curvature underwent almost a complete transition to laminar, even so much as matching with the Blasius solution in outer coordinates. While curvature and acceleration cannot be directly compared because of the different boundary conditions, the impact of the curved wall on the test cases in contrast to the flat walled cases showed a significant impact to cause laminarization.

The second finding to be emphasized is the compound effect of both curvature and acceleration. The most notable example is in comparison of test cases A2, B1 and B2. A2 and B1 each were subject to the low level of acceleration and curvature, respectively, while B2 was subject to them both. Cases A2 and B1 showed only slight departure from turbulent behavior, but case B2 showed a large growth in the viscous sublayer and rise in shape factor. Before these experiments it was logical to theorize that combining acceleration and curvature would result in a flow more susceptible to laminarization, these cases support that prediction.

This contrast in flow response between these three cases illustrates the incomplete picture that may occur when just using a single mechanism parameter to predict laminarization when the physics encompass two mechanisms. The corresponding acceleration parameter value was below the recommended critical value for case B2, but due to the combination of effects, the onset of laminarization still occurred. This has importance when considering the application of the acceleration parameter.

The final significant finding was the short distance over which laminarization occurred for some of the test cases. This has direct relevance to pebble bed reactors because of the small convergence channels that are created between pebbles. While the data does not give any reason to suspect that the transition is not gradual, it does show that it can occur quite quickly.

7.3 Areas of Future Work

Three areas of future work are recommended. Considering the stability map in Figure 6-1, the first area of future work would be to conduct more experiments with boundary conditions in the regions governed by the transition area. While it is quite likely that the resulting flow characteristics would simply by a gradual difference between extreme cases, further experiments would assist in better defining whether the boundaries are a blurry differentiation, or more defined phenomena.

The second area of future work would be to conduct experiments with similar levels of acceleration and curvature, but at higher and various momentum Reynolds numbers. This will assist in determining if there is a Reynolds number effect in the data. Previous findings in the literature are contradictory on the impact of the Reynolds number, so it would be informative to conduct these other experiments for comparison with the current experimental data when well defined transitions to laminar occurred.

The third area of future work is to conduct experiments for conditions more prototypical of that to be expected in the pebble bed reactor. This includes both local heating effects, and geometry effects for the random flow through pebbles.

8 REFERENCES

1. DOE, *Annual Energy Outlook 2010*. 2010, Department of Energy.
2. WNA. *World Nuclear Power Reactors and Uranium Requirements*. 2010; Available from: http://www.world-nuclear.org/info/reactors.html.
3. NRC. *Expected New Nuclear Power Plant Applications*. 2010; Available from: http://www.nrc.gov/reactors/new-reactors/new-licensing-files/expected-new-rx-applications.pdf.
4. DOE, *A Technology Roadmap for Generation IV Nuclear Energy Systems*. 2002, Department of Energy and Generation IV International Forum.
5. Hassan, Y.A., *Large Eddy Simulation in Pebble Bed Gas Cooled Core Reactors.* Nuclear Engineering and Design, 2008. 238: p. 530-537.
6. Macdonald, P.E., et al., *NGNP Preliminary Point Design -- Results of the Initial Neutronics and Thermal-Hydraulic Assessments*. 2003, Idaho National Engineering and Environmental Laboratory.
7. Narasimha, R. and K.R. Sreenivasan, *Relaminarization of fluid flows.* Adv. Appl. Mech., 1979. 19: p. 221-309.
8. Schultz.R.R., et al., *Next Generation Nuclear Plant Methods Technical Program Plan*. 2006, Idaho National Laboratory.
9. ORNL, *From Manhattan Project to Electricity Production*, in *Review*. 2003, Oak Ridge National Laboratory.
10. Moormann, R., *A Safety Re-evaulation of the AVR Pebble Bed Reactor Operation and its Consequences for Future HTR Concepts*. 2008.
11. Nicholls, D., *The Pebble Bed Modular Reactor, Desalination Challenges and Options.* Int. J. Nuclear Desalination, 2005. 1(4).
12. Goodjohn, A.J., *Summary of Gas-Cooled Reactor Programs.* Energy, 1991. 16(1-2): p. 79-106.
13. Frewer, H., W. Keller, and R. Pruschek, *The Modular High-Temperature Reactor.* Nuclear Science and Engineering 1985. 90: p. 411-426.

14. Gao, Z. and S. Lei, *Thermal Hydraulic Transient Analysis of the HTR-10.* Nuclear Engineering and Design, 2002. 218: p. 65-80.
15. Wu, Z., D. Lin, and D. Zhong, *The Design Features of the HTR-10.* Nuclear Engineering and Design, 2002. 218: p. 25-32.
16. Zhang, Z., et al., *Current Status and Technical Description of Chinese 2 x 250 MWt HTR-PM Demonstration Plant.* Nuclear Engineering and Design, 2009. 239: p. 1212-1219.
17. Hevia, F., *Pebble Bed Modular Reactor (PBMR Pty. Limited; South Africa).* Atw. Internationale Zeitschrift fur Kernenergie, 2005. 50(12).
18. Ion, S., et al., *Pebble Bed Modular Reactor -- The First Generation IV Reactor to be Constructed.* Nuclear Energy, 2004. 43(1): p. 55-62.
19. Schultz.R.R., et al., *Next Generation Nuclear Plant -- Design Methods Development and Validation Research and Development Program Plan*. 2004, Idaho National Engineering and Environmental Laboratory.
20. Koster, A., R. Matzie, and D. Matzner, *Pebble-Bed Modular Reactor: A Generation IV High-Temperature Gas-Cooled Reactor.* Proc. Instn Mech. Engrs, 2004. 218(A: J. Power and Energy): p. 309.
21. Koster, A., D. Matzner, and D.R. Nicholsi, *PBMR Design for the Future.* Nuclear Engineering and Design, 2003. 222: p. 231-245.
22. Jackson, R.B., *Dissertation Research Proposal: Laminarization in Pebble Bed Cores*. 2011, Oregon State University.
23. Taylor, G.I., *The Criterion for Turbulence in Curved Pipes.* Proc. R. Soc. London, Ser. A., 1929. 124: p. 243.
24. Viswanath, P.R., R. Narasimha, and A. Prabhu, *Visualization of relaminarizing flows.* J. Indian Inst. Sci., 1978. 60: p. 159.
25. Richardson, L.F., *The Supply of Energy to and from Atmospheric Eddies.* Proc. R. Soc. London, Ser. A., 1920. 97: p. 354.
26. Prandtl, L. and R. H., *Einflusse von Warmeschichtung aug die Eigenschaften einer turbulenten Stromung.* Dtsch. Forschungsges, 1934. 21.

27. Laufer, J., *Decay of nonisotropic turbulent field.* Mitteilungen der Angewandten Mechanik, 1962(166-174).
28. Sibulkin, M., *Transition from turbulent to laminar flow.* The Physics of Fluids, 1962. 5: p. 280-289.
29. Badri Narayanan, M.A., *An experimental study of reverse transition in two-dimensional channel flow.* J. Fluid Mech., 1968. 31: p. 609.
30. Sternberg, J., *The Transition from turbulent to laminar boundary layer*. 1954.
31. Holder, D.W., G.E. Gadd, and J.D. Regan, *from badriNarayanan.* 1956.
32. Senoo, Y., *The Boundary Layer on the End Wall of a Turbine Nozzle Cascade.* ASME Paper No. A-172, 1957.
33. Sergienko, A.A. and V.K. Gretsov, *Transition from turbulent to laminar boundary layer.* Dokl. Akad. Nauk, SSSR,, 1959. 746: p. 125, pg 275 in Eng translation.
34. Launder, B.E., *Laminarization of the Turbulent Boundary Layer by Acceleration*, in *Gas Turbine Lab. Report 77*, MIT, Editor. 1964.
35. Launder, B.E. and H.S. Stinchcombe, *Non-normal Similar Turbulent Boundary Layers.* Imp. Coll. Note TWF/TN 21. Dept. Mech. Eng., 1967.
36. Moretti, P.M. and W.M. Kays, *Heat transfer to a turbulent boundary layer with varying free-stream velocity and varying surface temperature--an experimental study.* Int. J. Heat Mass Transfer, 1965. 8(9): p. 1187-1202.
37. Schraub, F.A. and S.J. Kline, *A Study of the Structures of the Turbulent Boundary Layer with and without Longitudinal Pressure Gradients*, in *Rep. No. MD-12*, T. Div., Editor. 1965, Stanford University: California.
38. Kline, S.J., et al., *The Structure of Turbulent Boundary Layers.* J. Fluid Mech., 1967. 30(04): p. 741-773.
39. Patel, V.C., *Calibration of the Preston tube and limitations on its use in pressure gradients.* j. Fluid Mech., 1965. 23: p. 185.
40. Patel, V.C. and M.R. Head, *Reversion of turbulent to laminar flow.* J. Fluid Mech., 1968. 34(02, QA901 .J6): p. 371-392.

41. Townsend, A.A., *Equilibrium layers and wall turbulence.* j. Fluid Mech., 1961. 11: p. 97.
42. Townsend, A.A., *The behaviour of a turbulent boundary layer near separation.* J. Fluid Mech., 1962. 12: p. 536.
43. Mellor, G.L., *The effects of pressure gradients on turbulent boundary layers.* J. Fluid Mech., 1966. 24: p. 255.
44. Fiedler, H. and M.R. Head, J. Fluid Mech., 1966. 25: p. 719.
45. Back, L.H. and R.A. Seban, *On Constant Property Turbulent Boundary Layers with Variable Temperature of Heat Flow at the Wall.* ASME J. of Heat Transfer, 1965. 87(1): p. 151-156.
46. Back, L.H. and R.A. Seban, *Flow and heat transfer in a turbulent boundary layer with large acceleration parameter.* Proc. Heat Transfer Fluid Mech. Inst., 1967. 20: p. 410.
47. Badri Narayanan, M.A. and V. Ramjee, *On the criteria for reverse transition in a two-dimensional boundary layer flow.* J. Fluid Mech., 1969. 35: p. 225.
48. Bradshaw, P., *A note on reverse transition.* J. Fluid Mech., 1969. 35: p. 387-390.
49. Preston, J.H., *The minimum Reynolds number for a turbulent boundary layer and the selection of a transition device.* J. Fluid Mech., 1958. p. 373.
50. Bradshaw, P., D.H. Ferriss, and N.P. Atwell, *Calculation of Boundary-Layer Development using the Turbulent Energy Equation.* J. Fluid Mech., 1967. 28(3): p. 593.
51. Jones, W.P. and B.E. Launder, *The Prediction of Laminarization with a Two-Equation Model of Turbulence.* Int. J. Heat Mass Transfer, 1972. 15: p. 301-314.
52. Jones, W.P. and B.E. Launder, *Some properties of sink-flow turbulent boundary layer.* J. Fluid Mech., 1972. 56(QA901 .J6): p. 337-351.
53. Kovasznay, L.S.G., V. Kibens, and R.F. Blackwelder, *Large-scale motion in the intermittent region of a turbulent boundary layer.* J. Fluid Mech., 1970. 41(02): p. 283-325.

54. Blackwelder, R.F. and L.S.G. Kovasznay, *Large scale motion of a turbulent boundary layer during relaminarization.* J. Fluid Mech., 1972. 53: p. 61-83.
55. Narasimha, R. and K.R. Sreenivasan, *Relaminarization in highly accelerated turbulent boundary layers.* J. Fluid Mech., 1973. 61: p. 417-447.
56. Sreenivasan, K.R., *Laminarescent, relaminarizing and retransitional flows.* Acta Mechanica, 1982. 44(1-2): p. 1-48.
57. Murphy, H.D., F.W. Chambers, and M. D.M., *Laterally converging flow. Part 1. Mean Flow.* J. Fluid Mech., 1983. 127: p. 379-401.
58. Chambers, F.W., H.D. Murphy, and M. D.M., *Laterally Convering Flow. Part 2. Temporal wall Shear Stress.* J. Fluid Mech., 1983. 127: p. 379-401.
59. Finnicum, D.S. and T.J. Hanratty, *Effect of Favorable Pressure gradients on Turbulent Boundary Layers.* A.I.Ch.E. Journal, 1988. 34(TP1 .A2): p. 529-540.
60. Spalart, P.R., *Numerical Study of sink-flow boundary layers.* J. Fluid Mech., 1986. 172: p. 307-328.
61. Escudier, M.P., et al., *Laminarisation and re-transition of a turbulent boundary layer subjected to favourable pressure gradient.* Experiments in Fluids, 1998. 25: p. 491-502.
62. Fernholtz, H.H. and D. Warnack, *The effects of a favorable pressure gradient and of the Reynolds number on an incompressible asissymmetric turbulent boundary layer. Part 1. The turbulent boundary layer.* j. Fluid Mech., 1998. 359: p. 329.
63. Warnack, D. and H.H. Fernholtz, *The effects of a favorable pressure gradient and of the Reynolds number on an incompressible axissymmetric turbulent boundary layer. Part 2. The boundary layer with relaminarization.* j. Fluid Mech., 1998. 359: p. 357.
64. Greenblatt, D. and E.A. Moss, *Pipe-flow relaminarization by temporal acceleration.* Physics of Fluids, 1999. 11(11): p. 3478.

65. Ichimiya, M., I. Nakamura, and S. Yamashita, *Properties of a relaminarizaing turbulent boundary layer under a favorable pressure gradient.* Experimental Thermal and Fluid Science, 1998. 17: p. 37-48.
66. Cal, R.B. and L. Castillo, *Similarity analysis of favorable pressure gradient turbulent boundary layers with eventual quasilaminarization.* Physics of Fluids, 2008. 20.
67. Cal, R.B., et al., *The rough favourable pressure gradient turbulent boundary layer.* j. Fluid Mech., 2009. 641: p. 129-155.
68. Piomelli, U., E. Balaras, and A. Pascarelli, *Turbulent Structures in Accelerating Boundary Layers.* Journal of Turbulence, 2000. 1(Art.# N1).
69. Radhakrishnan, S., et al. *Large eddy simulation of high Reynolds number flow over a contoured ramp*. in *Proceedings of the 44th AIAA Aerospace Science Meeting and Exhibit*. 2006. Reno, NV: Paper No. AIAA-2006-0899.
70. Watterndorf, F.L., *A study of the effect of curvature on fully developed turbulent flow.* Proc. R. Soc., 1935. 148: p. 565.
71. Wilcken, H., Ing. Arch., 1930. 1(358-376).
72. Schmidbauer, H., N.A.C.A. Tech. Memo., 1936. no. 791.
73. Wilson, D.G. and J.A. Pope, *Convective Heat Transfer to Gas Turbine Blades.* Proc. Inst. Mech. Engrs., 1954: p. 861.
74. Wilson, D.G., *Equilibrium Turbulent Boundary Layers in Favorable Pressure Gradients*, in *Div. of Engineering and Applied Science*, C.n.f.a. -ILL, Editor. 1957, Harvard University.
75. Eskinazi, S. and H. Yeh, *An investigation on fully developed turbulent flows in a curved channel.* J. Aeronaut Sci., 1956. 23: p. 23-34.
76. Rotta, J.C., *Effect of Streamwise Wall Curvature on Compressible Turbulent Boundary Layers.* Phys. Fluids Suppl., 1967: p. S174-S180.
77. Bradshaw, P., *The analogy between streamwise curvature and buoyancy in turbulent shear flow.* J. Fluid Mech., 1969. 36: p. 177.
78. So, R.M.G. and G.L. Mellor, *Experiment on convex curvature effects in turbulent boundary layer.* j. Fluid Mech., 1972. 60: p. 43.

79. Businger, J.A., et al., J. Atmos. Sci., 1971. 28(181-189).
80. Ramaprian, B.R. and B.G. Shivaprasad, *The structure of turbulent boundary layers along mildly curved surfaces.* J. Fluid Mech., 1978. 85: p. 273.
81. Badri Narayanan, M.A., S. Rajagopalan, and R. Narasimha, *Experiments on the fine structure of turbulence.* J. Fluid Mech., 1977. 80: p. 237.
82. Brown, G.L. and A.S.W. Thomas, *Large structure in a turbulent boundary layer.* Phys. Fluids, 1977. 20: p. S243.
83. Rao, K.N., R. Narasimha, and M.A. Badri Narayanan, *The "bursting" phenomenon in a turbulent boundary layer.* J. Fluid Mech., 1971. 48: p. 339.
84. Gillis, J.C. and J.P. Johnston, *Turbulent Boundary Layer Flow and structure on a convex wall and its redevelopment on a flat wall.* j. Fluid Mech., 1983. 135: p. 123.
85. Muck, K.C., P.H. Hoffmann, and P. Bradshaw, *The effect of convex surface curvature on turbulent boundary layers.* J. Fluid Mech., 1985. 161: p. 347.
86. Moser, R.D. and P. Moin, *The effects of curvature in wall-bounded turbulent flows.* j. Fluid Mech., 1987. 175: p. 479-510.
87. *Frontiers in fluid mechanics: a collection of research papers written in commemoration of the 65th birthday of Stanley Corrsin*, ed. S.H. Davis and J.L. Lumley.
88. Patel, V.C. and F. Sotiropoulos, *Longitudinal curvature effects in turbulent boundary layers.* Prog. Aerosp. Sci., 1997. 33: p. 1-70.
89. Mokhtarzadeh-Dehghan, M.R. and Y.M. Yuan, *Measurements of turbulence quantities and bursting period in developing turbulent boundary layers on the concave and convex walls of a 90 square bend.* Experimental Thermal and Fluid Science, 2002. 27: p. 59.
90. Gretler, W. and M. Baltl, *Numerical calculation of fully developed flow in curved channels: An extended algebraic Reynolds-stress model.* Forschung in Ingenieurwesen, 2000. 66: p. 138.
91. Munch, C. and O. Metais, *Large eddy simulations in curved square ducts: variation of the curvature radius.* journal of Turbulence, 2007. 8.

92. Mukund, R., et al., *Relaminarization in highly favourable pressure gradients on a convex surface.* J. Fluid Mech., 2006. 566: p. 97-115.
93. Holloway, A.G.L., D.C. Roach, and H. Akbary, *Combined effects of favorable pressure gradient and streamline curvature on uniformly sheared turbulence.* j. Fluid Mech., 2005. 526: p. 303.
94. Bankston, C.A., W.L. Sibbit, and V.J. Skoglund. *Stability of Gas Flow Distribution Among parallel Heated Channels*. in *AIAA 2nd Propulsion Joint Specialist Conference*. 1966.
95. Perkins, H.C. and P.M. Worsoe-Schmidt, *Turbulent Heat and Momentum Transfer for Gases in a Circular Tube at Wall-to-Bulk Temperature Ratios to Seven.* Int. J. Heat Mass Transfer, 1965. 8: p. 1011-1031.
96. Bankston, C.A., *The Transition from turbulent to laminar gas flow in a heated pipe.* J. heat Transfer, 1970. 92: p. 569-579.
97. McEligot, D.M., C.W. Coon, and H.C. Perkins, *Relaminarization in tubes.* Int. J. Heat Mass Transfer, 1970. 13(TP363 .I5): p. 431-433.
98. McEligot, D.M., Ormand, and H.C. Perkins, *Internal Low Reynolds Number turbulent and transitional gas flow with heat transfer.* J. heat Transfer, 1966. 88: p. 239.
99. Coon, C.W. and H.C. Perkins, *Transition from the turbulent to the laminar regime for internal convective flow with large property variations.* j. heat Transfer, 1970. 92: p. 506.
100. Perkins, K.R., *Turbulence Structure in gas flows laminarizing by heating*. 1975, University of Arizona.
101. Perkins, K.R., K.W. Shade, and D.M. McEligot, *Heated laminarizing gas flow in a square duct.* Int. J. Heat Mass Transfer, 1973. 16: p. 897-916.
102. Kawamura, H. *Analysis of Laminarization of heated turbulent gas using a two-equation model of turbulence*. in *Second International Symposium on Turbulence Shear Flow.* 1979. London.
103. Rotta, J.C., *Statistische Theorie nichthomogener Turbulenz.* Zeitschrift fur Physik, 1951. 129(6): p. 547.

104. Torii, S. and W.J. Yang, *Laminarization of turbulent gas flow inside a strongly heated tube.* Int. J. Heat Mass Transfer, 1997. 40: p. 3105-3117.
105. Shehata, A.M. and D.M. McEligot, *Mean turbulence structure in the viscous layer of strongly heated internal gas flows: Measurements.* Int. J. Heat Mass Transfer, 1998. 41: p. 4297-4313.
106. Satake, S., et al., *Direct Numerical Simulation for Laminarization of Turbulent Forced Gas Flows in Circular Tubes with Strong Heating.* International J. of Heat and Fluid Flow, 2000. 21: p. 526-534.
107. Xu, X., et al., *Large eddy simulation of turbulent forced gas flows in vertical pipes with high heat transfer rates.* Int. J. Heat Mass Transfer, 2004. 47: p. 4113-4123.
108. Lee, J.I., et al., *Deteriorated turbulent heat transfer (DTHT) of gas up-flow in a circular tube: Heat transfer correlations.* Int. J. Heat Mass Transfer, 2008. 51: p. 5318-5326.
109. Lee, J.I., et al., *Deteriorated turbulent heat transfer (DTHT) of gas up-flow in a circular tube: Experimental data.* Int. J. Heat Mass Transfer, 2008. 51: p. 3259-3266.
110. Gnielinski, V., *New equations for heat and mass transfer in turbulent pipe and channel flow.* Int. Chem. Eng., 1976. 16(2): p. 359-387.
111. Kim, H., J.I. Lee, and H.C. No, *Thermal hydraulic behavior in the deteriorated turbulent heat transfer regime for a gas-cooled reactor.* Nuclear Engineering and Design, 2010. 240: p. 783-795.
112. *The Baals Wind Tunnel*. 2011 cited 2011; Available from: www.fi.edu/flights/first/makebigger/index.html.
113. Mehta, R.D. and P. Bradshaw, *Design Rules for Small Low Speed Wind Tunnels.* The Aeronautical Journal of the Royal Aeronautical Society, 1979. Nov.: p. 443.
114. Bradshaw, P., *The Effect of Wind-Tunnel Screens on Nominally Two-Dimensional Boundary Layers.* j. Fluid Mech., 1965. 22(4): p. 679-687.
115. Pope, A., *Low Speed Wind Tunnel Testing*. 1984, New York: Wiley.

116. Weighardt, K.E.G., *On the Resistance of Screens.* Aero Quarterly, 1953. 4.
117. Patel, R.P., *The Effects of Wind Tunnel Screens and Honeycombs on the Spanwise Variation of Skin Friction in "Two-Dimensional" Turbulent Boundary Layers*. 1964, McGill University: Montreal.
118. Mehta, R.D., *Turbulent Boundary Layer Perturbed by a Screen.* AIAA Journal, 1985. 23(9): p. 1335.
119. Groth, J. and A.V. Johansson, *Turbulence Reduction by Screens.* j. Fluid Mech., 1988. 197: p. 139-155.
120. Taylor, G.I., et al., *The Effect of Wire Gauze on Small Disturbances in a Uniform Stream.* Q J Mechanics Appl Math, 1949. 2(1): p. 1-29.
121. Rona, A. and H. Soueid. *Boundary Layer Trips for Low Reynolds Number Wind Tunnel Tests*. in *48th AIAA Aerospace Sciences Meeting Including the New Horizons Forum and Aerospace Exposition*. 2010. Orlando, FL: American Institute of Aeronautics and Astronautics (AIAA).
122. Lanspeary, P.V., *Establishing Very Low Speed, Disturbance-Free Flow for Anemometry in Turbulent Boundary Layers*, in *Mechanical Engineering*. 1997, University of Adelaide.
123. Schlichting, H. and K. Gersten, *Boundary Layer Theory*. 2000, Berlin: Springer.
124. George, W., *Is there a universal log law for turbulent wall-bounded flows?* Phil. Trans. R. Soc. A, 2006. 365: p. 789-806.
125. Muniz, L., *Particle Image Velocimetry Studies of Turbulent Nonpremixed Flames*, in *Department of Mechanical Engineering*. 2002, Stanford University: Palo Alto.
126. Adrian, R.J., *Particle-Imaging Techniques for Experimental Fluid Mechanics.* Annu. Rev. Fluid. Mech., 1991. 23: p. 261-304.
127. Raffel, M., et al., *Particle Image Velocimetry: A Practical Guide*. 2007, Berlin: Springer.
128. Adrian, R.J. and J. Wetserweel, *Particle Image Velocimetry*. 2011, Cambridge: Cambridge University Press.

129. DantecDynamics, *DynamicsStudio 3.14 User's Guide*. 2010.
130. Tichenor, N.R., *Particle Image Velocimetry in an Advanced, Serpentine Jet Engine Inlet Duct*, in *Aerospace Engineering*. 2007, Texas A&M University: College Station.
131. Kumar, V., *Flow Control in Adverse Pressure Gradient using Supersonice Microjets*, in *Department of Mechanical Engineering*. 2003, Florida State University.
132. Nunn, R.H., *Intermediate Fluid Mechanics*. 1989, New York City: Taylor & Francis Group.
133. Mathieu, J.J.S., *An Introduction to Turbulent Flow*. 2000, New York: Cambridge University Press.
134. Pope, S.B., *Turbulent Flows*. 2000, New York: Cambridge University Press.
135. Tennekes, H. and J.L. Lumley, *A first course in turbulence*. 1972, Cambridge, Mass.: The MIT Press.
136. Lazar, E., et al., *A Practical Approach to PIV Uncertainty Analysis*, in *27th AIAA Aerodynamic Measurement Technology and Ground Testing Conference*. 2010: Chicago, Ill.
137. Timmins, B.H., B.L. Smith, and P.P. Vlachos, *Automatic Particle Image Velocimetry Uncertainty Quantification*, in *ASME 2010 3rd Joint US-European Fluids Engineering Summer Meeting*. 2010: Motreal, CA. p. 2811.
138. DantecDynamics, *2D PIV Reference Manual*. 2005.
139. Keane, R.D. and R.J. Adrian, *Optimization of Particle image Velocimeters. Part I: Double Pulsed Systems*. Meas. Sci. Technol., 1990. 1: p. 1202-1215.
140. Keane, R.D. and R.J. Adrian, *Theory of Cross-Correlation Analysis of PIV Images*. Appl. Sci. Research, 1992. 49: p. 191-215.
141. Wu, Q., S. Weinbaum, and Y. Andreopoulos, *Stagnation-Point Flows in a Porous Medium*. Chemical Engineering Science, 2005. 60: p. 123-134.
142. Tropea, C., A. Yarin, and J. Foss, eds. *Springer handbook of Experimental Fluid Mechanics*. 2007.

143. Coleman, H. and G. Steele, *Experimentation and Uncertainty Analysis for Engineers*. 1999: Wiley-Interscience.
144. Ferziger, J.H. and M. Peric, *Computational Methods for Fluid Dynamics*, ed. Springer. 2002, Berlin.
145. Okamoto, T. and I. Misu, *Reverse Transition of Turbulent Boundary Layer on Plane Wall of Two-Dimensional Contraction.* Trans. Jpn. Soc. Aerosp. Sci., 1977. 20(1).
146. Schwarz, A.C. and M.W. Plesniak, *Convex Turbulent Boundary Layers with Zero and Favorable Pressure Gradients.* journal of Fluids Engineering, 1996. 118: p. 787.
147. Patel, V.C., *The Effects of Curvature on the Turbulent Boundary Layer*. 1969, Aeronautical Research Council, Ministry of Technology.
148. Boldman, D.R., J.F. Schmidt, and A.K. Gallagher, *Laminarization of a Turbulent Boundary Layer as Observed from Heat-Transfer and Boundary Layer Measurements in Conical Nozzles*. 1968, NASA: Washington, D.C.
149. Jackson, R.B., et al., *Gas Properties Technical Report*. 2011, Oregon State University, Department of Nuclear Engineering.
150. Knoll, G.F., *Radiation Detection and Measurement* 2000: John Wiley & Sons.

APPENDIX A: PITOT TUBE VELOCITY ERROR ANALYSIS

The total uncertainty in the pitot tube velocity measurement was a function of the individual uncertainty of the instruments used to measure pressure and temperature. The total uncertainty associated with the pitot tube velocity measurement system can be given by:

$$u_c^2 = s_x^2 + \sum_{k=1}^{M} b_k^2 \tag{47}$$

where s is the standard deviation estimate for the random uncertainty and b represents the sum of all the systemic uncertainties associated with the measurement system. The systemic uncertainty for each individual velocity measurement can be calculated from the individual uncertainties of the pressure transducers and the thermocouple. The equations for velocity and density are given by:

$$V = \sqrt{\frac{2\Delta P}{\rho}} \tag{48}$$

$$\rho = \frac{TP_o}{a + bT + cP_o + dT^2 + eP_o^2 + fTP_o} \tag{49}$$

where Po is ambient pressure. This equation for density comes from previous work setting a trend surface to NIST data for air [149]. The constants are given in Table A-1.

Table A-1. Coefficients for Air Density Calculation

a	-0.454763114513638	d	0.000285304540219806
b	0.00196454604062911	e	0.00538461801759682
c	-0.503152299414582	f	0.00145070421825171

The uncertainties for these equations were done in two parts. First the uncertainty in the density equation was calculated. Following the procedure of Kline and McClintock [150], the general uncertainty for a calculation dependent on primary measurement uncertainties is given as:

$$\sigma_u = \sqrt{\left(\frac{\partial u}{\partial x}\right)^2 \cdot \sigma_x^2 + \left(\frac{\partial u}{\partial y}\right)^2 \cdot \sigma_y^2} \tag{50}$$

Therefore the uncertainties for the density and velocity calculation are given as:

$$\varepsilon_\rho = \sqrt{\left(\frac{\partial \rho}{\partial T}\right)^2 \cdot \varepsilon_T^2 + \left(\frac{\partial \rho}{\partial P_o}\right)^2 \cdot \varepsilon_{P_o}^2} \tag{51}$$

and

$$\varepsilon_V = \sqrt{\left(\frac{\partial V}{\partial \Delta P}\right)^2 \cdot \varepsilon_{\Delta P}^2 + \left(\frac{\partial V}{\partial \rho}\right)^2 \cdot \varepsilon_\rho^2} \tag{52}$$

where ΔP is the pressure reading from the differential pressure transducer. As stated previously the uncertainty of both pressure sensors was 0.5% of the full scale, and of

the thermocouple was 1.1 C. For each pitot tube measurement in time, a uncertainty was calculated. Velocities as measured by the pitot tube system were averaged over a finite time interval. The system uncertainty of the average was calculated:

$$\varepsilon_{\bar{V}} = \frac{\sqrt{\sum_{i}^{N} \varepsilon_{V_i}^2}}{N} \tag{53}$$

This equation gives a plus or minus range within which we expect the systemic error to lie. We can then calculated the systemic error by assuming a rectangular distribution [143]:

$$b = \frac{\varepsilon_{\bar{V}}}{\sqrt{3}} \tag{54}$$

The LabVIEW VI for the pitot tube system can be set to record measurements at different frequencies and for different durations to obtain time averaged velocities. Typical measurements for screen characterization and during matrix testing were taken at a frequency of 10 hz and for 20-60 seconds. The standard deviation for these measurements is used in Eqn. 50 to obtain the total uncertainty of the time averaged velocity measurement. Given that the standard deviation is from a limited finite sample distributions, a t-distribution is used to estimate the standard deviation of the parent population of the measurements for a given confidence level. Assuming a large sample size, the following equation for the total uncertainty with 99% level of confidence was used:

$$u_{\bar{V}} = 2.6 \cdot \left[s_x^2 + \sum_{k=1}^{M} b_k^2 \right]^{0.5} \tag{55}$$

Typical uncertainties for the pitot velocity measurements for the 99% confidence level was 2.0%.

APPENDIX B: SCREEN CHARACTERIZATION

The following tables and plots give results for the screen characterization runs. Presented are results for the 50, 75 and 100% motor settings for screen configuration 7-9 which corresponded to three, four and five screens used. The span of the y-axis for all plots is consistent, though the range is shifted due to average velocity differences for the different configurations. In the tables, vertical position numbering from low to high corresponds to the physical position going from low to high in the test section. Configuration 8 was the final screen configuration chosen.

Table B-1. Motor Speed Setting 50%

Configuration 7							
	Pos7	Pos6	Pos5	Pos4	Pos3	Pos2	Pos1
Temp (F)	75.5	75.4	75.4	75.3	75.2	75.1	75.0
P (Pa)	100334	100325	100320	100331	100350	100351	100356
Vel (m/s)	1.885	1.951	1.996	2.117	2.016	2.135	2.093
St Dev.	0.0115	0.0125	0.0177	0.0179	0.0157	0.0146	0.0123
V Uncert	1.59	1.68	2.31	2.20	2.03	1.78	1.53
Configuration 8							
	Pos7	Pos6	Pos5	Pos4	Pos3	Pos2	Pos1
Temp (F)	75.0	75.1	75.2	75.3	75.6	75.6	75.7
P (Pa)	101061	101025	100994	100943	100915	100893	100877
Vel (m/s)	2.013	2.002	2.061	2.034	1.977	2.050	2.040
St Dev.	0.0134	0.0147	0.0176	0.0196	0.0177	0.0231	0.0148
V Uncert	1.73 %	1.92 %	2.23 %	2.51 %	2.33 %	2.93 %	1.89 %
Configuration 9							
	Pos7	Pos6	Pos5	Pos4	Pos3	Pos2	Pos1
Temp (F)	72.6	72.0	71.3	75.9	75.6	75.8	75.8
P (Pa)	100473	100465	100445	100820	100830	100854	100855
Vel (m/s)	1.849	1.855	1.906	1.859	1.808	1.886	1.957
St Dev.	0.0129	0.0135	0.0200	0.0194	0.0202	0.0153	0.0149
V Uncert	1.83 %	1.90 %	2.73 %	2.71 %	2.90 %	2.11 %	1.99 %

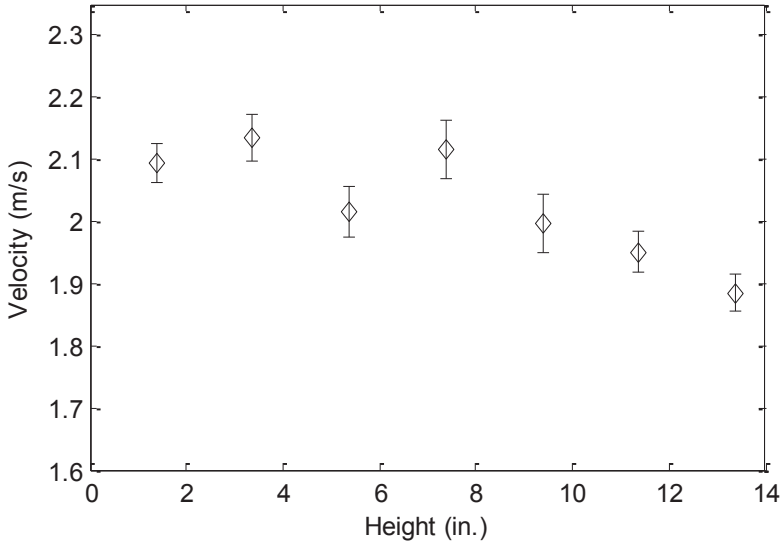

Figure B-1. Configuration 7, Motor 50%

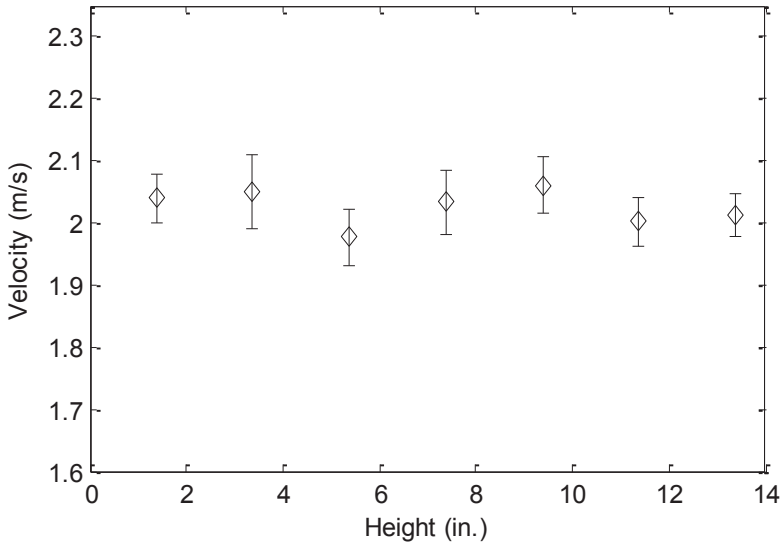

Figure B-2. Configuration 8, Motor 50%

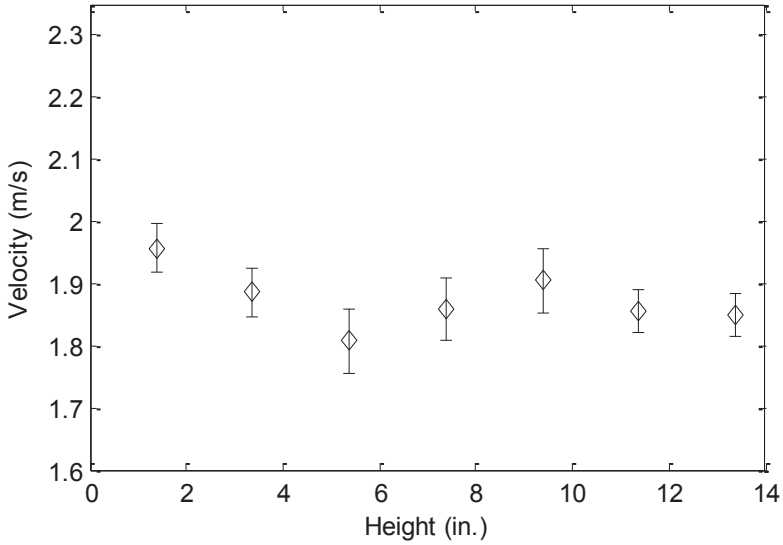

Figure B-3. Configuration 9, Motor 50%

Table B-2. Motor Speed Settings 75%

Configuration 7							
	Pos7	Pos6	Pos5	Pos4	Pos3	Pos2	Pos1
Temp (F)	75.4	75.4	75.3	75.2	75.1	75.0	74.9
P (Pa)	100333	100320	100316	100330	100347	100344	100351
Vel (m/s)	2.842	2.914	3.141	3.144	3.005	3.207	3.153
St Dev.	0.0138	0.01449	0.0228	0.0250	0.0221	0.0216	0.0155
V Uncert	1.27	1.29	1.89	2.07	1.92	1.76	1.28
Configuration 8							
	Pos7	Pos6	Pos5	Pos4	Pos3	Pos2	Pos1
Temp (F)	75.1	75.1	75.1	75.3	75.5	75.6	75.6
P (Pa)	101059	101021	100986	100934	100911	100889	100872
Vel (m/s)	3.068	3.020	3.084	3.065	2.965	3.070	3.108
St Dev.	0.0143	0.0159	0.0244	0.0244	0.0236	0.0176	0.0145
V Uncert	1.22 %	1.37 %	2.06 %	2.07 %	2.07 %	1.49 %	1.22 %
Configuration 9							
	Pos7	Pos6	Pos5	Pos4	Pos3	Pos2	Pos1
Temp (F)	72.6	72.2	71.5	75.9	75.7	75.6	75.7
P (Pa)	100476	100467	100444	100817	100830	100853	100855
Vel (m/s)	2.780	2.791	2.843	2.804	2.688	2.863	2.979
St Dev.	0.0149	0.0161	0.0200	0.0252	0.0255	0.0194	0.0196
V Uncert	1.40	1.51	1.83	2.34	2.47	1.76	1.71

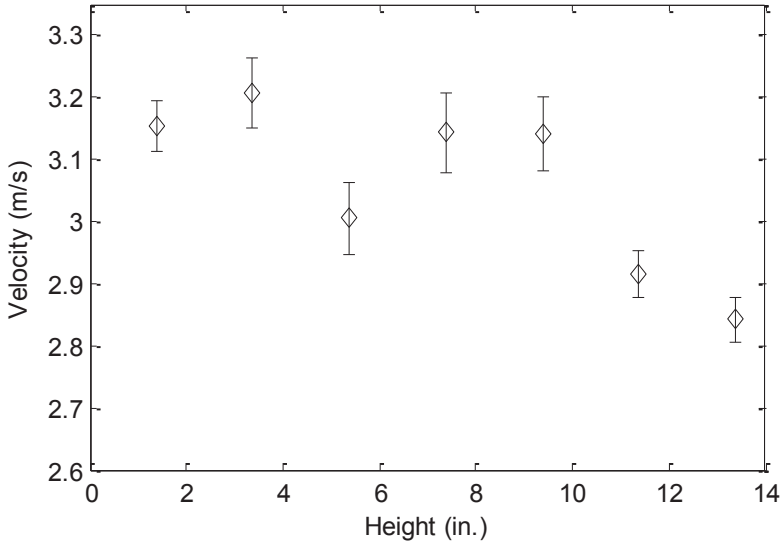

Figure B-4. Configuration 7, Motor 75%

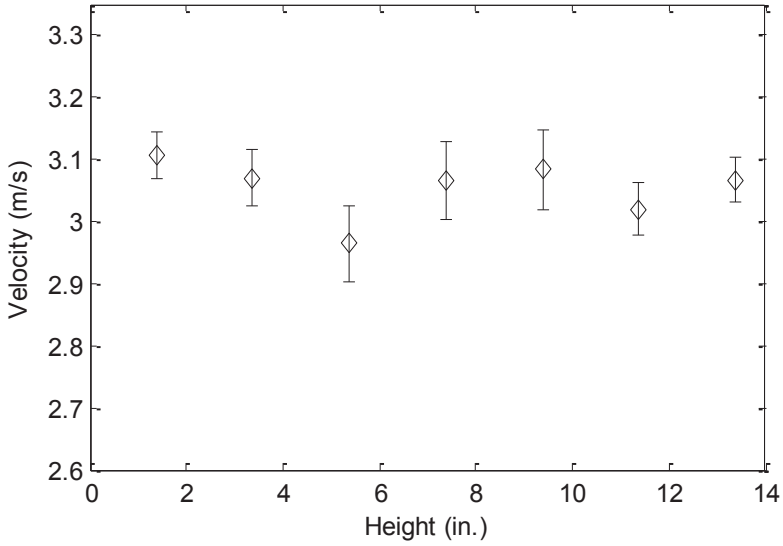

Figure B-5. Configuration 8, Motor 75%

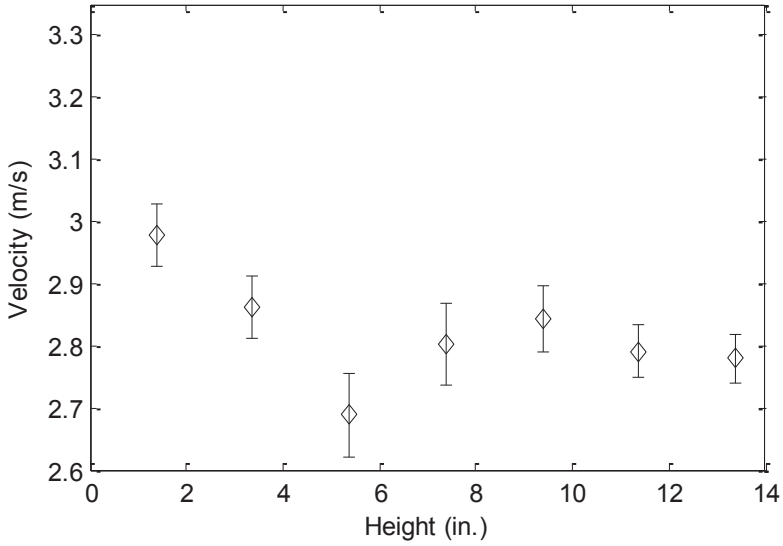

Figure B-6. Configuration 9, Motor 75%

Table B-3. Motor Speed Setting 100%

Configuration 7							
	Pos7	Pos6	Pos5	Pos4	Pos3	Pos2	Pos1
Temp (F)	75.3	75.2	75.3	75.2	75.1	75.0	75.0
P (Pa)	100340	100319	100323	100327	100345	100345	100351
Vel (m/s)	3.379	3.402	3.671	3.659	3.502	3.753	3.709
St Dev.	0.0158	0.0151	0.0273	0.0277	0.0272	0.0228	0.0129
V Uncert	1.22	1.16	1.93	1.97	2.02	1.58	0.90
Configuration 8							
	Pos7	Pos6	Pos5	Pos4	Pos3	Pos2	Pos1
Temp (F)	75.1	75.2	75.2	75.4	75.5	75.6	75.5
P (Pa)	101054	101017	100977	100930	100912	100888	100865
Vel (m/s)	3.577	3.554	3.621	3.590	3.488	3.619	3.686
St Dev.	0.0128	0.0185	0.0190	0.0259	0.0259	0.0206	0.0182
V Uncert	0.93	1.35	1.37	1.87	1.93	1.48	1.29
Configuration 9							
	Pos7	Pos6	Pos5	Pos4	Pos3	Pos2	Pos1
Temp (F)	72.7	72.3	71.6	75.7	75.6	75.6	75.7
P (Pa)	100474	100465	100444	100818	100831	100848	100851
Vel (m/s)	3.265	3.274	3.353	3.289	3.185	3.366	3.485
St Dev.	0.0139	0.0149	0.0235	0.0264	0.0311	0.0230	0.0219
V Uncert	1.11	1.18	1.82	2.09	2.54	1.77	1.64

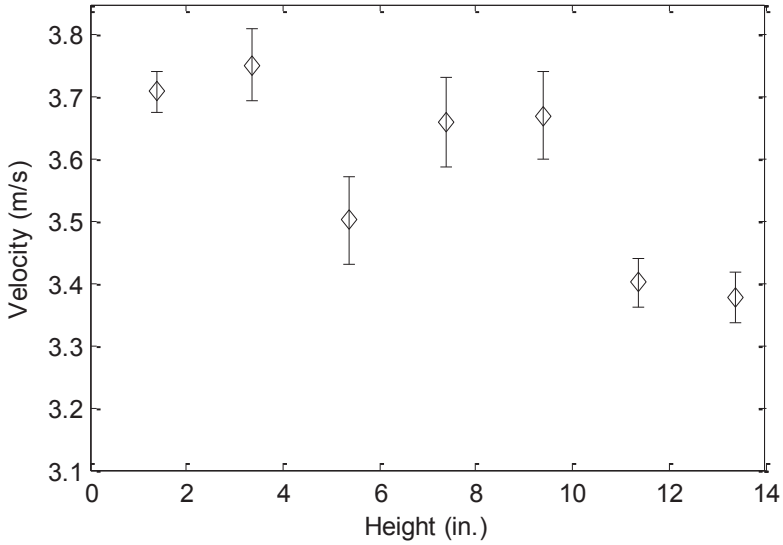

Figure B-7. Configuration 7, Motor 100%

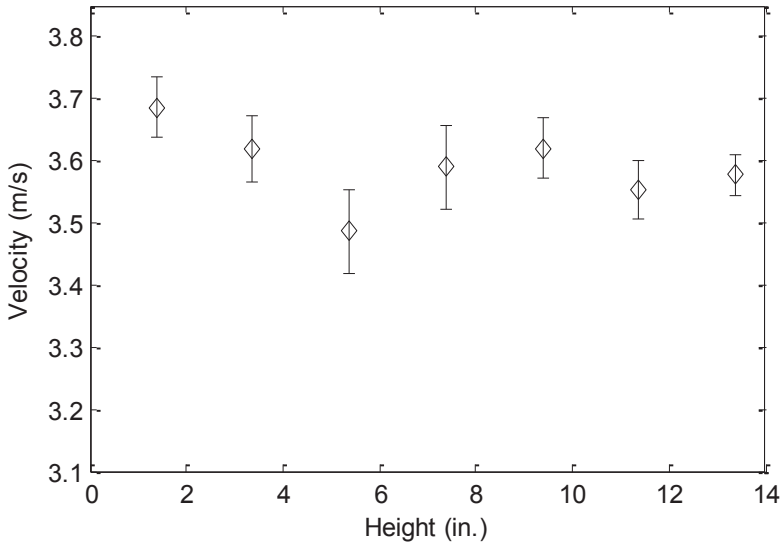

Figure B-8. Configuration 8, Motor 100%

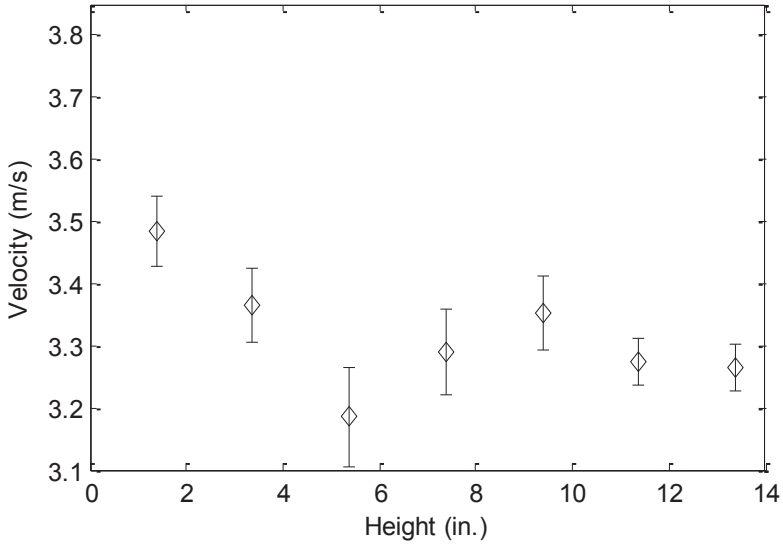

Figure B-9. Configuration 9, Motor 100%

APPENDIX C: TIME AVERAGED TEST CASE PITOT TUBE VELOCITIES

Table C-1 lists the time averaged pitot tube velocities that were measured during the test matrix. Before images were taken at each new axial location, these velocities were taken. These velocities are two minute averages. Gray highlighted represent when the motor setting was adjusted to bring measured velocities back to desired. The final column gives the maximum difference from the average. The percent range of variability in the measured velocities for each run is less than twice this value. The percent uncertainty associated with each velocity measurement is less than 2%. As can be seen, this variability is less than the uncertainty associated with the pitot tube velocity measurements, therefore within the bands of uncertainty, the velocity was constant during each test run.

Table C-1. Time Averaged Pitot Tube Velocities

	Axial Location							Max % difference from average
Run	-2 in	0 in	4 in	8 in	12 in	16 in	20 in	
A	2.499	2.503	2.504	2.502	2.497	2.499	2.498	0.14
B	3.298	3.289	3.287	3.296	3.296	3.293	3.287	0.17
C	2.409	2.399	2.407	2.402	2.400	2.398	2.398	0.28
D	1.304	1.300	1.302	1.309	1.308	1.301	1.299	0.43
E	2.505	2.501	2.499	2.503	2.501	2.503	2.500	0.13
F	3.306		3.301	3.308	3.300	3.300	3.295	0.20
G	2.394	2.400	2.404	2.406	2.403	2.405	2.402	0.34
H	1.301	1.297	1.300	1.303	1.306	1.297	1.300	0.42
I	2.052	2.502	2.504	2.502	2.500	2.509	2.502	0.23
J	3.207	3.208	3.198	3.217	3.199	3.186	3.181	0.56
K	2.500	2.501	2.501	2.505	2.495	2.501	2.499	0.19
L	1.307	1.309	1.308	1.308	1.308	1.306	1.305	0.16

APPENDIX D: PIV EQUIPMENT UNCERTAINTY ANALYSIS

Table D-1 gives the values and uncertainties for the individual components that contribute to equipment uncertainty.

Table D-1. Equipment Uncertainty Parameters

Parameter	Description	Value	Uncertainty
l	Physical calibration length	6.33333 mm	0.05 mm
L1	Image plane calibration length	302 px	1 px
L2	Image plane calibration length variability	302 px	5.2 px
λ	Separation length of target to camera lens	16.6 cm	2.0 mm
Δt	Timer box resolution	100 μsec	12.5 nsec

In the image plane the calibration length is rounded to the nearest pixel location, therefore there is a band of uncertainty of 1 pixel associated with the calibration length accounted for by L1. L2 is given as the standard deviation of the calibration length in pixels. The Kline-McClintock equation for uncertainty in velocity is given as:

$$\varepsilon_u = \sqrt{\left(\frac{\partial u}{\partial l}\varepsilon_l\right)^2 + \left(\frac{\partial u}{\partial L}\varepsilon_{L1}\right)^2 + \left(\frac{\partial u}{\partial L}\varepsilon_{L2}\right)^2 + \left(\frac{\partial u}{\partial \lambda}\varepsilon_\lambda\right)^2 + \left(\frac{\partial u}{\partial \Delta t}\varepsilon_{\Delta t}\right)^2} \tag{56}$$

$$\varepsilon_u = \sqrt{u^2\left[\left(\frac{1}{L}\varepsilon_l\right)^2 + \left(\frac{-l}{L^2}\varepsilon_{L1}\right)^2 + \left(\frac{-l}{L^2}\varepsilon_{L2}\right)^2 + \left(\frac{l}{\lambda L}\varepsilon_\lambda\right)^2\right] + \left(\frac{-u\cdot l}{\Delta t\cdot L}\right)^2\cdot\varepsilon_{\Delta t}^2} \tag{57}$$

This gives an uncertainty in units of m^2/(sec-px) which can be converted to m/s with use of the scaling factor. The resulting uncertainty in velocity due to equipment is 1.97%.

APPENDIX E: CONVERGENCE OF PIV MEASUREMENTS

Statistical and turbulent quantities were averaged from the 2308 realizations in each dataset. Various datasets were tested for convergence by averaging sequentially for each additional realization to guarantee that the specific quantity does converge on a value, and the number of realizations required for this convergence. After 1500 iterations, turbulence and mean quantities are converged to within 1%.

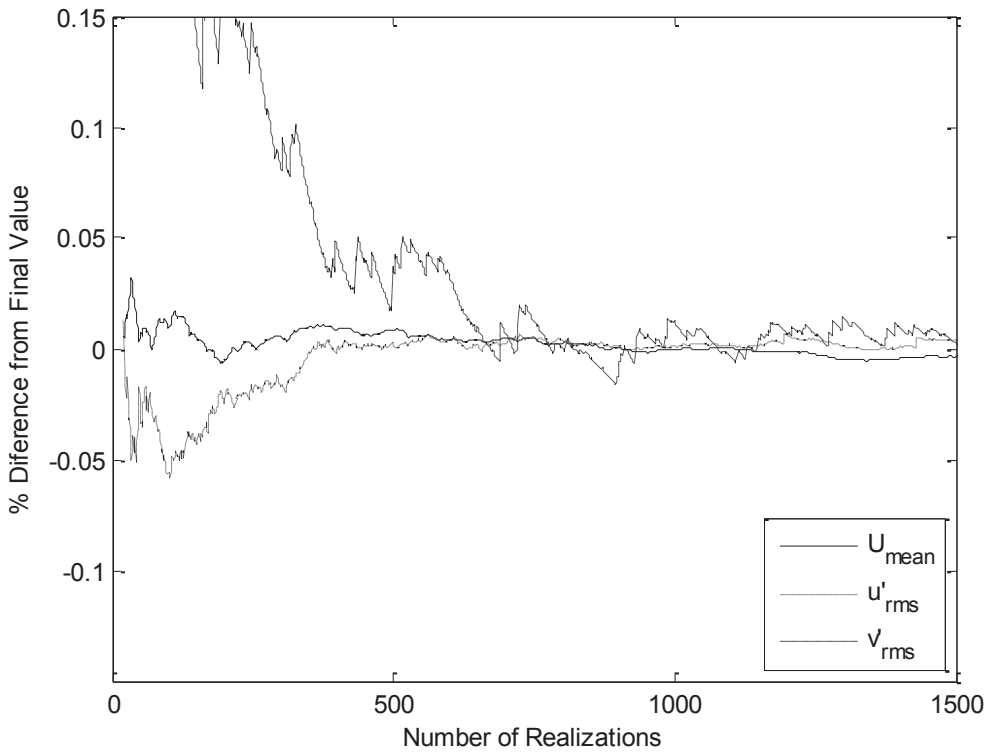

Figure E-1. Realizations Required for Convergence of Averaged Quantities

APPENDIX F: NON-SUBSTITUTED FRACTION OF TIME AVERAGED VECTOR PLOTS

The time averaged boundary layer profiles presented in the results section were obtained by time averaging only the non-substituted vectors in the instantaneous plot realizations. The time averaged values were then extracted for the interrogation areas in a line normal from the test section wall to create the boundary layer profile. Each dataset contained 2308 instantaneous realizations, with the number of non-substituted vectors for each interrogation area being a fraction of this. The non-substituted fraction of the interrogation areas that made up the boundary layer plots was sampled for approximately 1/3rd of the datasets. The average non-substituted fraction for most datasets was greater than 0.90. If the average non-substituted fraction was less than 0.80, all the datasets for that axial position were retaken. Two examples are shown below.

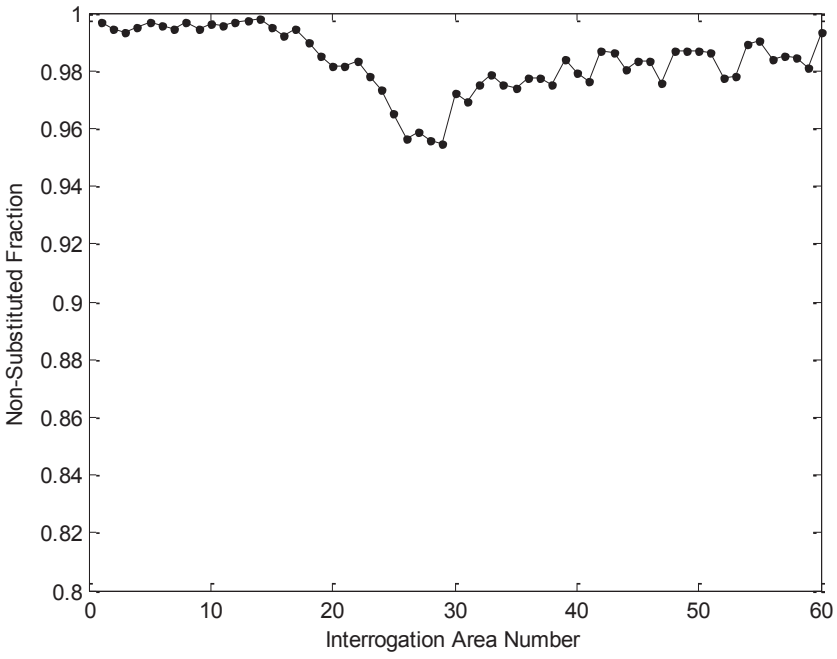

Figure F-1. Example Non-Substituted Fraction Plot

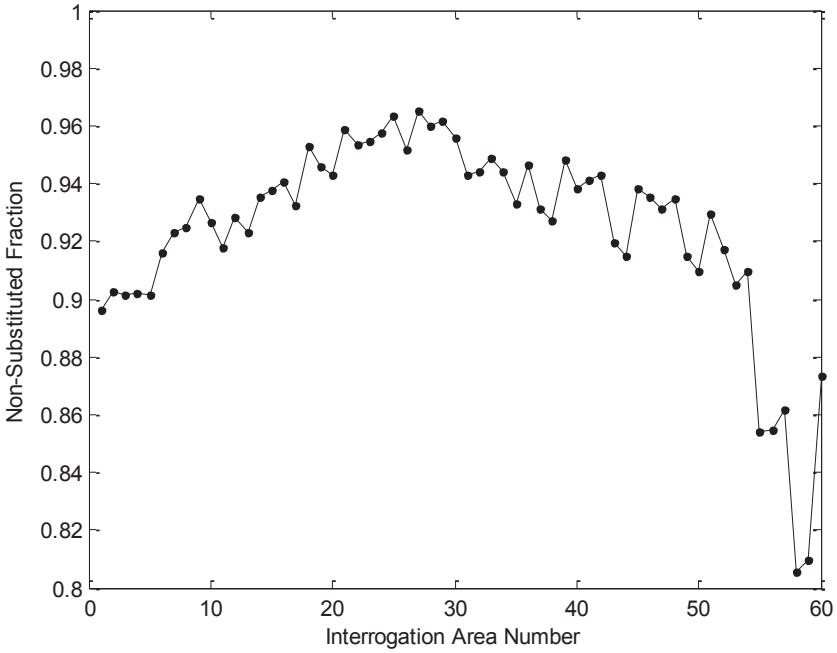

Figure F-2. Example Non-Substituted Fraction Plot

APPENDIX G. BOUNDARY LAYER VELOCITY PROFILES

All mean velocity plots for all axial positions of all test cases are contained here in the appendix. Each page represents one test case and contains six small plots for each axial location. Plots normalized with outer variables are presented first, and then those normalized with inner variables. Refer to Table 4-7 for numbering.

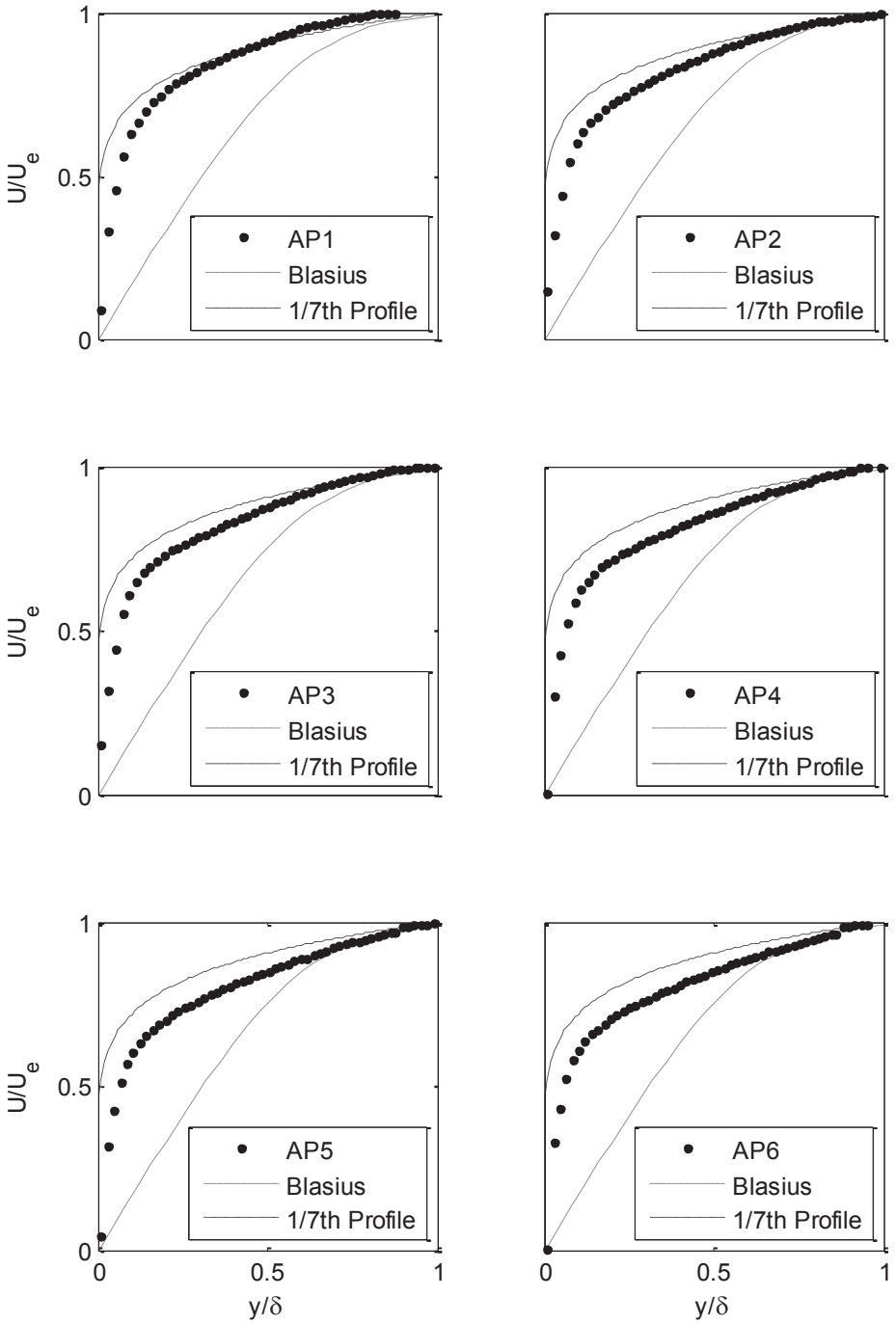

Figure G-1. Test Case A1 Mean Velocity Profiles in Outer Variables

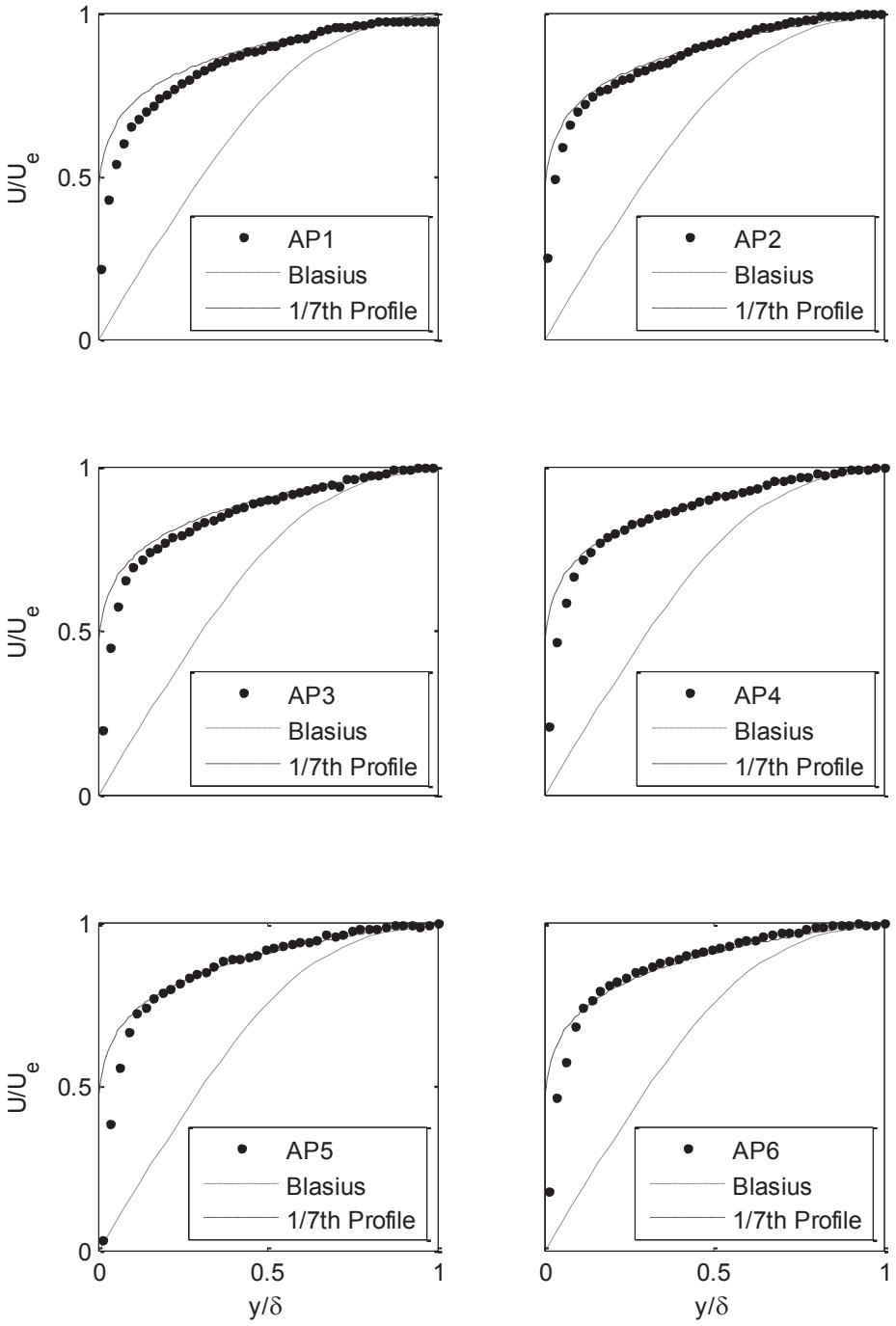

Figure G-2. Test Case A2 Mean Velocity Profiles in Outer Variables

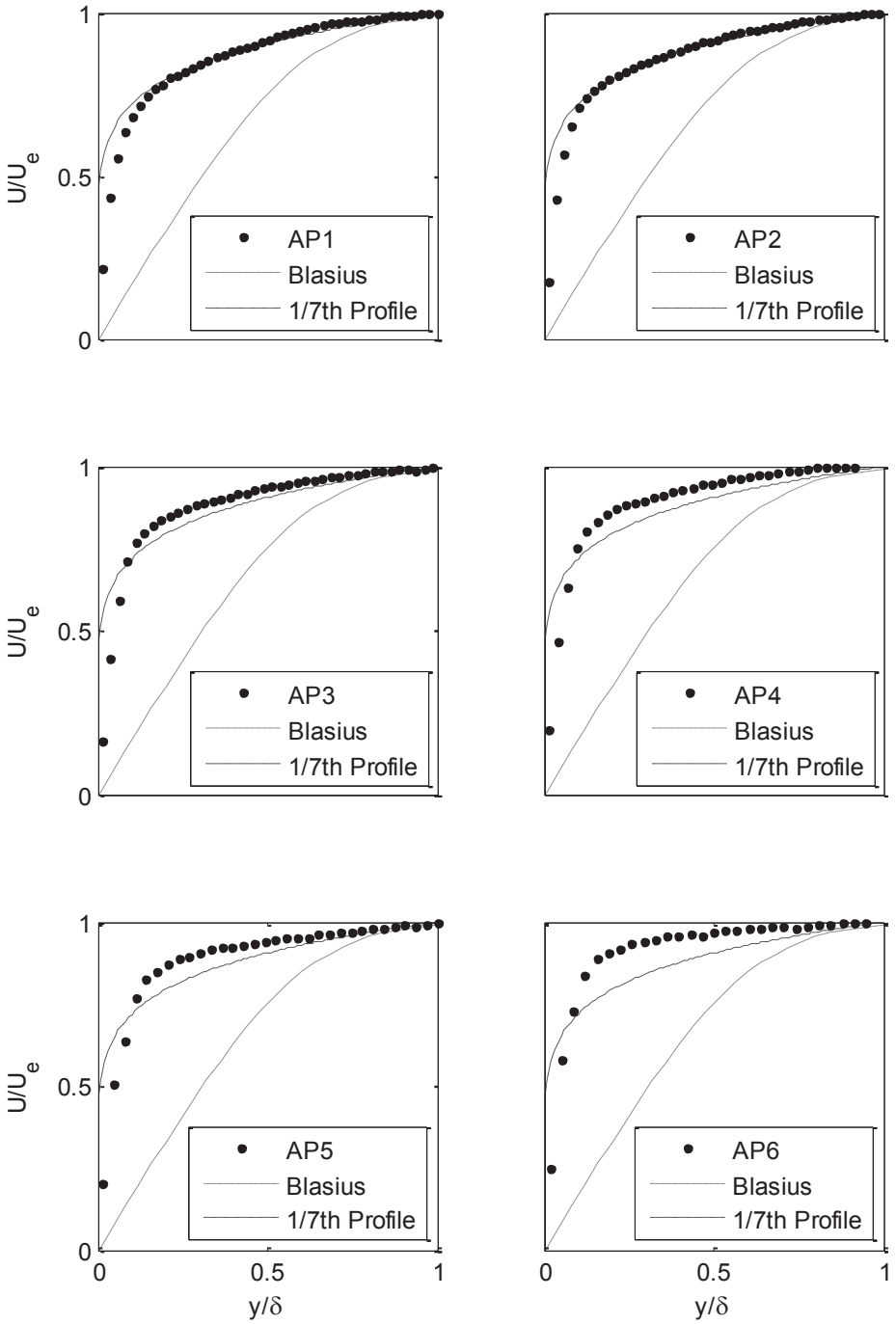

Figure G-3. Test Case A3 Mean Velocity Profiles in Outer Variables

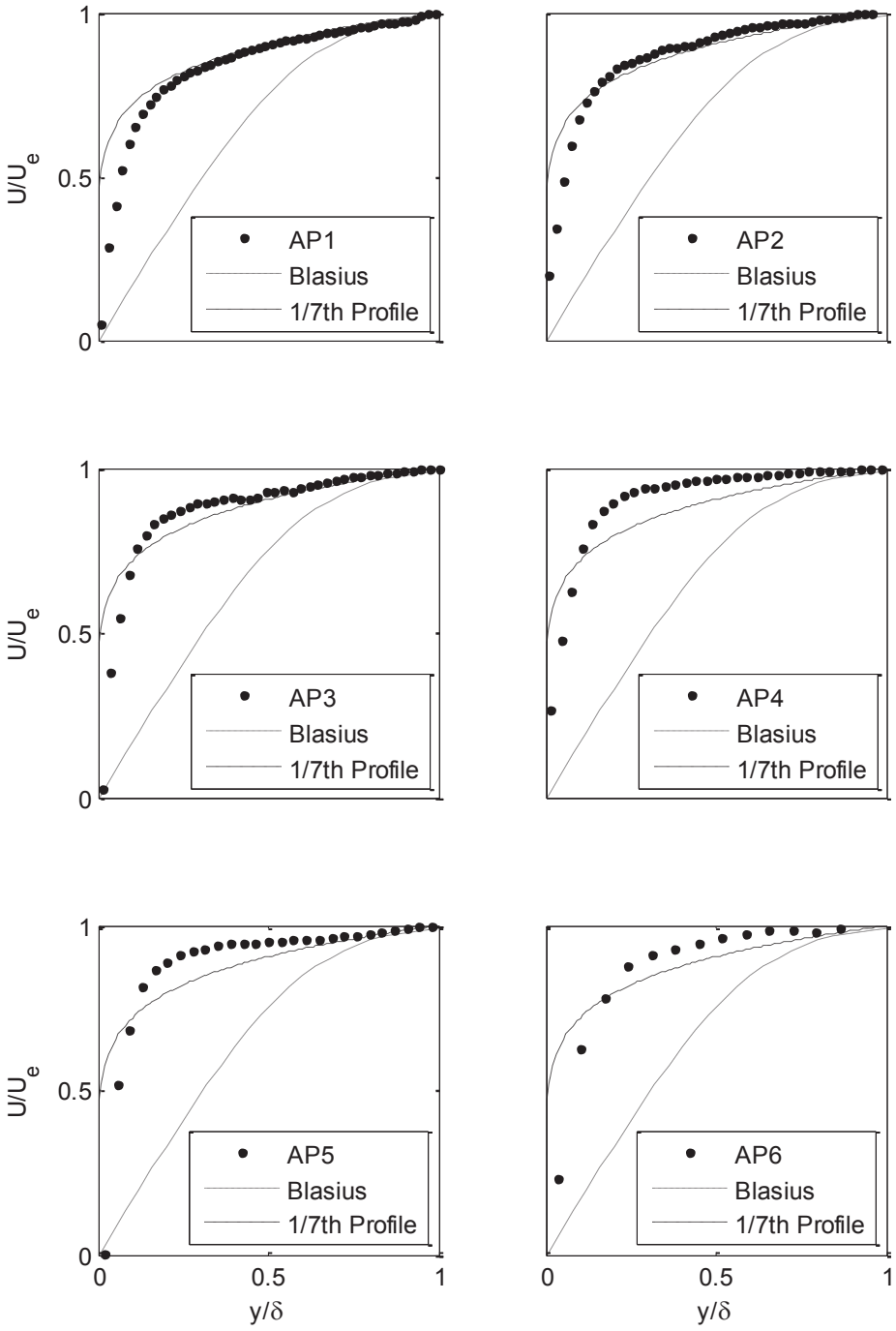

Figure G-4. Test Case A4 Mean Velocity Profiles in Outer Variables

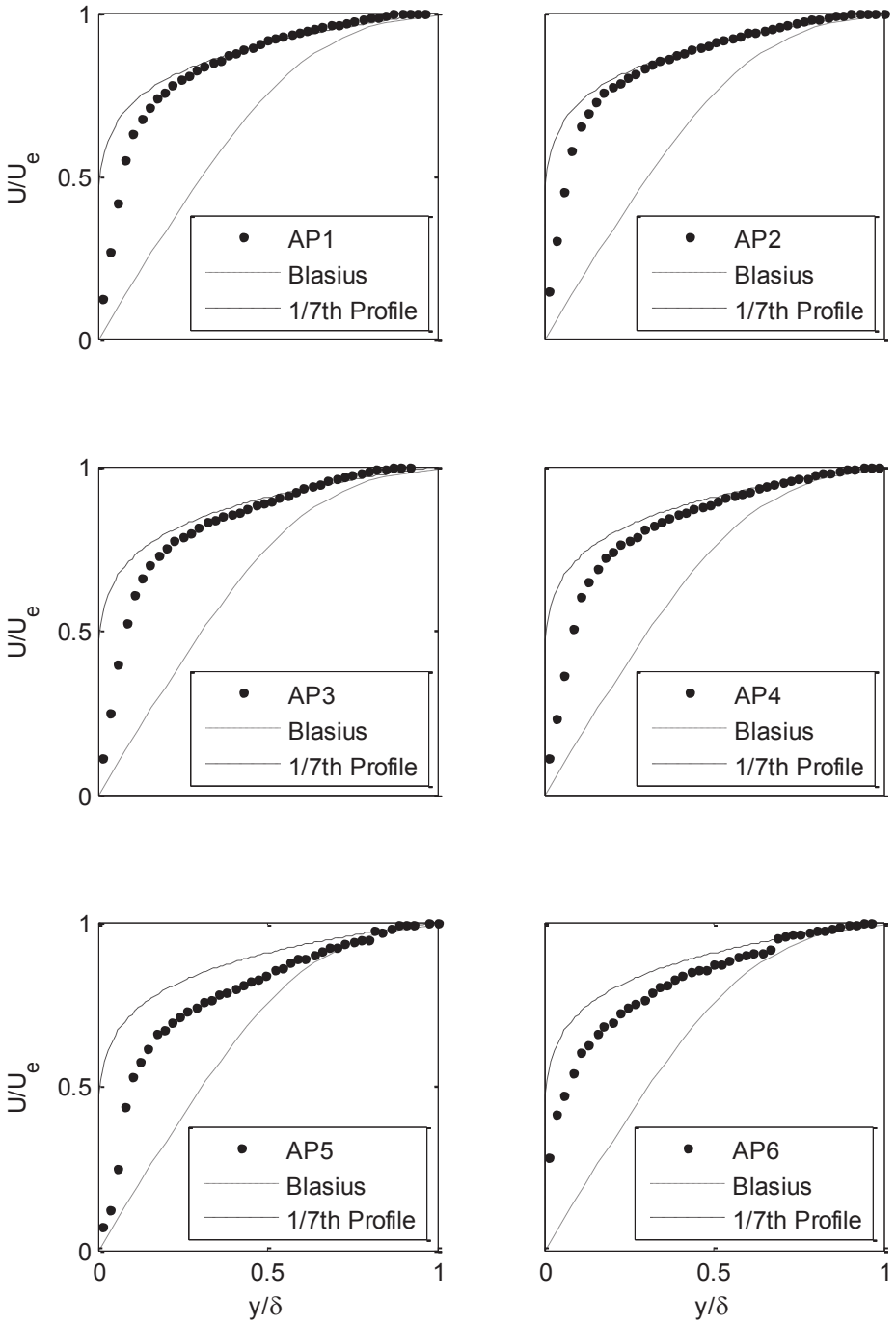

Figure G-5. Test Case B1 Mean Velocity Profiles in Outer Variables

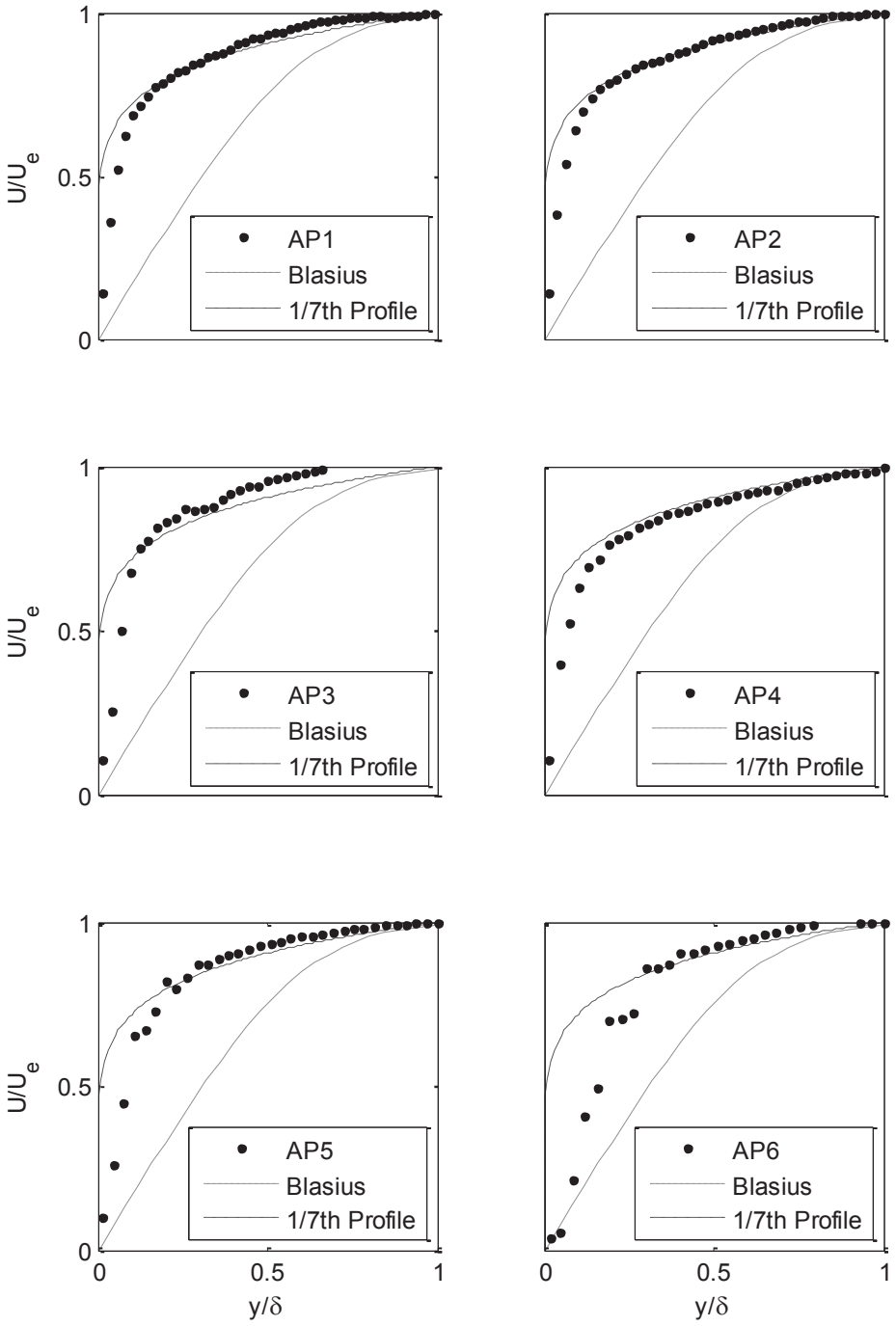

Figure G-6. Test Case B2 Mean Velocity Profiles in Outer Variables

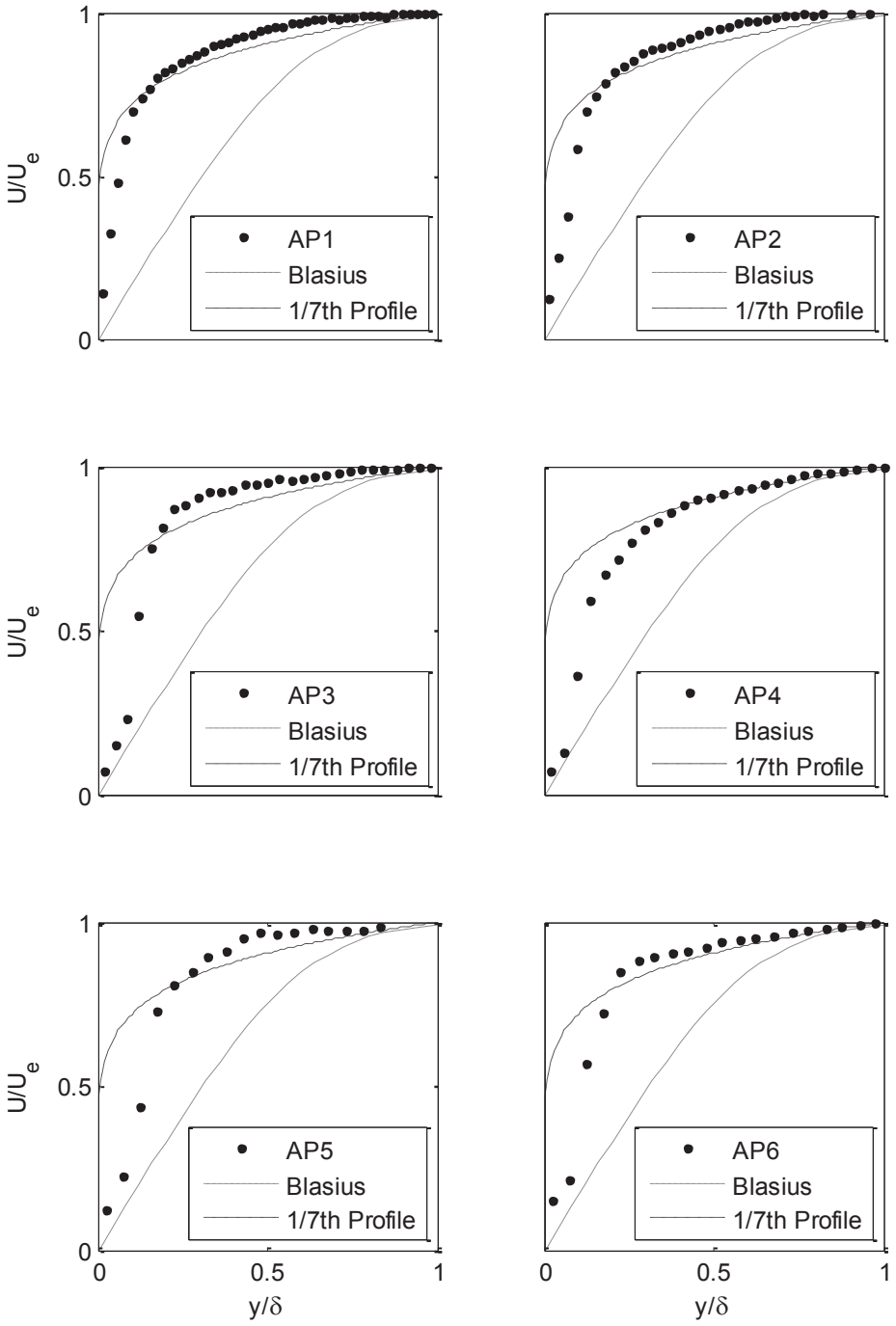

Figure G-7. Test Case B3 Mean Velocity Profiles in Outer Variables

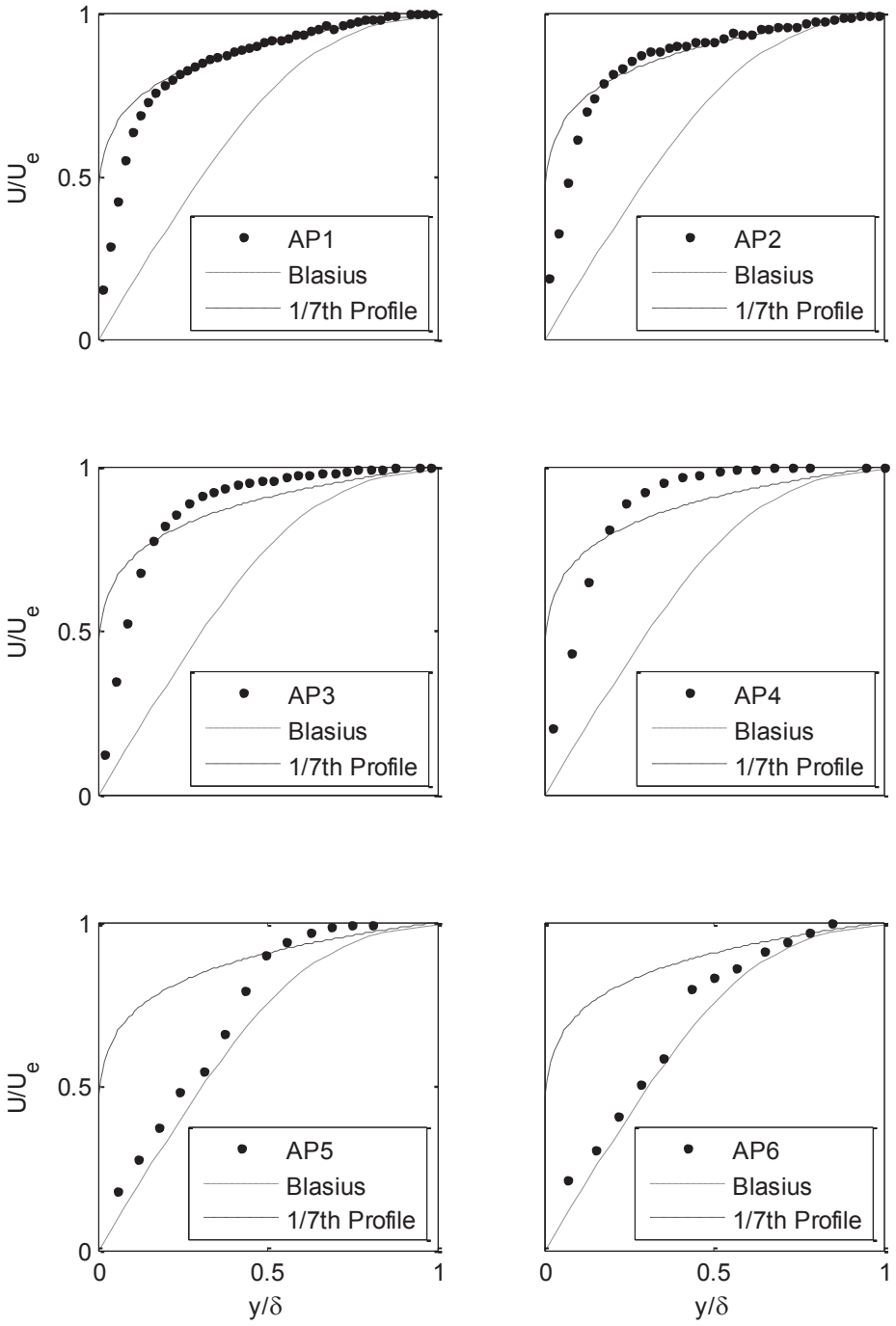

Figure G-8. Test Case B4 Mean Velocity Profiles in Outer Variables

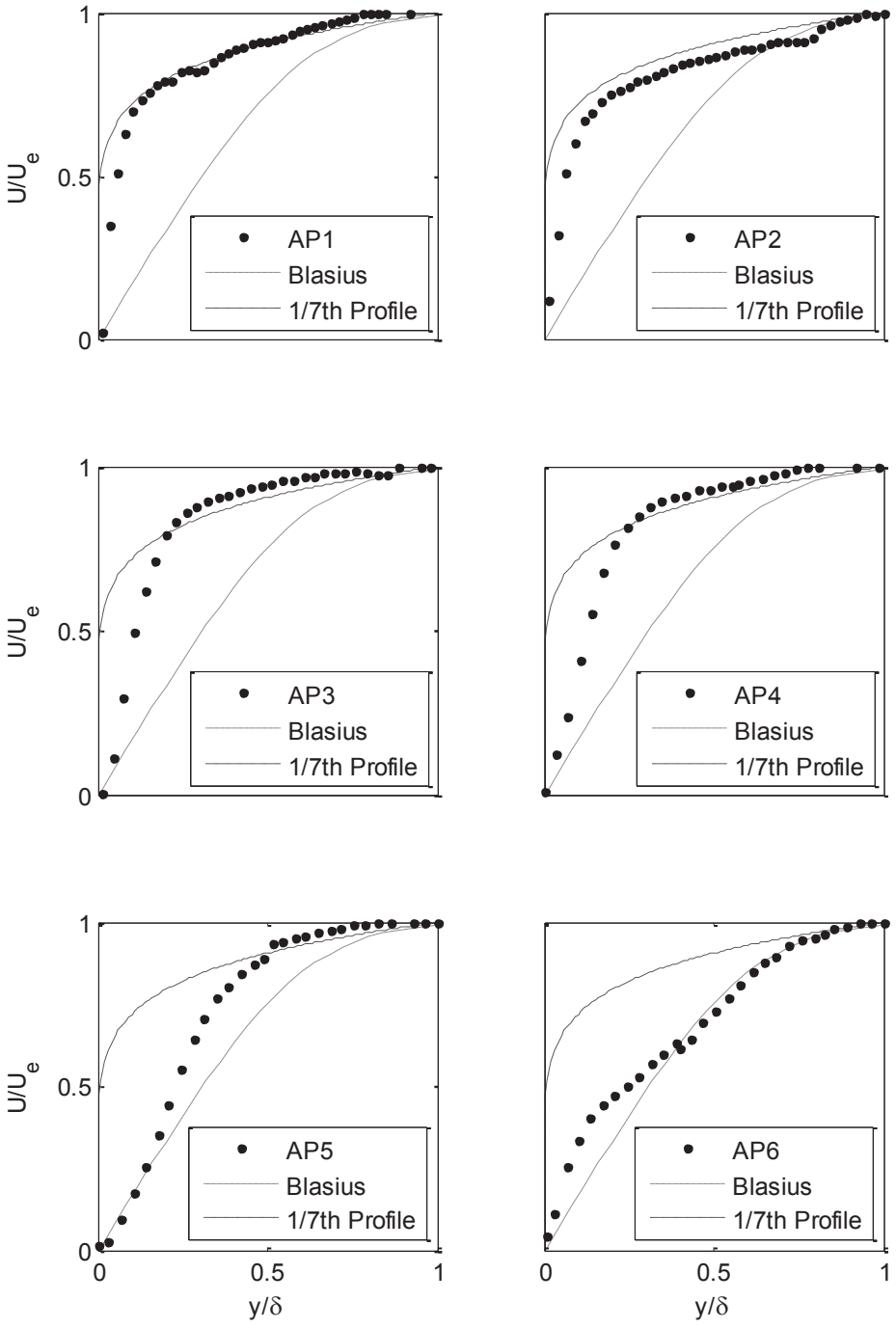

Figure G-9. Test Case C1 Mean Velocity Profiles in Outer Variables

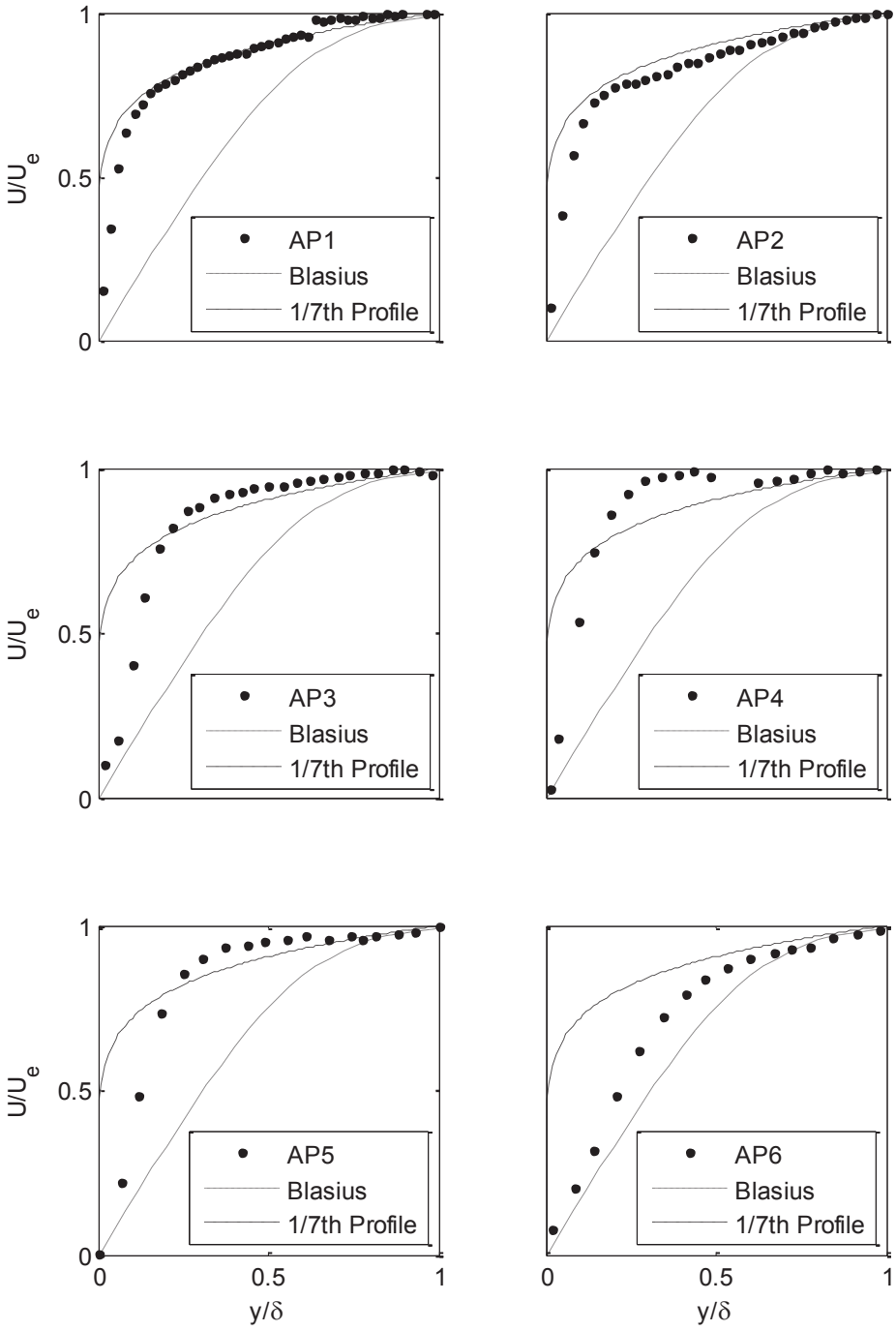

Figure G-10. Test Case C2 Mean Velocity Profiles in Outer Variables

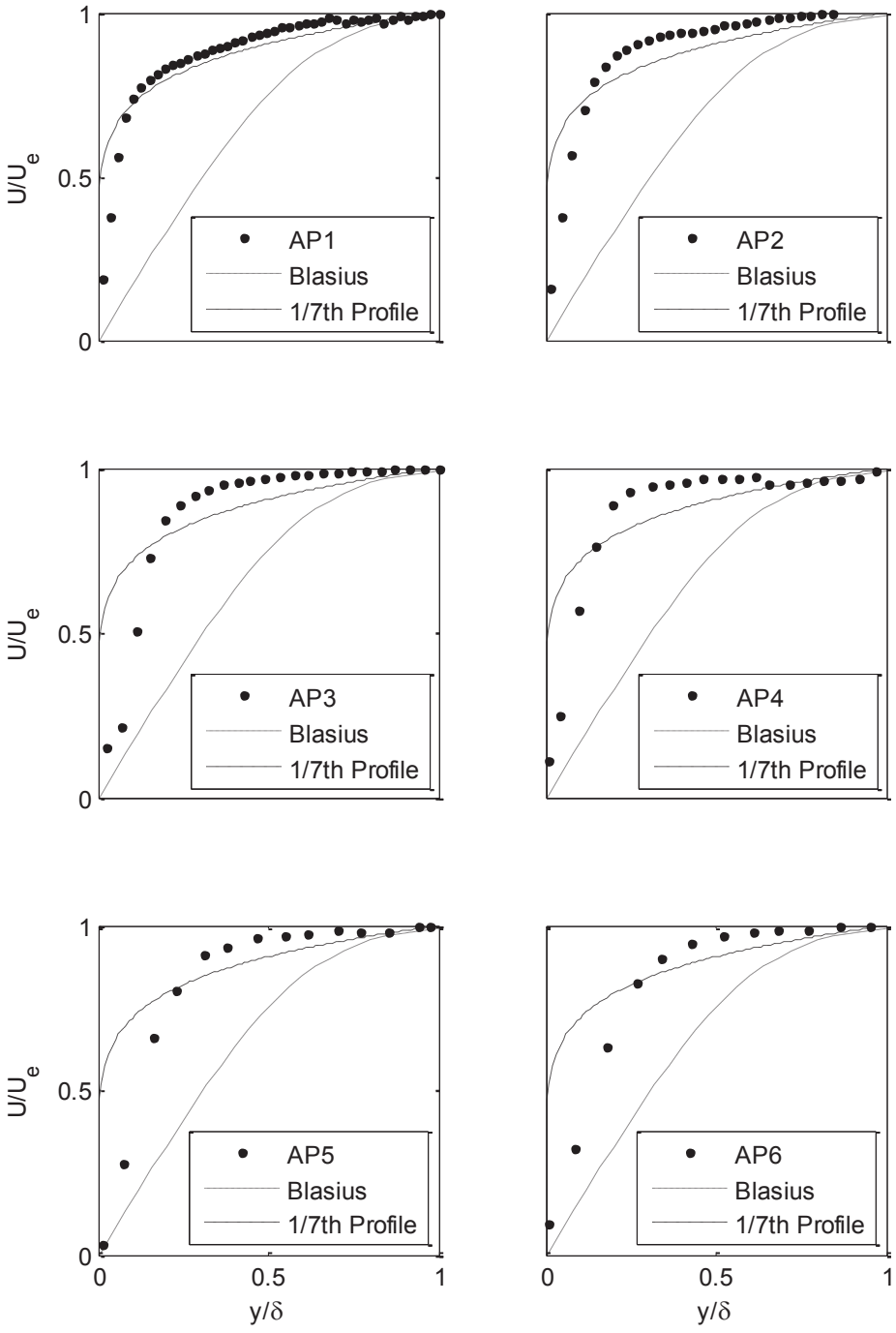

Figure G-11. Test Case C3 Mean Velocity Profiles in Outer Variables

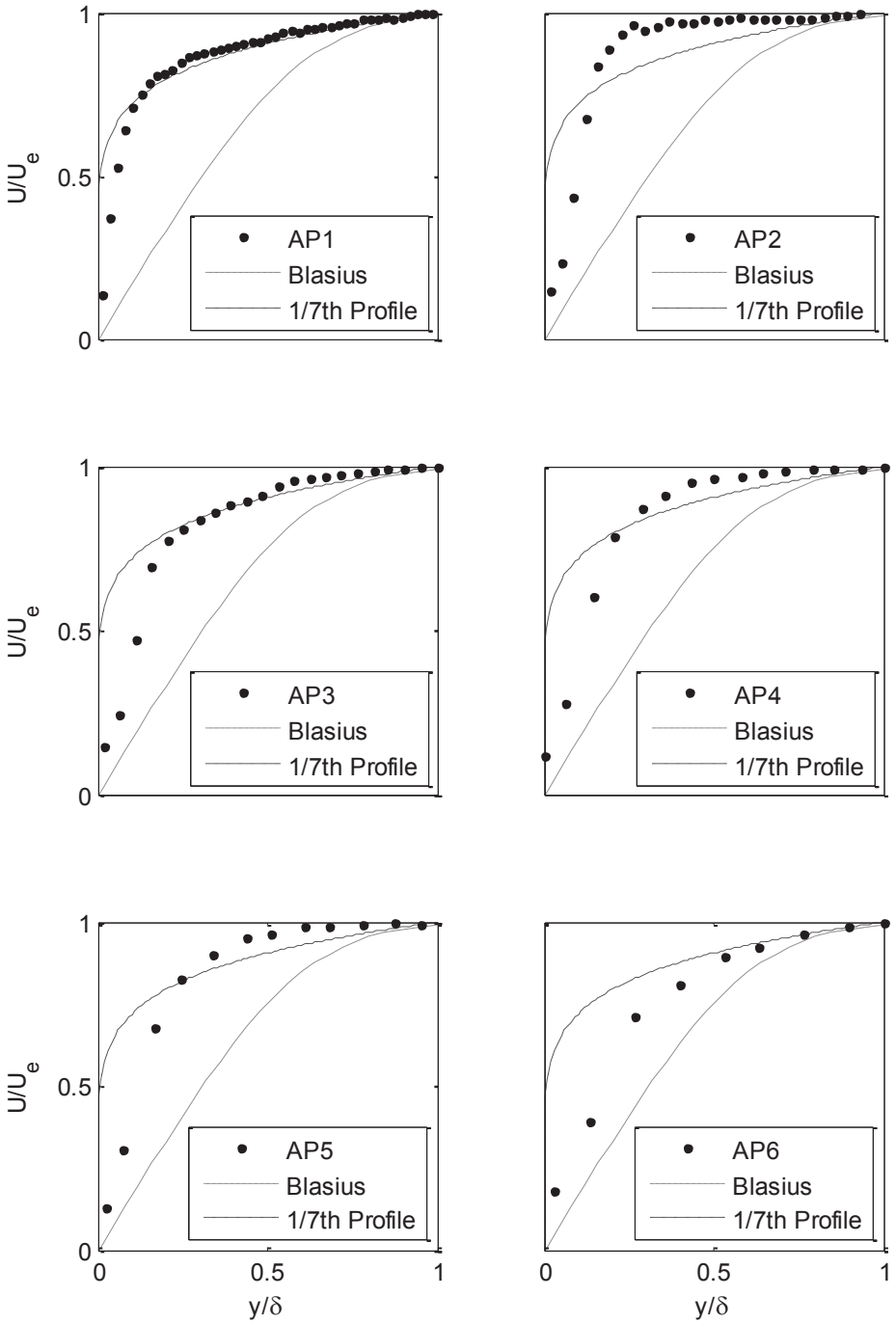

Figure G-12. Test Case C4 Mean Velocity Profiles in Outer Variables

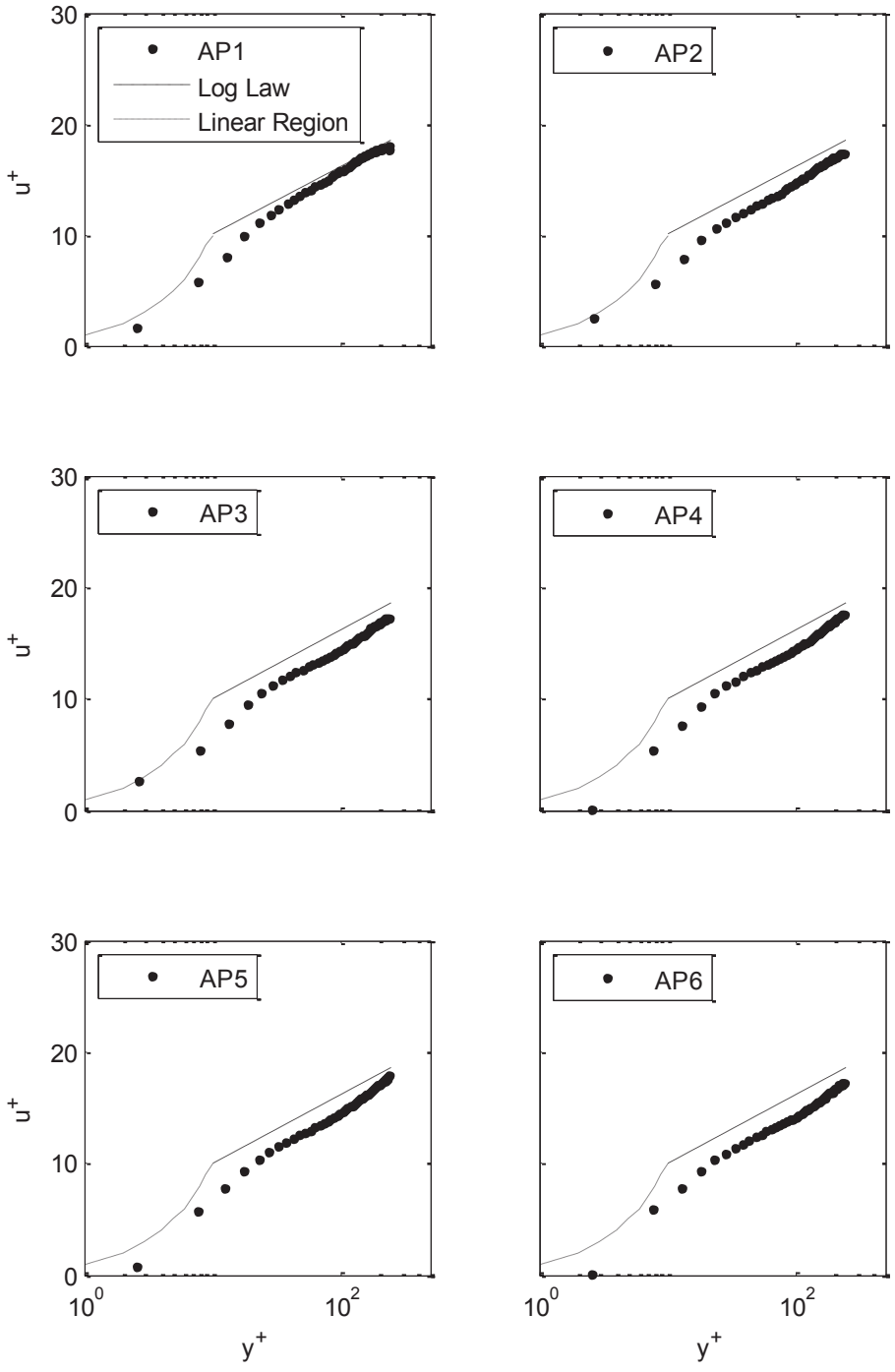

Figure G-13. Test Case A1 Mean Velocity Profiles in Inner Variables

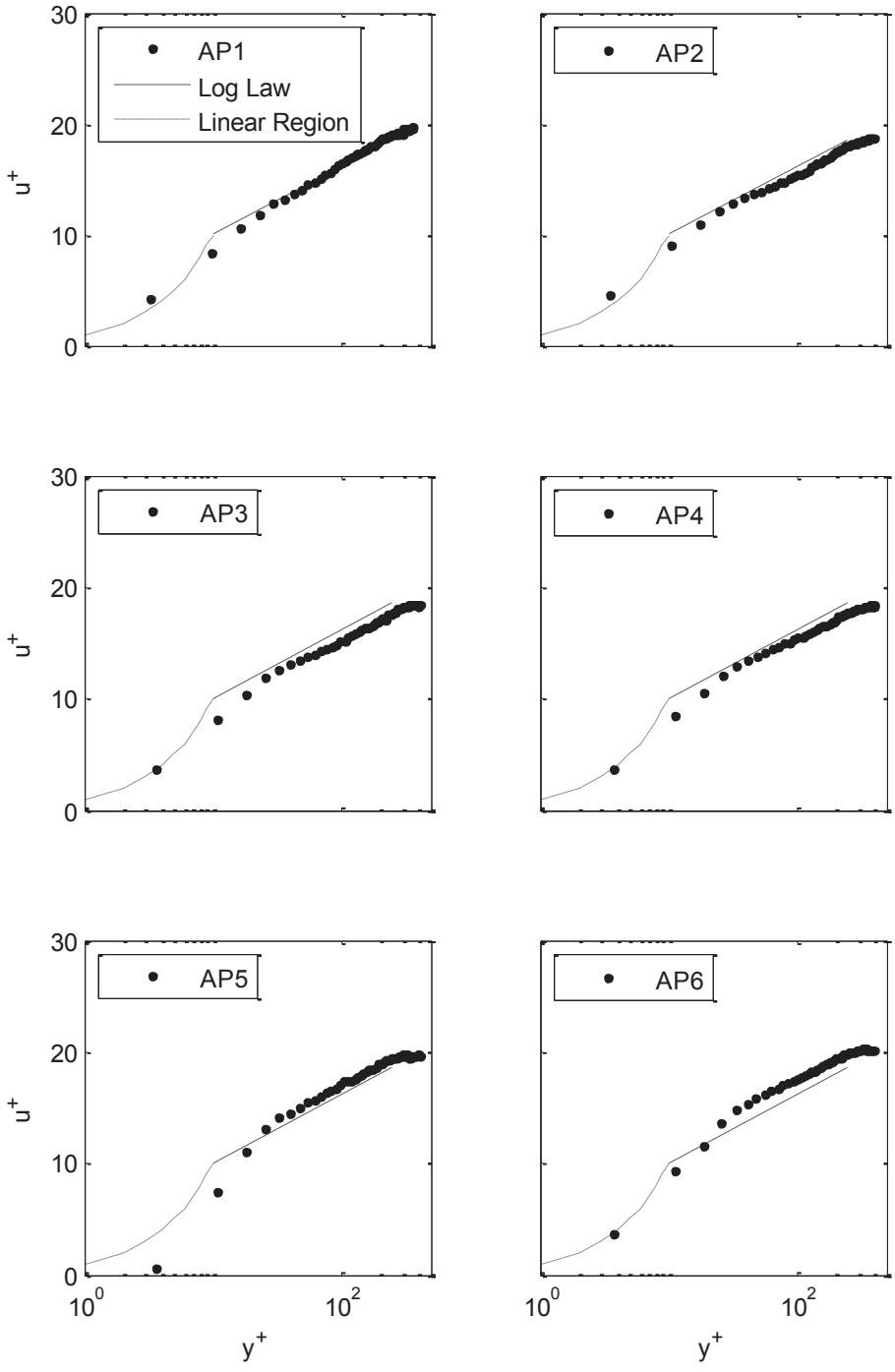

Figure G-14. Test Case A2 Mean Velocity Profiles in Inner Variables

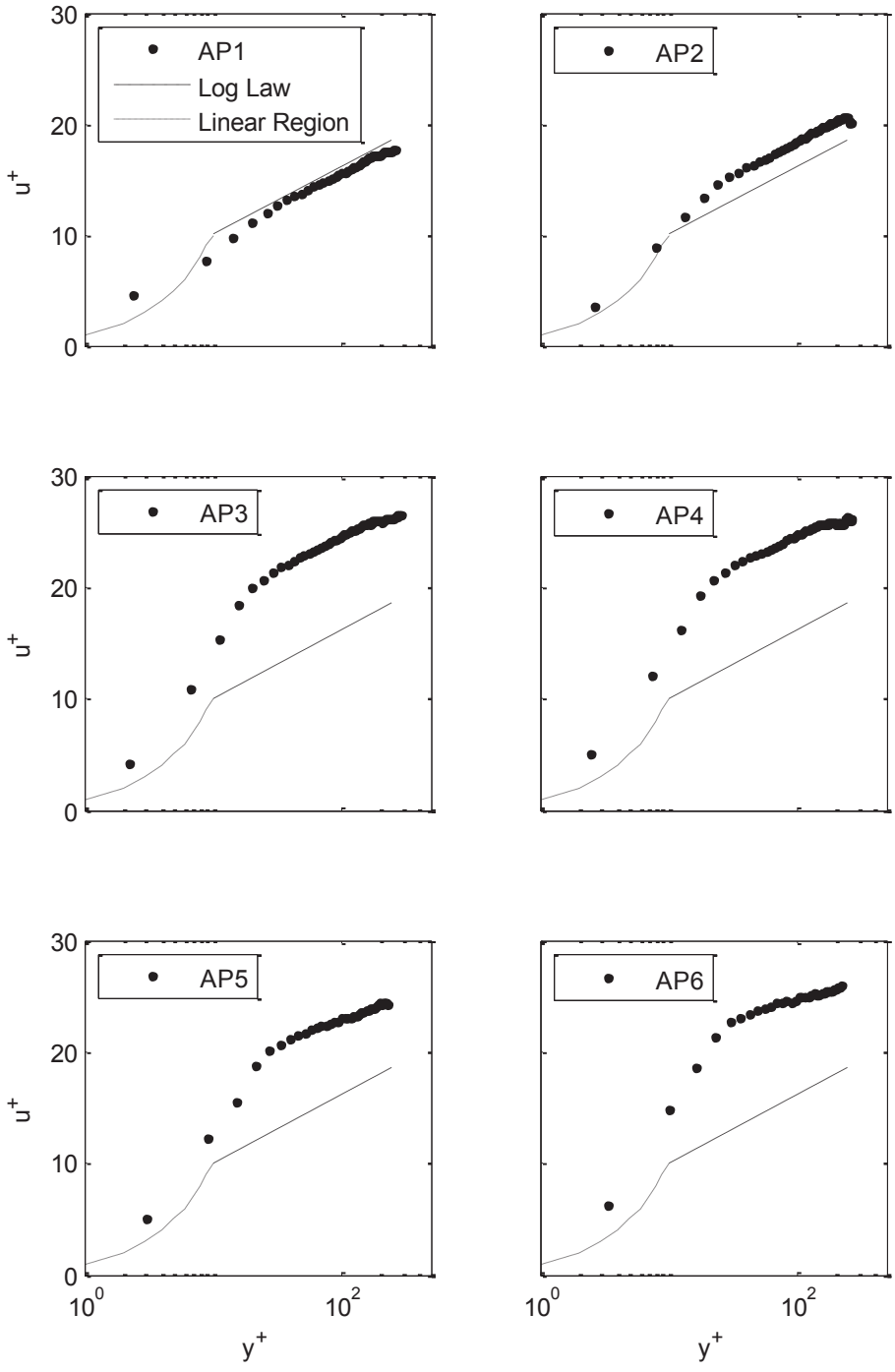

Figure G-15. Test Case A3 Mean Velocity Profiles in Inner Variables

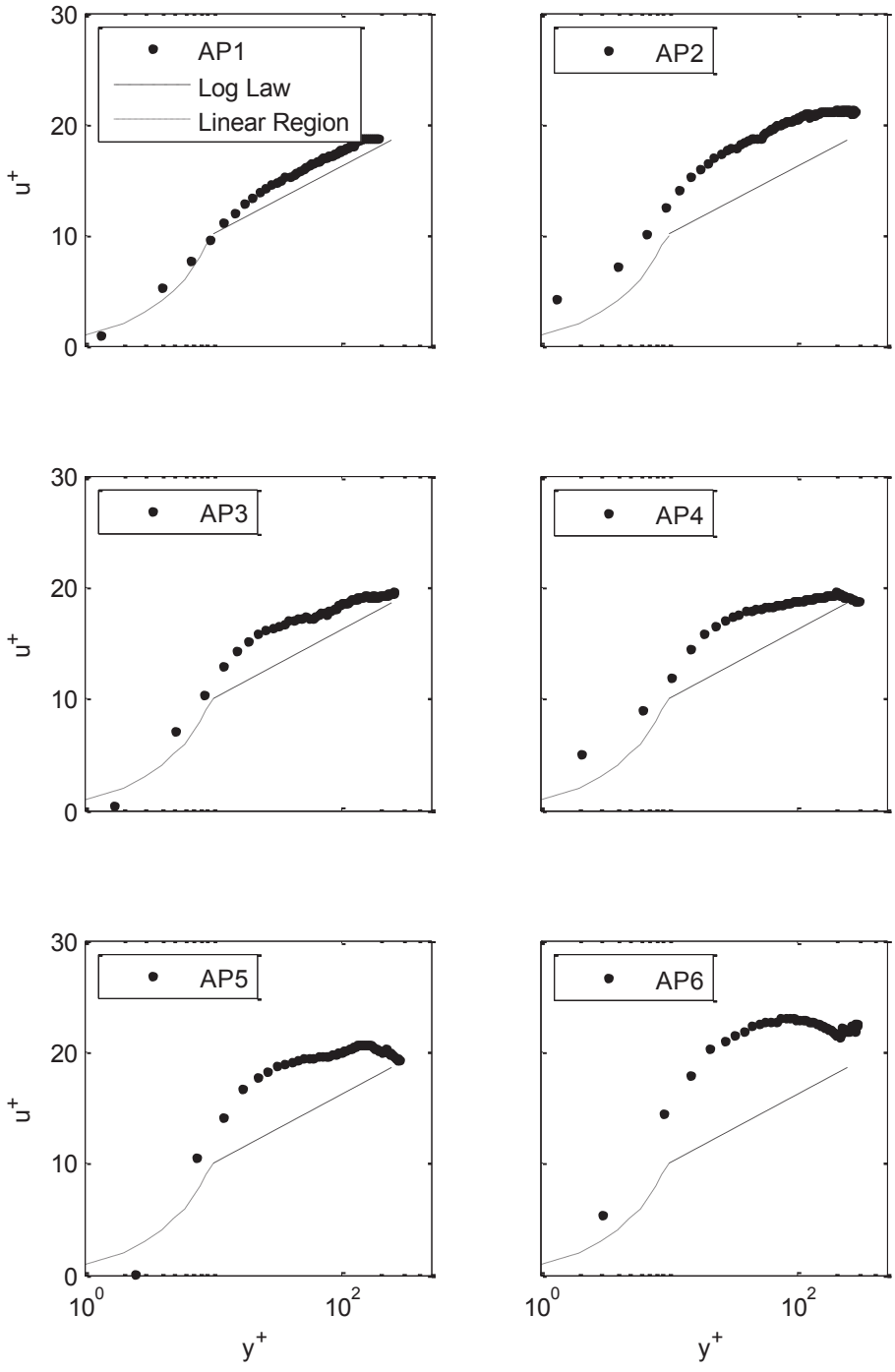

Figure G-16. Test Case A4 Mean Velocity Profiles in Inner Variables

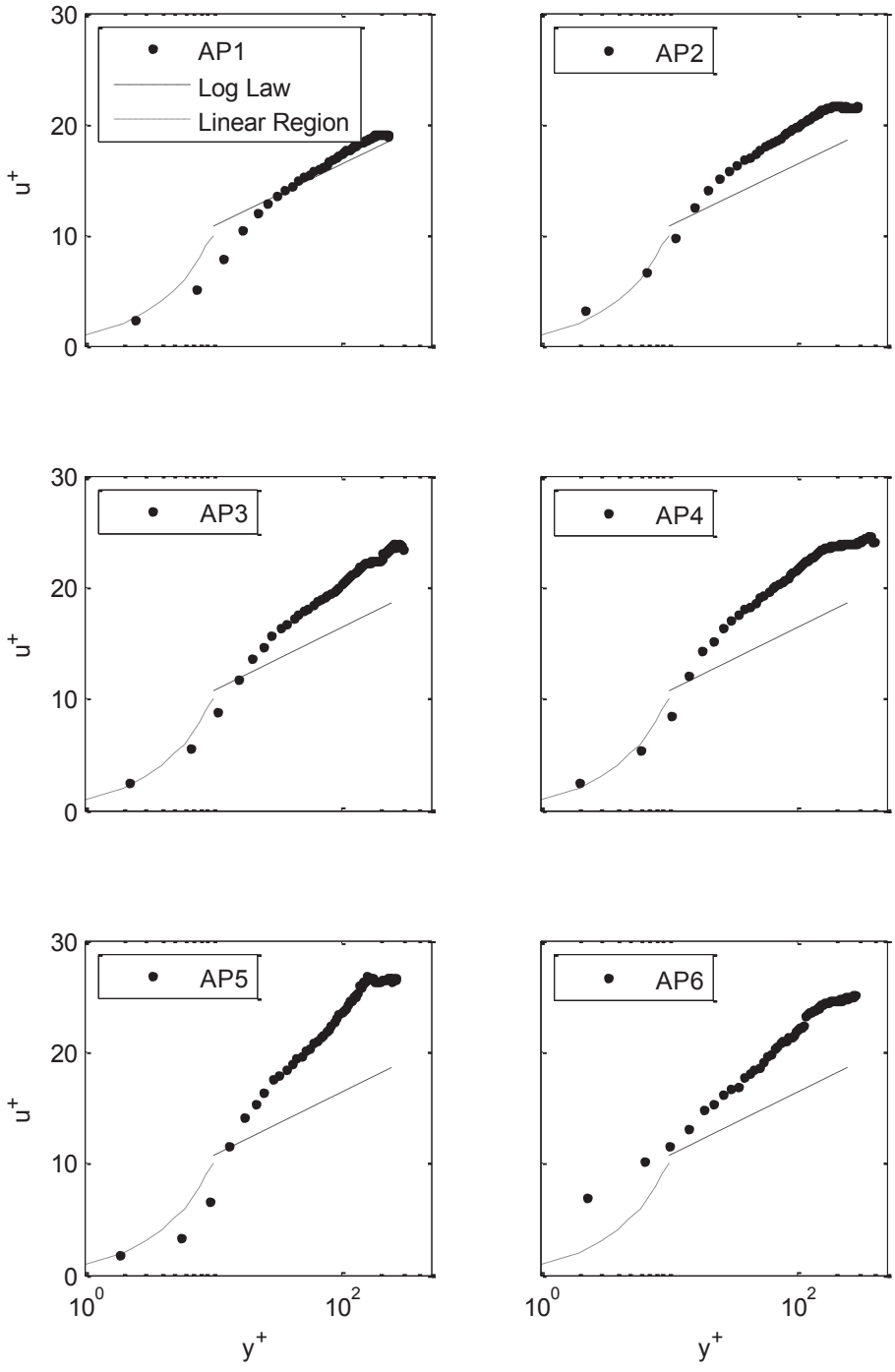

Figure G-17. Test Case B1 Mean Velocity Profiles in Inner Variables

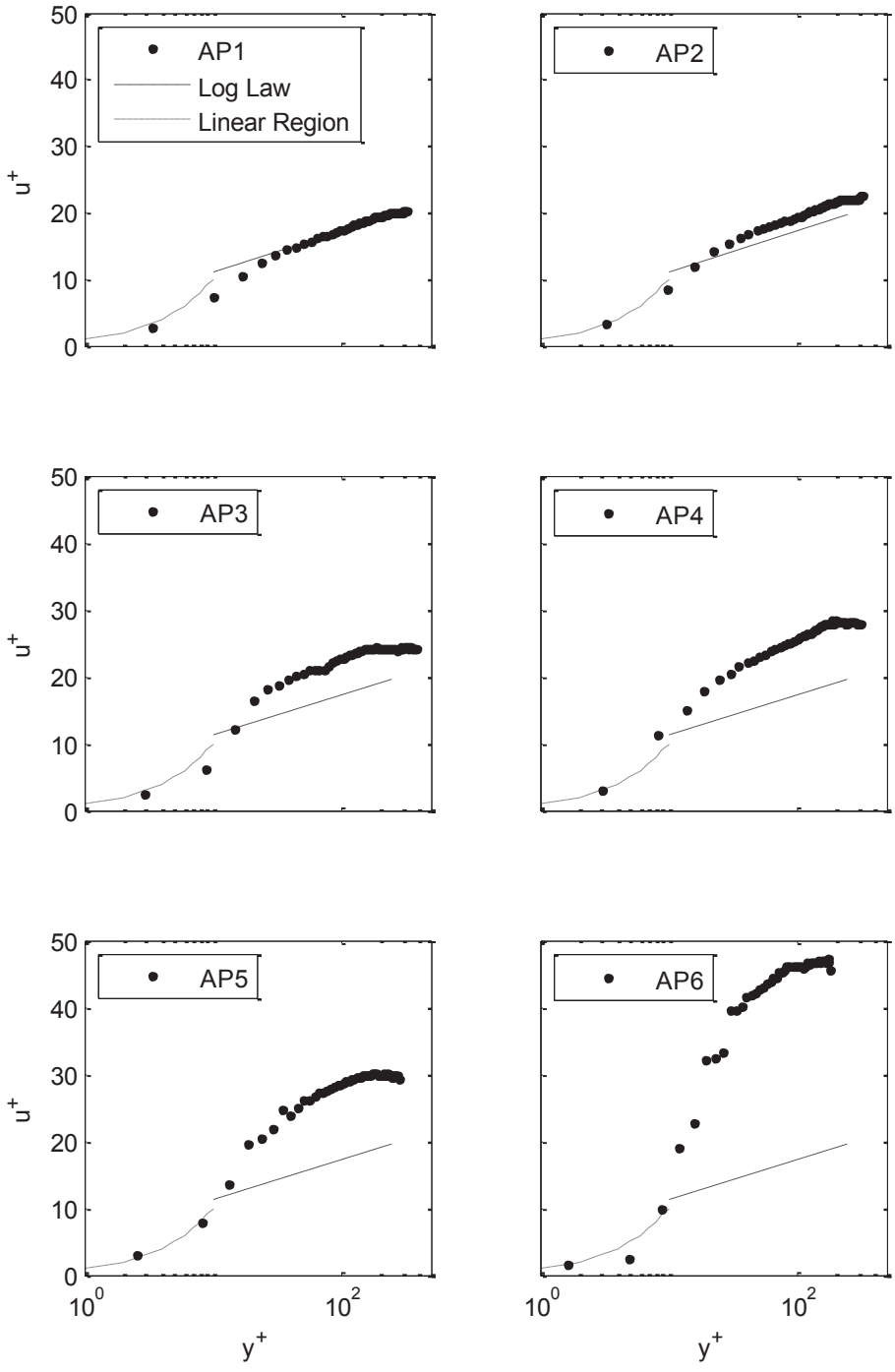

Figure G-18. Test Case B2 Mean Velocity Profiles in Inner Variables

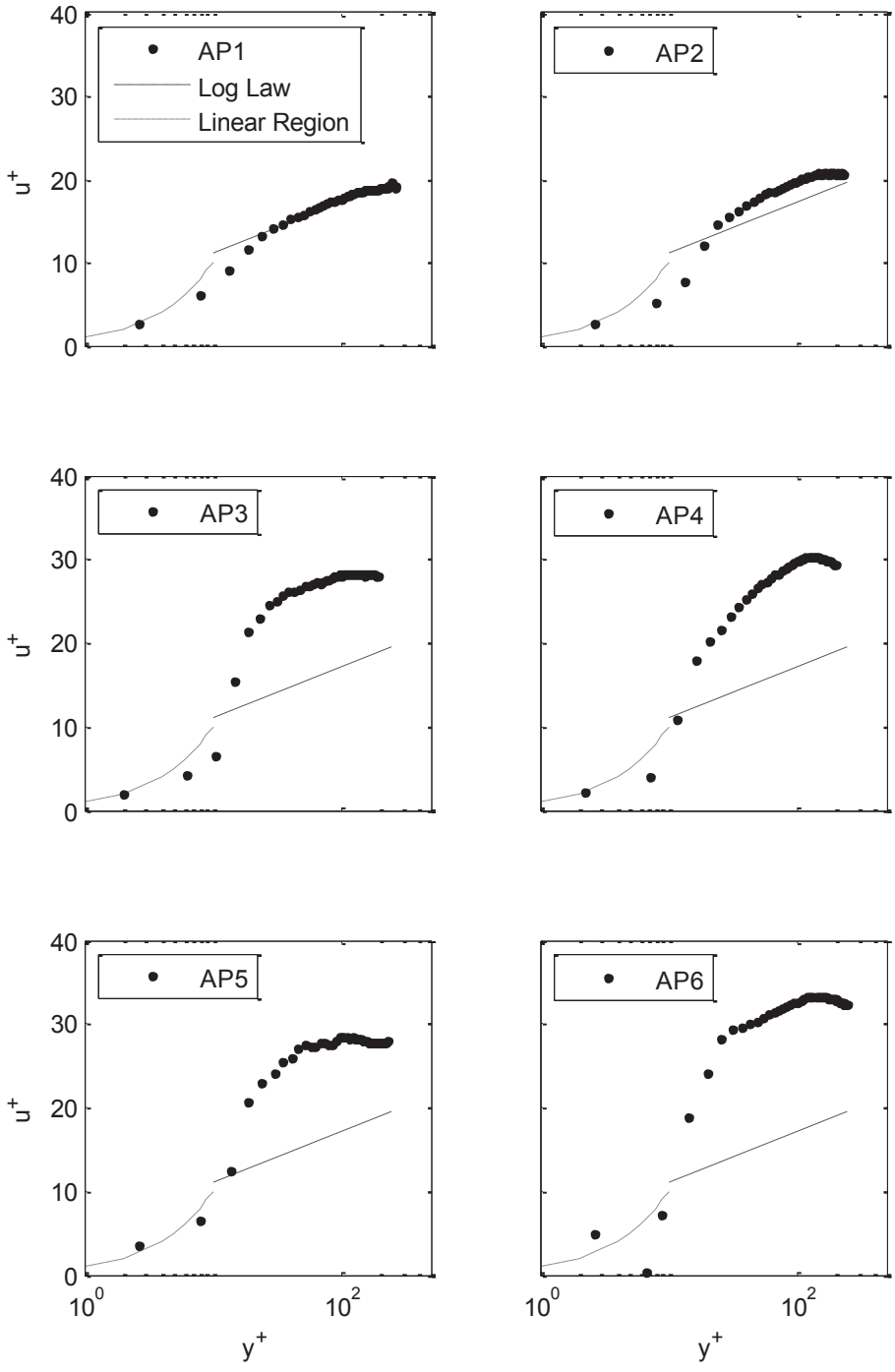

Figure G-19. Test Case B3 Mean Velocity Profiles in Inner Variables

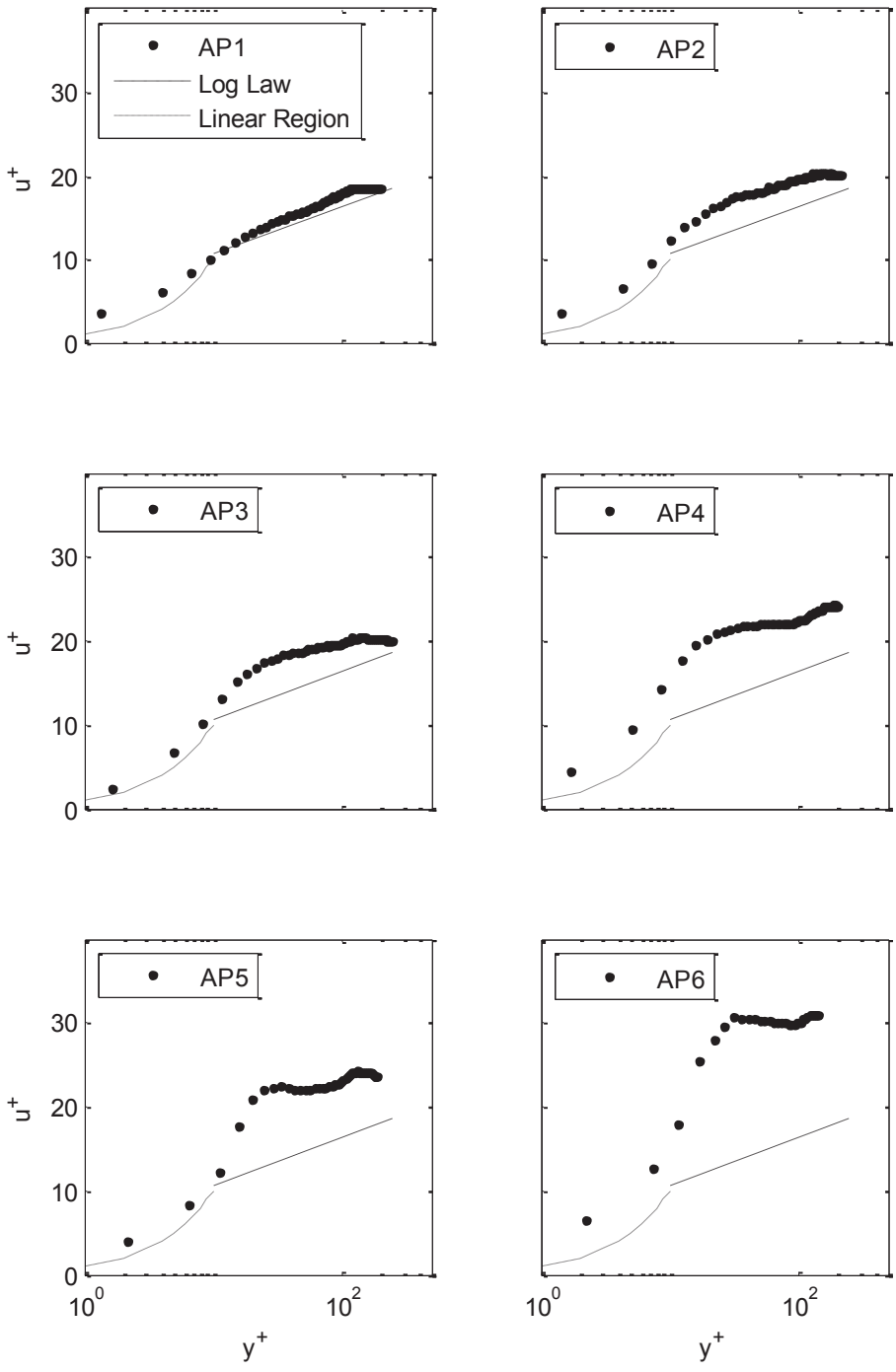

Figure G-20. Test Case B4 Mean Velocity Profiles in Inner Variables

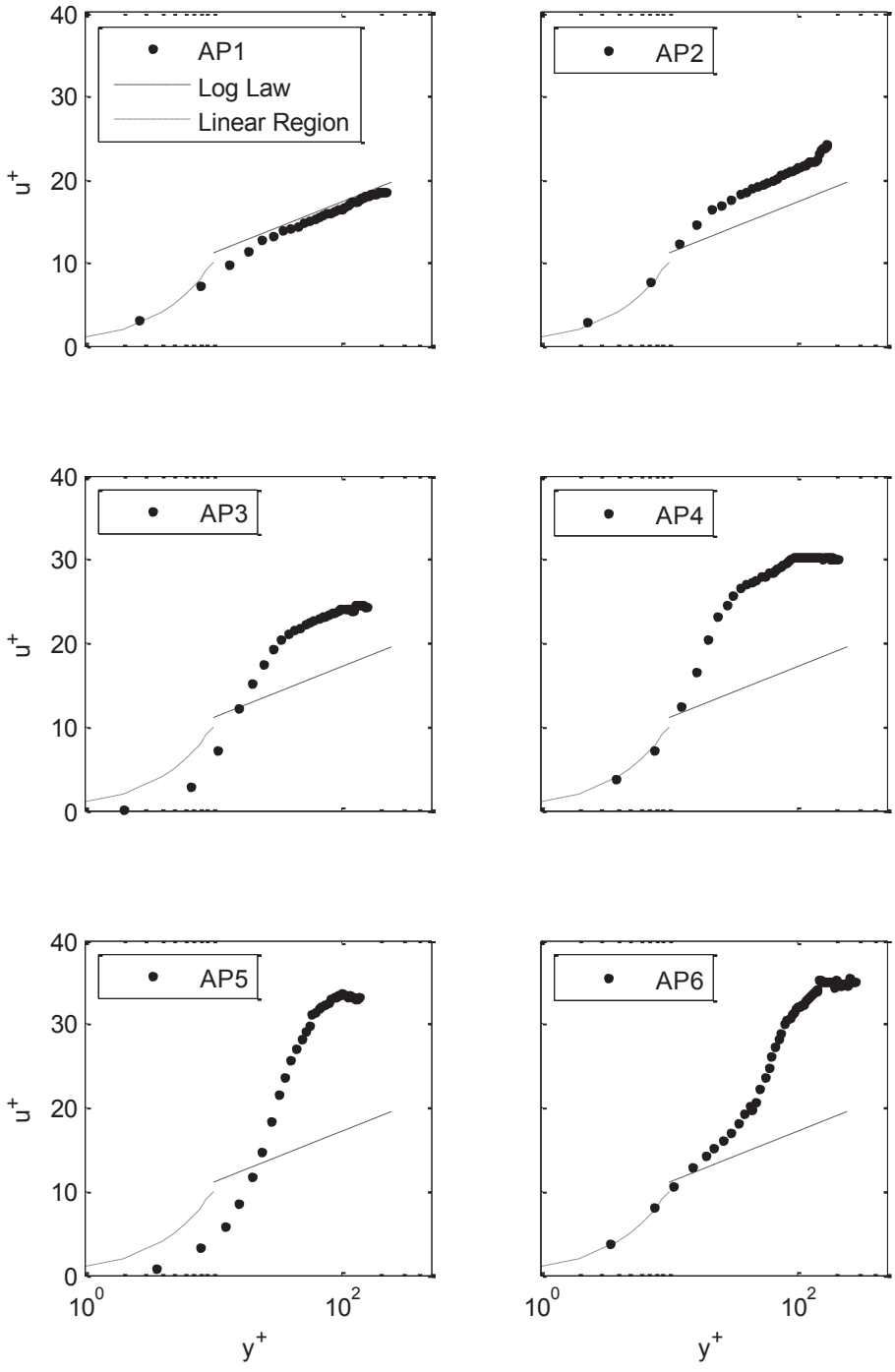

Figure G-21. Test Case C1 Mean Velocity Profiles in Inner Variables

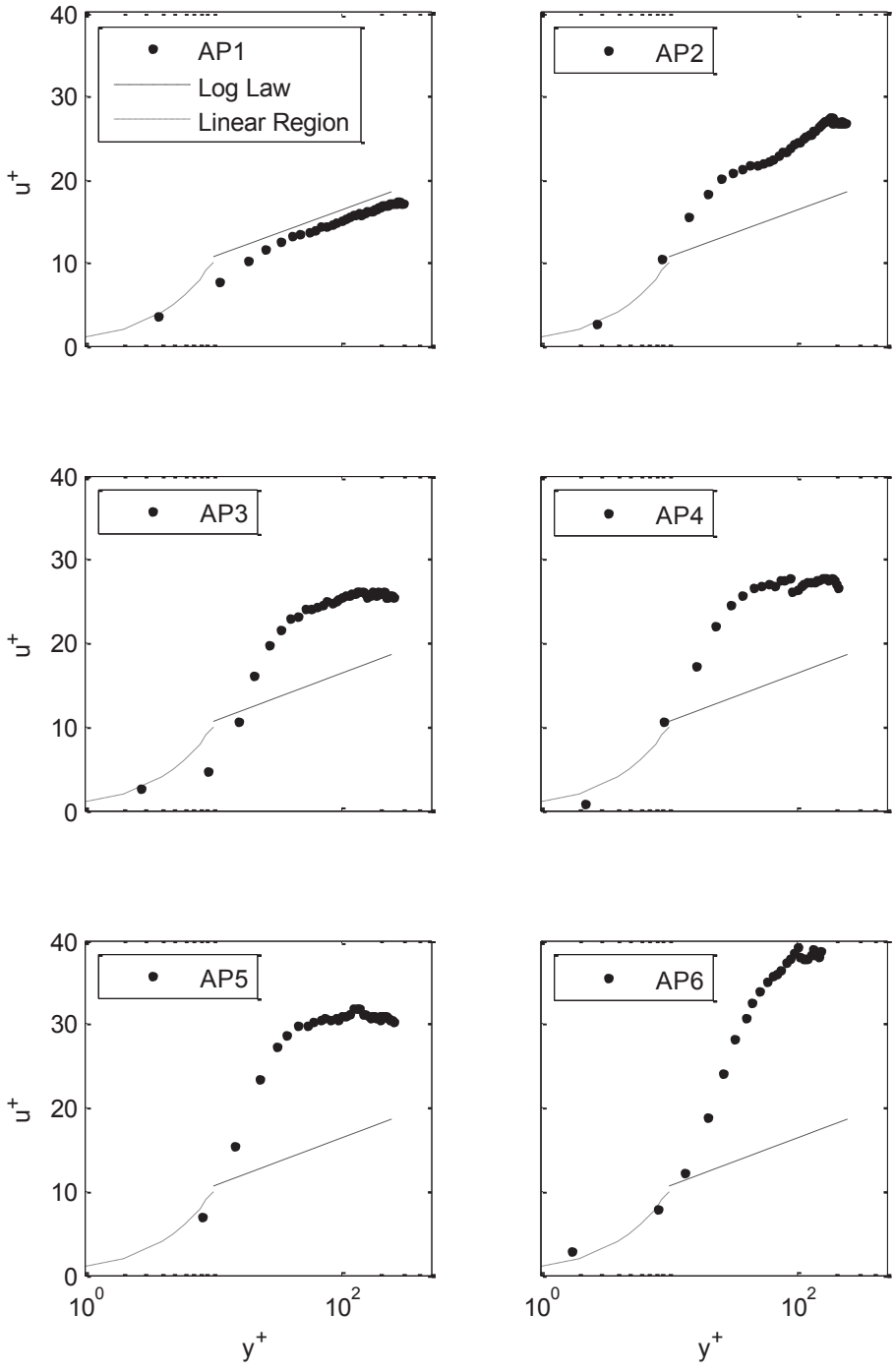

Figure G-22. Test Case C2 Mean Velocity Profiles in Inner Variables

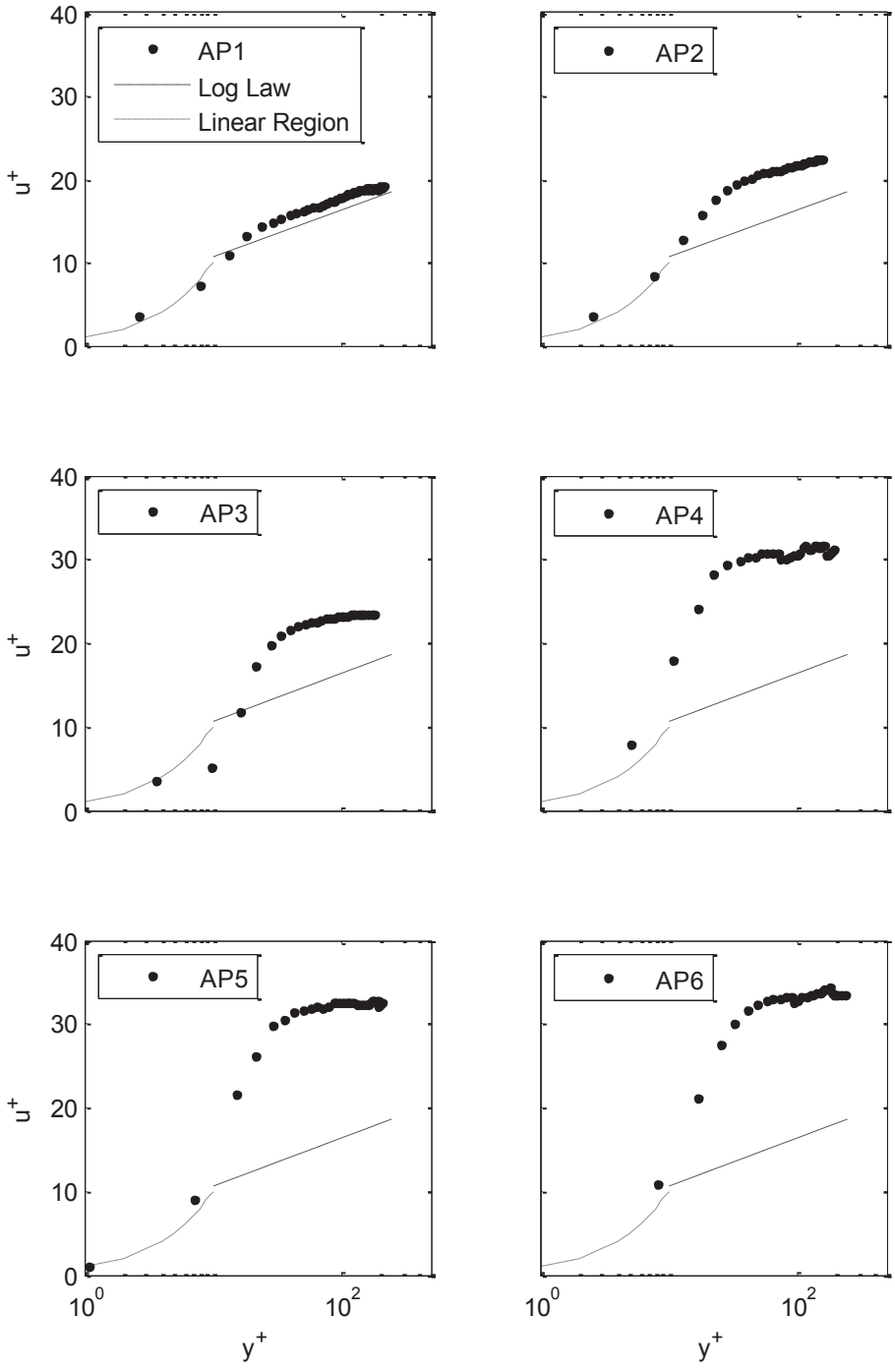

Figure G-23. Test Case C3 Mean Velocity Profiles in Inner Variables

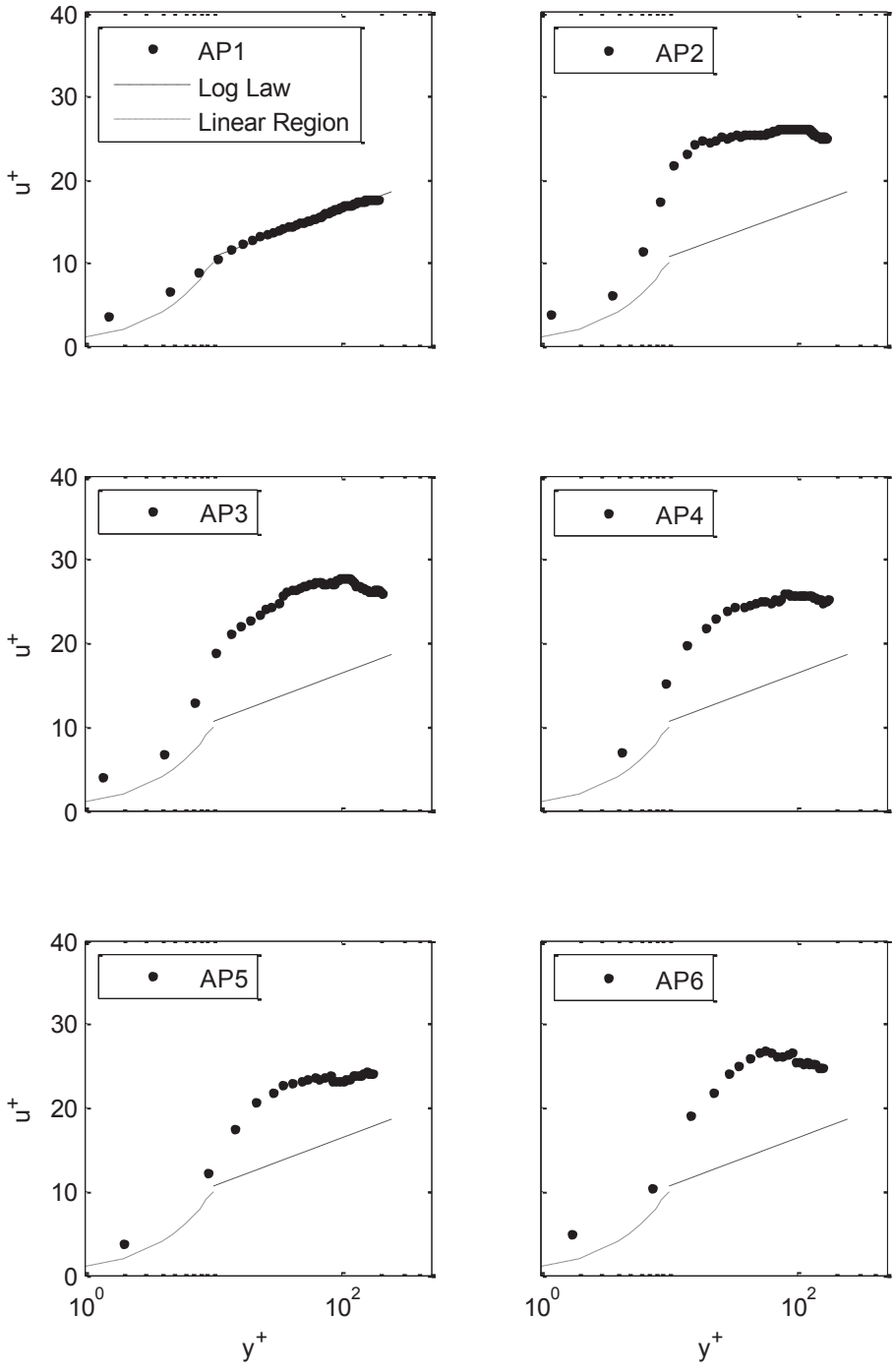

Figure G-24. Test Case C4 Mean Velocity Profiles in Inner Variables

APPENDIX H: MEAN FLOW PARAMETERS

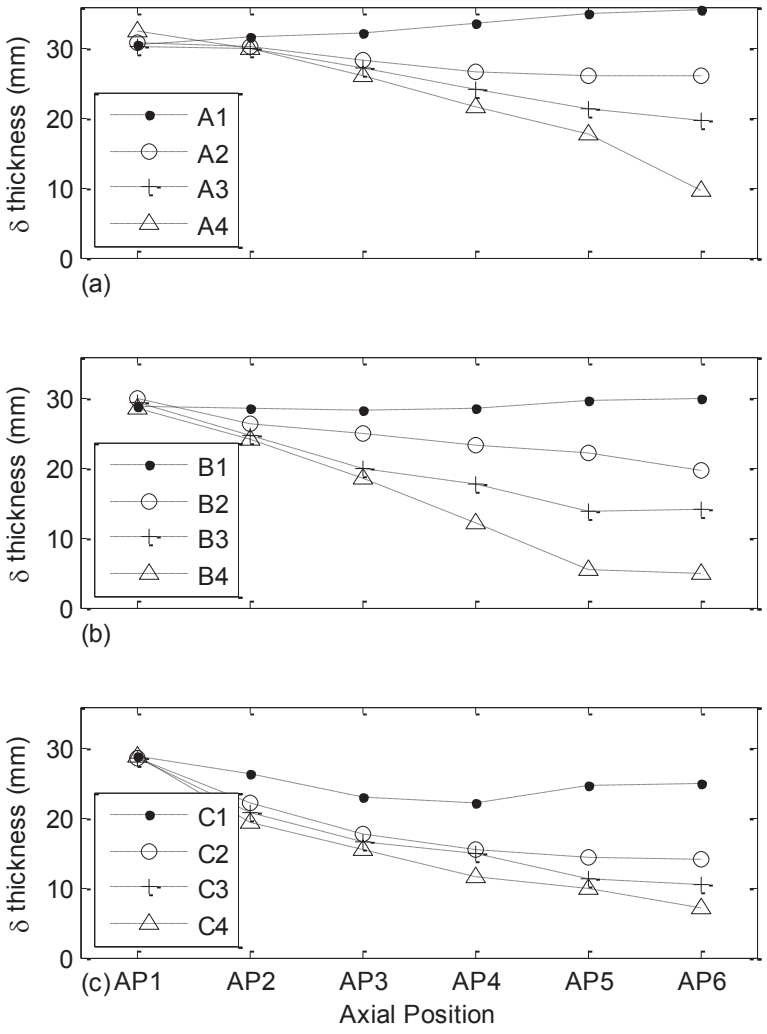

Figure H-1. Boundary Layer Thickness

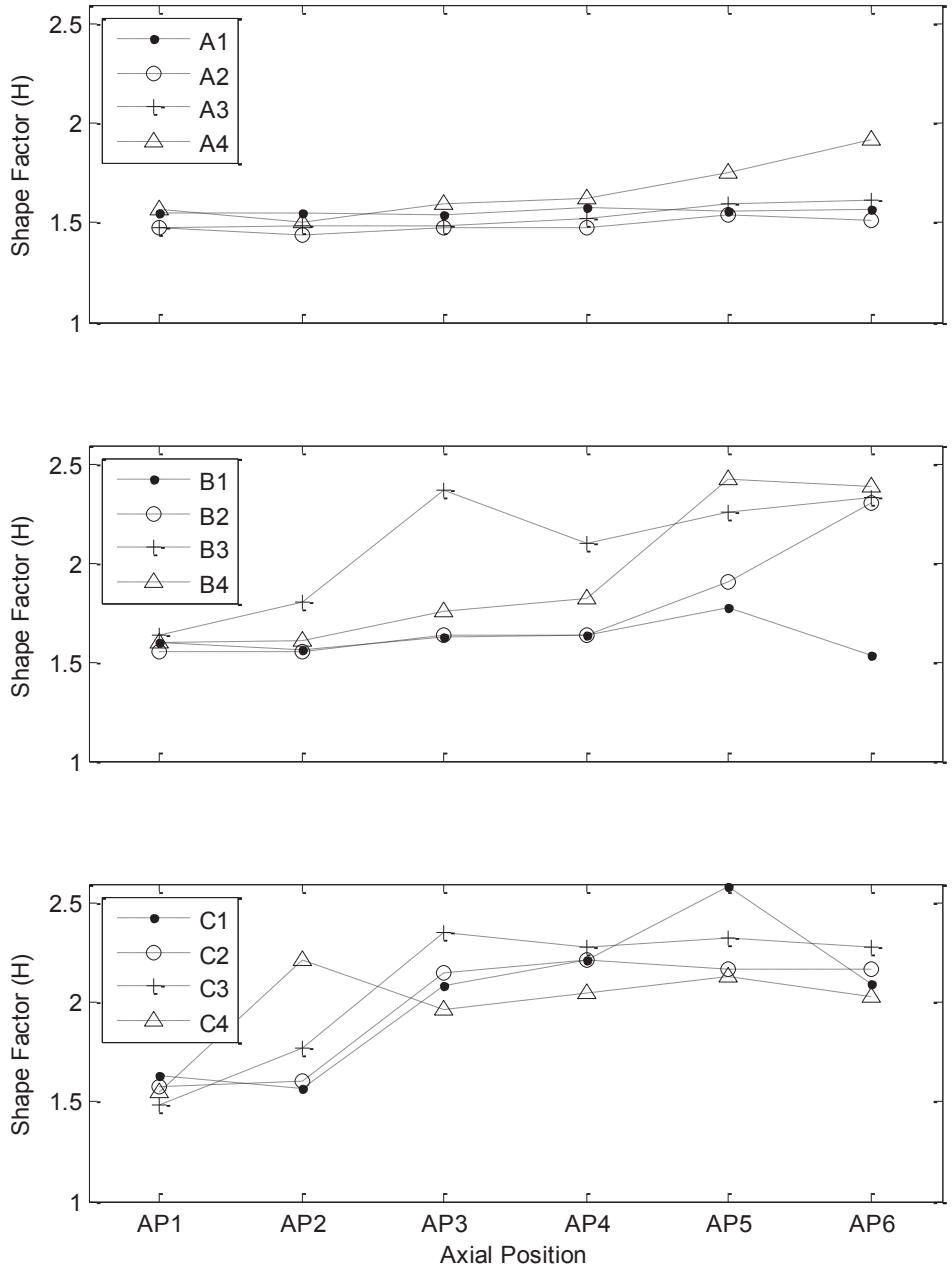

Figure H-2. Shape Factors

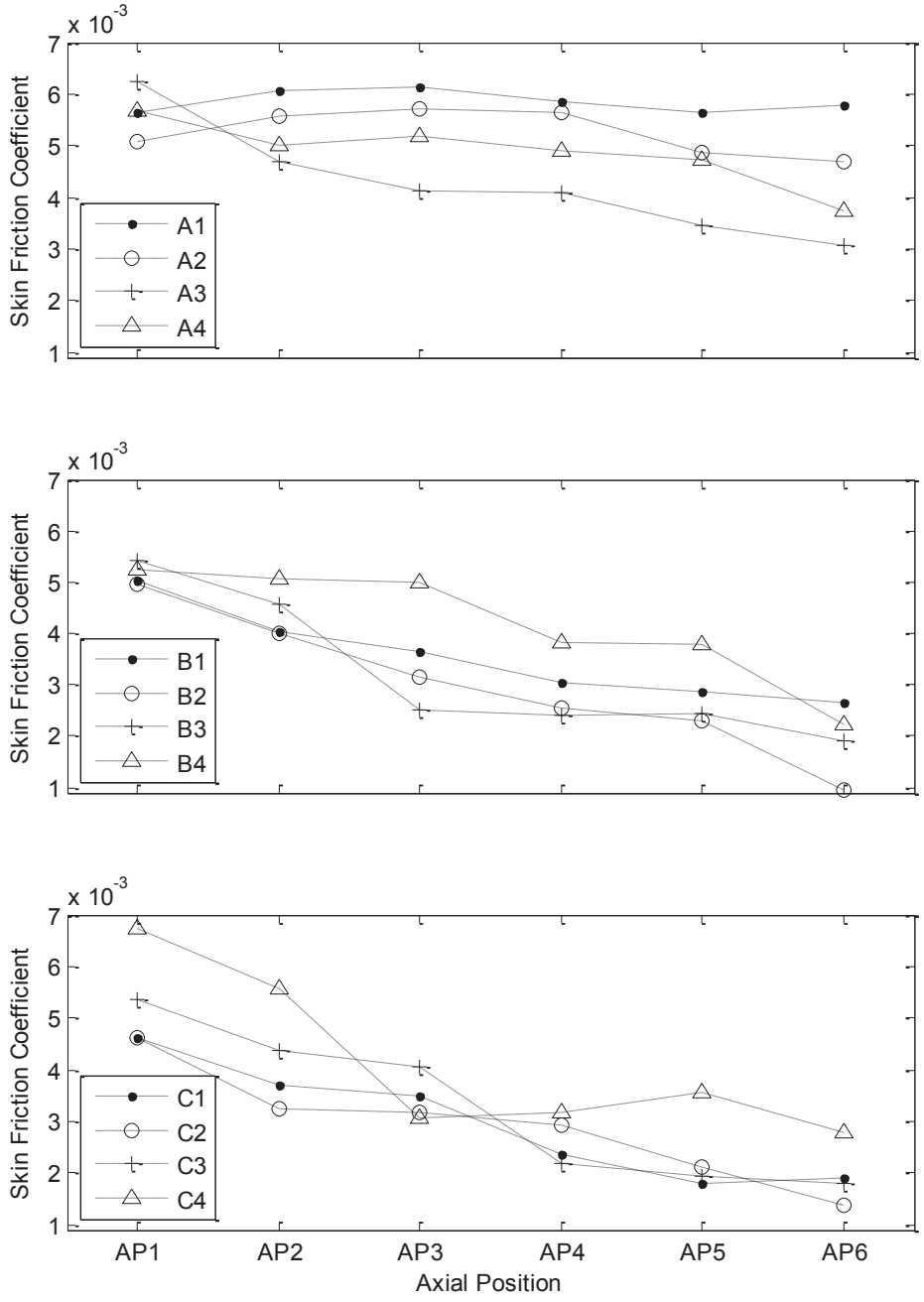

Figure H-3. Skin Friction Coefficients

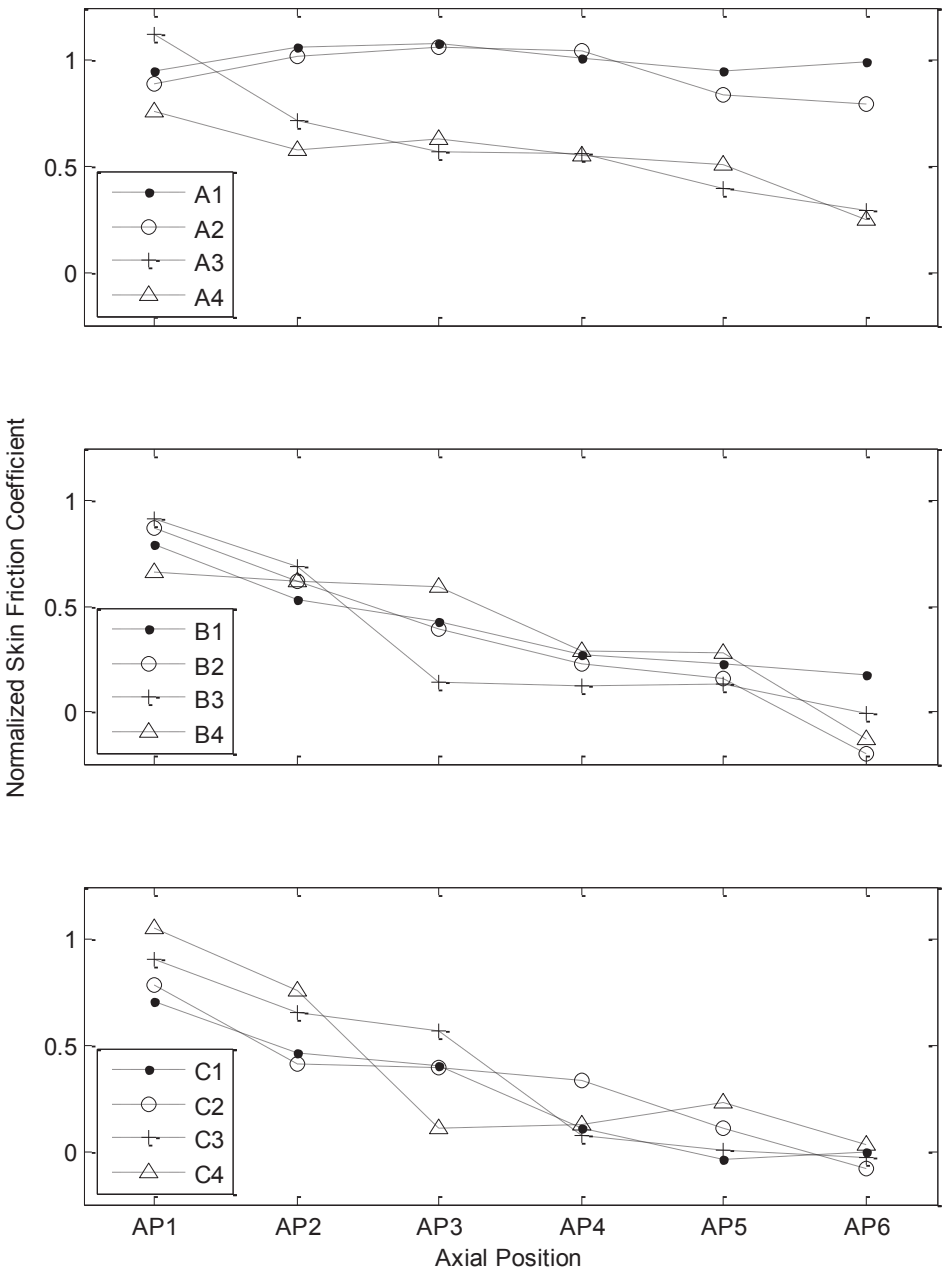

Figure H-4. Skin Friction Normalized by Flat Plate Predictions

Turbulent = 1.0; Laminar = 0.0